ISSN 1068-3755, Surface Engineering and Applied Electrochemistry, 2007, Vol. 43, No. 5, pp. 307–311. © Allerton Press, Inc., 2007.
Original Russian Text © V.F. Gologan, Zh.I. Bobanova, S.Kh. Ivashku, V.A. Mazur, B. Pushkashu, 2007, published in Elektronnaya Obrabotka Materialov, 2007, No. 5, pp. 4–8.

ELECTRICAL PRECISION TREATMENT OF MATERIALS

Features of How the Parameters of an Induction–Capacitance Device Affects the Nickel Plating Process

V. F. Gologan[a], Zh. I. Bobanova[a], S. Kh. Ivashku[a], V. A. Mazur[b], and B. Pushkashu[b]

[a] *Institute of Applied Physics, Academy of Sciences of Moldova, ul. Academiei 5, Chisinau, MD–2028 Republic of Moldova*
[b] *Center of Metrology and Automation of Scientific Research, Academy of Sciences of Moldova, ul. Academiei 3, Chisinau, MD–2028, Republic of Moldova*

Received April 13, 2007

Abstract—The experimental data obtained with various parameters of an inductance–capacitance device are discussed. It is possible to change the kinetics of the electrochemical process and the structure of nickel coatings by varying inductance *L* and capacity *C*, other electrolysis conditions being similar.

DOI: 10.3103/S1068375507050018

INTRODUCTION

Galvanic coatings of nickel are widely used due to their corrosion resistance and mechanical properties [1]. Numerous investigations have resulted in electrolyte compositions and electrolysis conditions that meet the modern requirements of industry. However, studies on the possibilities of increasing deposition efficiency and quality of coatings are still relevant. As was mentioned in earlier works, to solve these problems, special inductance–capacitance devices may be used, embedded or connected in series to rectifiers applied in galvanic works. Changing their parameters, one can significantly influence both the electrochemical process kinetics and physicomechanical properties of coatings [2]. Therefore, the goal of the present paper is to study the influence of the inductance–capacitance circuit parameters on the nickel plating process.

EXPERIMENTAL

In the present work, we used a single-phase power supply, which consisted of a 40-W transformer, a rectification block, and a parallel induction–capacitance circuit connected in series analogous to the one used in [3]. The induction was formed by connecting throttles allowing us to vary its value in the range of 2.5–30 H. The capacitance consisted of capacitors connected in parallel and varied within 2200–35 200 μF. This power supply was applied for measuring polarization curves and for coating deposition on samples for other tests.

The coatings were deposited in an electrolyte containing 320 g/l $NiSO_4$, 60 g/l $NiCl_2$, 40 g/l H_2SO_4 under the following electrolysis conditions: the electrolyte temperature was 40°C, pH was 4.5, and the current density was varied from 1 to 10 A/dm^2.

The cathode potential was recorded during nickel deposition on a 1 cm^2 platinum plate under stepwise current regulation with a lag of 20 s at each value nec-

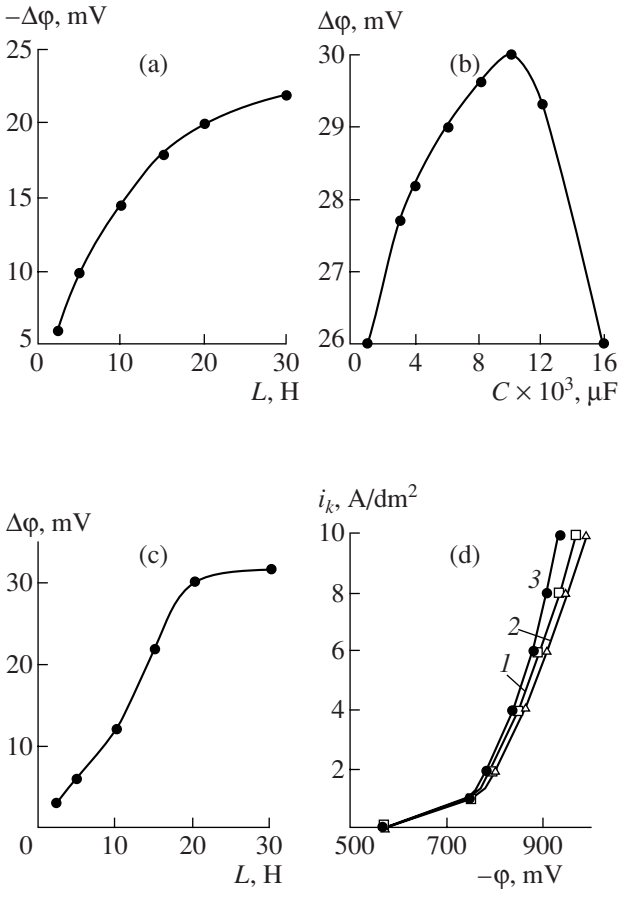

Fig. 1. Influence of the inductance–capacitance device parameters *L* and *C* on the cathode polarization: (a) influence of the inductance (*L*) on the electrode potential deviations (Δφ) from the cathode potential value for the case of the circuit absence at a current density of 10 A/dm^2; (b) influence of the capacitance on Δφ at connection of the optimal inductance (L_{op} = 20 H) at i_k = 10 A/dm^2; (c) influence of the inductance on Δφ at connection of the optimal capacitance (C_{op} = 2200 μF) at i_k = 10 A/dm^2; (d) polarization curves: *1* without the circuit; *2* at L_{op}; *3* at C_{op} and L_{op}.

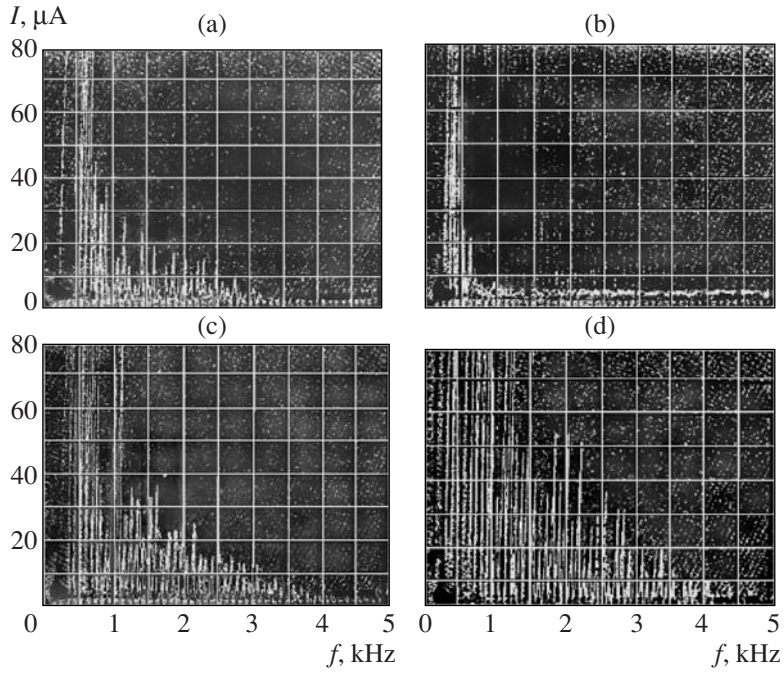

Fig. 2. Spectra of alternating components: (a) without the circuit at $i_k = 2$ A/dm^2; (b) at L_{op} and $i_k = 2$ A/dm^2; (c) at C_{op} and L_{op} at $i_k = 2$ A/dm^2; (d) at C_{op} and L_{op} at $i_k = 4$ A/dm^2.

essary for potential stabilization [4]. The current value was established by a resistance box and was measured by an M209 voltammeter. A saturated calomel electrode was used as a reference electrode. The cathode potential was measured with a B7-27A/1 voltmeter. The current form was recorded using a C1-55 oscillograph.

Alternating components in the power supply–bath circuit [5] were studied using a CK4-56 frequency analyzer.

Coatings with a thickness of 0.1 mm deposited on the samples with a surface of 0.04 dm^2 were used for studying their morphology and structure by virtue of a Tesla BS-340 scanning electron microscope. Microsections were prepared on the face-end sample surface.

RESULTS AND DISCUSSION

Our investigations have shown that variation of the inductance–capacitance device's parameters (L, C) significantly influenced cathode polarization. Figures 1a–1c, on the basis of measured polarization curves, show the difference in cathode potential deviation ($\Delta\varphi$) at a current density of 10 A/dm^2 at the connection of the inductance (Fig. 1a), L_{op} and capacitance (Fig. 1b), C_{op} and L (Fig. 1c), and the cathode potential at the same current density for the case when the circuit elements (L, C) are not connected. Figure 1d shows polarization curves at the connection of the rectifier without the circuit (curve *1*), of the rectifier and L_{op} (curve *2*), of the rectifier, L_{op}, and C_{op} (curve *3*). L_{op} and C_{op} correspond to the values of L and C at which the highest deviations $\Delta\varphi$ are obtained.

Connection of only inductance to the rectifier caused cathode potential deviation towards the more negative range. The highest deviation at a current density of 10 A/dm^2 was observed at the inductance $L = 20$ H (L_{op}). Its further increase did not cause considerable changes in the cathode potential (Fig. 1a). In experiments with $L_{op} = 20$ H and various capacitances, it was found that the capacitance value did not appreciably influence the cathode potential. At the selected values of C, the cathode potential varied by 4 mV only (Fig. 1b). The highest potential deviation towards the positive range was observed at $C = 22000$ μF (C_{op}). In the case of the inductance value variation at C_{op}, the cathode potential shifted towards the positive range, and the highest deviation was found at $L = L_{op}$. Further increase in inductance influenced the cathode polarization insignificantly (Fig. 1c). The obtained polarization curves show that at a connection only of L_{op}, the cathode potential shifted towards the negative range in comparison with the values obtained in the experiments without the circuit, and at a current density of 10 A/dm^2 it deviated by 20 mV. In the case of connection of L_{op} and C_{op}, the polarization curve shifted towards more positive range with respect to the curve obtained from the power supply without the circuit connection, and the maximal potential deviation was 30 mV at a current density of 10 A/dm^2 (Fig. 1d). Thus, changing the inductance–capacitance device parameters L and C, one can considerably influence the electrode polarization and, therefore,

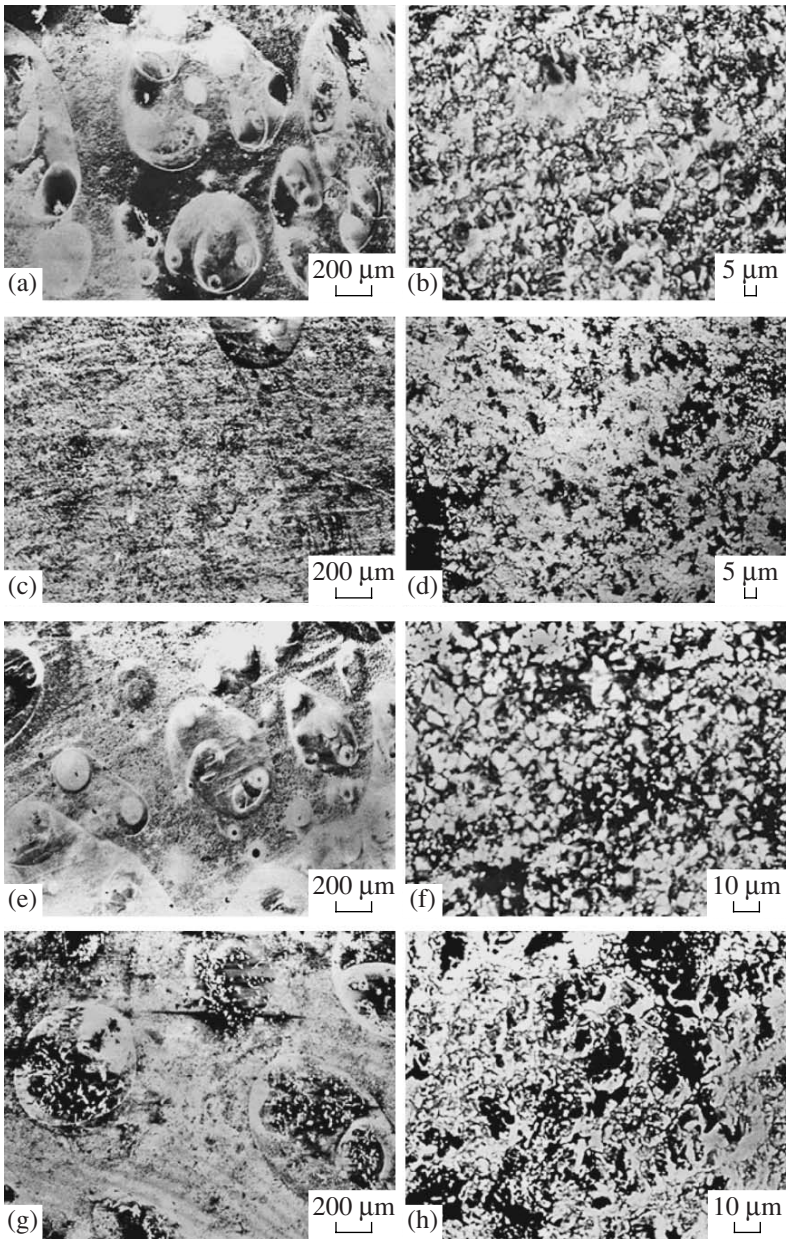

Fig. 3. Morphology of the coatings obtained: (a) (×100); (b) without the circuit at $i_k = 2$ A/dm^2; (c) (×100); (d) (×3000) at L_{op} and $i_k = 2$ A/dm^2; (e) (×100); (f) (×3000) at C_{op} and L_{op} at $i_k = 2$ A/dm^2; (g) (×100); (h) (×3000) at C_{op} and L_{op} at $i_k = 4$ A/dm^2.

structure and physicomechanical properties of nickel coatings.

Study of spectra of the alternating components in the power supply–bath circuit has shown that they differ appreciably. At a coating deposition without the circuit at a current of 80 mA (the current density being 2 A/dm^2), the maximal frequency of the alternating components was 3.3 kHz (Fig. 2a).

As well as in our previous investigations [2, 3], only the initial components of the spectrum were recorded at the inductance connection (Fig. 2b).

Connection of the inductance and capacitance (L_{op}, C_{op}) favored an increase of both the amplitude and the frequency of the spectrum components (Fig. 2c).

Similar changes took place at a current density increase ($i_k = 4$ A/dm^2, $I = 160$ mA) at the same circuit parameters (Fig. 2d).

Study of the coating morphology has shown that the coatings obtained at a current density of 2 A/dm^2 ($I = 80$ mA) without connection of the inductance–capacitance device were characterized by a high density of defects on the surface (Fig. 3a). Connection of the inductance L_{op} influenced the deposit morphology insignificantly (Fig. 3c).

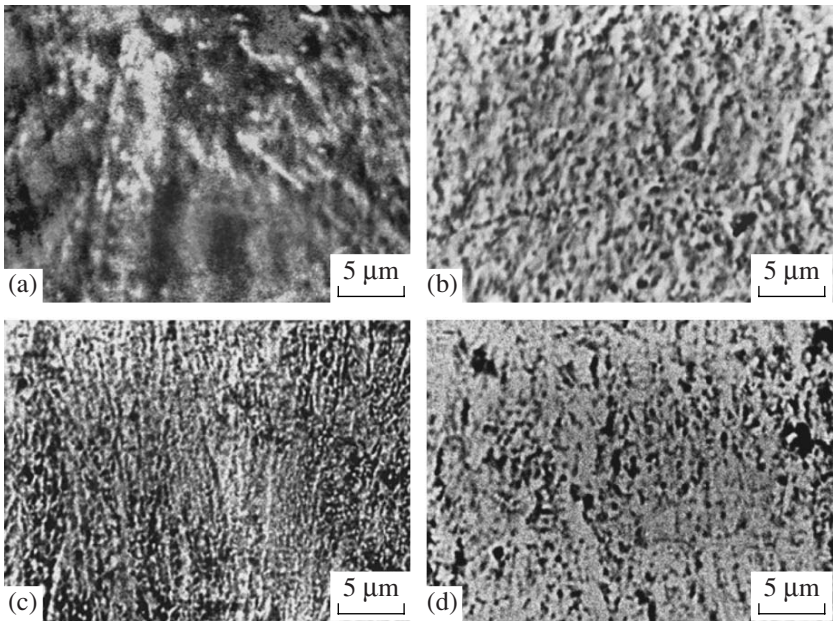

Fig. 4. Structure of the coatings obtained (×3000): (a) without the circuit at $i_k = 2$ A/dm^2; (b) at L_{op} and $i_k = 2$ A/dm^2; (c) at C_{op} and L_{op} at $i_k = 2$ A/dm^2; (d) at C_{op} and L_{op} at $i_k = 4$ A/dm^2.

In the case of the circuit connection (L_{op}, C_{op}), the quantity of defects on the surface decreased considerably (Fig. 3e). An increase of the current density up to 4 A/dm^2 ($I = 160$ mA) resulted in an absence of pitting and the formation of round outgrowths on the surface (Fig. 3g). The greatest roughness between the surface defects was found in the coatings obtained in the cases of deposition without the circuit and at connection of the inductance only (Figs. 3b and 3d). Coatings obtained with a complete device connection were smoother (Figs. 3f and 3h).

Study of the structure of coatings obtained by the above-mentioned methods has shown that connection only of the inductance L_{op} favored a decrease in crystalline aggregates (Figs. 4a and 4b). In the case of connection of the whole circuit (L_{op}, C_{op}) at the same current density of 2 A/dm^2, disperse small-crystal coatings were deposited. The increase in current density (4 A/dm^2) resulted in an enlargement of the crystalline aggregates.

The above results testify to the significant influence of the inductance–capacitance device parameters on the kinetics of deposition and structure of nickel coatings. Having compared these results with the data obtained during copper deposition (under the same conditions of experiments), one can conclude that selection of the optimal parameters of the inductance–capacitance device depends on the features of the deposited metal and the solution composition [3]. The optimal values of the inductance and capacitance for nickel plating differed from the values found for copper plating: the inductance increased from 10 to 20 H, and the capacitance, from 17600 to 19800 μF. In addition, in the case of connection of L_{op} only at a current density of 10 A/dm^2, $\Delta\varphi$ was −20 mV in the deposition of nickel coatings, and −50 mV in copper deposition. In the case of connection of L_{op} and C_{op} at the same current density, $\Delta\varphi$ was +30 mV for nickel coatings and to +50 mV for copper coating. These data show that the cathode potential varied within 50 mV in nickel deposition and within 100 mV in copper plating. Thus, optimal values of the inductance–capacitance circuit parameters depend on the nature of the deposited metal and they exert a different influence on the cathode polarization [2, 4].

Study of the alternating components has shown that at the same values of current and current density, the frequency width of the spectrum and the value of its components correlate with the cathode potential: as their value and quantity in the spectrum increase, the cathode potential shifts towards the more positive range. However, these indices of the spectrum depend on the current value (Figs. 2c and 2d). Comparing the spectra given in the present work with those obtained in copper deposition under the same conditions of electrolysis, one can see that in nickel deposition in experiments without the circuit, the highest frequency of alternating components decreased from 5 to 3.3 kHz, and in the case of connection of the circuit with the parameters L_{op} and C_{op} it decreased from 6 to 4.2 kHz. In this case, in nickel deposition, values of the alternating components decreased as well.

Changes of deposition kinetics and spectra of alternating components significantly influenced structure of nickel coatings. Under optimal conditions (L_{op}, C_{op}) more perfect structure was obtained.

CONCLUSIONS

Thus, the present study confirms the earlier obtained results [2, 3] on the possibility of applying inductance–capacitance devices for increasing the efficiency of galvanic process and for improving the physicomechanical properties of coatings.

REFERENCES

1. Vagramyan, A.T. and Petrov, Yu.N., *Fiziko–mekhanicheskie svoistva elektroliticheskikh osadkov* (Physicomechanical Properties of Electrolytic Deposits), Moscow, 1960.
2. Gologan, V.F., Electrochemical Process Control by Induction–Capacitance Devices (Review), *Elektron. Obrab. Mater.*, 2005, no. 6, pp. 39–43.
3. Gologan, V.F., Bobanova, Zh.I., Ivashku, S., Popov, V.A., and Mazur, V.A., Peculiarities of Galvanic Coating Electrodeposition Process in the Case of Single–Phase Power Supply with Embedded Induction–Capacitance Device, *Elektron. Obrab. Mater.*, 2007, no. 2, pp. 12–16.
4. Vagramyan, A.T. and Zhemagortsyants, M., *Elektroosazhdenie metallov i ingibiruyushchaya adsorbtsiya* (Metal Electrodeposition and Inhibiting Adsorption), Moscow, 1969.
5. Tyagai, V.A., Noises of Electrochemical Systems, *Elektrokhimiya*, 1975, vol. 10, no. 1, pp. 3–24.

ISSN 1068-3755, Surface Engineering and Applied Electrochemistry, 2007, Vol. 43, No. 5, pp. 312–317. © Allerton Press, Inc., 2007.
Original Russian Text © N.I. Tsyntsaru, S.S. Belevskii, G.F. Volodina, O.L. Bersirova, Yu.S. Yapontseva, V.S. Kublanovskii, A.I. Dikusar, 2007, published in Elektronnaya Obrabotka Materialov, 2007, No. 5, pp. 9–15.

ELECTRICAL SURFACE TREATMENT METHODS

Composition, Structure, and Corrosion Properties of Coatings of Co–W Alloys Electrodeposited under Direct Current

N. I. Tsyntsaru[a], S. S. Belevskii[a], G. F. Volodina[a], O. L. Bersirova[b], Yu. S. Yapontseva[b], V. S. Kublanovskii[b], and A. I. Dikusar[a]

[a] *Institute of Applied Physics, Academy of Sciences of Moldova, ul. Academiei 5, Chisinau, MD–2028 Republic of Moldova*
[b] *Vernadsky Institute of General and Inorganic Chemistry of National Academy of Sciences of Ukraine, pr. Akademika Palladina 32/34, Kiev–142, 03680 Ukraine*

Received March 20, 2007

Abstract—A correlation has been found between the composition, structure, and corrosion resistance of electrolytic Co–W coatings (on the basis of voltammeter and impedance measurements at pH-6.0 in a chloride–sulfate model solution) deposited at various densities of direct current from citrate electrolyte with a high concentration of sodium tungstate with addition of boric acid at a temperature of 58°C. It is found that these coatings possess a high corrosion resistance that is only insignificantly inferior to that of electrolyte chromium coatings. We have determined the interval of current densities of electrodeposition in which corrosion resistance of the coatings is maximum.

DOI: 10.3103/S106837550705002X

INTRODUCTION

In a number of works (e.g., [1–8]), results are presented on the investigation of composition and properties of coatings obtained in conditions of induced, i.e., joint, electrodeposition (e.g., [9]) of iron group metals (in particular, cobalt) and tungsten.

It is almost impossible to obtain functional coatings of tungsten and molybdenum from water solutions, whereas these metals may be successfully codeposited with d-metals with the obtaining of corresponding alloys.

As early as in works [1–3], it was shown that coatings of Co and W alloys possess unique mechanical, tribological, and corrosion properties. Citrate electrolytes are widely used for obtaining these alloys; the composition, structure, and properties of these coatings depend on the modes of electrodeposition [1–8]. The goal of the present work is to study the correlations of composition, structure, and corrosion properties of cobalt–tungsten coatings obtained by electrodeposition from citrate electrolytes.

EXPERIMENTAL

Electrolysis was carried out by technique [10] on steel from a citrate electrolyte [8], with the difference that the sodium tungstate concentration in the electrolyte was higher by a factor of 4 and that the deposition temperature was higher (58°C).

The electrolyte composition was the following: 0.2 mol/l Na_2WO_4·; 0.2 mol/l $CoSO_4$·; 0.04 mol/l $C_6H_8O_7$ (citric acid); 0.25 mol/l $Na_3C_6H_5O_7$ (sodium citrate); 0.7 mol/l H_3BO_3.

Two sets of experiments have been carried out: at a constant value of passed electricity (75 C) and a direct current passing up to the obtaining of a deposit with a thickness of 20 μm. For this, yields on current of the alloys were taken into account and the electrolysis time was calculated on their basis. The electrodeposition was realized by virtue of potentiostat ПИ-50-1 on round steel samples with an area of 0.025 dm^2.

For analysis of composition and morphology of the obtained deposits of cobalt–tungsten alloys, the following methods have been used:

(a) scanning electron microscopy (SEM) with a TESCAN VEGA scanning electron microscope;

(b) An INCA Energy EDX system for chemical composition investigation for determining the elemental composition of Co–W alloys. A specific feature of the method applied in the given work was that the analysis was carried out on a surface sector having a diameter of 1–2 μm and a depth of up to 2 μm. This means that in fact, a near-surface analysis was performed. The analysis was carried out at three points for each sample. For a set of measurements, average values with standard deviations were calculated.

For controlling the structure and crystal state of the obtained coatings, X-ray phase analysis was applied. Diffractograms were obtained with a DRON-3M diffractometer on CoK_α-radiation (Fe-filter, Θ/2Θ method).

Electrochemical corrosion of the obtained electrolytic Co–W alloys was studied by methods of electrochemical impedance spectroscopy and voltammetry with the AUTOLAB system (GPSTAT 20 + FRA) with GPES 4.9 and FRA 4.9 software. The effective area of

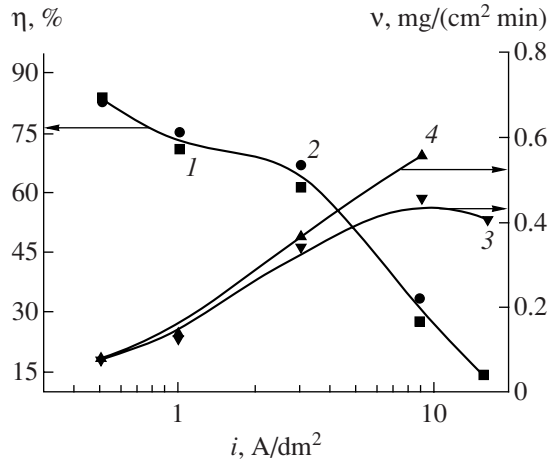

Fig. 1. Current density dependence of the yield on current (*1*, *2*) and the deposition rate (*3*, *4*) of Co–W alloys from citrate electrolyte deposited at 75 C electricity passing (*1*, *3*) and at obtaining of equal thickness of the coatings ~20 μm (*2*, *4*).

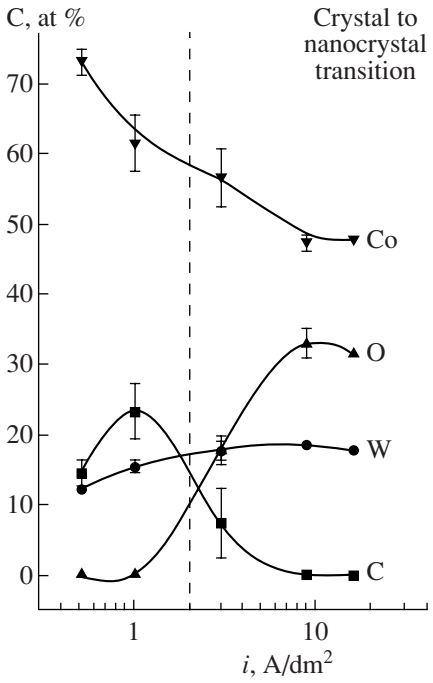

Fig. 2. Dependence of concentration of the components of Co–W alloy coatings obtained from citrate electrolyte at Q = 75 C on current density.

the samples for corrosion tests was 0.025 cm^2. Corrosion behavior for all the alloy samples was investigated in a neutral medium (pH 6.0 ± 0.1). As a model corrosion solution, a solution of mixture of sulfates and chlorides (7 g/l Na_2SO_4 + 7 g/l NaCl) was selected. The measurements were carried out at a temperature of 24 ± 1°C in a three-electrode cell with a saturated chlorine–silver reference electrode and an auxiliary electrode consisting of a platinum grid. All potential values have been reduced with respect to the saturated chlorine–silver electrode.

Spectra of the electrochemical impedance were obtained after keeping of the sample in the corrosion solution for 15 min so that a stationary potential was established. Voltage was applied in a sinusoidal mode with an amplitude of 5 mV. The corrosion process parameters were determined from an analysis of the obtained spectra (in the frequency range of 50 kHz–1 MHz).

Voltammeter measurement consisted in obtaining anode polarization curves by the point method. The rate of the potential setting was 1 mV s^{-1}. The curves were corrected by the value of ohmic voltage fall (IR). The corrosion parameters were estimated from the directions of these curves.

For comparison, on the basis of both voltammeter and impedance measurements, we determined the corrosion characteristics of electrolytic chromium coatings deposited from a standard chroming electrolyte at a current density of 0.3 A/cm^2 with a thickness of 20 μm.

RESULTS AND DISCUSSION

Influence of Current Density on Yield on Current, Electrodeposition Rate, Composition and Structure of Coatings

Earlier, in [10] it was shown that in the electrodeposition of Co–W alloys from citrate electrolytes, the yield on current decreases depending on current density. This dependence was obtained for solutions with a low concentration of tungsten salt in the electrolyte (0.05 mol/l Na_2WO_4·). In this study, a solution composition with increased content of sodium tungstate in the electrolyte was used in order to increase its content in the coating.

High deposition temperatures make it possible to improve the quality of the deposited coating surface: cracking is absent [10, 11].

Investigation of the yield-on-current dependence on the Co–W electrodeposition current density has shown that under the given conditions, a decrease in the yield on current is also observed; this dependence is sharper than in the earlier case of a "diluted" electrolyte [11]. Despite the decrease in the yield on current, the alloy deposition rate increases (Fig. 1). Since the influence of the current density was studied with both DC and AC, this made it possible to verify whether the deposition rate changes depending on coating thickness.

It follows from Fig. 1 that both the yield on current and deposition rate do not significantly depend on the method of deposition coating (Q = const, μ (coating thickness) = const); this in turn testifies to the fact that

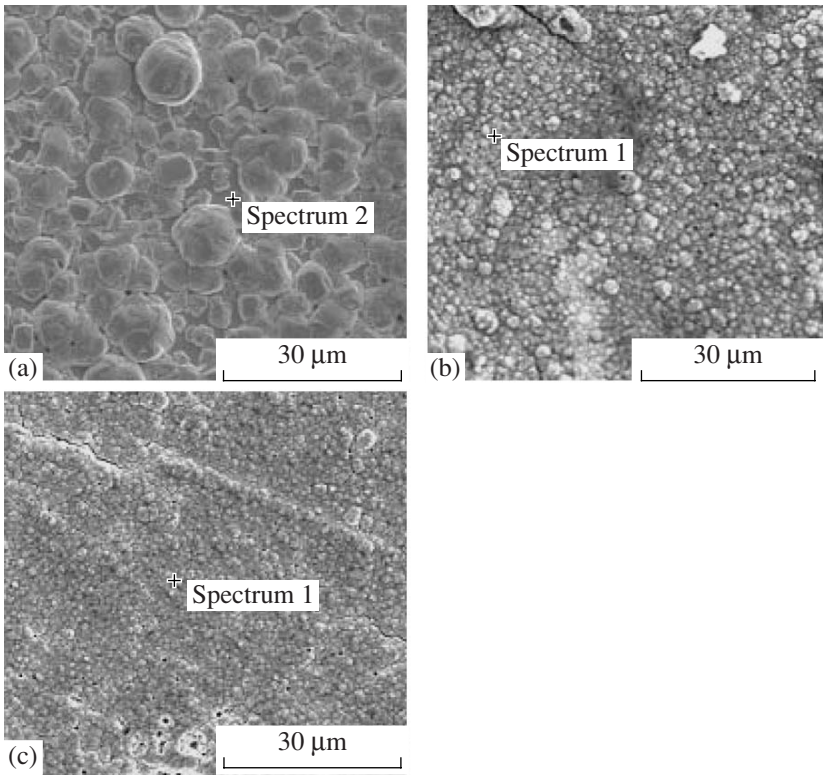

Fig. 3. SEM of the surface of Co–W alloys after electrodeposition at various current densities and temperatures, A/dm^2: 1 (a); 3 (b); 9 (c).

it is possible to deposit sufficiently thick coatings from the given electrolyte. At the same time, the data demonstrate the principal possibility of achieving a high scattering ability of the electrolyte, because in the studied range of current densities a decrease of the yield on current depending on current density at an increased coating deposition rate is observed (Fig. 1).

Investigation of electrodeposition of Co–W alloys on steel in a wide range of current densities (0.5–16 A/dm^2) has shown that the electrodeposition conditions have a significant effect on the formation of the structure and composition of coatings. The effect of current density on the composition of coatings is shown in Fig. 2. It is obvious that at relatively low current densities of 0.5–2 A/dm^2, the coatings contain mainly cobalt and tungsten. It should also be noted that at these current densities, a relatively high concentration of carbon is observed (not shown in the figure). The presence of a high measured concentration of carbon is likely due to peculiarities of the analysis, where the determining factor is the concentration of the components in the near-surface layer and, therefore, adsorbed layers with high concentration of the "organic" phase. However, as will be shown below, the presence of a high carbon concentration may be connected not only with its content in the adsorbed surface layer.

Comparative corrosion characteristics for the cobalt–tungsten coatings deposited at various current densities and for electrolytic chromium

		Voltammeter measurements			Impedance measurements
	i_{depos}, A/dm^2	$i_{corr} \times 10^5$, A/cm^2	E_{corr}, V	$V_{corr} \times 10^5$, mm/year	R_p, kΩ
Cobalt–tungsten	0.5	1.68	–0.58	1.96	5.5
	1	1.2	–0.62	1.73	6.2
	3	1.45	–0.70	1.91	11
	9	24	–0.83	34	1.0
Chromium	30	0.78	–0.77	0.75	17.8

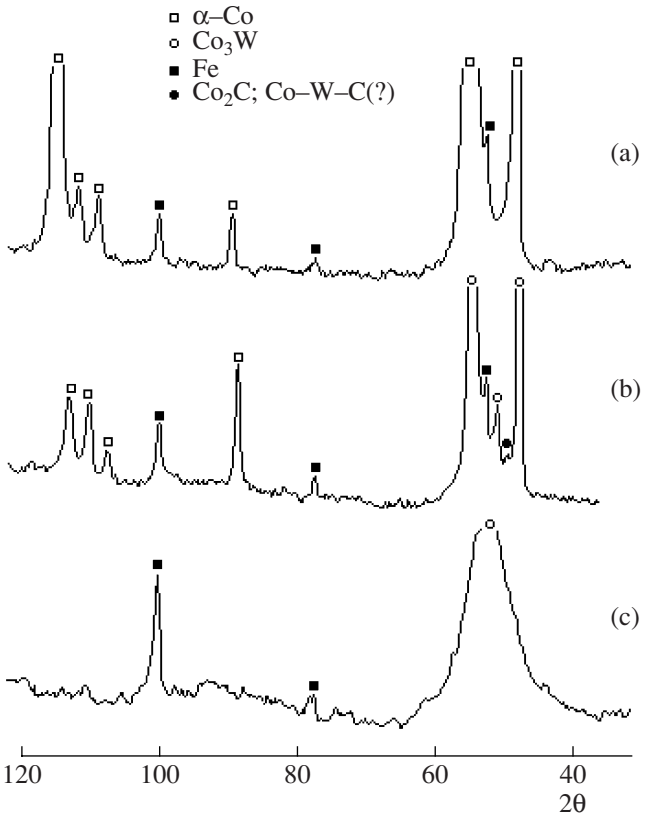

Fig. 4. Phase composition of the coatings obtained at Q = 75 C and at the current densities, A/dm^2: 0.5 (a); 1 (b); 3 (c).

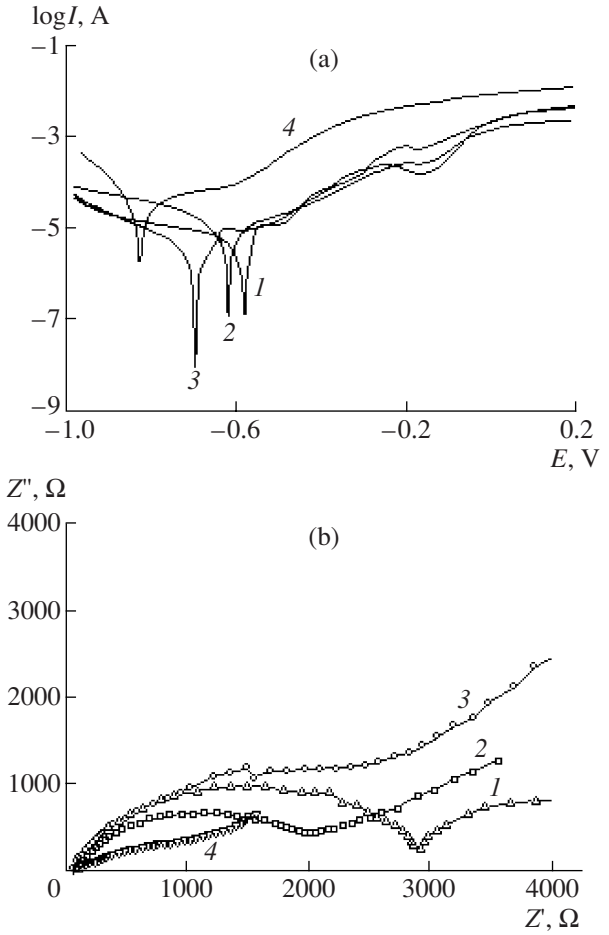

Fig. 5. Voltammeter corrosion diagrams of Co–W coatings (a) and impedance spectra of these coatings (b) obtained at the current densities, A/dm^2: 0.5 (*1*); 1.0 (*2*); 3.0 (*3*); 9.0 (*4*). Thickness of the coatings is 20 μm.

As the current density increases above 2 A/dm^2, oxygen appears in the coating composition. The oxygen content in the deposit appreciably increases as the electrodeposition current density increases. At current densities below 2 A/dm^2, the cobalt-to-tungsten ratio in the metal part of the alloys is higher or equal to three. At current densities above 2 A/dm^2, the cobalt-to-tungsten ratio in the metal part of the alloys is also close to three; that is, there is a high probability of the formation of Co_3W crystallites.

Figure 3 shows the results of investigation of the obtained layer morphology. One can see that an increase of the current density leads to formation of smaller crystal coatings, which is confirmed by the X-ray phase analysis results (Fig. 4).

Thus, the structure of the coatings obtained at 0.5 A/dm^2 is an obviously pronounced crystal one, which consists mainly of α–Co (Fig. 4a). In this case, the Co concentration in the coatings is maximal (Fig. 2). A small increase of interplanar distances in the diffraction spectrum α–Co is probably due to implantation of W atoms and formation of a solid solution (Co, W) (Fig. 4a). As the current density increases, the Co_3W crystal phase is formed. The line present in the spectrum with $d = 2.11_8$ Å ($2\Theta = 50°$) may be related to probable Co_2C or Co–W–C (Fig. 4b) phases.

One broad line, 002 Co_3W, with an interplanar distance of d = 2.06 Å is present in the diffractogram of the sample obtained at a current density of 3 A/dm^2 (Fig. 4c); that is, hexagonal Co_3W crystals lie on a substrate chiefly with the basal (0001) plane, causing an increase in the intensities of 001 and a decrease in the others. The thickness of the deposited crystallites approximated by the halfwidth of this line is about 14 Å.

Thus, an increase in the electrodeposition current density leads to formation of textured coatings of nanodimensional Co_3W crystallites and to their increased oxidation.

Influence of Electrodeposition Conditions on the Corrosion Properties of Coatings

The corrosion properties of coatings of cobalt–tungsten alloys were investigated for both relatively "thin" (7–8 μm) coatings deposited at a constant quantity of electricity and "thicker" coatings (20 μm).

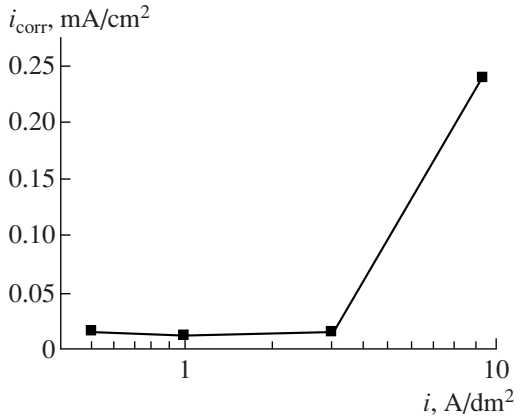

Fig. 6. Dependence of the corrosion current density in cobalt–tungsten electrolytic coatings on deposition current density. Thickness of the coatings is 20 μm.

The corrosion resistance of Co–W alloys weakly depends on the thickness of coatings. Thus, for example, according to the obtained voltammeter data, for coatings of various thickness deposited at an equal current density of 1 A/dm^2, the average values of the corrosion current density were close and just decreased insignificantly: from 4.6×10^{-5} (for thin coatings) to 1.4×10^{-5} A/cm^2 (for 20 μm). The corrosion potential for these samples in a neutral medium was –(0.60 ± 0.05) V with respect to the chlorine–silver reference electrode.

Our further investigations were concentrated on studying coatings of constant thickness (20 μm) deposited at various current densities.

For comparison, on the basis of voltammeter and impedance measurements, we have determined the corrosion characteristics of coatings of the same thickness (20 μm) of electrolytic chromium deposited from a standard chroming electrolyte at a current density of 0.3 A/cm^2.

Figure 5 shows the voltammeter corrosion diagrams of deposited Co–W alloys and their spectra of electrochemical impedance.

The corrosion characteristics of the studied alloys and electrolytic chromium calculated on the basis of the obtained data are given in the table.

One can see that lower values of the corrosion current density are observed for the coatings obtained at 1–3 A/dm^2 (see also Fig. 6). The same range of current densities corresponds to the highest values of the corrosion resistance R_p obtained from the impedance measurements. For the coatings deposited at higher current densities, a significant increase in the corrosion current (by approximately a factor of 20) is observed and, therefore, an increase of the corrosion rate as well as a decrease of the corrosion resistance (Fig. 6, table). It should be noted that according to the ten-point scale of estimating metal corrosion resistance [12], all of the studied Co–W coatings correspond to one; that is, they are corrosion-resistant in the given corrosion medium.

The last row of the table shows the corrosion characteristics of the electrolytic chromium coatings. One can see that the obtained coatings of the cobalt–tungsten alloy are close to the chromium ones in corrosion resistance, although the former are somewhat inferior to the latter.

For the coatings deposited at current densities of 3–9 A/dm^2, the corrosion potential value is close to that for the electrolytic chromium (–(0.77 ± 0.07) V). In an investigation of the voltammeter, at lower densities of the current of deposition of cobalt–tungsten alloy coatings, an enhancement of the corrosion potential is observed (table).

It is obvious that from the viewpoint of corrosion properties, optimal conditions of electrodeposition from the studied electrolyte are current densities of 1–3 A/dm^2. The increase in the current density (above 3 A/dm^2) leads to a sharp increase in the corrosion rate (Fig. 6, table). The observed effect is probably caused not only by difference in structure and morphology of deposits obtained at high current densities (Fig. 4), but also by their oxidation.

Improvement of the corrosion properties may be achieved by application of pulse electrodeposition [13]. As it was shown above, the corrosion resistance of coatings depends on their thickness; therefore, for relatively thin coatings, the pulse electrodeposition is one possible way of increasing the corrosion resistance of Co–W alloys.

CONCLUSIONS

We have studied the correlation between the composition, structure, and corrosion resistance of electrolytic Co–W coatings deposited at various densities of direct current from citrate electrolyte with a high concentration of sodium tungstate and addition of boric acid at 58°C.

On the basis of voltammeter and impedance corrosion measurements in a neutral chloride–sulfate solution, it has been found that cobalt–tungsten coatings possess high corrosion resistance, being insignificantly inferior to that of electrolytic chromium coatings. We have determined the range of electrodeposition current densities at which the coating corrosion resistance is maximum.

ACKNOWLEDGMENTS

The work was supported in part by an INTAS/Moldova grant no. 05–104–7540.

REFERENCES

1. Fedot'ev, N.P., Vyacheslavov, P.M., Kruglova, E.G., and Andreeva, G.P., Electrodeposition of Co–W Alloys and Its Properties, *Trudy Leningradskogo Tekhnol. Inst. imeni Lensoveta. Elektroosazhdenie metallov i ikh svoistva*, 1959, issue 53, pp. 82–97.

2. Brenner, F., *Electrodeposition of Alloys*, New York: Academic Press Inc., 1963.
3. Vas'ko, A.T., *Elektrokhimiya molibdena i vol'frama* (Electrochemistry of Molybdenum and Tungsten), Kiev, 1977.
4. Bondar', V.V., Grinina, V.V., and Pavlov, V.N., *Elektroosazhdenie dvoinykh splavov* (Electrodeposition of Binary Alloys), Moscow: Itogi Nauki Tekh., Ser.: Elektrokhim. 1980.
5. Zakharov, A.A. and Vyacheslavov, P.M., *Tverdye iznosostoikie gal'vanicheskie pokrytiya* (Solid Wear–Resistant Galvanic Coatings), Moscow, 1980, pp. 51–55.
6. Capel, H., Shipway, P.H., and Harris, S.J., Sliding Wear Behavior of Electrodeposited Cobalt–Tungsten and Cobalt–Tungsten–Ion Alloys, *Wear*, 2003, vol. 225, pp. 917–923.
7. Ibrahim, M.A., Abel El Kehim, S.S., and Moussa, S.O., Electrodeposition of Nanocrystalline Cobalt–Tungsten Alloys from Citrate Electrolyte, *J. Appl. Electrochem.*, 2003, vol. 33, pp. 627–633.
8. Grabco, G.Z., Dikusar, A.I., Petrenko, V.I., Harea, E.E., and Shikimaka, O.A., Micromechanical Properties of Co–W Alloys Electrodeposited under Pulse Conditions, *Surf. Eng. and Appl. Electrochem.,* 2007, vol. 43, no. 1, pp. 11–17.
9. Podlaha, T.J. and Landolt, D., Induced Codeposition. I. Experimental Investigation of Ni–Mo Alloys, *J. Electrochem. Soc.*, 1996, vol. 143, pp. 885–892.
10. Silkin, S.A., Tin'kov, O.V., Petrenko, V.I., Tsyntsaru, N.I., and Dikusar, A.I., Electrodeposition of the Co–W Alloys: Role of the Temperature, *Surf. Eng. and Appl. Electrochem.*, 2006, no. 4, pp. 7–13.
11. Tsyntsaru, N.I., Thermokinetic Processes at Electrodeposition of Chromium and Co–W Alloys, *Extended Abstract of Cand. Sci. (Chem.) Dissertation*, Chisinau, 2007.
12. Sukhotin, A.M., Chekulaeva, E.I., Knyazheva, V.M., and Zaitsev, V.A., *Korrozionnaya stoikost' oborudovaniya khimicheskikh proizvodstv: Sposoby zashchity oborudovaniya ot korrozii* (Corrosion Resistance of Equipment of Chemical Factories: Ways of Equipment Protection from Corrosion), Strokan, B.V. and Sukhotin, A.M., Eds., Leningrad: Khimiya, 1987.
13. Kublanovsky, V., Bersirova, O., Yapontseva, J., Tsintsaru, N., Belevskii, S., and Dikusar, A., Pulse Electrodeposition of Cobalt–Tungsten Alloys from Citrate Electrolyte on Steel, Its Corrosion Characteristics, *Physico–Chemical Mechanics of Materials*, 2007, no. 6, special issue, pp. 80–90.

ISSN 1068-3755, Surface Engineering and Applied Electrochemistry, 2007, Vol. 43, No. 5, pp. 318–335. © Allerton Press, Inc., 2007.
Original Russian Text © F.P. Grosu, M.K. Bologa, B.B. Bloshchitsyn, Yu.K. Stishkov, I.V. Kozhevnikov, 2007, published in Elektronnaya Obrabotka Materialov, 2007, No. 5, pp. 16–38.

ELECTRICAL PROCESSES IN ENGINEERING AND CHEMISTRY

Charge Formation in Liquid Dielectrics under the Influence of Electrostatic Field

F. P. Grosu[a], M. K. Bologa[a], B. B. Bloshchitsyn[b], Yu. K. Stishkov[b], and I. V. Kozhevnikov[a]

[a] *Institute of Applied Physics of the Academy of Sciences of Moldova, ul. Academiei 5, Chisinau, MD-2028 Republic of Moldova*

[b] *St. Petersburg State University, Physical Faculty, Electrophysics Research and Educational Center, ul. Ul'yanovskaya 3, St. Petersburg, Petrodvorets, 198504 Russia*

Received August 16, 2007

Abstract—Charge formation in liquid dielectrics under the influence of an electrostatic field is considered. Systematization of various types of electrization and their physical interpretations, as well as their mathematical descriptions are presented. Mechanisms of electrization, which can be subdivided into equilibrium, with and without taking into consideration diffusion currents, and nonequilibrium, with and without taking into consideration diffusion currents, are discussed. It is shown that, depending on the properties of the media, external field, and other factors, some mechanisms can be realized. Bipolar structures of the space charge are explained and the results of the numerical simulation of charge formation and current flow are given. Interrelation between media electrization and the Ohm law is considered.

DOI: 10.3103/S1068375507050031

1. Introductory remarks. Applying an external electrostatic field to a dielectric liquid results in its electrization and, with time, some distributions of electric potential $\varphi(\vec{r})$, field intensity $\vec{E}(\vec{r})$, and space charge density $\rho(\vec{r})$ are settled in it in accordance with electrodynamics formulas

$$\rho = \nabla(\varepsilon\vec{E}) = -\nabla(\varepsilon\nabla\varphi), \quad (1)$$

where $\varepsilon = \varepsilon_0\varepsilon_r$ is the medium absolute permittivity and $\vec{r}$ is the radius–vector of the observation point.

The phenomenon of electrization (charge formation) in a liquid dielectric has far-reaching consequences. Firstly, it substantially reflects on transfer processes in the liquid, in particular on the Ohm law. Secondly, as the case at hand is the flowing medium, secondary effects, called electrohydrodynamic (EHD) effects [1], originate that are caused by the interaction of the external field with the liquid that is electrically charged under its influence; i.e., Coulomb forces with volume density $\vec{f} = \rho\vec{E}$ EHD phenomena in turn lead to a new electricity-, heat-, and mass-transfer mechanism that is either molar or convective. More exactly, it leads to an electroconvective mechanism, as it is caused by electric convection [2], which is an analogue of a natural mechanism in the gravitation field. Fluid electrization, the physical mechanisms of which may be rather varied, including induction by a sudden nonuniformity in the electric field, such as at corona discharge, attended by the electric wind in gases [2,3] and liquids [4], is the initial cause. This type of electrization is reasonably well studied (see, for instance, [1–4]) and, in the following, we will dwell on only the *uniform external field*, by which we mean the field of the parallel-plate capacitor without the edge effects. Then distributions $\varphi(x)$, $E(x)$, $\rho(x)$ will signify the dependences of these quantities on coordinate x, transverse to the capacitor plates. As is evident from Eq. (1), knowing that it is possible to obtain ($\rho(x)$) and then $\varphi(x)$ by the method of numerical and graphical differentiation, the medium electrization $E(x)$ by the electric potential distribution $\rho(x)$ can be unambiguously judged. The distribution of $\varphi(x)$ is found experimentally by the electric-probe method [5–7]; sometimes the Kerr method [8] is used

The systematization and discussion of distributions $E(x)$ and $\rho(x)$, revelation of their physical mechanisms, and the creation of simple mathematical models that are descriptive of the considered phenomena are the purpose of this investigation. As the principle factor in electrohydrodynamics is the force $\rho\vec{E}$, the noted systematization has been conducted with respect to $E(x)$ and $\rho(x)$.

2. Variety of electrization types. The typical cases of electrization can be classified according to the mathematical peculiarities of dependences $E(x)$ and $E'(x) = \rho/\varepsilon$. For this purpose we will qualitatively build the plots of these functions (according to the experimental data for $\varphi(x)$ [5–7], or $E(x)$ [8]), presented and systematized in Fig. 1, where representative cases of relationships are situated in rectangular cells ("frames"); $E(x)$ is not shaded, $\rho(x)$ is crosshatched, and the anode is placed at the left. The table (Fig. 1) cannot be consid-

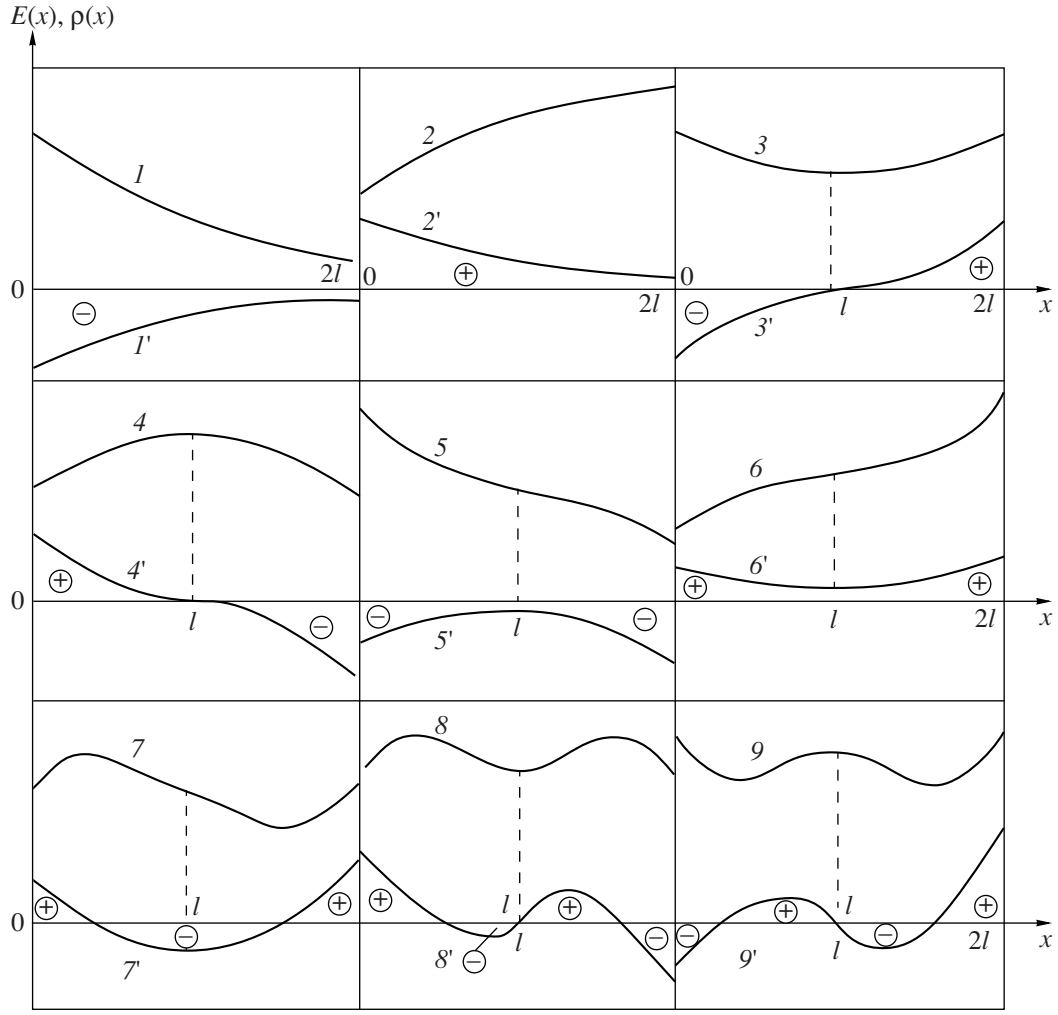

Fig. 1. Distributions of dependences: $E(x)$ is not shaded and $\rho(x)$ is crosshatched.

ered representative of all of the varieties of electrization and may be widened later on.

In the first two frames, the dependences $E(x)$ are monotonic, meaning that the interelectrode space $0 \le x \le 2l$ is filled with a similar space charge—in the case of curve *1*, the charge is negative ($\rho(x) < 0$, curve *1'*), while for curve *2*, it is positive, ($\rho(x) > 0$). Therefore, we can speak about monopolar charging, positive or negative according to curves (*2*, *2'*) and (*1*, *1'*). In frames *3*, *4* reduction of $E(x)$ passes into growth (curve *3*) and vice versa (curve *4*). Consequently, the interelectrode layer divides into two sublayers and, in case *3*, each of them is of the opposite sign of the adjacent electrode, while in case *4*, they are of the same sign. Thus, this type of charging is commonly called [5] hetero- and homocharging or hetero- or homoelectrization. Distribution *5* is presented in [8] and belongs to monopolar electrization as *1*; however, unlike the last one, relationship $\rho(x)$ has an extremum. Curve *6* is an analogue of curve *5* when their charges exchange their roles, which is easily seen from distributions for charge densities (curves *5'*, *6'*).

In frames *7–9*, cases of so-called "bipolar" structures are depicted [6, 7] in which the semilayers themselves are bipolar charged, with the layer (Fig. 1, curve *7*) immediately adjacent to the anode being charged similar to the electrode; hence, sublayer $0 < x < l$ is homopolar and the right one ($l < x < 2l$) is heterobipolar. Similarly, in frames *8* and *9* we have, respectively, homo- and heterobipolar structures. Furthermore, curves *3–9* (*3'–9'*) reflect some symmetry (about the central plane $x = l$), yet actually the symmetry is far from complete, as electrophysical properties (mobility, valency, potential of ionization, etc.) of charge carriers can differ significantly. Notice that distributions of type *7* and *8* are found by the authors [6, 7], while those of type *9* are theoretical [9].

A further problem consists of the physical study of the distributions presented in Fig. 1 and their mathematical description.

3. General initial equations. When considering the physical mechanisms of charge formation processes, we consider EHD phenomena as secondary mechanisms to be absent, i.e., that the hydrodynamic velocity is $\vec{\upsilon} \equiv 0$.

As in practice, we frequently deal with multi-ion systems, Nernst–Planck equations for every component of current density should be assigned to the principal systems [1], for example,

$$\vec{j}_i^{\pm} = k_i^{\pm}\rho_i^{\pm}\vec{E} \mp D_i^{\pm}\nabla\rho_i, \tag{2}$$

where i sweeps all the values of the numbers of positive and negative charge carriers. Coefficients of mobility $k_i^{\pm}$ and diffusion $D_i^{\pm}$ are connected by the known Einstein relation [10]

$$D_i^{\pm} = \frac{k_B T}{q_i^{\pm}} k_i^{\pm} = \frac{k_B T}{e z_i^{\pm}} k_i^{\pm}, \tag{3}$$

where k_B is Boltzmann's constant, $z_i^{\pm}$ is the charge carrier valency, and e is the electron charge.

Each component (2) should satisfy the complex equation of the conservation of charge of the type (steady case)

$$\nabla \vec{j}_i^{\pm} = W_i - k_{ri} n_i^{+} n_m^{-}, \tag{4}$$

where the first term of the right part reflects the process of neutral (molecules, ion pairs, etc.) decay to charged components corresponding to the known Onsager formula [11]

$$W_i = W_{0i}\exp[2(e^3 E/\varepsilon)^{1/2}/k_B T], \tag{5}$$

the second one reflects the reverse process of the charged carrier recombination (k_r is the recombination coefficient); and $n_i^{\pm}$ is the concentrations of carriers related by charge densities by the formulas

$$\rho_i^{\pm} = e z_i^{\pm} n_i^{\pm}. \tag{6}$$

A category of problems of liquid electrophysics exists in which the decay effects and interaction of charges are neglected. These are cases when both of the addends in the right part (4) are zero, which is likely to be expected in high-resistance liquid dielectrics or when these effects are mutually compensated for, i.e., at dynamical equilibrium between the processes of birth and death of charge carriers. In both cases, the right part of (4) is zero. Such a category of problems can be called the "equilibrium" category as opposed to the case of the inequality to zero of the right part of (4) when the mentioned equilibrium is absent ($\nabla \vec{j}^{\pm} \neq 0$); thus, we can speak about nonequilibrium processes of current passage, charge formation, etc.

In the initial stages of the solution of the liquid dielectric electrization problem, efforts have been undertaken to simplify complex equations of the processes under examination. In particular, the problem can be approximately boiled down to a two-component problem in much the same way as Levich [12] accomplished through the introduction of the averaged coefficients of mobility and diffusion [9]

$$k^{\pm} \equiv \frac{\sum k_i^{\pm}\rho_i^{\pm}}{\sum \rho_i^{\pm}}; \quad D^{\pm} \equiv \frac{\sum D_i^{\pm}\rho_i^{\pm}}{\sum \rho_i^{\pm}}. \tag{7}$$

Then, equations (2)–(6) are simplified significantly as follows:

$$\vec{j}^{\pm} = k^{\pm}\rho^{\pm}\vec{E} \mp D^{\pm}\nabla\rho^{\pm}, \tag{8}$$

where

$$\rho^{\pm} \equiv \sum \rho_i^{\pm} \Rightarrow \rho = \rho^{+} - \rho^{-} \equiv \sum \rho_i^{+} - \sum \rho_i^{-}. \tag{9}$$

Continuity equation (4) assumes the form

$$\nabla \vec{j}^{\pm} = \pm W \mp K_r \rho^{+}\rho^{-}, \tag{10}$$

where (6) is taken into account.

Notice that field distribution around the plate capacitor middle plane ($x = l$, Fig. 1, curves *3–9*) can be symmetric (even or odd). Evidently, this should be expected only if the charge carrier properties are the same, in particular,

$$k^{+} = k^{-} \equiv k; \quad z^{+} = z^{-} \equiv z; \quad D^{+} = D^{-} \equiv D.$$

Consequently, if field distribution symmetric structures are found, then, besides other possible conditions, these equalities should be taken into account. However, they are not of fundamental importance, as only the symmetry of the corresponding distributions breaks when they are not fulfilled; thus, for simplicity, we take into consideration $k^{\pm} = k$, $D^{\pm} = D$.

4. Main set of equations. By the addition and subtraction of equations (8), (10), in view of (9), Gauss–Ostrogradskii equations, and field potentiality, we obtain the main set in the form

$$\begin{cases} \vec{j} = \sigma\vec{E} - D\nabla\rho; \quad \nabla\vec{j} = 0; \\ \rho = \nabla(\varepsilon\vec{E}); \quad \vec{E} = -\nabla\varphi; \\ \vec{\delta}_j = k\rho\vec{E} - \dfrac{D}{k}\nabla\sigma; \\ \nabla\vec{\delta}_j = R; \\ \rho = \rho^{+} - \rho^{-}, \end{cases} \tag{11}$$

with the following designations:

$$\begin{cases} R = 2W_0 \exp[2(e^3E/\varepsilon)^{1/2}/k_BT] - 2K_r\rho^+\rho^-; \\ \vec{j} \equiv \vec{j}^+ + \vec{j}^-; \quad \vec{\delta}_j \equiv \vec{j}^+ - \vec{j}^-; \quad \sigma \equiv k(\rho^+ + \rho^-). \end{cases} \tag{12}$$

The set is written in vector form to be applicable to arbitrary electrodes (further stages of investigations). In the case of the parallel-plate capacitor, the set of equations (11), solved with respect to the derivatives, assumes the form

$$\begin{gathered} \rho' = \frac{\sigma}{D}E - \frac{j}{D}; \quad \rho(x)|_{x=l} = \rho_0 \\ E' = \rho/\varepsilon; \quad E(x)|_{x=l} = E_0 \\ \sigma' = \frac{k^2}{D}\rho E - \frac{k}{D}\delta_j; \quad \sigma(x)|_{x=l} = \sigma_0 \\ \delta_j' = R; \quad \delta_j(x)|_{x=l} = \delta_{j_0} \\ \varphi' = -E; \quad \varphi(x)|_{x=l} = 0; \quad \varphi(x)|_{x=0} = U; \\ \varphi(x)|_{x=2l} = -U, \end{gathered} \tag{13}$$

where the initial conditions are also presented, where the function determination domain is $0 \le x \le 2l$, $2l$ is the interelectrode spacing, and the origin of the coordinates is made coincident with the anode. Taking into account expressions (11) and (12) for ρ and σ, the charge source function R becomes

$$R = 2W_0 \exp[2(e^3E/\varepsilon)^{1/2}/k_BT] - \frac{1}{2}K_r\left(\frac{\sigma^2}{k^2} - \rho^2\right). \tag{14}$$

Set (13) with regard for (14) is of the first order with the initial conditions (Cauchy problem). The existence of the solution and its uniqueness are ensured by the known theorems.

5. Possible mechanisms and mathematical models of electrization. Having formulated the main sets (11)–(13), we can begin an examination of particular cases from the viewpoint of the interpretation of experimental results, partly reflected in Fig. 1.

5.1. Conduction mechanisms ($j \neq 0$, $D = 0$). First, we consider the case of the presence of a current in the circuit and the negligible role of diffusion.

5.1.1. Electrization caused by medium nonuniformity. $\{\tau\} \neq 0$; $T \neq$ const. From the first three equations of set (11), at $D = 0$, we obtain the simplest mechanism of electrization

$$\rho = \vec{j}\nabla\tau, \quad \tau \equiv \varepsilon/\sigma, \tag{15}$$

meaning that penetration of the medium that is nonuniform in the electric relaxation time τ by electric current, in the general case, results in its electrization. It is particularly clear that if the current crosses the interface of two media with different τ, when it stems from formula (1), surface charge with density originates

$$\gamma = j_n(\tau_2 - \tau_1). \tag{16}$$

Due to this charge, a compensating field arises that provides the continuity of the current ($\sigma_1E_{1n} = \sigma_2E_{2n}$). Another case, which is well-explained by formula (15), is a thermally nonuniform medium ($T \neq$ const) by virtue of the known relationship $\varepsilon(T)$, $\sigma(T)$, and, consequently, $\tau(T)$. From (15), it follows that

$$\rho = \vec{j}\frac{d\tau}{dT}\nabla T \equiv -\tau\beta_\tau\vec{j}\nabla T, \tag{17}$$

where $\beta_\tau = \beta_\varepsilon + \beta_\sigma$ is the time relaxation thermal coefficient determined by formulas

$$\beta_\tau = -\frac{1}{\tau}\frac{d\tau}{dT} = -\frac{1}{\varepsilon}\frac{d\varepsilon}{dT} + \frac{1}{\sigma}\frac{d\sigma}{dT} \equiv \beta_\varepsilon + \beta_\sigma, \tag{18}$$

usually, $\beta_\varepsilon > 0$, $\beta_\sigma > 0$ (for liquid dielectrics).

Formulas (16) and (17) are successfully used to explain and generalize the experimental data on convective heat transfer in electric fields in heterogeneous (formula (16)) and homogeneous media (formula (17)) [2].

5.1.2. Homogeneous isothermal media $\{\tau\} = 0$; $T =$ const. The experiments, in particular in Fig. 1, show that in this case, the liquid is also electrized and formula (15) remains valid. On the contrary, however, from the fact of electrization, it follows that the liquid becomes nonuniform in τ, yet, unlike the previous case 5.1, this nonuniformity is implicit and the solution of the electrization problem is tantamount to the problem of its appearance in the medium $\operatorname{grad}\tau \neq 0$ under the influence of the field.

The next simplest electrization mechanism emerges from the formulas for current density (8) taking into account $D = 0$ and the collinearity of vectors $\vec{j} \parallel \vec{E}$:

$$\rho = \frac{1}{E}\left(\frac{j^+}{k^+} - \frac{j^-}{k^-}\right) = \frac{\delta_j}{kE}. \tag{19}$$

It is evident that because of the difference of charge carrier electrophysical properties, including rates of near-electrode electrochemical reactions, this mechanism may be rather efficient. In particular, for equilibrium case ($R = 0$), the field distribution takes the form

$$E(x) = E_0\sqrt{1 + a(x - l)}; \quad a \equiv \frac{2\delta_j}{\varepsilon k E_0^2}. \tag{20}$$

If $\delta_j > 0$, the distribution is of type 2 (see Fig. 1), while at $\delta_j < 0$, it is of type 1. When dimensionless parameter

$$al \equiv \frac{2\delta_j l}{\varepsilon k E_0^2} \ll 1, \tag{21}$$

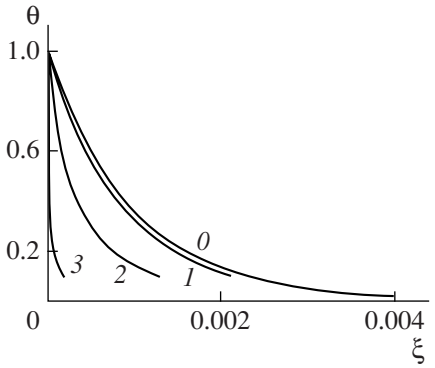

Fig. 2. Relationship θ(ξ). 0 – θ = exp(–1000*x*), (*1–3*) β = 0.1, 1.0, 10.

relationship (20) becomes approximately linear as follows:

$$E(x) \cong E_0\left(1 + \frac{al}{2}\left(\frac{x}{l} - 1\right)\right) \cong \frac{E_0}{1 - \frac{al}{2}\left(\frac{x}{l} - 1\right)} \qquad (22)$$

and we can explain the middle part of dependences *5* and *6* (see Fig. 1) or, linear to the reverse voltage $E^{-1}(x)$ and σ(*x*) from [1], distribution τ(*x*) can be found from (15), (19).

5.1.3. Separation of "charged" component in electric conductivity. In homogeneous liquid under isothermal conditions, as was mentioned above, nonuniformity in τ is caused by the external field and has a latent character. Some authors take this fact into consideration, assuming the relationship to be of type [13]

$$\sigma = \sigma_н e^{\alpha(E - E_н)}, \quad E > E_н \qquad (23)$$

or [14]

$$\sigma \sim \sqrt{F(E)}, \qquad (24)$$

where *F*(*E*) is an exponent in the function of source (5). The equation for current density

$$\sigma(E)E = j = \text{const} \qquad (25)$$

in respect to *E* is algebraic or transcendent with solutions *E* = const and, consequently ρ ~ *E*' ≡ 0, the direct application of relationships (23) or (24) in the form of equation (25) for a parallel-plate capacitor doesn't solve the problem of electrization. To solve it in the framework of the simplest model of equation (25), it is necessary for it not to be finite, but rather differential. This is achieved, for instance, by taking into account the diffusion currents (~∇ρ) or convection (ρυ ~ *E*'υ). However, under hydrostatic conditions and neglect of diffusion currents, there is another possibility, i.e., the separation in the formula for σ, the "charged" component *k*ρ, where *k* is the mobility of carriers by determining ρ ≠ 0 (k^+ at ρ > 0 and k^- at ρ < 0) and assuming the relationship [15]

$$\sigma = \sigma^0 + k\rho = \sigma^0 + \varepsilon k E', \qquad (26)$$

where σ^0 is the constant "background" conductivity (under the conditions of ρ = 0). Incidentally, formula (26) is used at solution of relaxation problems [16], as well as under the conditions of corona discharge [3] when the second addend in (26) gives gas conductivity (unipolar discharge), the first one being negligible.

Substituting (26) into (15), we obtain

$$\varepsilon k \vec{j} \nabla\rho = -\rho(\sigma^0 + k\rho)^2. \qquad (27)$$

Expanding the fraction into factors

$$\frac{1}{\rho(\sigma^0 + \kappa\rho)^2} = \frac{1}{(\sigma^0)^2\rho} - \frac{k}{(\sigma^0)^2(\sigma^0 + \kappa\rho)} - \frac{k}{\sigma^0(\sigma^0 + k\rho)^2},$$

we find

$$\vec{j}\nabla\left(\ln\frac{k\rho}{\sigma^0 + k\rho} + \frac{\sigma^0}{\sigma^0 + k\rho}\right) = -\frac{(\sigma^0)^2}{\varepsilon k}.$$

Taking into account $\nabla\vec{j} = 0$, we obtain the general solution for classic symmetries of fields

$$\ln\frac{k\rho}{\sigma^0 + k\rho} + \frac{\sigma^0}{\sigma^0 + k\rho} = -\frac{\sigma^{02}}{n\varepsilon kj}\vec{e}_j \cdot \vec{r} + \frac{\vec{e}_j}{j}\text{rot}\vec{F}, \qquad (28)$$

where $\vec{e}_j \equiv \vec{j}/j - ort$ are the current density vectors; $\vec{F}$ is the arbitrary vector function; and *n* = 1, 2, 3 for plate, cylinder and sphere symmetries of the electric field, respectively.

In the case of the parallel-plate capacitor, from (28), we find

$$\ln\frac{k\rho}{\sigma^0 + k\rho} + \frac{\sigma^0}{\sigma^0 + k\rho} = -\frac{(\sigma^0)^2}{\varepsilon kj}x + C. \qquad (29)$$

Taking the known charge density on the anode

$$\rho(x)|_{x=0} = \rho_0, \qquad (30)$$

from (29), (30), we obtain

$$\ln\frac{\theta(1+\beta)}{1+\beta\theta} + \frac{1}{1+\beta\theta} - \frac{1}{1+\beta} = -\xi, \qquad (31)$$

where

$$\theta \equiv \rho/\rho_0;\ \xi \equiv x/\delta_\rho;\ \beta \equiv k\rho_0/\sigma^0;\ \delta_\rho \equiv \varepsilon kj/(\sigma^0)^2. \qquad (32)$$

At β ≪ 1, the solution of (31) has the form

$$\rho = \rho_0 e^{-x/\delta_\rho}. \qquad (33)$$

Similar falling dependences $\rho(x)$ take place at other β as well, drop accelerating with the growth of β (Fig. 2). Note that according to (33), the charge sign is defined by the sign of ρ_0, so formulas (31)–(33) are true for the cases of both homo- and heterocharges.

From (33), we find distribution $E(x)$,

$$E(x) = E_0 + \frac{\delta_\rho \rho_0}{\varepsilon}\left(1 - e^{-\frac{x}{\delta_\rho}}\right), \quad (34)$$

where $E_0 = E(x)|_{x=0}$ on the anode.

Relationships (33) and (34) have near-electrode characters, as the initial prerequisites themselves are as follows: at the counter-electrode, similar phenomena should occur but with the opposite sign, whereas the mobility coefficient does not incorporate the change of sign as the counterelectrode is approached.

In other dependences (see below) there are similar exponential regularities; only the characteristic thicknesses differ in the near-electrode layer. This model is preferential to $\delta_\rho \sim j$, as it explains the effect of charge formation penetration into the depth of liquid as the discharge current grows.

5.2. Diffusion mechanisms and models of electrization ($D \neq 0$). Separation of two subclasses of electrization mechanisms is fundamentally important, as at conductive electrization ($D = 0$, $j \neq 0$), where the current disappears in the outer circuit, the effect itself disappears. At the same time, the electrization (steady) of the interelectrode space of the capacitor is possible when it is switched off from the power supply, which is understood to have been previously charged. We are dealing with an antagonism between two processes, i.e., the polarization of free charges and their outflow due to diffusion. Let us consider this case.

5.2.1. Electrization in the absence of external current. This case is realized at small external voltages (under critical) that are insufficient to activate charge carriers. Substituting $j^\pm = 0$ into (8), $j = j^+ + j^- = 0$ and, accounting for $\vec{E} = -\nabla\varphi$, we obtain the distribution of space charges as follows:

$$\rho^\pm = \rho_0^\pm e^{\pm\frac{k^\pm\varphi}{D^\pm}}; \quad \rho_0^\pm = \rho^\pm(\varphi)|_{\varphi=0}. \quad (35)$$

Taking into account the Einstein relation

$$\frac{k^\pm}{D^\pm} = \frac{q^\pm}{k_B T} \equiv \frac{1}{\varphi_*} = \frac{ez^\pm}{k_B T} = \frac{z^\pm}{\varphi_0}, \quad (36)$$

where $\varphi_0 \equiv k_B T/l$ is the constant and depends only on temperature, at $T = 300$ K, for $\varphi_0 \cong 2.6$ B, we find

$$\rho = \rho^+ - \rho^- = -2\rho_* \sinh\frac{\varphi}{\varphi_*}; \quad \rho_* \equiv \rho_*^\pm. \quad (37)$$

Having the solved Poisson equation, we obtain the distribution of the electric field as follows:

$$E(\varphi) = E_*\sqrt{1 + \frac{4\rho_*\varphi_*}{\varepsilon E_*^2}\left(\cosh\frac{\varphi}{\varphi_*} - 1\right)}; \quad E(\varphi)|_{\varphi=\varphi_*} = E_*. \quad (38)$$

This evidently is the heterodistribution of type 3 (see Fig. 1) with a rather sharp near-electrode that falls at $\varphi/\varphi_* \gg 1$. The heterocharge layer is narrow and dense, actually shielding the entire interelectrode space.

This electrization can be called low-voltage (for the lack of current), which completely agrees with the Boltzmann distribution (35) of charged particles in potential energy, and equations for current themselves

$$j^\pm = k^\pm\rho^\pm(-\varphi') \mp D^\pm(\rho^\pm)' = 0$$

express the condition of dynamic equilibrium between through conduction current (the first addend) and diffusion current (the second addend). Hence, the physical essence of diffusion electrization becomes clear; removing diffusion ($D^\pm = 0$), we obtain $\rho^\pm \equiv 0 \Rightarrow \rho \equiv 0$.

5.2.2. Approximation of electroconductivity constancy ($\sigma = \text{const}$; $j \neq 0$). High-voltage polarization is attended by the electric current, which should favor widening the areas embraced by charge formation. One of the approximations that can help to explain the reasonably specific cases of electrization is the assumption in the first equation (11) that $\sigma = \text{const}$. This approximation can be partly substantiated by the fact that in the same equation, the diffusion term is accounted for as the "compensating" factor that makes the equation differential (see 5.1.3) and approximation $\sigma \approx \text{const}$ agrees with the frequent assumption that, for instance [1], $\rho^+ + \rho^- \ll k|\rho^+ - \rho^-|$, that is, $\sigma \cong \sigma^0 = \text{const}$, which can be broken in nonuniform and sharply nonuniform (corona discharge) fields.

By implying some averaged constant value with account taken for the second one in the first equation of (13) under σ, we obtain the following equation for E with initial conditions:

$$E'' - E/\delta_D^2 \cong j/\varepsilon D; \quad E(x)|_{x=l} = E_0; \quad E'(x)|_{x=l} = 0, \quad (39)$$

where

$$\delta_D \equiv \sqrt{\tau D}. \quad (40)$$

As is seen from (39), solution $E(x)$ is even in relation to the layer middle $x = l$ and takes the form

$$E(x) = \left(E_0 - \frac{j}{\sigma}\right)\cosh\left[\frac{l}{\delta_D}\left(1 - \frac{x}{l}\right)\right] + \frac{j}{\sigma}. \quad (41)$$

We express the voltage in the layer middle E_0 through the capacitor plate potential ($\pm U$) according to the initial conditions (13) for

$$\varphi(0) = U; \quad \varphi(l) = 0. \tag{42}$$

Then,

$$E_0 - \frac{j}{\sigma} = \frac{k(\bar{E} - j/\sigma)}{\delta_D \sinh\dfrac{l}{\delta_D}}, \quad \bar{E} \equiv \frac{U}{l}. \tag{43}$$

Substituting (43) into (41), we finally find

$$E(x) = \frac{l(\bar{E} - j/\sigma)}{\delta_D \sinh(l/\delta_D)} \cosh\left[\frac{l}{\delta_D}\left(1 - \frac{x}{l}\right)\right] + \frac{j}{\sigma}, \tag{44}$$

where it follows that (a) $j = \sigma\bar{E} \Rightarrow E(x) = \text{const}$ is the trivial case of electrization absence; (b) $j < \sigma\vec{E}$ is the case heterocharging, curve *3*, Fig. 1; and (c) $j > \sigma\bar{E}$ is the case of homocharging, curve *4*, Fig. 1. The electrization processes are accompanied by the breaking of Ohm's law in the last two cases.

The physical meaning of these regularities is rather simple. As follows from the equation for current density,

$$j = \sigma E - D\rho' \equiv j_\sigma \pm |j_D|, \tag{45}$$

in case (a), the diffusion current is absent and, consequently, $\rho \equiv 0$, $E = \bar{E}$, thereby justifying the name "electrization mechanism." Condition (b) being fulfilled, the heterocharge diffusion current is directed oppositely to the conduction current $j_\sigma = \sigma E$, decreasing it (the sign "–" in (45)), which reflects this very condition. In case (c), the currents of conduction and diffusion coincide in their directions, that is, $j > \sigma\bar{E}$. Thus, in the case of heteroelectrization, the diffusion current is subtracted from the conduction current, but at homoelectrization, on the contrary, it is shown in the second equality (45).

Peculiarities are observed also for the sign of the second derivative $E''(x)$ in (39).

5.2.3. Account of $\sigma \neq \text{const}$, at $j^+ = \text{const} \neq 0$; $j^- = \text{const} \neq 0$, $j^+ - j^- \equiv \delta_j = \text{const}$. The third equation of set (13) is integrated and, as a result,

$$\sigma = \sigma_0 + \frac{\varepsilon k^2}{2D}(E^2 - E_0^2) + \frac{k\delta_j}{D}(l - x). \tag{46}$$

Substituting (46) in to the first equation of (13) leads to the main equation

$$E'' = \frac{k^2}{2D^2}E^3 + \frac{1}{\varepsilon D}\left(\sigma_* + \frac{k\delta_j}{D}(l - x)\right)E - \frac{j}{\varepsilon D} \tag{47}$$

with initial conditions (39).

We bring this equation to the dimensionless form

$$\eta'' = \pi_0\eta^3 + \pi_1(1 + \pi_2(1 - \xi))\eta - \pi_3; \quad \eta(1) = 1; \quad \eta'(1) = 0, \tag{48}$$

where the following notations are introduced:

$$\eta \equiv E/E_0; \quad \xi \equiv x/l; \quad \pi_0 \equiv \frac{l^2k^2E_0^2}{2D^2}; \quad \pi_1 \equiv \frac{l^2}{\tau_* D};$$
$$\pi_2 \equiv \frac{lk\delta_j}{\sigma_* D};$$
$$\pi_3 \equiv \frac{jl^3}{\varepsilon D E_0}; \quad \tau_* \equiv \frac{\varepsilon}{\sigma_*}; \quad \sigma_* \equiv \sigma_0 - \frac{\varepsilon k^2 E_0^2}{2D};$$
$$\pi_* \equiv \frac{l^2}{\tau_0 D}. \tag{49}$$

Equations (47), (48) of Painleve type [17] and, at $j^+ = j^- = \text{const} \neq 0$, that is $\delta_j = 0 \Rightarrow \pi_2 = 0$, the separation of variables and exact integration through elliptic integrals are permitted. The solution thus obtained can serve as a standard for comparisons with other approximations, in particular 5.2.2, as well as those obtained by different methods, for instance, expansion into a Tailor series. Therefore, we will present these solutions beginning with the exact one.

(a) *Exact solution.* Given, in (48), that $\pi_2 = 0$, we obtain

$$\eta'' = \pi_0\eta^3 + \pi_1\eta - \pi_3; \quad \eta(1) = 1; \quad \eta'(1) = 0; \quad 0 \le \xi \le 1. \tag{50}$$

Having integrated taking into account the initial conditions, we find

$$\eta'^2 = \frac{\pi_0}{2}[(\eta^2 + a)(\eta + 1) - b^2](\eta - 1), \tag{51}$$

where

$$a \equiv \frac{2\pi_1}{\pi_0} + 1; \quad b^2 \equiv \frac{4\pi_3}{\pi_0}. \tag{52}$$

Notice that parameters π_1 and a can also assume negative values. According to Descartes' rule, square brackets of (51) admit only one positive root; denoting it $\eta \equiv \alpha > 0$, we obtain

$$b^2 = (\alpha^2 + a)(\alpha + 1) > 0. \tag{53}$$

Substituting (53) into (51) and dividing the obtained expression by $\eta - \alpha$, we find expansion of (51) into factors

$$\eta'^2 = \frac{\pi_0}{2}[\eta^2 + (\alpha + 1)\eta + \alpha(\alpha + 1)a](\eta - 1)(\eta - 1). \tag{54}$$

With the help of (53), it is easy to make certain that the expression in square brackets (54) is positive; therefore, the sign of the entire right part of (54) is determined by the sign of the product

$$(\eta - \alpha)(\eta - 1) > 0, \tag{55}$$

as $\eta'^2 > 0$. The solutions of this inequality are as follows:

$$\alpha > 1 \quad \text{and} \quad \eta \le 1 \tag{56}$$

and

$$\alpha < 1 \quad \text{and} \quad \eta \ge 1. \tag{57}$$

As $\eta(1) = 1$, it follows from (56) and (57) that relationship $\eta(\xi)$ is convex at $\alpha > 1$; consequently, in this case, electrization is homopolar (see Fig. 1, curve *4*) and heteropolar at $\alpha < 1$(see Fig. 1, curve *3*).

Dividing variables in (54), we obtain

$$\int_{\eta}^{1} \frac{dz}{\sqrt{(z-\alpha)(z-1)[(z-m)^2 + n^2]}} = \pm \int_{\xi}^{1} \sqrt{\frac{\pi_0}{2}}\, dt. \tag{58}$$

The integral on the left is elliptic of the 1st kind, i.e., $F(\varphi, k)$, and, according to [18],

$$\frac{1}{\sqrt{qp}} F(\varphi, k) = -\sqrt{\frac{\pi_0}{2}}(\xi - 1) \equiv \sqrt{\frac{\pi_0}{2}}\lambda, \tag{59}$$

where $\lambda \equiv 1 - \xi$ is the coordinate, counted from the middle ($x = l$) to the left to the anode ($x = 0$), k and φ are module and argument of the integral $F(\varphi, k)$, defined by equalities [18] as follows:

$$\varphi = 2\arctan\sqrt{\frac{q}{p}\frac{1-\eta}{\alpha-\eta}}; \quad k = \frac{1}{2}\sqrt{\frac{(p+q)^2 + (\alpha-1)^2}{pq}}; \tag{60}$$

$$p^2 = (m-\alpha)^2 + n^2; \quad q^2 \equiv (m-1)^2 + n^2;$$
$$m \equiv -\frac{\alpha+1}{2}; \quad n^2 \equiv \alpha(\alpha+1) + a - \left(\frac{\alpha+1}{2}\right)^2. \tag{61}$$

From the first expression of (60), we find formula

$$\eta(\varphi) = \frac{\alpha\left(q/p\alpha - \tan^2\frac{\varphi}{2}\right)}{q/p - \tan^2\frac{\varphi}{2}}, \tag{62}$$

which, along with the previous ones, gives a complete, exact solution of problem (50), root α (51) being determined according to the values π_0, π_1, π_3, i.e., a and b, then m and n can be found, followed by p and q from formulas (61). Subsequently, k becomes known from the second formula of (60). Knowing k, prescribing λ, and beginning with zero, from tables $F(\varphi, k)$, we found the corresponding values φ and, from formula (62), we finally obtained $\eta(\varphi)$. We solve the same problem approximately.

(b) *Approximate solution.* As the initial conditions and the equation itself are given, the simplest approximate solution can be obtained by expansion into the Tailor series and coefficients can be obtained by the equation-differentiation method (unlike the method of undetermined coefficients) as the resultant series occurs based on the differences $(\xi - 1)$ between even powers, i.e.,

$$\eta(\xi) = \eta(1) + \frac{1}{2}\eta''(1)(\xi-1)^2 + \frac{1}{4!}\eta^{IV}(1)(\xi-1)^4 + \frac{1}{6!}\eta^{VI}(1)(\xi-1)^6 + \ldots, \tag{63}$$

due to the fact that problem (50) has a deliberately even solution.

Then,

$$\eta''(1) = \pi_* - \pi_3 \equiv A; \quad \eta^{IV}(1) = (2\pi_0 + \pi_*)A;$$
$$\eta^{VI}(1) = [18\pi_0 A + (2\pi_0 + \pi_*)^2]A \tag{64}$$
$$\pi_* \equiv \pi_1 + \pi_0 = l^2/\tau_0 D; \quad \tau_0 \equiv \varepsilon/\sigma_0.$$

(c) *Comparison of solutions.* To estimate accuracy and to approve the approximated solutions (44) and (63) we compare them with exact one (62) by the numerical example.

By exact formula (62). We assume $\pi_*/\pi_0 = 0.1$; $\pi_3/\pi_0 = 0.55$; $\pi_0 = 1$. Initial equation (50) is $\eta'' = \eta^3 - 0.90\eta - 0.55$; $a = 2(\pi_* - \pi_0)/\pi_0 + 1 = 2\pi_*/\pi_0 - 1 = -0.80$; $b^2 = 4 \times 0.55 = 2.20$ and the equation for α is (53),

$$\alpha^3 + \alpha^2 - 0.8\alpha - 3 = 0 \Rightarrow \alpha = 1.3219 \Rightarrow m = -1.1610;$$
$$n^2 = 0.9215; \quad p = 2.6620; \quad q = 2.3848; \quad k = 0.9999 \Rightarrow \eta' \tag{65}$$
$$= \frac{1}{\sqrt{2}}\sqrt{[(\eta + 1.661)^2 + 0.9215](\eta - 1)(\eta - 1.3219)}.$$

The exact solution by (62) is as follows:

$$\bar{\eta}(\varphi) = 1.3219\frac{0.6720 - \tan^2\frac{\varphi}{2}}{0.8883 - \tan^2\frac{\varphi}{2}}. \tag{66}$$

We find the angle φ from (59) as follows:

$$F(\varphi; 0.9999) = 1.7741\lambda. \tag{67}$$

Using the values of $0 \le \lambda \le 1$ and Table $F(\varphi, k)$ [19], we find φ; then, from formula (66), we find $\bar{\eta}(\varphi)$ (see Table 1, row 3).

By approximate formula (63). Substitution of numerical values (64) into (63) results in the calculating formula

$$\eta(\lambda) \cong 1 - 0.2250\lambda^2 - 0.0394\lambda^4 + 0.0023\lambda^6. \tag{68}$$

Table 1. Calculations of $\eta(\lambda)$

No.	λ	0	0.2	0.4	0.6	0.8	1.0	δ_{av}
1	$F(\varphi, 0.99)$	0	0.35	0.71	1.06	1.42	1.77	–
2	φ^0	0	20	37	52	63	69	–
3	$\bar{\eta}$	1.00	0.99	0.96	0.89	0.77	0.64	–
4	$\tilde{\eta}$	1.00	0.99	0.96	0.91	0.84	0.73	–
5	η_*	1.00	0.99	0.96	0.82	0.85	0.77	–
6	$\Delta\tilde{\eta}/\bar{\eta}$	0	0	0	0.02	0.09	0.14	4%
7	$\Delta\tilde{\eta}_*/\bar{\eta}$	0	0	0	0.03	0.10	0.20	6%

The results are presented in Table 1, row 4.

By exact formula (44) of approximate equation (39). We bring (44) to the dimensionless form, introducing notations (49). We obtain

$$\eta(\lambda) = \left(1 - \frac{\pi_3}{\pi_*}\right)\cosh\left(\sqrt{\pi_*}\lambda\right) + \frac{\pi_3}{\pi_*}, \qquad (69)$$

in numbers $\eta(\lambda) = -4.50\cosh(0.32\lambda) + 5.50$. The results are presented in Table 1, row 5.

In Fig. 3, diagrams of the respective relationships are presented that show that we have homocharge distributions, exact solution $\bar{\eta}$ yielding the largest density of near-electrode charge, while η^* yields the least one, which appears to be due to the smoothing of dependence $\rho(x)$ in the approximation of $\sigma \cong$ const. Thus, the approximated solutions both with assuming σ = const in exact equation (39) and at expansion into series in difference $\xi - 1$ (formulas (63), (64)) lead to acceptable results. Particularly at this initial stage of research, the approval of the last case is very important, as the method of Tailor-series expansion is fairly universal and can be applied to the complicated variants of the problems.

Curves *5–9* and, especially, *7–9*, i.e., bipolar structures, have not been reflected in the examined models. In the framework of the equilibrium class, case $\pi_2 \neq 0$ remained unconsidered and evidently cannot result in symmetrical solutions of the mentioned type. Nevertheless, we examine the last equilibrium mechanism δ_j = const $\neq 0$ and again, $R = 0$.

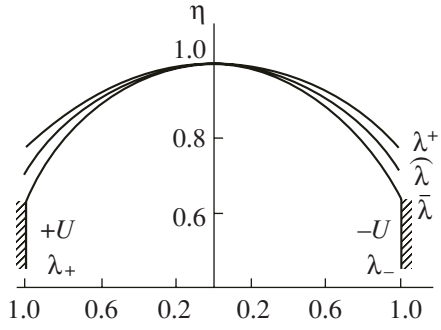

Fig. 3. Relationships $\bar{\eta}$ (λ), $\tilde{\eta}$ (λ), $\eta^*(\lambda)$.

(d) *Unsymmetrical case* δ_j = const $\neq 0$. *Approximated solution*. Expand the solution into a Tailor series accurate to $(1 - \xi)^4$ as follows:

$$\eta(\xi) \cong 1 + \frac{1}{2}A(1-\xi)^2 + \frac{1}{6}B(1-\xi)^3 + \frac{1}{24}(1-\xi)^4, \qquad (70)$$

where according to the previous results,

$$A = \pi_* - \pi_3; \quad \pi_* = \frac{l^2}{\tau_0 D}; \quad B \equiv \pi_1\pi_2 = \frac{k\delta_j l^3}{\varepsilon D^2}; \qquad (71)$$
$$C = NA; \quad N = (2\pi_0 + \pi_*).$$

Passing to variable $\lambda = 1 - \xi$, from (70), (71), we find

$$\eta(x) \cong 1 + \frac{A}{2}\lambda^2 + \frac{B}{6}\lambda^3 + \frac{C}{24}\lambda^4. \qquad (72)$$

As one would expect, the asymmetry factor is coefficient $B \sim \delta_j$.

We find, in the range (semilayer) $0 < \lambda < 1$, the following extremums (72):

$$\eta'(\lambda) = A\lambda\left(1 + \frac{B}{2A}\lambda + \frac{N}{6}\lambda^2\right) = 0 \qquad (73)$$

and its roots in addition to the zero one

$$\lambda_\pm = -\frac{3B}{2NA}\left(1 \pm \sqrt{1 - \frac{8}{3}\frac{NA^2}{B^2}}\right). \qquad (74)$$

Under conditions

$$\beta = -B/A > 0; \quad 8N/3\beta^2 < 1 \qquad (75)$$

the following two positive roots $\lambda_+ > \lambda_-$ exist:

$$\lambda_\pm = \frac{3\beta}{2N}(1 \pm \sqrt{1 - 8N/3\beta^2}) > 0. \qquad (76)$$

Let us consider the sign of the second derivative

$$\eta''(\xi) = \eta''(\lambda) = A\left(1 + \frac{B}{2A}\lambda + \frac{N}{6}\lambda^2\right) + A\lambda\left(\frac{B}{2A} + \frac{N}{3}\lambda\right). \quad (77)$$

Hence,

$$\eta''(\lambda_+) = -\frac{BM}{2}\lambda_+; \quad \eta''(\lambda_-) = \frac{BM}{2}\lambda_-, \quad (78)$$

where

$$M \equiv \sqrt{1 - 8N/3\beta^2}.$$

From the first relationship (75), it follows that, at $j_+ > j_-$, that is, $b > 0 \Rightarrow A < 0$, and according to (78), at the root value $\lambda = \lambda_+$, we have the maximum and, at $\lambda = \lambda_-$, we have the minimum. Because $\eta''(0) = A < 0$, $\lambda = 0$ is the point of the second maximum. A sample form of diagram $\eta(\lambda)$ ($E(x)$) is presented in Fig. 4, which shows that in the semilayer near the anode, a bipolar structure with a maximum is generated. The appearance of the near-electrode bipolar structure occurred due to a constant, but not zero, difference of partial currents $j_+ - j_- = \delta_j \neq 0$. This fact suggests that bipolar symmetrical and other structures should be looked for in the class of nonequilibrium mechanisms of electrization ($R \neq 0$), that is, $\delta_j \neq$ const.

5.2.4. The simplest nonequilibrium mechanism. Consideration of the class of problems ($R \neq 0$) is the following stage of research, yet let us examine the simplest case R = const $\neq 0$, not requiring special basis.

Then, we find δ_j by integration as follows:

$$\int_{\delta_{j0}}^{\delta_j} d\sigma_j = \int_l^x R dx \Rightarrow \delta_j = R(x - l) + \delta_{j0} = Rl(\xi - 1) + \delta_{j0}, \quad (79)$$

where

$$\delta_{j0} = j_0^+ - j_0^- = \delta_j(x)\big|_{x=l}. \quad (80)$$

We look for symmetrical structures, then $\delta_{j0} = 0$ and, in (48), instead of $\pi_2(1 - \xi)$, it should be written as

$$\pi_2'(1 - \xi^2); \quad \pi_2' \equiv \frac{ek\delta_0}{2\sigma_* D}; \quad \delta_0 = (j^+ - j^-)\big|_{x=0}. \quad (81)$$

Equation (48) becomes

$$\eta'' = \pi_0\eta^3 + \pi_1(1 + \pi_2'(1 - \xi)^2)\eta - \pi_3; \quad \eta(1) = 1; \quad \eta'(1) = 0. \quad (82)$$

With an accuracy up to the fourth-order terms,

$$\eta(\xi) = 1 + \frac{1}{2!}A(\xi - 1)^2 - \frac{1}{4!}(\beta - N)(\xi - 1)^4, \quad (83)$$

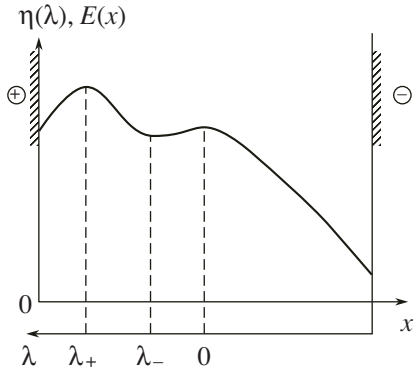

Fig. 4. Relationship $E(x)$ at δ_j = const > 0.

where

$$A \equiv \pi_* - \pi_3; \quad N \equiv 2\pi_0 + \pi_*; \quad \beta \equiv -B/A; \quad B \equiv \pi_1\pi_2. \quad (84)$$

Let us examine (83) for extremum as follows:

$$\eta'(\xi) = A(\xi - 1) - \frac{A(\beta - N)}{6}(\xi - 1)^3 = A(\xi - 1)\left(1 - \frac{\beta - N}{6}(\xi - 1)^2\right). \quad (85)$$

Extremum points

$$\xi_\pm = 1 \pm \sqrt{\frac{6}{\beta - N}}; \quad \beta > N \quad (86)$$

$$\eta''(\xi) = A - \frac{A(\beta - N)}{2}(\xi - 1)^2 = A\left(1 - \frac{\beta - N}{2}(\xi - 1)^2\right) \Rightarrow \eta''(\xi_\pm) = A\left(1 - \frac{\beta - N}{2}\frac{6}{\beta - N}\right) = -2A. \quad (87)$$

We consider the two following cases:

(a) $A > 0 \Leftrightarrow \pi_3/\pi_* < 1 \Rightarrow B < 0 \Leftrightarrow j^+(0) \le j^-(0) \Rightarrow \eta(\xi_\pm) = \eta_{\max}$. In this case we have a bipolar ("two-humped") structure of type 8 (see Fig. 1) that is formed against the background of heterodistribution 3 as it should be at $A > 0$. On the anode $j^-(0) > j^+(0)$, consequently, negative ions are more active; therefore, they disperse more quickly than positive ions. As a result, the homocharge is immediately generated on the anode on the general background of a heterocharge.

(b) $A < 0 \Leftrightarrow \pi_3/\pi_* > 1 \Rightarrow B > 0 \Leftrightarrow j^+(0) > j^-(0) \Rightarrow \eta(\xi_\pm) = \eta_{\min}$. Here, we have a "two-pit" bipolar structure of type 9 (see Fig. 1) against the background of homocharge formation at $A < 0$ (curve *4*, Fig. 1). Further analysis shows that in the following linear approx-

imation for source function $R(x) = a_0 + a_1x$, we have a distribution of type 5–7.

So, curves *1–4* could at least be qualitatively explained in the framework of equilibrium, partly nonequilibrium (curves *3*, *4*) mechanisms of electrization. Curves *5–9* appear to be explicable in the simplest approximations of source functions $R(x)$ as constant or linear.

Consequently, in general terms, all curves in Fig. 1 are qualitatively explained; thus, the prerequisite has been created for further refinements and quantitative investigations, including those utilizing computers.

6. Computer simulation of charge formation. The method, program, and results of numerical simulation of space charge generation processes in low-conducting liquid dielectrics are presented in [20–22].

In our work, we created a program with a convenient interface that allows one to conduct operative calculations and analyze the obtained results in an online regime. However, specific calculations in accordance with this program will be carried out at later stages of research, as the above-examined analytical solutions near completion. Computation of the current passage and charge formation processes in the case of the cylindrical capacitor according to the previously debugged program is an example of a numerical experiment.

6.1. Program for flat layer. One-dimensional hydrostatic case is simulated, the liquid is assumed incompressible and immovable, the temperature in the bulk is constant, and variables depend on only one spatial coordinate x, normal to electrodes, while the computing origin corresponds to the anode.

The source function in the charge conservation law is represented by formula (5) $W - \alpha n_+ n_-$, where W is the dissociation by Fraenkel–Onsager[1]

$$W = W_0 \exp\left[\frac{2e^{3/2}(E)^{1/2}}{(\varepsilon\varepsilon_0)^{1/2}kT}\right],$$

and α is the recombination coefficient by Lanjeven,

$$\alpha = \frac{e(b_+ + b_-)}{\varepsilon\varepsilon_0} = \frac{2eb}{\varepsilon\varepsilon_0}. \quad (88)$$

Here, ε is the relative permittivity. The complete set of ion conductivity describing the charge formation process can be rewritten in the form

$$\frac{\partial n_\pm^*}{\partial t^*} + \frac{\partial}{\partial x^*}(n_\pm^* v_\pm^*) = W^* - \alpha^* n_+^* n_-^*; \quad (89)$$

$$-\frac{\partial^2 \varphi^*}{\partial x^{*2}} = \frac{1}{\varepsilon\varepsilon_0} e(n_+^* - n_-^*); \quad (90)$$

$$\frac{j_\pm}{e} = n_\pm^* v_\pm^* = -D_\pm^* \frac{\partial n_\pm^*}{\partial x^*} - b_\pm^* n_\pm^* \frac{\partial \varphi^*}{\partial x^*} \quad (91)$$

with the boundary conditions being written as follows:

$$-D\frac{\partial n_\pm^*}{\partial x^*} \pm n_\pm^* E^* = A_\pm^{a*} - K_\pm^{a*} n_\pm^* \text{ on the anode,} \quad (92)$$

$$-D\frac{\partial n_\pm^*}{\partial x^*} \pm n_\pm^* E^* = -A_\pm^{k*} + K_\pm^{k*} n_\pm^* \text{ on the cathode,} \quad (93)$$

where in the right part of (92) and (93), there are coefficients of the birth and death of ions on the electrodes. Dependence of birth coefficients on field and of ion death on the electrodes on near-electrode concentrations can be taken into account in the program.

Set (88)–(93) is solved in dimensionless form. To solve the set numerically, the implicit difference scheme is provided, linearized, and solved by the scalar-pass method. Computation finishing criterion is the moment when the solution becomes stationary (current density j = const).

The program BPNP for simulation of low-conducting liquids comprises a set of subprograms Matlab provided with an interface. The program has been tested with MATLAB 7.0.1.24704 (R14) Service Pack 1.

The computation results are conserved in MATLAB structures and the structure diagram building functions are realized. The structures constitute a convenient construction for the conservation of field distributions with time.

To start up the program, it is necessary to start up MATLAB, pass into the directory with a set of subprograms (say, cd/path/to/bpnp), and set up the command wrapper in Command Windows Matlab, which starts up an intuitively intelligible interface.

The program interface (Fig. 5) is divided into the following three parts (columns):

- problem parameters (preprocessor),
- solver parameters,
- solution of problem (postprocessor).

Characteristics of low-conducting liquid (values in system SI) and some other parameters of the problem are as follows:

- temperature (evidently, does not appear in the complete system of EHD and is used to calculate the diffusion coefficient by the Einstein formula (3)) [300][2];
- permittivity [4.4];
- medium low-voltage conductivity [1.76E-13];
- recombination (the value is calculated by Lanjeven formula) [switch off];
- alternating voltage (with the possibility to change voltage) [switch off];

[1] Some other notations, for instance "$b_\pm$" instead of $k_\pm$, that are inherent in the program notation specificity could be met below.

[2] In brackets, [ ], the value at default is indicated.

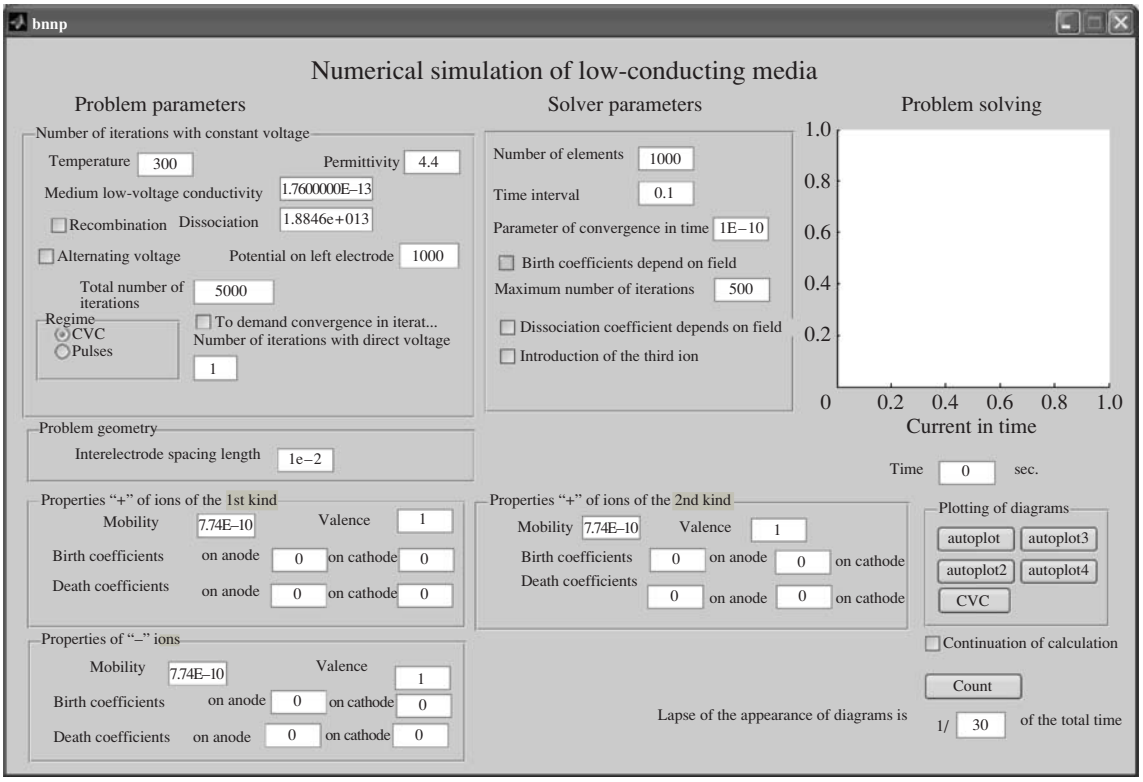

Fig. 5. The program interface.

• potential on the left electrode (if the alternating voltage is switched off, the potential difference between electrodes is given; in the case of switching on the "alternating voltage" option, the function of changing voltage with variable *t*, say 1000 + 1000*cos(2*3.14**t*/50), is given) [1000];

• general number of iterations (the maximum number of iterations under the conditions of changing voltage is determined as the product of iteration number at the prescribed voltage by the amount of steps to change voltage) [5000];

• conditions (in the case of the current-voltage characteristic (CVC) conditions, the program continues the calculations at the given voltage until the system achieves a steady state or exceeds the iteration limit) [CVC]

• to demand convergence in iterations (if at some voltage the solution does not achieve steady state, the option being switched on the solution stops; otherwise, it will continue until the iteration limit is exceeded and then passes to the following value of voltage) [switched off];

• iteration number with alternating voltage (iteration number under the pulse mode before applying the following value of voltage) [1].

Subsequently, the problem geometry is prescribed and a one-dimensional problem is solved; the electrolytic cell length is the only parameter.

Liquid-ion parameters (of the first and third kinds). Prescription of parameters of positive ions of the first kind will be considered as an example:

• mobility [7.74E-10],

• valence [1],

• coefficients of birth on the anode [0], cathode [0],

• coefficients of death on the anode [0], cathode [0].

As the solver parameters, the following quantities are prescribed:

• number of elements (total quantity of elements and the size and shape of elements are preassigned in the subprogram mesh.m) [1000],

• time range (a step by time in iterations) [0.1],

• parameter of convergence in time (given in percents, for differences in solutions that are less than the prescribed percent the solution is assumed to be becoming steady) [0.01],

• birth coefficients depend on the field [switch off],

• dissociation coefficient depends on the field (the value is calculated with Onsager formula) [switch off],

• introducing the third ion (at switching on the option the equation is being solved for three ions) [switch off].

Specific computations with this program are planned for the following stage of research. We below present as an example some results of an investigation

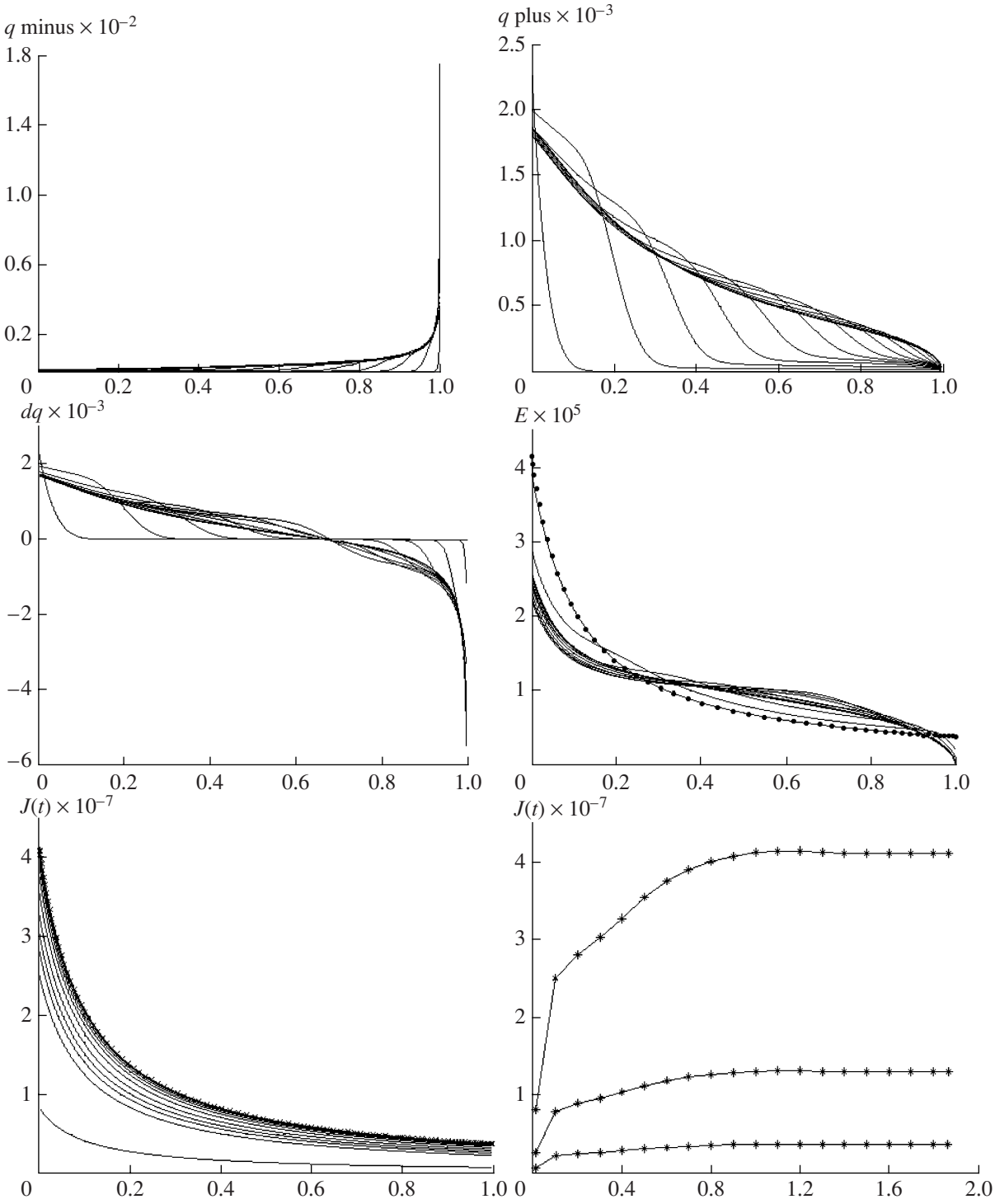

Fig. 6. Solution for cylindrical system of coordinates.

in accordance with a debugged program for the cylindrical layer.

6.2. An example of numerical experiment on simulation of charge formation process in the liquid cylindrical layer.

The results of the process development at symmetric birth of ions on the both electrodes at recombination and dissociation are presented in Fig. 6.

The diagrams from left to right and from top to bottom reflect the change dynamics in the concentration of

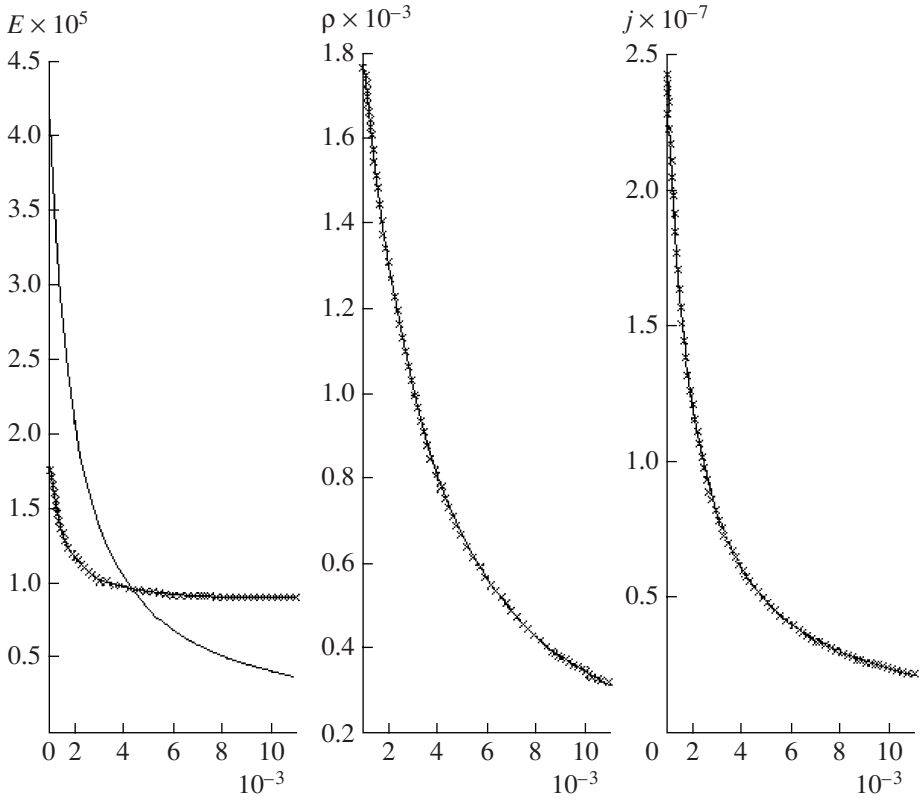

Fig. 7. Electric field intensity, charge density, current density; heavy line represents the theoretical solution and crosses represent numerical calculations.

negative and positive ions, space charge, electric intensity, total current density distribution and dependence on time. The interelectrode distance is 0.01 and the inner electrode radius is 0.001 m.

At the steady state, an asymmetry is seen in the space charge distribution and the zero point is shifted to the right relative to the interelectrode spacing center. The field near every electrode has a dip relative to the electrostatic value (without space charge). The total current density on the inner and outer electrodes becomes different, current growth rate changes. It should be noted that total current density distribution diminishes ~1/r with time.

Tests of the program by a comparison of the calculation results for unipolar injection in the case of coaxial electrodes with the theoretical solution are shown in Fig. 7. The numerical solution agrees with theoretical (classical) one with an accuracy of 0.6%.

The results of simulation of a ternary (three kinds of ions) system are presented in Fig. 8. The current with the presence of two kinds of positive ions passes into a steady regime in two stages; initially, the current passes, generated by high-speed ions; then, the current grows due to low-speed ions.

It is particularly remarkable that in the steady state (heavy curve), the intensity distribution in the cylindrical layer also becomes "two-humped" as in the analytic solution in 5.2.4. Thus, this distribution is characteristic for nonequilibrium mechanisms of electrization. The program allows one to simulate the pulse effect on the cell and obtain current-voltage characteristics automatically (Fig. 9).

Various distributions of the field in the interelectrode spacing can be obtained by varying the program input parameters, including coefficients of the birth and death of ions on the electrodes, dissociation coefficient amplitude, potential difference between the anode and cathode, ionic electrovalence, and mobility.

Thus, a numerical experiment in the form of an algorithm for solving the nonlinear nonequilibrium problem of the passage of electric current in low-conducting liquid in hydrostatic approximation has been realized. The influence of diffusion and migration currents, bulk and surface electrochemical processes, and the dependence of the birth coefficient dissociation rate on the electric intensity have been taken into account. The programs for solving problems in the one-dimensional case of the plane have been written in the Matlab system. The programs have a convenient interface and allow one to carry out calculations online, which is planned for the future stages of investigation. The outcome of computation with the debugged program for cylindrical layer is presented as a numerical example.

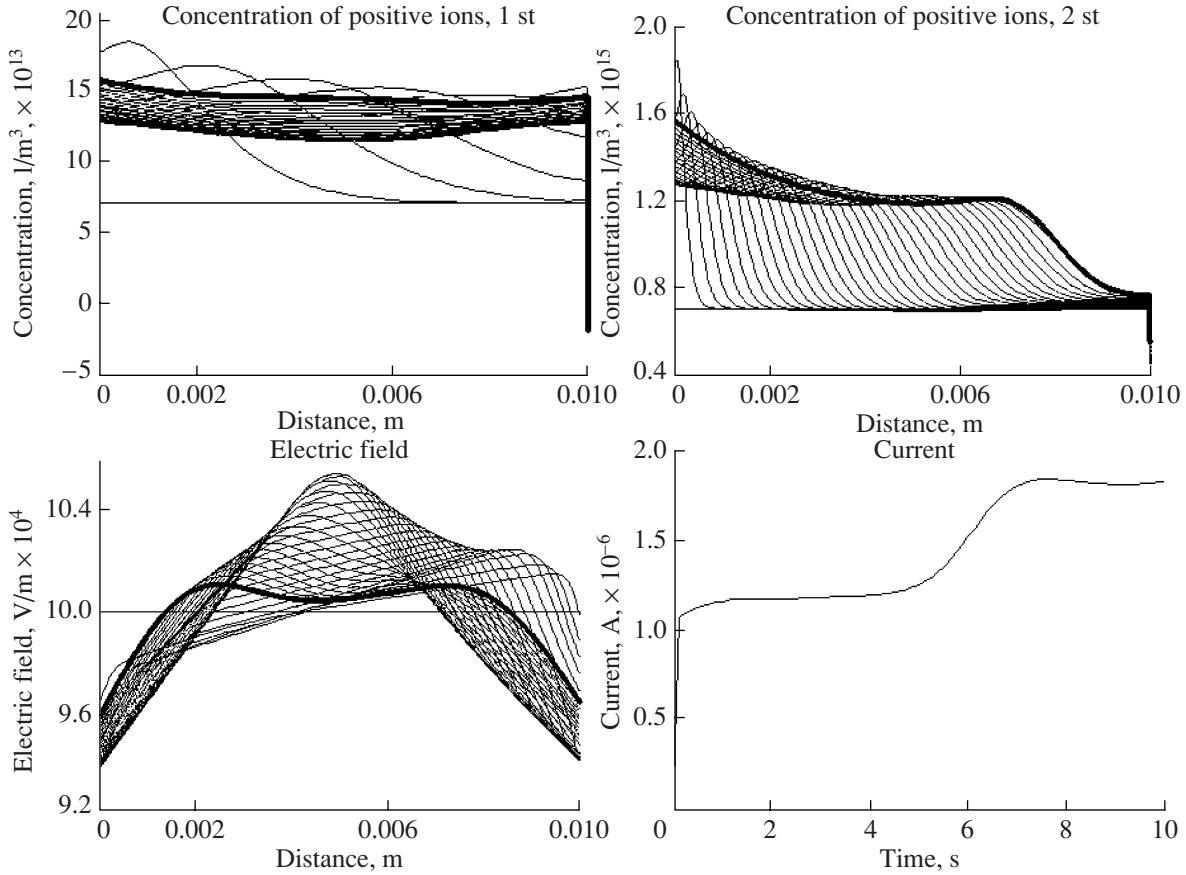

Fig. 8. Simulation of ternary system.

7. Electrization and Ohm's law. We basically consider the problems of electrization of low-conducting dielectric ($\sigma \neq 0$) and fulfillment of Ohm's law on the qualitative level of model (44), which, as was noted, adequately and clearly explains the most frequently encountered electrization types (curves *1–4*, Fig. 1).

7.1. Connection of Ohm's law with distribution $E(x)$. From (44) for current density we find ($\sigma = \sigma_0 =$ const)

$$j = \sigma \frac{E(x)\sinh\mu - \bar{E}\mu\cosh\upsilon(x)}{\sinh\mu - \mu\cosh\upsilon(x)}, \tag{94}$$

where

$$\mu \equiv l/\sqrt{\tau D} \equiv l/\delta_D;\ \ \upsilon(x) \equiv (l-x)/\delta_D;\ \ \bar{E} = u/l. \tag{95}$$

Table 2. Quantities x, υ

x	0	l
υ	μ	0
$\cosh\upsilon$	$\cosh\mu$	1

We bring expression (94) to the more compact form

$$\omega \equiv \frac{ar(x) - \cosh\upsilon(x)}{a - \cosh\upsilon(x)}, \tag{96}$$

where the notations

$$\omega \equiv \frac{j}{\sigma\bar{E}};\quad a \equiv \frac{\sinh\mu}{\mu};\quad r(x) \equiv \frac{E(x)}{\bar{E}} \tag{97}$$

are introduced.

The x, υ, $\cosh\upsilon$ variables' change intervals are presented in Table 2. Constant $a > 1$, and $\lim\limits_{\mu \to 0} a(\mu) = 1$. As $\cosh\mu > a$, then in the range $(0; l)$, point $x = x_*$ exists in which denominator (96) becomes zero; i.e.,

$$a - \cosh\upsilon(x_*) = 0 \Leftrightarrow \cosh\frac{l - x_*}{\delta_D} = \frac{\sinh\mu}{\mu}. \tag{98}$$

Moreover, inequalities

$$\begin{aligned} 0 < x < x_* &\Rightarrow a - \cosh\upsilon(x) < 0, \\ x_* < x < l &\Rightarrow a - \cosh\upsilon(x) > 0. \end{aligned} \tag{99}$$

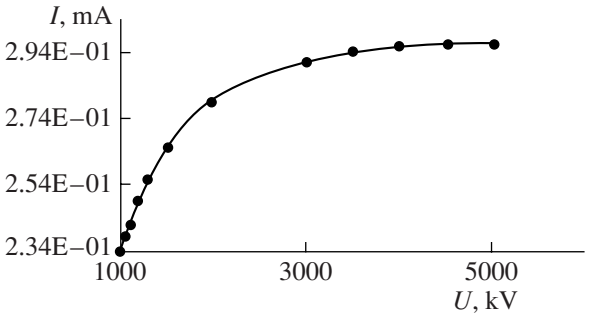

Fig. 9. Current–voltage characteristics.

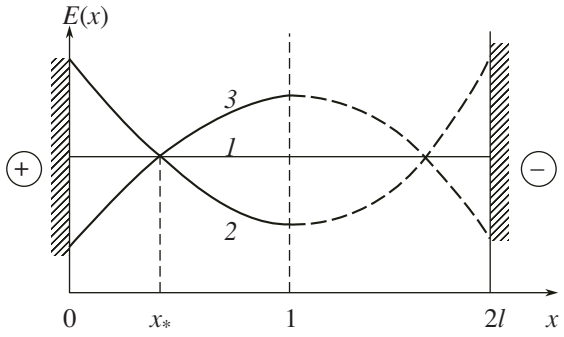

Fig. 10. $E(x)$: (*1*) E = const; (*2*) $E'' > 0$; (*3*) $E'' < 0$.

exist. Averaging the equality derived from (81) and applying the mean-value theorem, we write

$$\omega(a - \overline{\cosh\upsilon}) = a\bar{r} - \overline{\cosh\upsilon}, \tag{100}$$

where

$$\bar{r} \equiv r(x_*) = \frac{1}{l_0}\int_0^l r(x)dx;$$
$$\overline{\cosh\upsilon} = \cosh\upsilon(x_*) = \frac{1}{l_0}\int_0^l \cosh\upsilon(x)dx. \tag{101}$$

From (100), (101) follows $\bar{r} = r(x_*) \equiv r_* = 1$, and expressions (94) and (96) at $x \longrightarrow x_*$ lead to indeterminacy of the type, which we expand to

$$\omega = \lim_{x\to x_*}\frac{ar(x) - \cosh\upsilon(x)}{a - \cosh\upsilon(x)}$$
$$= \lim_{x\to x_*}\frac{\upsilon'(x)\sinh\upsilon(x) - ar'(x)}{\upsilon'(x)\sinh\upsilon(x)}$$
$$= \lim_{x\to x_*}\frac{\sinh\dfrac{l-x}{\delta_D}\left(-\dfrac{1}{\delta_D}\right) - ar'(x)}{\left(-\dfrac{1}{\delta_D}\right)\sinh\dfrac{l-x}{\delta_D}} \tag{102}$$
$$\Rightarrow \omega = 1 + \frac{a\delta_D r'(x_*)}{\sinh\upsilon_*};\quad \delta_D \equiv \sqrt{\tau D};\quad \upsilon_* \equiv \frac{l-x}{\delta_D}.$$

Thus, assuming that, in the discontinuity point $\omega(x)$, in (96), the right term of equality (102), we remove the discontinuity of this function.

It is noticed above that the quantity of the parameter ω ($\omega = 1$, neutral medium; $\omega < 1$, heterocharge; $\omega > 1$, homocharge) can serve as the criterion of hetero- and homocharging. It follows that $r'(x_*) = 0$ corresponds to $\omega = 1$, $r'(x_*) < 0$ corresponds to heterocharge, and $r'(x_*) > 0$ corresponds to homocharge. The physical meaning of the considered characteristics can be followed by the behavior of function $r(x) \equiv E(x)/\bar{E}$.

1. $\omega < 1$. From (96), taking into account (98), we have the necessity of taking the following two subcases into consideration:

(a) $0 \le x < x_* \Rightarrow a - \cosh\upsilon(x) < 0$; then,

$$\frac{\cosh\upsilon(x) - ar(x)}{\cosh\upsilon(x) - a} < 1 \Rightarrow \cosh\upsilon(x) - ar(x) < \cosh\upsilon(x) - a \Rightarrow r > 1.$$

(b) $x_* < x \le l \Rightarrow a - \cosh\upsilon(x) > 0$. In this case,

$$\frac{ar(x) - \cosh\upsilon(x)}{a - \cosh\upsilon(x)} < 1 \Rightarrow ar(x) - \cosh\upsilon(x) < a - \cosh\upsilon(x) \Rightarrow r(x) < 1.$$

2. $\omega > 1$. We find (a) $0 \le x < x_* \Rightarrow r(x) < 1$; (b) $x_* < x \le l \Rightarrow r(x) > 1$.

These peculiarities become clear from Fig. 10.

7.2. Electrization type and the second Ohm's law. In the second Ohm's law, the dependence of the current on the interelectrode distance, which should be inversely proportional at the "precise" fulfillment of Ohm's law, is implied.

It follows from Ohm's differential law in form (96) that the effective electric conductivity (let us denote it as σ_f), defined as the proportionality factor between the current j (or I) and mean intensity $\bar{E} \equiv U/l$, has the form

$$\sigma_f \equiv \sigma\frac{ar(x) - \cosh\upsilon(x)}{a - \cosh\upsilon(x)} \tag{103}$$

with the expression retaining the constant value at any x from the range $0 \le x \le l$.

Let $x = 0$ from the region (a). We obtain $r(0) \equiv r_s$; $\upsilon(x)|_{x=0} = \mu$. Consequently,

$$\sigma_f = \sigma\frac{ar_s - \cosh\mu}{a - \cosh\mu} \equiv \sigma\frac{1 - r_s\psi(\mu)}{1 - \psi(\mu)};$$
$$\psi(\mu) \equiv \frac{\tanh\mu}{\mu}. \tag{104}$$

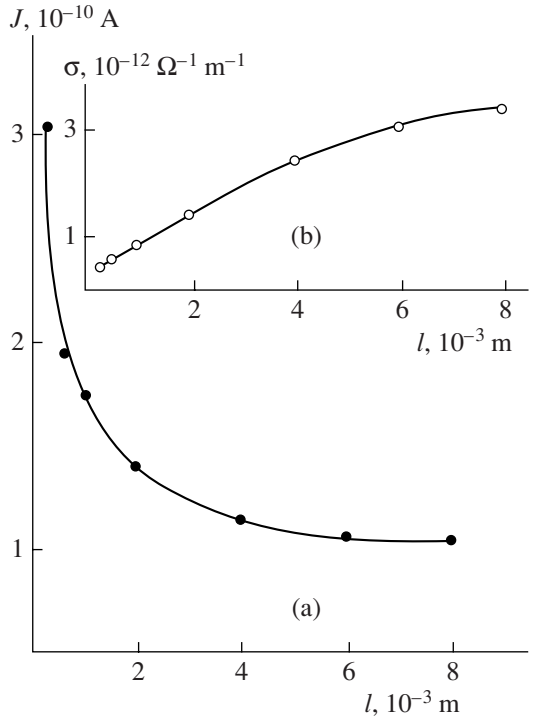

Fig. 11. Leakage current and electric conductance versus distance l characteristics in freon 113 at $U = 500$ V.

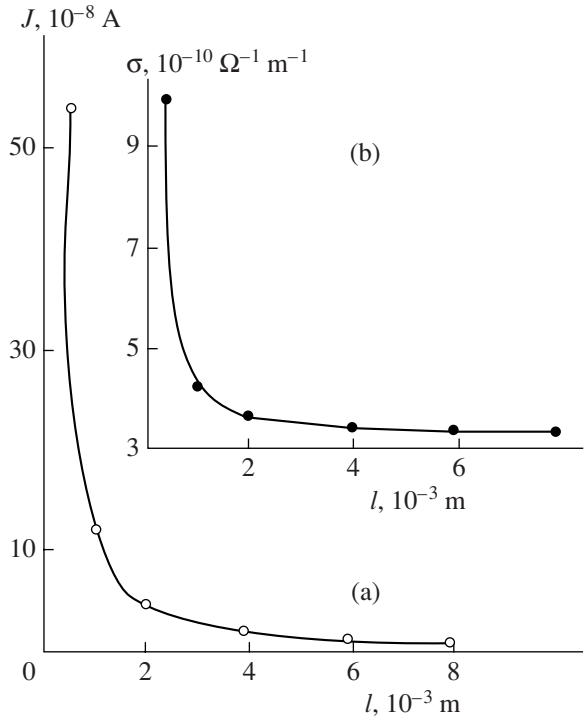

Fig. 12. Leakage current and electric conductance versus distance l characteristics in the mixture of butyl alcohol with transformer oil at $U = 600$ V.

Taking the derivative of this expression, we find

$$\frac{1}{\sigma}\sigma_f'(\mu) = \frac{(1-r_s)\psi'(\mu)}{(1-\psi)^2}. \qquad (105)$$

In the case of heterocharges (curve *2*, Fig. 10) $r_s > 1$ ($E_s > \bar{E}$) and considering $\psi'(\mu) < 0$, we come to the conclusion about $\sigma_f'(\mu) > 0$ in regards to the effective electric conductivity growth with the increase of interelectrode spacing $\mu \sim l$ that agrees with the experimental data (Fig. 11b).

Similarly, for the second semi-interval, let (104) $x = l$, from which we get

$$\sigma_f = \sigma\frac{ar_0 - 1}{a-1},\ r_0 \equiv r(l);\ \upsilon(0) = 0 \Rightarrow \cosh\upsilon = 1.$$

Hence,

$$\frac{\sigma_f'}{\sigma} = \frac{(1-r_0)a'(\mu)}{(a-1)^2}. \qquad (106)$$

At heterocharging on the second interval, $r(x) < 1 \Rightarrow r_0 < 1$; however, $a'(\mu) = (\sinh\mu/\mu)' > 0$. Consequently, by (106), $\sigma_f' > 0$. Thus, on the entire interval $0 \le x \le l$, in the case of heterocharging, $\sigma_f(\mu)$ rises with the increase of interelectrode spacing $\mu \sim l$.

Similar analysis shows that for liquids possessing the property of homoelectrization ($r < 1$ at $0 \le x < x_*$ and $r > 1$ at $x_* < x \le l$, Fig. 10, curve *3*) and the regularity $\sigma_f(\mu)$ is opposite, i.e., σ_f diminishes with the growth of distance μ, which also agrees with the experimental relationships (Fig. 12b).

As for the dependence of the current intensity on interelectrode spacing, it is directly proportional to σ_f and inversely proportional to μ; $I \sim \sigma_f(\mu)/\mu$. At heteroelectrization, $\sigma_f(\mu)$ rises with the growth of μ, although it does so more slowly than the first power of μ, (denominator of formula for I); therefore, the current will diminish (Fig. 11a). In both cases, the current intensity decreases with the increase of the distance between electrodes. The found theoretical regularities agree with the experimental ones (Figs. 11, 12).

CONCLUSIONS

1. Experimental investigations on electrization of dielectric liquids under the effect of the uniform external electrostatic field have been systematized. The types of electrization have been ascertained.

2. The general problem of electrization has been stated and a number of physical mathematical models explaining the established types of electrization, such as heteropolar, homopolar, unipolar positive, unipolar negative, bipolar homostructures, and bipolar heterostructures, have been examined.

3. A program of numerical simulation of ion conductivity processes as applied to charge formation in the liquid flat layer is presented.

4. Numerical experiment on the simulation of these processes for the cylindrical symmetry of electrodes has been carried out. It is established that for this case, bipolar near-electrode structures are common.

5. The electrization problems in connection with Ohm's law have been considered and it is shown that it is possible to establish the electrization type by the dependence of the effective electric conductivity on interelectrode distance; conductivity grows with the distance between the electrodes in the case of heteroelectrization and decreases at homoelectrization.

6. The conducted investigations can serve as a prerequisite for the solution of new EHD problems on stability of mechanical equilibrium (electroconvective instability) and EHD flow development.

ACKNOWLEDGMENTS

The paper is prepared thanks to the support of the grant RFFI 06-08-91020-Mol/A and the Academy of Sciences of Moldova 06.13CRF.

REFERENCES

1. Ostroumov, G.A., *Vzaimodeistvie elektricheskikh i gidrodinamicheskikh polei* (Interaction of Electric and Hydrodynamic Fields), Moscow: Nauka, 1979.
2. Bologa, M.K., Grosu, F.P. and Kozhukhar', I.A., *Elektrokonvektsiya i teploobmen* (Electroconvection and Heat Transfer), Chisinau: Shtiintsa, 1977.
3. Kaptsov, N.A., *Elektricheskie yavleniya v gazakh i v vakuume* (Electric Phenomena in Gases and Vacuum) Moscow: Gostekhizdat, 1950.
4. Petrichenko, N.A., *Elektricheskii veter v izoliruyushchikh zhidkostyakh* (Electric Wind in Insulating Liquids), *Extended Abstract of Cand. Sci. Dissertation*, Leningrad, 1973.
5. Taris, F. and Quizonier, R., *J. Phys.*, 1964, vol. 35, no 6, p.1110
6. Rychkov, Yu.M. and Stishkov, Yu.K., Electric Field Intensity and Space Charge in Technical Liquid Dielectrics, *Kolloidn. Zh.*, 1978, no 6.
7. Stishkov, Yu.K. and Ostapenko, A.A., *Elektrogidrodinamicheskie techeniya v zhidkikh dielektrikakh* (Electrohydrodynamic Flows in Liquid Dielectrics), Leningrad, 1989.
8. Mitskevic, P.A. and Kazatskaya, L.S., Investigation of Potential Distribution in Liquid Dielectrics by the Kerr Effect Method, Elektron. Obrab. Mater., 1968, no 2, pp. 71–74.
9. Grosu, F.P. and Bologa, M.K., Bipolar Structures of Space Charge in Low-Conducting Dielectric Liquid in the External Electric Field, Elektron. Obrab. Mater., 2007, no 1, pp. 47–51.
10. Landau, L.D. and Lifshits, E.M., *Mekhanika sploshnykh sred* (Mechanics of Continuous Media), Moscow, 1954.
11. Onsager, L., Deviation from Ohm's Law in Weak Electrolytes, *J.Chem.Phys*. 1934, vol. 2, pp. 599–615.
12. Levich, V.G., *Fiziko-khimicheskaya gidrodinamika* (Physicochemical Hydrodynamics), Moscow: Fizmatgiz, 1959.
13. Skanavi, G.I., *Fizika dielektrika (oblast' sil'nykh polei* (Physics of Dielectric (Region of Strong Fields)), Moscow, Leningrad: GIITL, 1949.
14. Zhakin, A.I., Electrohydrodynamics: Basic Concepts, Problems, and Applications, Kursk University Press, 1996.
15. Grosu, F.P. and Bologa, M.K., The Problem of Space Electrization of Low-Conducting Dielectrics, Elektron. Obrab. Mater., 2005, no 6, pp. 22–26.
16. Tsyrlin, L.A., Non-Steady-State Currents in Bodies with Low Intrinsic Conduction, Vopr. Mat. Fiz., 1976, pp. 143–151.
17. Kamke, E., *Spravochnik po obyknovennym differentsial'nym yravneniyam* (Reference Book on Ordinary Differential Equations), Moscow: Nauka, 1971.
18. Gradshtein, I.S. and Ryzhik, I.M., *Tablitsy integralov summ, ryadov i proizvedenii* (Tables of Integrals of Sums, Series, and Products), Moscow: GFML, 1962.
19. Yanke, E., Amde, F. and Lesh, F., *Spetsial'nye funktsii* (Special functions), Moscow: Nauka, 1977.
20. Pankrat'eva, I.L. and Polyanskii, V.A., Simulation of EHD Flows in Low-Conducting Liquids, *PMTF*, 1995, vol. 36, no 4, pp. 36–44.
21. Polyanskii, V.A., Faizulin, R.T., Pankrat'eva, I.A., and Sakharov, V.I., Numerical Simulation of Electrohydrodynamic Flow in the Channel with Injection of the Charge into the Stream, *Dolkady IV mezhdunarodnoi konferentsii "Sovremennye problemy elektrogidrodinamiki I elektrofiziki zhidkih dielektrikov"* (Proc. IV Int. Conf. on Modern Problems of Electrohydrodynamics and Electrophysics of Liquid Dielectrics), St. Petersburg, 1996, pp. 121–129.
22. Mirotvorskii, V.O. and Stishkov, Yu.K., The Structure and the Properties of Bipolar Near-Electrode Layers in Liquid Dielectrics, *Annual Report Conference on Electrical Insulation and Dielectric Phenomena*, Atlanta, 1998, vol. 2, pp. 428–432.

ISSN 1068-3755, Surface Engineering and Applied Electrochemistry, 2007, Vol. 43, No. 5, pp. 336–343. © Allerton Press, Inc., 2007.
Original Russian Text © A.N. Zharov, S.O. Shiryaeva, I.G. Zharova, A.I. Grigor'ev, 2007, published in Elektronnaya Obrabotka Materialov, 2007, No. 5, pp. 39–47.

ELECTRICAL PROCESSES IN ENGINEERING AND CHEMISTRY

Linear Analysis of Oscillations of a Charged Viscous Liquid Drop in the Context of Boundary Layer Theory

A. N. Zharov, S. O. Shiryaeva, I. G. Zharova, and A. I. Grigor'ev

Demidov State University, ul. Sovetskaya 14, Yaroslavl, 150000 Russia

Received March 6, 2007

Abstract—The boundary layer theory in connection with a periodically moving free surface of viscous liquids is applied to solving the problem of calculating linear oscillations of a charged viscous liquid drop. The approximate solution is compared with the exact one.

DOI: 10.3103/S1068375507050043

INTRODUCTION

Analytical investigations of nonlinear waves on flat and cylindrical charged surface of a viscous liquid and nonlinear oscillations of charged viscous liquid drops are of interest due to their numerous applications in industry and technology [1–7]. Recent analytical calculations of nonlinear oscillations of a charged viscous liquid drop [5–8] and the analytical calculation procedure itself have shown that the results obtained are too bulky for successful application. Therefore, it seems efficient to simplify the procedure of these calculations, using notions of the theory of the boundary layer in connection with a periodically moving free liquid surface [9] and to try to obtain less bulky final expressions preserving, nevertheless, the basic information of the exact solution.

It should be emphasized that in [9] the theory of the boundary layer connected with a periodically moving free liquid surface is described schematically; therefore, in the present consideration, the results obtained by calculations in the boundary layer model are compared with analogous results obtained in the exact asymptotic calculation [10].

FORMULATION OF THE PROBLEM OF CALCULATION OF LINEAR OSCILLATION FOR A VISCOUS LIQUID DROP

Let us take a spherical drop of an ideally conducting, incompressible, viscous, electrically conducting liquid with a radius r_0, mass density ρ, coefficients of kinematic viscosity ν, and surface tension σ, having an electric charge Q, oscillating axially symmetrically. Let us study analytically the time evolution of oscillations in the linear approximation by the initial deformation amplitude. The entire study will be carried out in the spherical system of coordinates r, ϑ, φ with the origin at the center of mass of an unperturbed spherical drop. Let us designate the liquid flow velocity field in the drop connected to its oscillations by $\vec{U}(r, \vartheta, \varphi)$, the appearing pressure field connected to the liquid movement by $p(r, \vartheta, t)$, the electric field potentials in the vicinity of the drop and on its surface by $\phi(r, \vartheta, t)$ and $\phi_S(t)$, respectively. The equation of the oscillating drop free surface is written in the form

$$F(r, \vartheta, t) \equiv r - r_0 - \xi(\vartheta, t) = 0. \quad (1)$$

The initial drop deformation is defined in the form of a superposition of axially symmetrical modes

$$t = 0: \xi(\vartheta) \equiv \sum_{n \in \Xi} h_n P_n(\mu); \quad \sum_{n \in \Xi} \frac{h_n}{r_0} = \varepsilon; \quad \mu \equiv \cos\vartheta; \quad (2)$$

where ε is the perturbation characterizing the initial deformation amplitude; h_n is the constant determining partial contribution of a separate oscillation mode to the initial deformation form; $P_n(\mu)$ is the Legendre polynomial; Ξ is the set of mode numbers, their superposition determining the initial drop deformation.

It should be noted that in dimensionless variables, wherein the surface tension coefficient, the drop radius, and the liquid density are assumed to be basic units, the liquid flow velocity field in the drop connected with its oscillations $\vec{U}(r, \vartheta, t)$ and the pressure field $p(r, \vartheta, t)$ appearing at oscillations are first-order infinitesimals with respect to the initial deformation amplitude ε.

Mathematical formulation of the problem of calculating axially symmetrical capillary oscillations of a charged viscous liquid drop, its form in the initial moment of time determined by (1)–(2), in the linear approximation with respect to ε has the form [10]

$$\operatorname{div}\vec{U} = 0; \quad (3)$$

$$\partial_t \vec{U} = -\frac{1}{\rho}\operatorname{grad} p + \nu\Delta\vec{U}; \quad (4)$$

$$r \longrightarrow 0\colon \vec{U} \longrightarrow 0;\ t = 0\colon \vec{U} = 0; \tag{5}$$

$$\Delta\phi = 0; \tag{6}$$

$$r \longrightarrow +\infty\colon \nabla\phi \longrightarrow 0;\ r = r_0 + \xi(\vartheta, t)\colon \phi = \phi_S(t); \tag{7}$$

$$\int_S \vec{n}\nabla\phi dS = -4\pi Q; \tag{8}$$

$$S = \{r, \vartheta, \varphi | r = r_0 + \xi;\ 0 \le \vartheta \le \pi;\ 0 \le \varphi \le 2\pi\};$$

$$r = r_0 + \xi(\vartheta, t)\colon \partial_t F + (\vec{U}\nabla)F = 0; \tag{9}$$

$$\begin{aligned} \vec{\tau}(\vec{n}\nabla)\vec{U} + \vec{n}(\vec{\tau}\nabla)\vec{U} &= 0; \\ \vec{\tau}(\vec{n}\nabla)\vec{U} + \vec{n}(\vec{\tau}\nabla)\vec{U} &= 0; \end{aligned} \tag{10}$$

$$-p + 2\rho\nu\vec{n}(\vec{n}\nabla)\vec{U} - \frac{1}{8\pi}(\nabla\phi)^2 + \sigma\mathrm{div}\vec{n} = 0; \tag{11}$$

$$\int_V r^2 \sin\vartheta dr d\vartheta d\varphi = \frac{3\pi}{3} r_0^3; \tag{12}$$

$$V = \{r, \vartheta, \varphi | 0 \le r \le r_0 + \xi;\ 0 \le \vartheta \le \pi;\ 0 \le \varphi \le 2\pi\};$$

$$\int_V \vec{r} r^2 \sin\vartheta dr d\vartheta d\varphi = 0. \tag{13}$$

The symbol ∂_t denotes the partial derivative with respect to the variable t; $\vec{\tau}$ and $\vec{n}$ are the unit vectors of tangential and outward normals to the free drop surface determined by ratio (1).

The exact solution of this problem for the nth oscillation mode taking part in the formation of the initial drop deformation, found in the linear approximation, has the form [10]

$$\xi_N(t) = \sum_{k=1}^{+\infty} h_n a_{\xi n}(S_n^{(k)}) \exp(S_n^{(k)} t);$$

$$U_{rn}(r, t) = \sum_{k=1}^{+\infty} h_n \left(a_n(S_n^{(k)}) \left(\frac{r}{r_0}\right)^{n-1} + b_n(S_n^{(k)}) \frac{1}{r} \frac{j_n(\chi_n^{(k)} r)}{j_n(\chi_n^{(k)}) r_0} \right) \exp(S_n^{(k)} t);$$

$$U_{\vartheta n}(r, t) = \sum_{k=1}^{+\infty} h_n \left[a_n(S_n^{(k)}) \left(\frac{r}{r_0}\right)^{n-1} + b_n(S_n^{(k)}) \left(\frac{1}{r} \frac{j_n(\chi_n^{(k)} r)}{j_n(\chi_n^{(k)} r_0)} + \frac{\chi_n^{(k)} r_0}{n+1} \frac{j_n + 1(\chi_n^{(k)} r)}{j_n(\chi_n^{(k)} r_0)} \right) \right] \frac{\exp(S_n^{(k)} t)}{n};$$

$$p_n^{(1)}(r, t) = -\rho r_0 h_n \sum_{k=1}^{+\infty} a_n(S_n^{(k)}) S_n^{(k)} \left(\frac{r}{r_0}\right)^n \frac{\exp(S_n^{(k)} t)}{n};$$

$$\begin{aligned} a_{\xi n}(S_n^{(k)}) = \Bigg[& S_n^{(k)} + 2(n-1)(2n+1)\frac{\nu}{r_0^2} \\ & + 2(n-1)^2(n+1)\frac{\nu}{r_0^2}\left(1 - \frac{\chi_n^{(k)} r_0}{2} \frac{j_n(\chi_n^{(k)} r_0)}{j_n + 1(\chi_n^{(k)} r)}\right)^{-1} \Bigg] \\ & \times \frac{1}{\partial_{S_n^{(k)}} D_n(S_n^{(k)})}; \end{aligned} \tag{14}$$

$$a_n(S_n^{(k)}) = \left(\left(2(n^2-1) + \frac{r_0^2 S_n^{(k)}}{\nu} \right) \frac{1}{2\chi_n^{(k)} r_0} \frac{j_n(\chi_n^{(k)} r_0)}{j_{n+1}(\chi_n^{(k)} r_0)} - 1 \right) \times \left(1 - \frac{\chi_n^{(k)} r_0}{2} \frac{j_n(\chi_n^{(k)} r_0)}{j_{n+1}(\chi_n^{(k)} r_0)} \right)^{-1} \frac{\omega_n^2}{\partial_{S_n^{(k)}} D_n(S_n^{(k)})};$$

$$b_n(S_n^{(k)}) = 2(n^2-1)\left(1 - \frac{2}{\chi_n^{(k)} r_0} \frac{j_{n+1}(\chi_n^{(k)} r_0)}{j_n(\chi_n^{(k)} r_0)}\right)^{-1} \times \frac{\omega_n^2 \nu}{r_0 S_n^{(k)} \partial_{S_n^{(k)}} D_n(S_n^{(k)})};$$

$$\begin{aligned} D_n(S_n^{(k)}) = {} & (S_n^{(k)})^2 + 2(n-1)(2n+1)\frac{S_n^{(k)}\nu}{r_0^2} \\ & + 2(n-1)^2(n+1)\frac{S_n^{(k)}\nu}{r_0^2}\left(1 - \frac{\chi_n^{(k)} r_0}{2} \frac{j_n(\chi_n^{(k)} r_0)}{j_{n+1}(\chi_n^{(k)} r_0)}\right)^{-1} + \omega_n^2; \end{aligned}$$

$$\chi_n^{(k)} \equiv \sqrt{S_n^{(k)}/\nu},$$

where $S_n^{(k)}$ is the k-fold root of the dispersion equation $D_n(S_n^{(k)}) = 0$ and $j_n(\chi_n^{(k)} r)$ is the modified spherical Bessel's function of the first kind [11]. Now let us try to formulate the same problem in the boundary layer notions and to find whether its solution is simplified significantly and what its error is in comparison with the exact solution.

SIMPLIFICATION OF THE PROBLEM IN THE CONTEXT OF THE BOUNDARY LAYER THEORY

It is well known [6–7, 12–13] that the viscous liquid flow velocity field in both flat and cylindrical geometries, as well as in a spherical one (for waves on a flat liquid surface, on a jet surface, and on a spherical drop

surface) may be represented in the form of a sum of the potential and vortex components:

$$\vec{U}(r, \vartheta, t) = \vec{U}^{(p)}(r, \vartheta, t) + \vec{U}^{(c)}(r, \vartheta, t); \quad p(r, \vartheta, t) \equiv p^{(p)}(r, \vartheta, t); \tag{15}$$

where the index (p) corresponds to the potential movement and (c) to the vortex one. To write the expression for pressure in the liquid, it was taken into account that according to [6–7, 13] in calculations of first-order infinitesimals, the pressure in the liquid is wholly determined by the potential component of the velocity field. This division of the velocity field into the potential and vortex parts was used in [10] for finding exact solution (14). Let us formulate the theory of the boundary layer connected with periodical movement of a free liquid surface as follows. We skip the equations describing the potential part of the solution, which does not depend on liquid viscosity, and simplify the problem part describing the vortex liquid movement.

Substituting (15) into continuity equation (3) and linearized Navier–Stokes equation (4), we obtain the equations describing the potential movement,

$$\operatorname{div}\vec{U}^{(p)} = 0; \quad \partial_t \vec{U}^{(p)} = -\frac{1}{\rho}\operatorname{grad} p^{(p)}; \tag{16}$$

and the equations for the vortex component of the velocity field written in scalar form,

$$\frac{1}{r^2}\partial_r(r^2 U_r^{(c)}) + \frac{1}{r\sin(\vartheta)}\partial_\vartheta(\sin(\vartheta)U_\vartheta^{(c)}) = 0; \tag{17}$$

$$\partial_t U_r^{(c)} = \frac{\nu}{r\sin(\vartheta)}\partial_\vartheta\left(\sin(\vartheta)\left(\frac{1}{r}\partial_\vartheta U_r^{(c)} - \partial_r U_\vartheta^{(c)} - \frac{1}{r}U_\vartheta^{(c)}\right)\right); \tag{18}$$

$$\partial_t U_\vartheta^{(c)} = \nu\left(\partial_{rr}U_\vartheta^{(c)} + \frac{2}{r}\partial_r U_\vartheta^{(c)} - \frac{1}{r}\partial_{r\vartheta}U_r^{(c)}\right). \tag{19}$$

One can easily see that in the system of three equations (17)–(19), only two unknown quantities $U_r^{(c)}$ and $U_\vartheta^{(c)}$ are subject to definition. This means that one of equations (17)–(19) must be neglected. To solve this problem and obtain approximate equations describing the vortex components of the velocity field inside the boundary layer, we estimate individual terms appearing in Eqs. (17)–(19). For this, let us take into account that the vortex components of the velocity field as functions of the coordinate r must appreciably vary on a characteristic linear scale equal to the boundary layer thickness δ, whereas as functions of the vectorial angle ϑ, they must appreciably vary on a characteristic angular scale equal to π. Therefore, to estimate individual vortex terms, derivatives with respect to radial and angular variables are evaluated on the basis of the ratios $\partial_r \longrightarrow 1/\delta$ and $\partial_\vartheta \longrightarrow 1/\pi$.

Estimating this and taking into account that a solution for a low-viscous liquid is shown, we find that in the low viscosity asymptote, Eq. (18) must be neglected and in Eq. (19) only two terms remain, their value increasing at $\nu \longrightarrow 0$:

$$\partial_t U_\vartheta^{(s)} = \nu\partial_{rr}U_\vartheta^{(c)}. \tag{20}$$

Equations (17) and (20) give us the desired system of equations of the boundary layer in the vicinity of the oscillating free surface of the viscous liquid drop.

As a result, we find that the system of equations describing the dynamics of a charged low-viscous liquid drop contains Eqs. (16), (17), and (20), as well as boundary and initial conditions (2), (5), and (9)–(13). Kinematic and dynamic conditions for tangential and normal components of the stress tensor (10)–(11), condition of constant volume (12), and condition of immobility of the center of mass (13) remain unmodified. Electrostatic problem (6)–(7) with condition of constant charge (8), on the basis of which the electric field pressure on the drop surface is calculated, is not modified either. One can easily see that, taking into account simplifications allowable in the boundary layer model, the initial problem of calculating linear oscillations of the charged viscous liquid drop has been appreciably simplified. Let us skip the procedure of finding solution that is standard for problems of the kind described in detail in [6–7, 10, 12–14]; we write a ready solution for the problem simplified in the context of the boundary layer notions for the nth oscillation mode taking part in formation of the initial drop deformation:

$$\xi_n(t) = h_n\left(\cos(\varpi_n t) + \frac{\gamma_n}{\varpi_n}\sin(\varpi_n t)\right)\exp(-\gamma_n t);$$

$$p_n^{(p)}(r, t) = \rho\omega_n^2 h_n r_0\left(\frac{r}{r_0}\right)^n \frac{\exp(-\gamma_n t)}{n} \times\left(\cos(\varpi_n t) + \frac{(n-1)\nu}{\varpi_n r_0^2}\sin(\varpi_n t)\right);$$

$$U_{rn}^{(p)}(r, t) = -h_n\left(\frac{r}{r_0}\right)^{n-1}\left(\frac{\omega_n^2}{\varpi_n}\sin(\varpi_n t) - 2(n^2-1)\frac{\nu}{r_0^2}\cos(\varpi_n t)\right)\exp(-\gamma_n t);$$

$$U_{\vartheta n}^{(p)}(r, t) = -\frac{h_n}{n}\left(\frac{r}{r_0}\right)^{n-1}\left(\frac{\omega_n^2}{\varpi_n}\sin(\varpi_n t) - 2(n^2-1)\frac{\nu}{r_0^2}\cos(\varpi_n t)\right)\exp(-\gamma_n t);$$

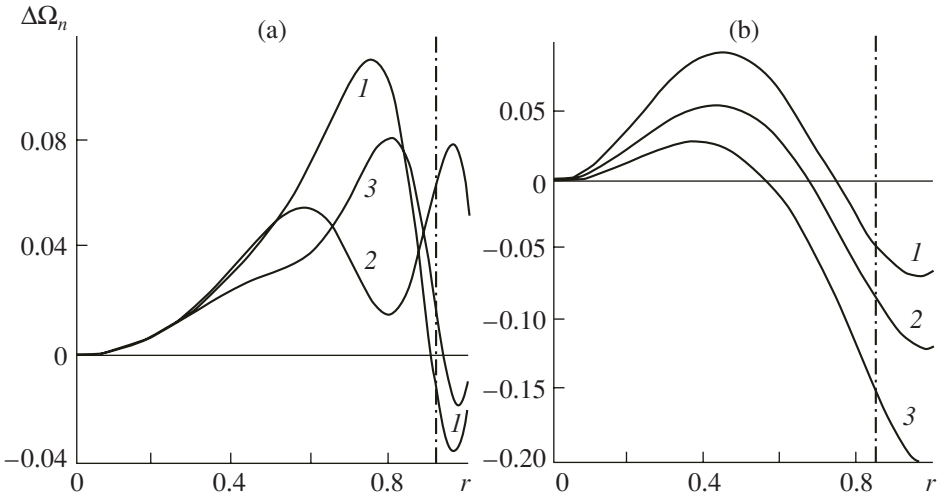

Fig. 1. Dependences on radial variable r of the difference between (23) and (24)—exact and approximate expressions for the velocity vortex $\Delta\Omega_n$ built in dimensionless variables, where $\rho = \sigma = r_0 = 1$ at $n = 2$, $\nu = 0.01$, $t = 4$ (curve *1*), $t = 5$ (curve *2*), $t = 6$ (curve *3*). The vertical dot–dash line shows the boundary layer thickness determined by expression (22): (a) $W = 0$; (b) $W = 4.1$.

$$U^{(c)}_{\vartheta n}(r, t) = \frac{(n-1)}{n}\frac{ih_n\omega_n^2}{\varpi_n}\left[\frac{\eta_n^{(-)}}{\chi_n^{(-)}r_0}\frac{\sinh(\chi_n^{(-)}r)}{\cosh(\chi_n^{(-)}r_0)}\exp(-i\varpi_n t) - \frac{\eta_n^{(+)}}{\chi_n^{(+)}r_0}\frac{\sinh(\chi_n^{(+)}r)}{\cosh(\chi_n^{(+)}r_0)}\exp(i\varpi_n t)\right]\exp(-\gamma_n t); \quad (21)$$

$$U^{(c)}_{rn}(r, t) = (n^2-1)\frac{\omega_n^2}{\varpi_n}\frac{ih_n}{r_0 r}\left[\left(\cosh(\chi_n^{(-)}r) - \frac{\sinh(\chi_n^{(-)}r)}{\chi_n^{(-)}r}\right)\times\frac{\exp(-i\varpi_n t)}{(\chi_n^{(-)})^2\cosh(\chi_n^{(-)}r_0)} - \left(\cosh(\chi_n^{(+)}r) - \frac{\sinh(\chi_n^{(+)}r)}{\chi_n^{(+)}r}\right)\times\frac{\exp(i\varpi_n t)}{(\chi_n^{(+)})^2\cosh(\chi_n^{(+)}r_0)}\right]\exp(-\gamma_n t);$$

$$\chi_n^{(-)} = \sqrt{\frac{-i\varpi_n - \gamma_n}{\nu}}; \quad \chi_n^{(+)} = \sqrt{\frac{i\varpi_n - \gamma_n}{\nu}};$$

$$\eta_n^{(-)} = 1 + \frac{\tanh(\chi_n^{(-)}r_0)}{\chi_n^{(-)}r_0}; \quad \eta_n^{(+)} = 1 + \frac{\tanh(\chi_n^{(+)}r_0)}{\chi_n^{(+)}r_0};$$

$$D_n(S) = S^2 + 2(n-1)(2n+1)\frac{\nu S}{r_0^2} + \omega_n^2 + O(\nu^{3/2});$$

$$\omega_n^2 = \frac{\sigma}{\rho r_0^3}n(n-1)(n+2-W); \quad W = \frac{Q^2}{4\pi\sigma r_0^3}.$$

One can see from comparison of (14) and (21) that the solution found in the context of the boundary layer theory is written much more simply and, therefore, it is more convenient for postanalysis (at least, it does not contain modified spherical cylindrical functions [11]).

Requiring the vortex movement damping into the drop depth, decreasing its amplitude by a factor of $e \cong 2.718$ on a characteristic linear scale of the order of the boundary layer thickness δ, we connect the characteristics of the boundary layer thickness with the physical characteristics of the problem in the form of the following ratios:

$$\delta = \begin{cases} \sqrt{2\nu/(\omega_n - \gamma_n)}, & 0 \le W < W_*; \\ \sqrt{\nu/(|\varpi_n| - \gamma_n)}, & W > W_{cr} = n + 2. \end{cases} \quad (22)$$

The value of the Rayleigh parameter $W = W_*$ separates periodic and aperiodic liquid movements in the drop [15]. It is known (see, e.g., [15]) that, depending on the mode number at any viscosity coefficient value different from zero, such a value of the Rayleigh parameter W_* exists that when at $W < W_*$ the drop surface can move periodically, i.e., oscillate, and at $W \ge W_*$ the drop surface can move only aperiodically (Fig. 1). In this case W_* is sufficiently close to the critical value for realization of the drop instability with respect to self-charge $W_{cr} = (n + 2)$, and the difference $W_{cr} - W_*$ tends to zero at $\nu \longrightarrow 0$. When the Rayleigh parameter is in the range of values $W_* < W < W_{cr}$, i.e., when the free drop surface makes aperiodic, though stable, movements, the vortex movement penetrates deep into the drop at a significant distance and the boundary layer theory is inapplicable in this situation. For a low-viscous liquid, the range $W_* < W < W_{cr}$ is very narrow, and the fact that in this

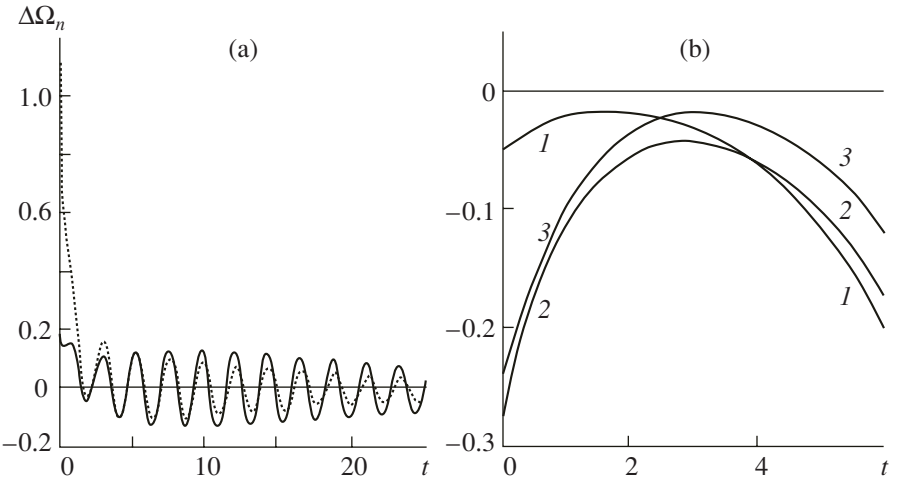

Fig. 2. Dependences of the vortex difference $\Delta\Omega_n$ determined by expressions (23) and (24) on time t: (a) at $n = 2$, $\nu = 0.02$, $W = 0$, $r = 1$ (solid line), and $r = 0.95$ (dash line); (b) at $n = 2$, $\nu = 0.01$, $W = 4.1$, $r = 1$ (curve *1*), $r = 0.9$ (curve *2*), and $r = 0.8$ (curve *3*).

range the vortex movement fills the whole drop volume is apparently due to regularities of realization of instability of the liquid charged surface with respect to the excess charge. According to [16], as the surface density of the charge approaches the critical value for realization of the free surface instability, the liquid under the free surface becomes unstable with respect to the appearance of convective type vortex movements in it, even in the absence of temperature gradients.

COMPARISON OF THE OBTAINED SOLUTION AND THE EXACT ONE

To estimate the exactness of the calculation in the context of the boundary layer theory, for calculating oscillations of the charged viscous liquid drop, we compare obtained solution (21) with the exact solution of the system (14).

On the basis of exact solution (14), in the first-order infinitesimal with respect to the amplitude of the initial deformation of an equilibrial spherical drop, we find an expression for the velocity rotor characterizing the degree of vorticity of the velocity field:

$$\operatorname{rot}\vec{U}(r,\vartheta,t) = \left(\sum_{n\in\Xi}\Omega_n(r,t)\partial_\vartheta P_n(\mu)\right)\vec{e}_\varphi;$$
$$\Omega_n(r,t) = \sum_{k=1}^{+\infty}\frac{h_n b_n(S_n^{(k)})}{n(n+1)}\frac{S_n^{(k)}}{\nu}\frac{j_n(\chi_n^{(k)}r)}{j_n(\chi_n^{(k)}r_0)}\exp(S_n^{(k)}t). \quad (23)$$

Now let us find an expression for the rotor on the basis of approximate solution (21) obtained in the context of the boundary layer theory:

$$\Omega_n(r,t) = \frac{(n-1)}{n}\frac{ih_n\omega_n^2}{\varpi_n r_0}\Bigg[\eta_n^{(-)}\Bigg(\beta_n^{(-)}\frac{\cosh(\chi_n^{(-)}r)}{\cosh(\chi_n^{(-)}r_0)} + \frac{\chi_n^{(-)}}{\chi_n^{(-)}r}\frac{\sinh(\chi_n^{(-)}r)}{\cosh(\chi_n^{(-)}r_0)}\Bigg)\exp(-i\varpi_n t)$$
$$-\eta_n^{(+)}\Bigg(\beta_n^{(+)}\frac{\cosh(\chi_n^{(+)}r)}{\cosh(\chi_n^{(+)}r_0)} + \frac{\chi_n^{(+)}}{\chi_n^{(+)}r}\frac{\sinh(\chi_n^{(+)}r)}{\cosh(\chi_n^{(+)}r_0)}\Bigg) \times \exp(i\varpi_n t)\Bigg]\exp(-\gamma_n t); \quad (24)$$

$$\chi_n^{(-)} = 1 + \frac{n(n+1)}{(\chi_n^{(-)})^2 r^2}; \quad \chi_n^{(+)} = 1 + \frac{n(n+1)}{(\chi_n^{(+)})^2 r^2};$$
$$\beta_n^{(-)} = 1 - \frac{n(n+1)}{(\chi_n^{(-)})^2 r^2}; \quad \beta_n^{(+)} = 1 - \frac{n(n+1)}{(\chi_n^{(+)})^2 r^2}.$$

Let us analyze the dependences of the expression for the velocity vortex $\Omega_n(r, t)$ on radial variable r at the fixed time t = const, proceeding from expressions (23) and (24) obtained in the exact theory and in the boundary layer theory, respectively. Results of calculation by (23) and (24) are given in Figs. 1 and 2. Detailed calculations show that the boundary layer theory approximates the exact solution well, only beginning from a certain time t_0 from which the roots of the dispersion equation $D_n(S_n^{(k)}) = 0$ with numbers $n \geq 3$ become insignificant in expression (23). In the initial moment of time $t = 0$, the modified boundary layer theory gives larger deviations from the exact theory in a wide range of r values, as one can see in Fig. 3. From the mathematical viewpoint, appearance of the feature under dis-

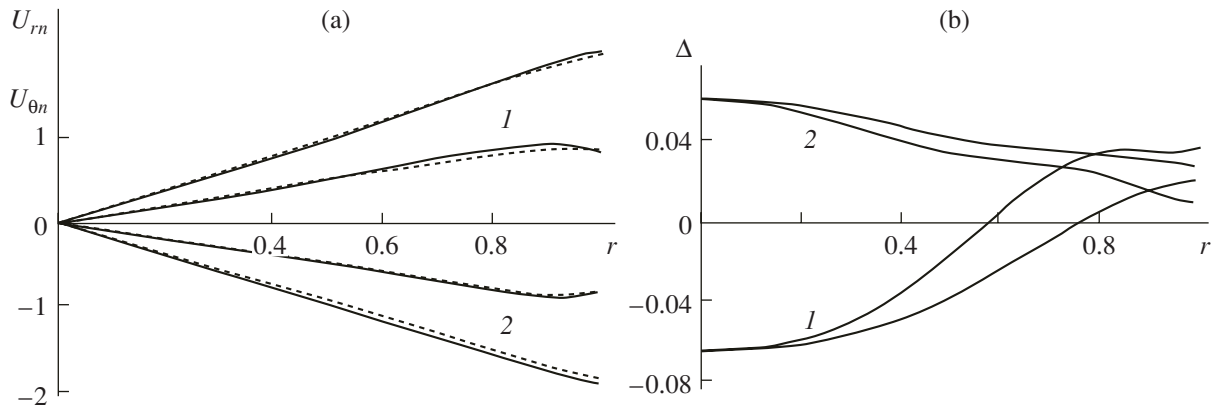

Fig. 3. Dependences on coordinate r: (a) of the velocity projections $U_{rn}^{(1)}$ (thick curve) and $U_{\vartheta n}^{(1)}$ (thin curve) (solid curves correspond to the exact solution and dashed ones to the boundary layer theory approximation); (b) of the relative deviation of these velocities Δ from their exact value at $n = 2$, $W = 1$, $\nu = 0.02$, $t = 2$ (curves *1*), and $t = 3.2$ (curves *2*).

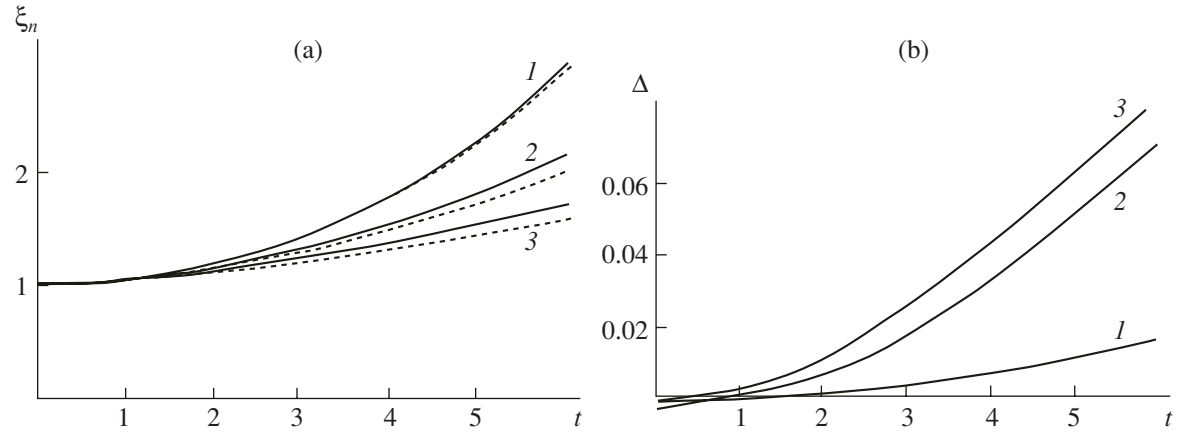

Fig. 4. Dependence on time t: (a) of the coefficient $\xi_n^{(1)}$ determining the drop form shaping (solid curve corresponds to the exact value calculated by (14) and the dot one to the boundary layer theory approximation calculated by (21)); (b) of the absolute error Δ at determination of this coefficient in the boundary layer theory at $n = 2$, $W = 4.05$, $\nu = 0.01$ (curve *1*), $\nu = 0.05$ (curve *2*), and $\nu = 0.1$ (curve *3*).

cussion is due to the fact that in the exact theory, the summation in expression (23) is performed over a large number of roots of the dispersion equation $D_n(S_n^{(k)}) = 0$ until series (23) converges, and in the approximate theory of the boundary layer, only one or two roots of the dispersion equation are taken into account. In the physical sense, this is due to the zero initial condition for the velocity field in the problem being solved: the full distribution of the liquid flow velocity field connected to the drop oscillations is set up in the time range on the order of the oscillation period.

One can see from Fig. 4 that the value of time t_0, beginning from which the boundary layer theory well approximates the exact theory, is much less than the time of damping of movement on the surface of the drop and in its volume.

The fact that the boundary layer theory describes real liquid movements in the drop only beginning from a certain moment shows that on its basis it is impossible to describe the boundary layer formation near the free drop surface. For this description, one should apply exact expression (23) for the velocity vortex. Assuming the boundary layer thickness δ is the distance from the free drop surface, where the vortex value described by exact solution (23), decreases by a factor of $e \approx 2.718$, we denote the dependence $\delta = \delta(t)$ in Fig. 5. In this figure, the point curve gives us the boundary layer determined in the modified theory by ratio (24). Analysis of Fig. 5 shows that the boundary layer thickness near the free drop surface determined by the exact solution at small times increases and then remains nearly constant, approximately equal to the boundary layer thickness (24) determined in the modified theory.

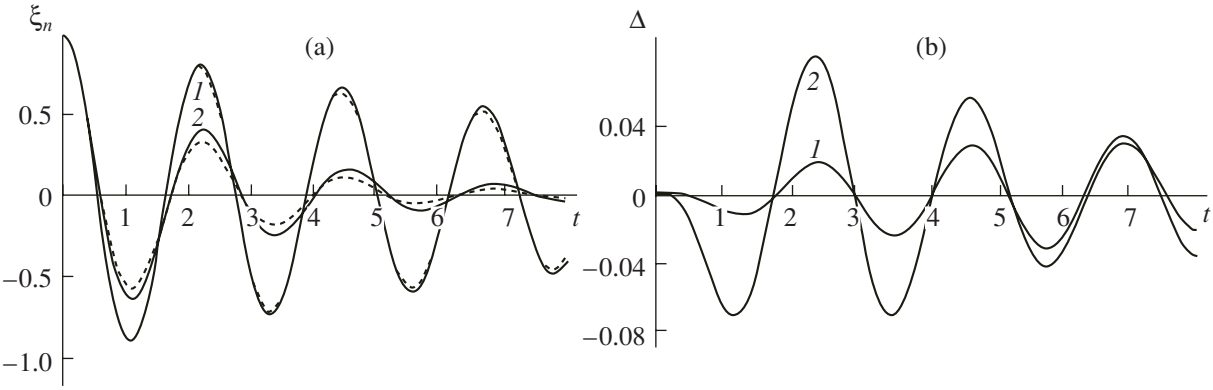

Fig. 5. Dependence on time t: (a) of the coefficient $\xi_n^{(1)}$ determining the drop form shaping (solid curve corresponds to the exact value calculated by (14) and the dot one to the boundary layer theory approximation calculated by (21)); (b) of the absolute error Δ at determination of this coefficient according to the boundary layer theory at $n = 2$, $W = 0$, $\nu = 0.02$ (curve *1*), and $\nu = 0.1$ (curve *2*).

One can see from Fig. 5 that the time of formation of the boundary velocity layer near the viscous liquid drop surface is small in comparison with characteristic times of viscous damping of the drop surface oscillations and it is approximately equal to the oscillation period in the range of stability or to the reciprocal of the instability increment at $W \geq W_{cr}$.

Thus, the analysis of the exactness of the boundary layer theory shows that at $t \geq t_0$, the boundary layer theory describes the real vortex liquid movement in the drop highly exactly. If the liquid viscosity is a small value, the vortex components proportional to $U_{rn}^{(c)}(r, t) \sim \nu$ and $U_{\vartheta n}^{(c)}(r, t) \sim \sqrt{\nu}$ appear to be small values in comparison with large-scale potential liquid movement in the drop. All this leads to the fact that liquid velocity projections on the unit vectors of the spherical system of coordinates, determined taking into account the potential and vortex components at a low viscosity of the liquid, in the boundary layer theory and in the exact theory differ insignificantly, as one can see in Fig. 5.

CONCLUSIONS

A simpler mathematical model of the problem of calculating charged drop oscillations in the boundary layer model leads to results differing from exact ones by a few percent. This is encouraging as regards application of the boundary layer theory for calculating bulky problems of nonlinear oscillations of charged drops in external force fields.

ACKNOWLEDGMENTS

The work was supported by a grant from the President of the Russian Federation (no. MK–2209–2006–1), the Russian Foundation for Basic Research (project no. 06–01–00066–a), and a grant from the Governor of Yaroslavl oblast.

REFERENCES

1. Belonozhko, D.F., Grigor'ev, A.I., Kurochkina, S.A., and Sanasaryan, S.A., Nonlinear Periodic Waves on the Charged Surface of Viscous Electrically Conducting Liquid, *Elektron. Obrab. Mater.*, 2004, no. 2, pp. 27–31.
2. Belonozhko, D.F., Grigor'ev, A.I., Klimov, A.V., Shiryaeva, S.O., and Kurochkina, S.A., On Stability of Wave Flows in Thin Liquid Layers with Charged Free Surface. Part 2. Periodic Waves of Finite Amplitude in Viscous Liquid (Review), *Elektron. Obrab. Mater.*, 2004, no. 4, pp. 66–78.
3. Grigor'ev, A.I., Shiryaeva, S.O., Zharov, A.N., and Koromyslov, V.A., Nonlinear Oscillations of Charged Drops. Part I. Analytical and Numerical Investigations of Common Regularities of Nonlinear Oscillations. Experimental Works (Review), *Elektron. Obrab. Mater.*, 2005, no. 3, pp. 25–36.
4. Grigor'ev, A.I., Shiryaeva, S.O., Zharov, A.N., and Koromyslov, V.A., Nonlinear Oscillations of Charged Drops. Part II. Internal Resonance Interaction and Measurement. Influence of External Fields. Account of Viscosity (Review), *Elektron. Obrab. Mater.*, 2005, no. 4, pp. 24–35.
5. Klimov, A.V., Belonozhko, D.F., Grigor'ev, A.I., and Sanasaryan, S.A., Nonlinear Capillary–Gravitational Waves on the Surface of a Viscous Liquid Layer, *Elektron. Obrab. Mater.*, 2005, no. 5, pp. 24–34.
6. Grigor'ev, A.I., Shiryaeva, S.O., and Zharov, A.N., *Nelineinye ostsilyatsii zaryazhennoi kapli* (Nonlinear Oscillations of a Charged Drop), Yaroslavl: Izd. YarGU, 2006.
7. Belonozhko, D.F., Shiryaeva, S.O., and Grigor'ev, A.I., *Nelineinye volny na zaryazhennoi poverkhnosti zhidkosti* (Nonlinear Waves on a Charged Liquid Surface), Yaroslavl: Izd. YarGU, 2006.
8. Zharov, A.N., Grigor'ev, A.I., and Shiryaeva, S.O., Nonlinear Oscillations of a Charged Viscous Liquid Drop, *Elektron. Obrab. Mater.*, 2005, no. 4, pp. 35–44.
9. Longuet–Higgins, M.S., Mass Transport in Water Waves, *Royal. Soc. London. Trans. Ser. A,* 1953, vol. 245, no. 903, pp. 535–581.
10. Zharov, A.N. and Grigor'ev, A.I., On Time Evolution of the Surface Form Deformed in Initial Moment of a

Charged Viscous Liquid Drop, *Zh. Teor. Fiz.,* 2005, vol. 75, issue 1, pp. 22–31.

11. *Spravochnik po spetsial'nym funktsiyam* (Handbook on Special Functions), Abramovits, M. and Stigan, I., Eds., Moscow: Nauka, 1979.
12. Grigor'ev, A.N. and Lazaryants, A.E., On One Method of Solution of the Navier–Stokes Equation in Curvilinear Coordinates, *ZhVMMF*, 1992, vol. 32, no. 6, pp. 929–938.
13. Levich, V.G., *Fiziko–khimicheskaya gidrodinamika* (Physicochemical Hydrodynamics), Moscow: Fizmatgiz, 1959.
14. Landau, L.D. and Lifshits, E.M., *Gidrodinamika* (Hydrodynamics), Moscow: Nauka, 1986.
15. Grigor'ev, A.N., Shiryaeva, S.O., and Munichev, M.I., Wave and Vortex Liquid Movements in Strongly Charged Drop*, Zh. Teor. Fiz.*, 1996, vol. 66, issue 7, pp. 1–8.
16. Belonozhko, D.F. and Grigor'ev, A.I., Convective Movements in a Layer of Viscous Liquid with Homogeneously Charged Free Surface, *Zh. Teor. Fiz.*, 2006, vol. 76, issue 9, pp. 41–45.

ISSN 1068-3755, Surface Engineering and Applied Electrochemistry, 2007, Vol. 43, No. 5, pp. 344–346. © Allerton Press, Inc., 2007.
Original Russian Text © A.V. Khlyustova, M.G. Dydykin, A.I. Maksimov, M.S. Polyakov, 2007, published in Elektronnaya Obrabotka Materialov, 2007, No. 5, pp. 48–51.

ELECTRICAL PROCESSES IN ENGINEERING AND CHEMISTRY

Investigation of Solvent Transfer Kinetics by Weight Method under Atmospheric Pressure Glow Discharge Conditions

A. V. Khlyustova[a], M. G. Dydykin[b], A. I. Maksimov[a], and M. S. Polyakov[b]

[a] *Institute of Solution Chemistry of Academy of Sciences of Russia, ul. Academicheskaya 1, Ivanovo, 153045 Russia*
[b] *Ivanovo State Chemical Technological University, pr. F. Engel'sa 7, Ivanovo, 153000 Russia*

Received April 19, 2007

Abstract—The kinetics of nonequilibrium solution evaporation was investigated by the weigh method under glow discharge action. The transfer process velocity is changed during burning discharge and depends on interelectrode spacing. The quantitative features of transfer process, namely, transfer coefficients, are substantially higher than coefficients of cathode sputtering during classic glow discharge.

DOI: 10.3103/S1068375507050055

INTRODUCTION

It is known that cathode sputtering is one of the important effects involved in the glow discharge burning under pressure with metal electrodes. This effect is also observed in the case of atmospheric pressure glow discharge, electrolyte solution being a cathode [1]. Such a process can be called solution nonequilibrium evaporation under the action of ionic bombardment. The kinetics of this process is virtually not studied; meanwhile, one might expect that the transfer of solution components into plasma zone can significantly affect both the physical properties of the discharge and the chemical transformations initiated by it. In this work, the kinetics of cathode sputtering of the electrolyte aqueous solution was investigated by the weight method.

EXPERIMENTAL

Figure 1 is a schematic diagram showing the principle of the operating plant. Solutions KCl 0.01 mol/l and Na_2SO_4 0.1 mol/l are used as working electrolytes. The cell's working volume comprises 50 ml. The cell is placed on EK 300 i electron scales, which permit objects to be weighed with an accuracy of 0.01 g. Potential electrode (anode) is mounted above the electrolyte solution surface at a distance ranging from 1–2.5 mm, the initial value of which is fixed with a precision of 0.1 mm. Wire made of stainless steel or platinum with a diameter about 0.5 mm serves as anode material. The grounded electrode (cathode) is immersed in the solution, not touching the wall or the bottom of the cell, with an aim to minimize the influence of the outcome of weighing.

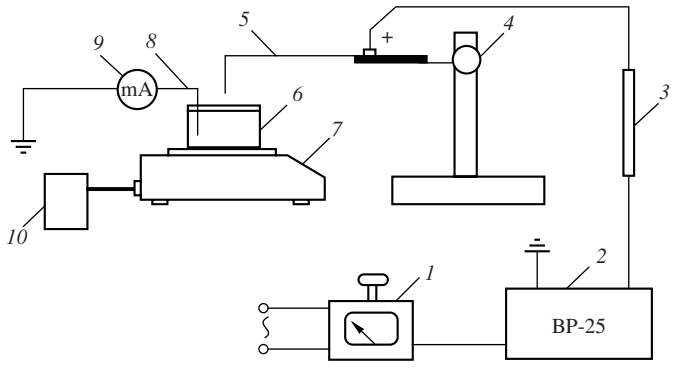

Fig. 1. A schematic diagram showing the principle of the operating plant. (*1*) Autotransformer; (*2*) high-voltage rectifier; (*3*) ballast resistor; (*4*) a device with micrometer screw to regulate the anode position; (*5*) anode; (*6*) a cell with electrolyte solution; (*7*) electron scales; (*8*) cathode; (*9*) milliammeter; (*10*) computer.

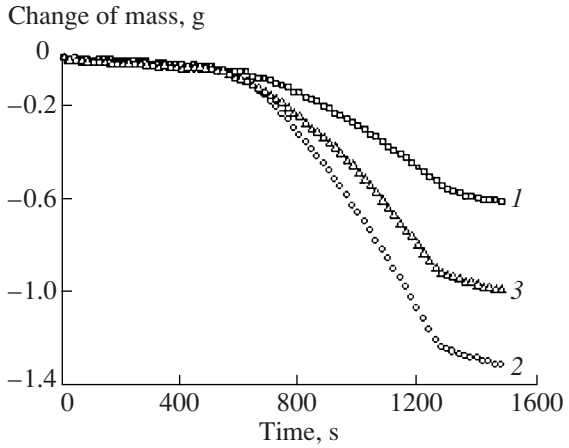

Fig. 2. The solution-mass change versus discharge-burning time at different initial distances between electrodes. Solution Na_2SO_4, concentration 0.1 mol/l, discharge current, 10 μA.

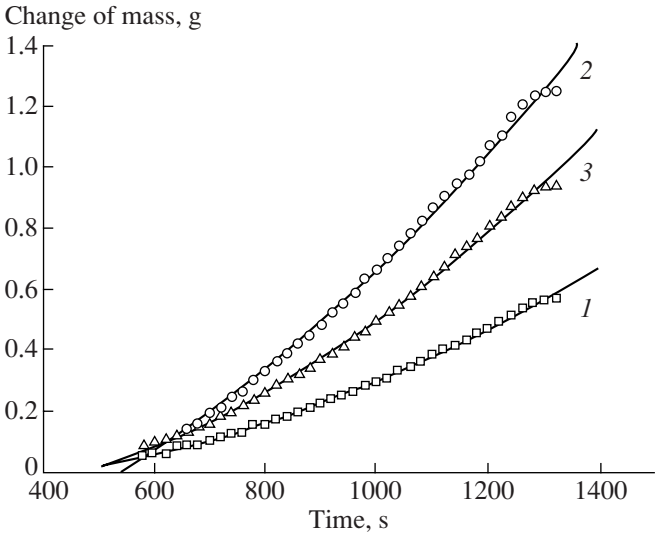

Fig. 3. Quadratic approximation of the time change of the solution mass. Solution Na_2SO_4, concentration 0.1 mol/l, discharge current 10 μA.

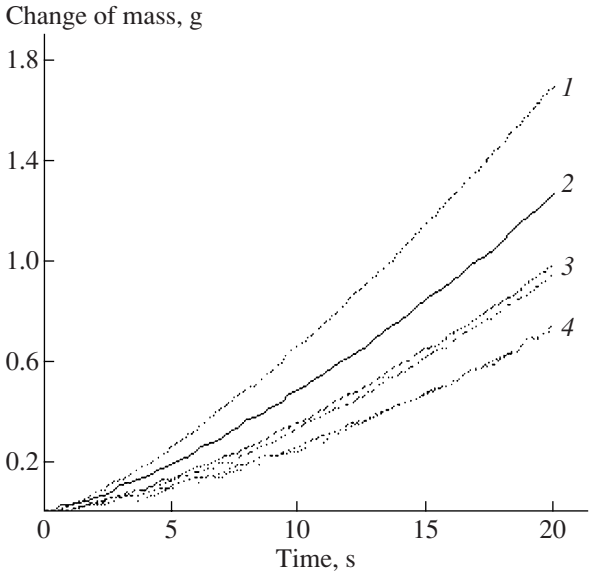

Fig. 4. The solution mass change in the course of discharge burning, described by a quadratic polynomial at different initial distances. (*1*) 2.5, (*2*) 2.0, (*3*) 1.5, (*4*) 1.0 mm. Cathode, solution Na_2SO_4, concentration 0.1 mol/l, discharge current, 10 mA.

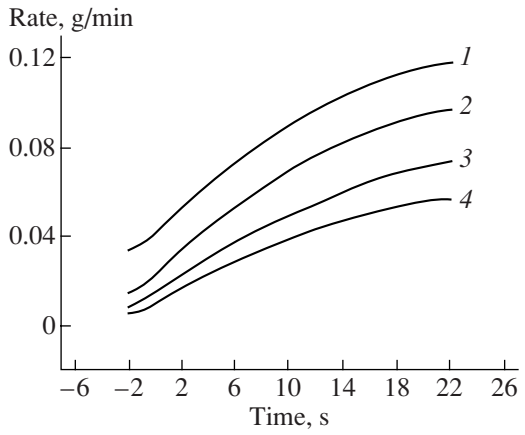

Fig. 5. Solution nonequilibrium evaporation rate change under the action of glow discharge, described by cubic polynomial at different initial inter-electrode distances. (*1*) 2.5, (*2*) 2.0, (*3*) 1.5, (*4*) 1.0 mm. Cathode–solution Na_2SO_4, concentration 0,1 mol/l, discharge current 10 μA

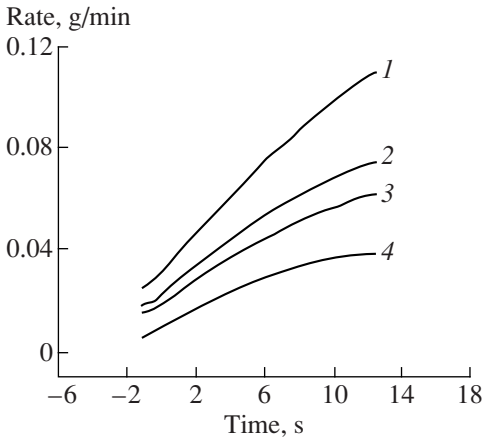

Fig. 6. Comparison dependencies of mass changes of solutions Na_2SO_4 and KCl at different discharge currents and initial inter-electrode distances. (*1*) 2.0 mm for solution Na_2SO_4, concentration 0.1 mol/l, I = 10 mA; (*2*) 2.0 mm for solution KCl, concentration 0.01 mol/l, I = 7 mA; (*3*) 1.0 mm for solution Na_2SO_4, concentration 0.1 mol/l, I = 10 mA; (*4*) 1.0 mm for solution KCl, concentration 0.01 mol/l, I = 7 mA.

The possible influence of surface tension at the solution–cathode metal interface at the outcome of weighing is checked experimentally. Such influence has not been detected when thin wire made of stainless steel or platinum is used as a cathode. The experiments were conducted at weak discharge currents (7–10 mA). Stabilized voltage source BP-0.25-2 allows one to carry out tests with currents of up to 100 mA and voltages of 7–8 kV. Ballast resistor 80 kΩ provides stable discharge burning at weak currents. As a rule, the solution treatment duration is 20 min. The solution mass change during discharge burning is noted at 20-s intervals.

RESULTS AND DISCUSSION

To take into account the contribution of the solvent quasi-equilibrium thermal evaporation to the process under investigation, the control of the mass change in

Coefficients of solvent transfer from diluted solutions by glow discharge, determined by weigh method

Solution composition	Concentration	Discharge current, mA	Transfer coefficient
KCl	0.01 M	7	161 (initial)
KCl	0.01 M	7	268 (limiting)
Na_2SO_4	0.1 M	10	168 (initial)
Na_2SO_4	0.1 M	10	273 (limiting)

the cell with solution was performed to find the solvent evaporation rate before the firing of the discharge and after its extinguishing. The types of relationships obtained are illustrated in diagrams in Fig. 2. As is evident from the presented data, rates of quasi-equilibrium and nonequilibrium evaporations differ in their orders of magnitude, so that the contribution of quasi-equilibrium evaporation does not radically change the result.

Initial experimental-data handling shows that the transfer-process rate, determined as the time derivative of the cell mass, changes during discharge burning and substantially depends on the distance between the metal anode and the solution. As is obvious from the data in Fig. 3, the solution-mass change with time is actually approximated rather well by the quadratic dependence, which is within the boundaries of the experiment limited time; the transfer rate grows approximately linearly with time of the solution treatment.

Clearly, long-term discharge burning should result in the attainment of a steady transfer rate. A direct experimental evaluation of this rate appears to be difficult since the discharge burning is greatly prolonged, resulting in increases in the spacing between electrodes and changes in the discharge parameters, including the stability. However, it is possible to recognize the tendency to attain the top transfer rate by approximating the initial kinetic curves through using a third-degree polynomial and differentiating the obtained fitted curve. The results of handling of experimental data in such a way for some conditions of the experiment are exhibited in Figs. 4–6.

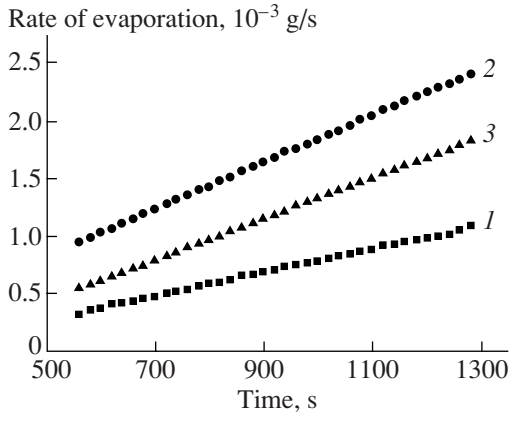

Fig. 7. Time change of transfer rate at different initial interelectrode distances: (*1*) 1.12, (*2*) 3.4, (*3*) 2.0 mm.

The transfer rate versus the discharge-burning time characteristics, which were obtained on the basis of these data at different interelectrode spacings, are shown in Fig. 7.

The transfer coefficient, defined as the relation of water-molecule flow from the solution into the gas phase to positive-ion flow from the plasma on the solution surface. As is evident from the above experimental data, the transfer coefficient grows during discharge burning. Estimations of the initial and final values of the transfer coefficient for two different experimental conditions are presented in the table. These data agree well with those obtained previously by the volumetric method [2]. It should be noted that during the search for these coefficients, it was suggested that due to the low concentration of the solutions, their mass change was governed by virtually only carrying the solvent away. As the data exhibited in the table show, the coefficient of solvent transfer from the diluted solutions hardly depends at all on their composition. Notice the large values of the coefficients found that exceeded the coefficient of cathode sputtering in the glow discharge under pressure with metal electrodes by a factor of 100 [3].

Experimental data on the solvent transfer nonequilibrium coefficients are presented for the first time in this work. As the results show, the transfer coefficient is not a constant and grows with the rise of irradiation dose and increase of interelectrode spacing.

REFERENCES

1. Kutepov, A.M., Zakharov, A.G. and Maksimov, A.I., *Vakuum-plazmennoe i plazmenno-rastvornoe modifitsirovanie polimernykh materialov (Vacuum-Plasma and Plasma-Solution Modification of Polymer Materials),* Moscow: Nauka, 2004.

2. Khlyustova, A.V. and Maksimov A.I., Transfer of Solution Components into Plasma Zone under the Conditions of Glow Discharge at Atmospheric Pressure with Electrolyte Cathode, *Elektron. Obrab. Mater.,* 2003, no 1, pp. 44-47.

3. Pleshivtsev, N.V., *Katodnoe raspylenie* (Cathode Sputtering), Moscow: Atomizdat, 1968.

ISSN 1068-3755, Surface Engineering and Applied Electrochemistry, 2007, Vol. 43, No. 5, pp. 347–349. © Allerton Press, Inc., 2007.
Original Russian Text © A.N. Yushchishina, N.I. Kuskova, A.P. Malyushevskaya, 2007, published in Elektronnaya Obrabotka Materialov, 2007, No. 5, pp. 52–55.

ELECTRICAL PROCESSES IN ENGINEERING AND CHEMISTRY

Study of Chemical Reactions during Electric Discharge in Water and Aqueous Solutions of Inorganic Substances

A. N. Yushchishina, N. I. Kuskova, and A. P. Malyushevskaya

Institute of Pulse Processes and Technologies of National Academy of Sciences of Ukraine, Oktyabr'skii pr. 43-A, Nikolaev, 54018 Ukraine

Received January 26, 2007

Abstract—A comparative study of the chemical activity of inorganic substances under conditions of electric discharge in a liquid has been carried out. It has been shown that the electric discharge in water is accompanied by formation of chemically active particles possessing oxidizing properties and that the electric discharge action results in an increase in the oxidation power of inorganic substances dissolved in water. These data should be taken into account for development of discharge–pulse technologies.

DOI: 10.3103/S1068375507050067

INTRODUCTION

Discharge–pulse technologies have a long history of application in various fields, such as clearing of castings from cores, cleaning of perforation of oil- and water wells, modification of melt crystallization conditions in a ladle, vibration-pulse pressing, intensification of chemical engineering processes, etc. [1–6].

The operating element in these technologies is an electric discharge chamber of various constructions, wherein an electric breakdown of water occurs with subsequent hydrodynamic impact on the treated material.

Distilled water was usually used as a working medium. Engineers developing technologies of this kind concerned themselves only with the electrophysical water properties providing stability of the discharge and its energy efficiency.

Recently, there have been new developments in this field where a spatial coincidence of a working medium and a treated material takes place. Among them there are such processes as clearing of flax fiber from encrusting matter, clearing of diamond sinters from metals–catalysts, bleaching of flax wool, disinfection of potable water, chromium-containing sewage purification, and obtaining of fullerenes [7–9].

The aim of the present work is to study chemical reactions proceeding during an electric discharge in water and aqueous solutions of inorganic substances and to determine the nature of physicochemical transformations and possibilities of controlling them.

Due to a complex of various physicochemical factors during an underwater electric explosion, it is clear that studying the change of chemical reactant properties in situ is impossible; therefore, the change in substance reactivity was estimated by indirect data.

EXPERIMENTAL

Substances used in specific discharge-pulse technologies were selected as the object of investigations: ammonium nitrate (NH_4NO_3) as a basic reactant of the working medium for the clearing of diamond sinters from metals–catalysts [7], potassium iodide (KJ) as a reactant for determining the degree of cavitation processes in the electric discharge conditions [8], calcium hypochlorite (CaClO) as a reactant of the working medium in the discharge-pulse technology of flax wool bleaching [9].

The experimental setup for the investigations (Fig. 1) contains the following: a charging unit (CU) consisting of a RNO-250-5 autoconnected transformer, a OMTV–5/50–U4 rectifier–transformer and a charging resistor (two KEV–40–2.4 mΩ resistors connected in parallel), a bank of capacitors (C), an air gap (AG), and a discharge chamber (DC).

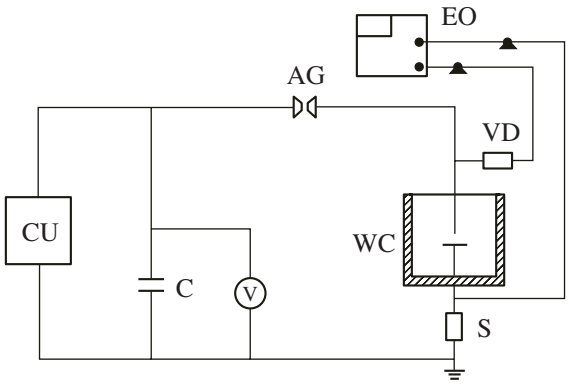

Fig. 1. Scheme of the experimental setup: EO—electron oscillograph; AG—air gap; VD—voltage divider; WC—working chamber; C—bank of capacitors; CU—charging unit; S—shunt.

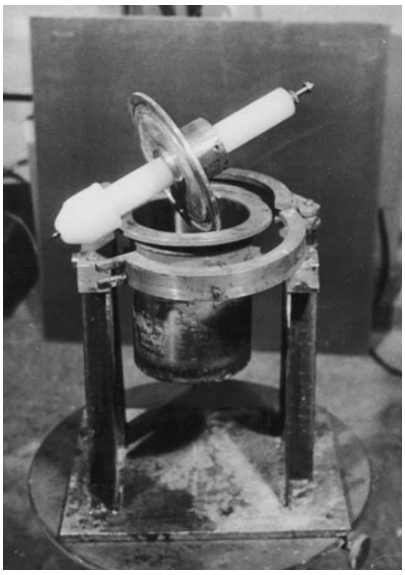

Fig. 2. Working chamber with an electrode system of the point–plane type.

The DC had a volume of 5 l (Fig. 2), was made of stainless steel, and contained an electrode system of the point–plane type.

The experiments were carried out with variation of the electric parameters: operating voltage, capacitance of the bank of capacitors, and frequency of pulse repetition, the energy in a pulse being from 300 J up to 3 kJ.

RESULTS AND DISCUSSION

In an underwater electric explosion in distilled water, many physicochemical processes take place, changing the electrophysical properties of water. The reason for these changes is decomposition of water molecules due to both the homolytical break of bonds between oxygen and hydrogen atoms and heterolytic break. In the first case, radical particles ($H^{\bullet}$, $OH^{\bullet}$, $O^{\bullet}$) are formed, and in the second, case hydronium (H_3O^+) and hydroxyl–ions (OH^-) appear. These processes are proved by various oxidation–reduction reactions, resulting in the formation of hydroxides of iron, aluminum, titanium, and metals for electrode preparation and leading to a decrease in the pH of the medium from 6.6 to 5.6.

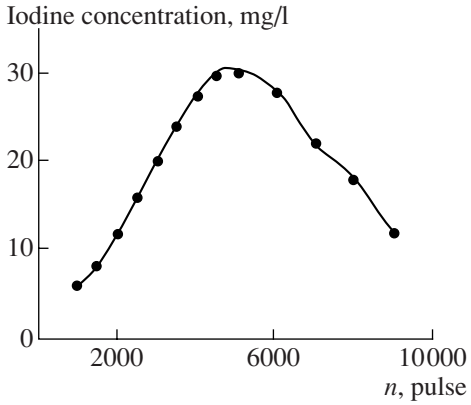

Fig. 3. Dependence of the evolved J_2 concentration on number of the electric discharge pulses.

In order to determine the degree of oxidation power of the working medium in an underwater electric explosion, we have studied the reaction of potassium iodide oxidation during treatment of its aqueous solution by underwater electric discharges. It was preliminarily found that factors of an electric explosion, such as the working medium heating up to 60°C, pulse photolysis, pulse electrolysis, and the acoustic (ultrasonic) component of the discharge, individually do not significantly influence the reaction of the formation of free iodine [10]. Figure 3 shows the dependence of iodine formation on the pulse number in the electric discharge treatment of a potassium iodide aqueous solution with a concentration of 1g/l. One can see that under the influence of electric discharge, the accumulation of molecular iodine takes place; that is, the oxidation–reduction

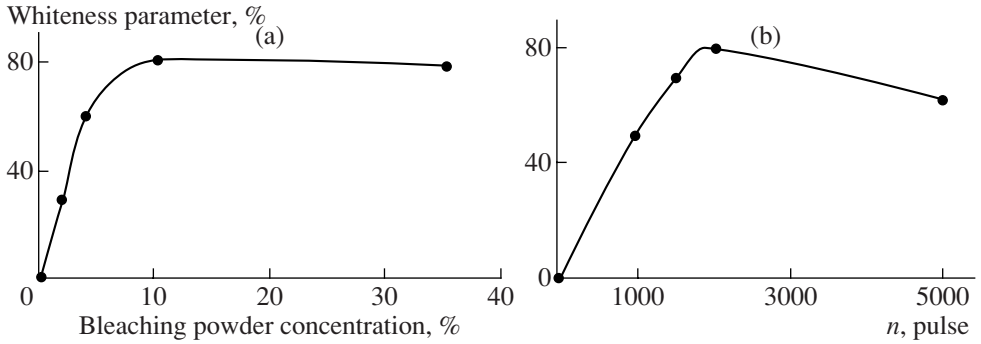

Fig. 4. Dependence of the flax wool whiteness parameter: (a) on bleaching powder concentration without the electric discharge treatment (treatment duration is 60 min, the solution temperature is 60–80°C) and (b) on the number of pulses at a bleaching powder concentration of 2%.

process occurs, where oxidants are active particles of the water medium:

$$2J^- + [O^\bullet] + H_2O \longrightarrow J_2 + 2OH^-.$$

The observed decrease in the concentration of evolved iodine at a great number of pulses (>5000) may be due to its interaction with fine particles of the eroded metal of the electrode. Thus, these results prove the formation of oxidant particles in the electric breakdown of water.

The reason for the increase in the oxidation power of the working medium containing ammonium nitrate in underwater electric discharge is the same as the application of this reactant in the process of clearing of diamond sinters from metals–catalysts [7]. Here may take place both an additive effect from the contribution of active water particles and an additional activation of the molecules of ammonium nitrate itself due to the homolytical breaking of bonds and the formation of more active radical particles ($NO_3^\bullet$). The experiments were carried out with application of nickel–manganese catalysts; the degree of their solubility was determined by the photocolorimetric method (КФК-2) by the formation of ammoniac complexes of nickel and manganese and by the SEM method (Superprobe-733 scanning electron microscope, Jeol, Japan) in characteristic rays K_αNi. It is shown that an almost complete solubility of metals–catalysts is achieved only under the simultaneous influence of the chemical reactant and the underwater electric discharge on a diamond sinter. The electric discharge treatment of diamond sinters in distilled water, as well as their dissolution in ammonium nitrate without discharge, does not allow achieving the same level of procession of the metal–catalyst dissolution reaction.

One more confirmation of the increase in the oxidation power of the working medium in an underwater electric discharge is the process of flax wool bleaching with application of bleaching powder as a chemical reactant [9]. Figure 4 shows the dependence of the whiteness parameter of flax wool on the concentration of bleaching powder during treatment (a) without additional intensification of electric discharge and (b) with application of underwater electric discharge.

Comparison of the conditions for these processes shows that during simultaneous application of the electric discharge treatment and the chemical reactant, it is possible to significantly decrease the technological time of the process, the concentration of the chemical reactant, and the temperature of the working medium. The observed electric discharge activation of the flax wool bleaching process is apparently caused by the same reasons as in the case of ammonium nitrate: activation of the molecules of the chemical reactant itself and influence of oxidant particles from water on the treated material.

Thus, the investigations prove that in an underwater electric discharge, chemically active particles and/or substances possessing oxidation power are formed. Under the influence of electric discharge on solutions of inorganic substances, activation of the latter occurs, resulting in an increase in the observed oxidation power. These data should be taken into account in the development of discharge—pulse technologies, where a coincidence of the working medium and the treated material takes place.

REFERENCES

1. Malyushevskii, P.P., *Osnovy razryadno–impul'snoi tekhnologii* (Bases of Discharge–Pulse Technology), Kiev: Naukova Dumka, 1983.
2. Kostyrkin, B.V. and Vasil'eva, A.N., Investigation of the Process of EH Clearing of Investment Castings, *Liteinoe Proizvodstvo*, 1986, no. 12, pp. 25–30.
3. Sizonenko, O.N. and Khvoshchan, O.V., On the Problem of Electric Discharge Technology of Intensification of Oil Influx in Wells, *Elektron. Obrab. Mater.*, 2003, no. 5, pp. 80–86.
4. Tsurkin, V.N. and Sinchuk, A.V., Thermodynamic Analysis of External Electrohydropulse Influence on the Melt State before Casting and on Metal Crystallization, *Protsessy Lit'ya*, 2004, no. 1, pp. 6–9.
5. Miroshnichenko, E.K. Radutman, Ya.S., Ivliev, A.I., and Malyushevskii, P.P., Pulse Electric Discharge Application in Liquid for Pressing of Products of Solid Alloy Powder, *Fizika i tekhnologiya elektrogidroimpul'snoi obrabotki materialov: Sb. nauchn. trudov* (Physics and Technology of Electrohydropulse Treatment of Materials: Coll. Sci. Papers), Kiev: Naukova Dumka, 1984, pp. 94–97.
6. Malyushevskii, P.P. and Yushchishina, A.N., Electric Explosion in Chemical Engineering Processes (part I), *Elektron. Obrab. Mater.*, 2001, no. 4, pp. 58–72.
7. Yushchishina, A.N., Malyushevskii, P.P., Smal'ko, A.A., and Volkov G.V., High–Voltage Pulse Discharge Application in the Process of Metal–Catalyst Removal from Diamond Sinters, *Elektron. Obrab. Mater.*, 2001, no. 3, pp. 33–36.
8. Yushchishina, A.N. and Malyushevskii, P.P., Intensification of Oxidation Processes in Technology of Water Treatment, *Khimiya Tekhnol. Vody*, 1998, vol. 20, no. 3, pp. 306–310.
9. Yushchishina, A.N. and Malyushevskii, P.P., Electric Discharge Application for Intensification of Flax Wool Bleaching Technology, *Elektron. Obrab. Mater.*, 2000, no. 1, pp. 55–57.
10. Yushchishina, A.N., Malyushevskii, P.P., Smal'ko, A.A., Petrichenko, L.A., and Tikhonenko, S.M., Iodometric Test of Electric Discharge Volume Cavitation, *Elektron. Obrab. Mater.*, 2002, no. 2, pp. 76–79.

ISSN 1068-3755, Surface Engineering and Applied Electrochemistry, 2007, Vol. 43, No. 5, pp. 350–353. © Allerton Press, Inc., 2007.
Original Russian Text © S.G. Poklonov, V.G. Zhekul, A.P. Smirnov, 2007, published in Elektronnaya Obrabotka Materialov, 2007, No. 5, pp. 56–60.

ELECTRICAL PROCESSES IN ENGINEERING AND CHEMISTRY

Technique and Results of Experimental Investigations of the Influence of the Elastic Barrier on Pressure Wave Parameters in Electric Discharge in Water

S. G. Poklonov, V. G. Zhekul, and A. P. Smirnov

Institute of Pulse Processes and Technologies, National Academy of Sciences of Ukraine, Oktyabr'skii pr. 43-A, Nikolaev, 54018 Ukraine

Received March 30, 2007

Abstract—The paper describes the technique and results of experimental investigations on the influence of the elastic barrier of various materials on transformation of the pressure wave parameters in electric discharge in water for application in closed electrode systems of high-voltage electric discharge immersion installations for treatment of water and oil wells.

DOI: 10.3103/S1068375507050079

INTRODUCTION

For restoration of the fluid influx in water and oil wells, electric discharge immersion installations (EDII) are applied [1]. The essence of the process is as follows. As the EDII is lowered into a well filled with a liquid, in the electrode system (ES), the EDII realizes a high-voltage pulse breakdown of the liquid, causing excitation of pressure waves, a pulsing vapor-gas cavity influencing the polluted filter part of the well, purifying it.

It is known that operational efficiency of the ES and the installation as a whole depends on the properties of the liquid and the conditions in the well [2, 3]. Such intrawell conditions are possible when prebreakdown energy losses achieve more than 50% of the stored energy; in addition, the efficiency and stability of discharges decrease. To overcome these obstacles, ESs of the closed type (CESs) are applied [4, 5]. The difference between a CES and an open ES is the presence of a liquid-impermeable but acoustically transparent shell. It protects the internal ES cavity from the external medium. The cavity is filled with a working liquid having optimal specific electric conductivity that allows discharge stabilization and decreasing energy loss to 10% or less.

PROBLEM ANALYSIS

Let us take the efficiency of the process of sequential transformation of electric energy in the CES into the energy of force action on an object of treatment η_{TOT} and represent it in the form of the product of the efficiencies of four stages of energy transformation:

$$\eta_{TOT} = \eta_{PP}\eta_{EL}\eta_{AC}\eta_{TR}, \quad (1)$$

where η_{PP} is the efficiency of energy transformation during the formation of the discharge channel; η_{EL} is the efficiency of the capacitor electric energy transformation into the internal energy of the discharge channel during first half-period of the discharge current; η_{AC} is the efficiency of the discharge channel internal energy transformation into pressure wave acoustic energy; and η_{TR} is the efficiency of acoustic energy transfer through a transferring medium to the object of treatment.

As was already mentioned, in the CES, the prebreakdown energy losses decrease; this favors an increase in energy transformation efficiency during formation of the discharge channel, η_{PP}:

$$\eta_{PP} = \frac{W_0 - W_{PP}}{W_0}, \quad (2)$$

where $W_0 = CU_0^2/2$ is the initial stored energy in the reservoir capacitor, J; C is the capacitance of the reservoir capacitor, Φ; U_0 is the voltage of charging the reservoir capacitor, V; W_{PP} are the prebreakdown energy losses, J.

The efficiency of the transformation of capacitor energy into the internal energy of the discharge channel in the first half-period of the discharge current [6] during which the acoustic (shock) wave is formed is determined as

$$\eta_{EL} = \left(\frac{\pi A I_{IE}^2}{U_0^2 \eta_{PP}\sqrt{LC}}\right), \quad (3)$$

where A is the spark constant ($A = 0.25 \times 10^5$ V^{2}s/m^2 for initiated discharges; $A = 10^5$ V^{2}s/m^2 for uninitiated ones); l_{IE} is the length of the interelectrode space, m; and L is the inductance of the discharge circuit, H.

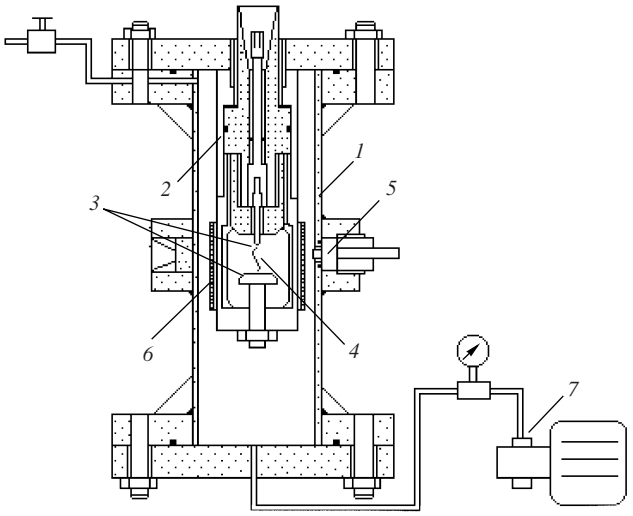

Fig. 1. Technological part of the experimental stand: (*1*) high-pressure discharge chamber; (*2*) the coaxial electrode system; (*3*) electrodes of the electrode system; (*4*) discharge channel; (*5*) waveguide pressure gage; (*6*) protective shell; (*7*) high-pressure pump.

The efficiency of the transformation of the energy of the discharge channel into pressure wave acoustic energy [7] may be expressed by the formula

$$\eta_{AC} = \frac{0.8}{c_0}\left(\frac{\eta_{EL} W_0 \eta_{PP}}{\rho_0 l_{IE} \tau^2}\right), \quad (4)$$

where c_0 is the sound velocity in the unperturbed liquid, m/s; ρ_0 is the liquid density, kg/m^3; and $\tau = (1 + \eta_{EL}^3)\pi\sqrt{LC}$ is the duration of the first half-period of the discharge current, s.

Let us determine the efficiency of acoustic energy transfer through a transferring medium to the object of treatment η_{TR} according to the equation

$$\eta_{TR} = \frac{W_{AC2}}{W_{AC1}}, \quad (5)$$

where W_{AC1} is the acoustic energy transferred to the object of treatment in the absence of losses in the transferring medium, J; W_{AC2} is the acoustic energy transferred to the object of treatment in the presence of losses in the transferring medium, J.

As follows from (1), the maximal value of η_{TOT} is possible at the highest value of each multiplier, including η_{TR}. If for an open ES, η_{TR} may be considered equal to one, then for a CES, this value must be less than one due to the presence of the protective shell in the path of the spread of the loading wave from the discharge channel to the object of treatment.

It is known [4] that a thin rubber shell of thickness $\delta = 1$ mm decreases the shock wave amplitude by 15–20%, and a similar shell of polyethylene does not weaken the pressure wave hardly at all [8]. However, taking into account the specificity of the CES operation under conditions of deep wells (up to 5000 m) with a medium temperature of up to 100°C, hydrostatic pressures up to 50 MPa, and significant mechanical loads in lowering and lifting, the real thickness of the shell may be more than 6 mm.

On the basis of a mathematical simulation [9], the process of pressure pulse transfer to the casing through the discharge chamber wall was studied for three types of material: polyethylene, rubber, and steel with $\delta = 6$, 6, and 1 mm, respectively. Results of the study have shown that the presence of a screen of these materials leads to a decrease in the amplitude of the pressure wave on the internal casing surface by a factor of 2, 2.2, and 2.6, respectively.

However, the given calculation did not take into account the hydrostatic pressure influence on properties of the shell itself and lacked accurate data on such parameters as the Young's modulus for really used complex multilayered shells [10].

Therefore, the goal of the present work is an experimental investigation of the transformation of the pressure wave parameters, such as amplitude, specific pulse, and acoustic energy, for shells of various materials at various hydrostatic pressures corresponding to those in wells.

TECHNIQUE OF INVESTIGATIONS

The shell material's influence on the pressure wave transfer to the object was studied with an experimental stand [3], its technological part shown in Fig. 1, by a technique based on measurement of the time profile of the pulse pressure $P(t)$ by a special waveguide pressure gage (WPG) (Fig. 2).

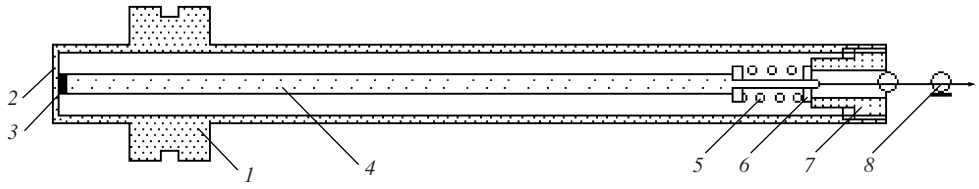

Fig. 2. Waveguide pressure gage: (*1*) gage body; (*2*) bottom of the gage; (*3*) piezoelectric ceramic transducer; (*4*) copper waveguide; (*5*) spring; (*6*) dielectric washer; (*7*) clamping screw; (*8*) measuring cable.

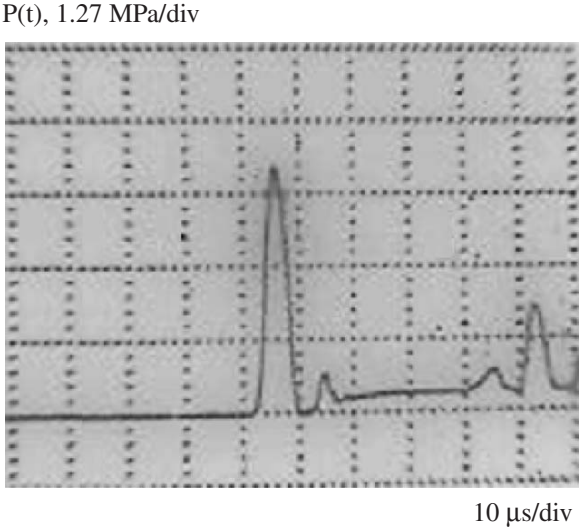

Fig. 3. Typical oscillogram of the pressure wave.

On the basis of data on $P(t)$ the maximal amplitude of the pulse pressure P_m and the specific pulse J calculated were determined by the formula

$$J = \int_0^t P(t)dt, \tag{6}$$

and the density of flux of the pressure wave acoustic energy W [6],

$$W = \frac{1}{\rho_0 c_0}\int_0^t P^2(t)dt. \tag{7}$$

The investigations were carried out at the following energy parameters of the installation: the charge voltage $U_0 = 20$ kV, the capacitor bank capacitance $C = 0.25$ μF, and the discharge circuit inductance $L = 4.58$ μH.

For stabilization of length and hydrodynamic parameters of discharge channel *4* (Fig. 1) the discharge was initiated by a copper conductor with a diameter of 0.1 mm and a length of 46 mm. Distilled water served as the hydraulic medium.

Protective shells *6* (Fig. 1) of high–density polyethylene ($\delta = 6$ mm), rubber (a smooth rubber pressure hose with textile reinforcement according to All-Union State Standard 10362–76, $\delta = 7.5$ mm), and steel ($\delta = 0.6$ mm) were tested.

The experiments were carried out at the following levels of the hydrostatic pressure in the chamber: 0.1, 0.6, 1.8, 3.0, 12.0, and 30.0 MPa.

The applied waveguide pressure gage (Fig. 2) allowed measurement of the pulse pressure on the internal surface of the high-pressure chamber. A sensitive element of the WPG is transducer *3* of TsTS-19 piezoelectric ceramics.

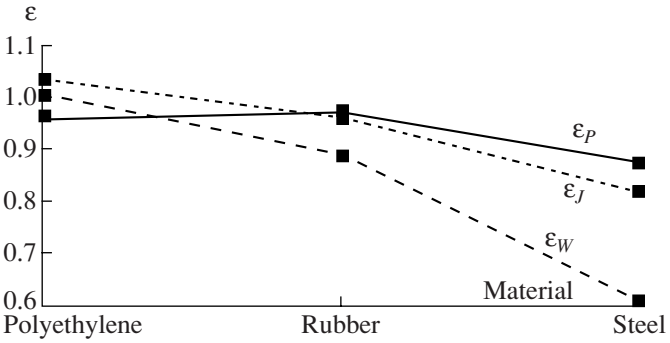

Fig. 4. Coefficients of the pressure wave parameter transformation by protective shells of various materials.

A dynamic calibration of the WPG for determining its sensitivity, together with a measuring cable 6 m in length, was realized with an impact-testing machine by the technique described in [11]. The gage sensitivity was $\mu_G = 19.65$ μV/Pa.

Five experiments were carried out for each level of the hydrostatic pressure with and without a protective shell. Statistical averages of $\bar{P}_{m1}$, $\bar{J}_1$, and $\bar{W}_1$ for the case without a protective shell and of $\bar{P}_{m2}$, $\bar{J}_2$, and $\bar{W}_2$ for the case with one were determined in the time range from 0 to 60 μs, during which the pulse pressure value decreased by a factor of 5 (Fig. 3).

On the basis of the data, we determined the coefficients of the transformation of amplitude of the pulse pressure ε_P, the specific pulse ε_J, and the acoustic energy $\varepsilon_W = \eta_{TR}$ in the electrode system of the closed type in comparison with that of the open type by the expressions

$$\varepsilon_P = \frac{\bar{P}_{m2}}{\bar{P}_{m1}}, \tag{8}$$

$$\varepsilon_J = \frac{\bar{J}_2}{\bar{J}_1}, \tag{9}$$

$$\varepsilon_W = \frac{\bar{W}_2}{\bar{W}_1} = \eta_{TR}. \tag{10}$$

RESULTS OF INVESTIGATIONS

A comparative analysis of the transformation coefficients of the studied materials at a hydrostatic pressure of 1.8 MPa is presented in Fig. 4. It follows from the analysis that the polyethylene shell is characterized by the highest coefficients. In particular, the efficiency of transfer η_{TR} for polyethylene is close to one, whereas it is about 0.87 for rubber and 0.6 for steel.

However, as was already mentioned, due to special conditions inside the well, the most applicable material for the CES shell is a rubber hose, which, being inferior to polyethylene in transformation efficiency, exceeds it

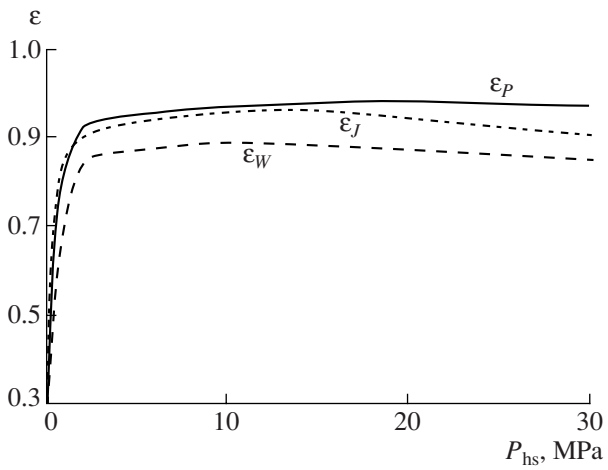

Fig. 5. Dependences of the coefficients of the pressure wave parameter transformation by the protective shell of a rubber hose on hydrostatic pressure.

in technological properties and provides smaller losses in comparison to the steel shell.

Results of investigation of the transformation coefficients for the rubber hose in the whole range of the hydrostatic pressure variation are shown in Fig. 5. One can see that their value depends on the hydrostatic pressure. Thus, when the pressure is varied from 0.1 to 1.8 MPa their values increase on average from 0.3 to 0.85. With a further increase in the pressure, their changes are insignificant. Such a behavior of the mentioned parameters is probably due to the presence of entrapped air in the multilayered structure of the shell, and their weakening influence on the acoustic wave passing becomes less with reduction in volume and compression with increasing hydrostatic pressure in the chamber.

CONCLUSIONS

1. The highest coefficients of transformation of the pressure wave parameters (close to one) are found for polyethylene, which makes its application as a shell for electrode systems of the closed type promising during relevant technological study.

2. Application of a rubber hose, being the most adaptable to conditions of deep wells, as a material for the shell of a closed electrode system is efficient at a hydrostatic pressure above 1.8 MPa, when the transfer efficiency is 0.85.

REFERENCES

1. Dubovenko, K.V., Kurashko, Yu.I., Shvets, I.S., and Onishchenko, L.I., Discharge–Pulse Equipment for Increasing Discharge of Oil and Water Wells, *Vestn. Natsion. Tekh. Univ.* "KhPI" (Kharkov), 2002, vol. 1, no. 7, pp. 96–103.
2. Poklonov, S.G., Modes of Operation of the Electrode System of Electrohydropulse Well Device, *Vestn. Natsion. Tekh. Univ.* "KhPI" (Kharkov), 2003, vol. 1, no. 1, pp. 154–162.
3. Poklonov, S.G., Glushenko, V.Zh., Trofimova, L.P., Tsurkin, V.N., and Kovyazin, N.I., Electric Discharge Efficiency for Conditions of Oil Wells, *Neftyanoe Khozyaistvo*, 1992, no. 3, pp. 20–23.
4. Romanenko, V.A. and Vol'nitskaya, E.M., *Vosstanovlenie proizvoditel'nosti vodozabornykh skvazhin* (Restoration of Efficiency of Water Wells), Leningrad: Nedra, Leningrad Department, 1986.
5. Saenko,V.A. and Poklonov, S.G., Ukraine Patent 27436, *Byull.,* 2000, no. 4.
6. Krivitskii, E.V. and Shamko, V.V., *Perekhodnye protsessy pri vysokovol'tnom razryade v vode* (Transition Processes at High–Voltage Discharge in Water), Kiev: Naukova Dumka, 1979.
7. Krivitskii, E.V., *Effektivnost' preobrazovaniya energii pri vysokovol'tnom iskrovom razryade* (Efficiency of Transformations of Energy during High-Voltage Discharge), *Fiziko-mekhanicheskie protsessy pri vysokovol'tnom razryade v zhidkosti* (Physical–Mechanical Processes at High–Voltage Discharge in Liquid), Kiev: Naukova Dumka, 1980, pp. 60–67.
8. Alekseev, V.S. and Grebennikov, V.T., *Vosstanovlenie debita vodozabornykh skvazhin* (Restoration of Discharge of Water Wells), Moscow: Agropromizdat, 1987.
9. Kovyazin, N.I., Ippolitov, V.V., Urosov, S.A., Sorokin, V.F., Kosenkov, V.M., Zhekul, V.G., and Poklonov, S.G., Influence of Screens on Dynamic and Kinematic Behavior of Casing under Perturbations from a Source of Electric Discharge Type, *Izv. Vuzov "Neft' Gaz"*, 1999, no. 6, pp. 13–19.
10. Smirnov, A.P., Zhekul, V.G., Kosenkov, V.M., and Poklonov, S.G., Study of Elastic Properties of Multilayered Materials Applied as Cylindrical Shells of Closed Electrode Systems, *Geotekhnicheskaya mekhanika: Mezhved. sb. nauchn. tr.* (Geotechnical Mechanics: Interdepartmental Coll. Sci. Papers), Dnepropetrovsk: Inst. Geotekh. Mekhaniki im. M.S. Polyakova NAN Ukrainy, 2003, issue 47, pp. 196–204.
11. Telyashov, L.L., Chekanov, Yu.S., and Gnatenko, E.K., Installation for Dynamic Calibration of Broadband Pressure Gages, *Fizicheskie osnovy elektro–gidravlicheskoi obrabotki materialov: Sb. nauch. tr.* (Physical Bases of Electrohydraulic Treatment of Materials: Coll. Sci. Papers), Kiev: Naukova Dumka, 1988, pp. 160–165.

ISSN 1068-3755, Surface Engineering and Applied Electrochemistry, 2007, Vol. 43, No. 5, pp. 354–358. © Allerton Press, Inc., 2007.
Original Russian Text © V.N. Tsurkin, A.V. Sinchuk, A.V. Ivanov, Yu.N. Degtev, 2007, published in Elektronnaya Obrabotka Materialov, 2007, No. 5, pp. 61–66.

ELECTRICAL PROCESSES IN ENGINEERING AND CHEMISTRY

Selection of the Electric Discharge Mode for Electrohydropulse Melt Treatment

V. N. Tsurkin, A. V. Sinchuk, A. V. Ivanov, and Yu. N. Degtev

Institute of Pulse Processes and Technologies, National Academy of Sciences of Ukraine, Oktyabr'skii pr. 43-A, Nikolaev, 54018 Ukraine

Received April 3, 2007

Abstract—The influence of electric discharge mode on the power characteristics of electrohydropulse treatment at the first and second stages and on the structure and properties of a hard metal is considered. It is shown experimentally that an oscillation discharge mode has an advantage, because it provides improvement of the hard metal quality.

DOI: 10.3103/S1068375507050080

Among numerous modern developing methods of out-of-the-furnace physicotechnical melt treatment, the electrohydropulse treatment method (EHPT) stands out due to low specific energy consumption, simplicity of incorporation into the technological process of casting production, and the possibility of treating larger industrial volumes of melt. Investigations carried out for ferrous and nonferrous metals [1–3] show that the EHPT is a relatively inexpensive and effective tool for improving the quality of cast metal products. Among the results obtained due to treatment are the following: degassing and refining of the melt, homogenization in macrovolume with respect to temperature and chemical composition, and activation of potential nucleation centers—that is, the whole complex of phenomena that in total improve the quality of a crystallized metal.

In the physical sense, EHPT is a complex treatment method including the elements of both ultrasonic and oscillation action on the melt. Here, each pressure pulse received by the melt can be represented by two basic stages. At the first stage, in the interelectrode space a plasma channel appears; its pressure through a waveguide-radiating system is applied into the melt in the form of a polyfrequency pulse in the microsecond range of time. At the second, postdischarge, stage, the plasma channel is transformed into a pulsing vapor-gas cavity that deforms an elastic membrane (lower wall of the discharge chamber); pressure due to mechanical waveguide displacement is also applied into the melt, though for a longer period of time, a millisecond. Thus, in the treated melt a nonstationary pressure field is formed, with the discreteness of its appearance determined by the discharge pulse repetition frequency f. Depending on the technological requirements and equipment capabilities, the f value varies in the range of 1–20 Hz. As a rule, the role of the first, discharge, stage of EHPT is reduced to establishing acoustic cavitation and acoustic microflows in the melt, and role of the second, postdischarge, stage consists in the development of powerful hydrodynamic flows. Often it is impossible to separate the contribution of each considered process to the final melt state. For example, it is obvious that the source stimulating transition of gases dissolved in metal into bubbles and their consequent emersion is acoustic cavitation. However, intensity of gas removal is also affected by ascending convection currents carrying to the melt surface the gas bubbles formed at the first stage. Up to the present, temperature equalization and uniform distribution of chemical elements over the melt volume have also been connected with convection currents. However, a number of recent works [4, 5] show that in this aspect the cavitation phenomenon must not be underestimated, because it increases the homogeneity of the melt at the atomic level.

Thus, interrelation of the processes taking place at the first and second stages of EHPT realizes the functional capabilities of this method for complex solution of the problem of improving the quality cast metal. On the other hand, due to the availability of the two stages of the method, one question still remains—selection of optimal energy parameters of treatment, in particular, electric discharge modes, for meeting the triune requirement: treatment efficiency estimated by the metal quality, minimization of energy consumption, and durability of electrode system.

The aim of the present work is to show the electric discharge mode influence on the characteristics of power loading of the melt, realized at the first and second stages of the EHPT, and on indices of quality of a hard metal.

FIRST STAGE

As is shown in [6], the dependences of current, resistance, and pressure in the channel on controllable parameters of the discharge circuit (the voltages of accumulator charging U_0, the accumulator capacitance C, the circuit inductance L, the discharge channel length l_p) may be reduced to a family of curves depending on one dimensionless combination only:

$$\eta = \sqrt[3]{\frac{\pi A_p^2}{U_0^2\sqrt{LC}}}, \qquad (1)$$

where A is the spark constant, which has a value of 10^5 V^2 s/m^2 at free discharge. The value η is determined by a part of the energy evolved in the first half-period of the discharge current. At η = idem, the dimensionless functions of current, resistance, and pressure of the plasma channel are, respectively, equal in similar moments of time; that is, η is a similarity criterion for the discharge electric and hydrodynamic characteristics, and it is convenient to classify modes of underwater spark discharge on its basis. Among probable discharge modes applicable to the EHPT of melts there are the matched mode ($\eta = 0.79$), when the discharge current oscillogram contains one oscillation or one and a half oscillations, and the oscillation mode ($0 < \eta < 0.79$) close to the short-circuit mode. Nonperiodic discharge ($\eta > 0.79$) corresponding to a breakdown of large interelectrode spaces via an initiating conductor is not applied in electrohydropulse devices. The matched mode of discharge is characterized by equality of an active plasma channel's resistance to wave circuit resistance and the highest electric efficiency. As follows from (1), at constant parameters of the discharge circuit one can change the energy evolution mode in the discharge channel as the distance between the electrodes increases. The increasing interelectrode space leads to improvement in the operation of the electrode system and to a decrease in electrode wear. Therefore, up to the present, in EHPT devices, the electrode system has been tuned for realization of the matched mode, as a rule.

Figure 1 shows equipment for the electrohydropulse treatment of the melt.

Earlier we presented calculation technique [7], which permits determination of the effective pressure $P_B(t)$ appearing at the first stage at the face-end of a waveguide of constant radius r_B depending on the discharge mode by virtue of the following ratios:

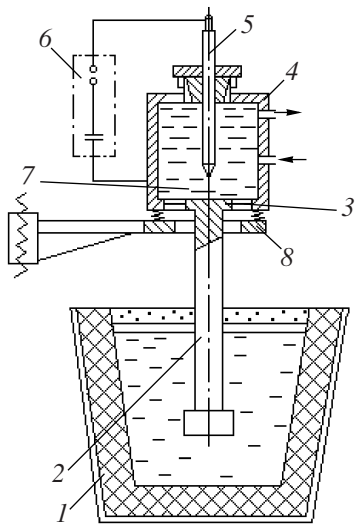

Fig. 1. Equipment for EHPT of the melt: (*1*) melt; (*2*) waveguide; (*3*) membrane; (*4*) discharge chamber; (*5*) electrode; (*6*) generator of pulse currents; (*7*) interelectrode space; (*8*) elastic suspension.

$$\left.\begin{aligned}
P_B(t) &= 19.44\frac{U_0}{r_B^2}L^{-1.97}C^{-0.97}t^{3.44}\\
&\times \exp\left(-0.94\frac{t}{\sqrt{LC}}\right) \text{ at } \eta = 0.37;\\
P_B(t) &= 3.1\frac{U_0}{r_B^2}L^{-2.115}C^{-1.115}t^{3.74}\\
&\times \exp\left(-0.86\frac{t}{\sqrt{LC}}\right) \text{ at } \eta = 0.79;\\
P_B(t) &= 0.73\frac{U_0}{r_B^2}L^{-1.96}C^{-0.96}t^{3.42}\\
&\times \exp\left(-0.42\frac{t}{\sqrt{LC}}\right) \text{ at } \eta = 1.
\end{aligned}\right\} \qquad (2)$$

Graphic representation of these ratios given in Fig. 2a allows us to see that for fixed parameters of the discharge circuit, the effective pressure from the matched discharge mode is sufficiently low and may not exceed the metal liquid cavitation strength. Let us recall that, according to literature sources [8], the cavitation threshold, e.g., for aluminum melts, is 0.65–1.3 MPa. A considerably higher level of pressure and the broadest acoustic spectrum (Fig. 2b) are obtained in the oscillation discharge mode, i.e., at short interelectrode spaces. Thus, the oscillation discharge mode, not the matched one, realizes the application of a more powerful polyfrequency pressure pulse into the melt at the first treatment stage. This ensures development of intense cavitation processes in the treated medium at equal energy

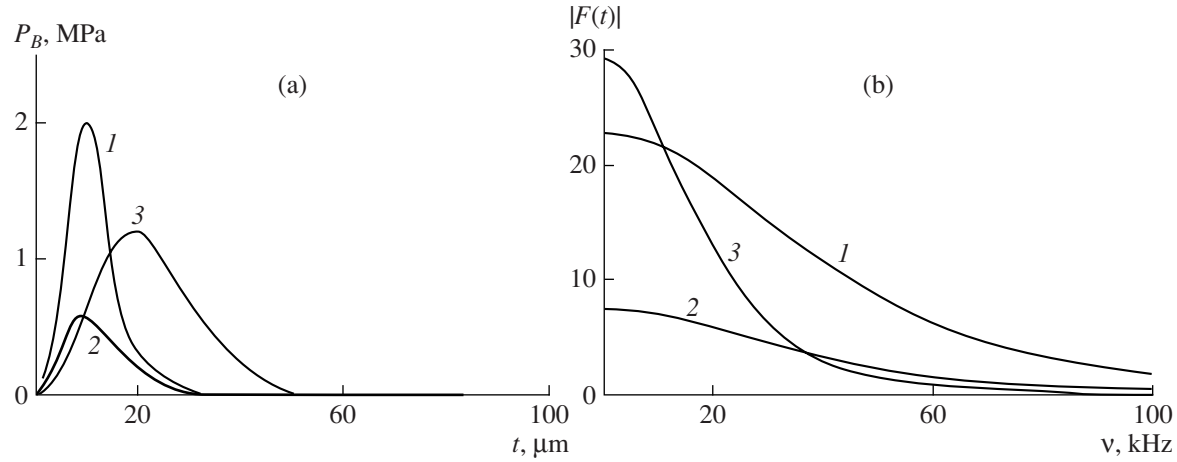

Fig. 2. Characteristics of the discharge pulse: (a) pressure on the face end of the waveguide; (b) Fourier spectrum.

consumption, despite obvious advantages of the matched mode with respect to efficiency.

It is not difficult to show that the amplitude pressure of a single discharge pulse P_B^{max} is proportional to the stored energy in the pulse W_0:

$$P_B^{max} \sim \kappa\sqrt{W_0}, \quad (3)$$

where κ is the coefficient taking into account the discharge nature and the waveguide cross-sectional area; $\kappa \approx 76.14$ for the oscillation discharge and $\kappa \approx 26.79$ for the matched one. As follows from (3), in order to increase the pressure in the melt (for example, for pure metals with a high cavitation threshold) it is necessary to increase the intensity of the treatment energy. Meanwhile, transition from the matched discharge mode to the oscillation one provides an almost threefold increase in pressure at the same energy consumption determined by the condition W_0 = const. Thus, the calculations show that the oscillation discharge mode is optimal in ensuring cavitation processes in the melt.

SECOND STAGE

In contrast to the discharge stage, the postdischarge stage cannot be mathematically described in practice. In our opinion, the main reason for this is that the vapor-gas cavity behavior in a closed volume, which is what the discharge chamber is, significantly depends on its geometry. This complicates description of the elastic membrane loading process and predetermines the application of chiefly experimental methods of studying afterdischarge processes. Analyzing the influence of the electric discharge mode on the nature of vapor-gas cavity pulsation, one can assume that during the transition from the matched discharge mode to the oscillation one, the pressure exerted by the cavity on the elastic membrane decreases. This is logical, since the decrease in the interelectrode space leads to a decrease in the volume of the vapor-gas cavity V_{max} and its potential energy E:

$$E = V_{max}P_0, \quad (4)$$

where P_0 is the hydrostatic pressure in the discharge chamber. The experiment shows [9] that up to 95% of the potential energy of the cavity are consumed during the first cycle "expansion–compression"; at consequent pulsations, the cavity does not have a clear geometrical shape and insignificantly influences the membrane, which further produces free damped oscillations. Thus, the impact action of the vapor-gas cavity may be experimentally estimated by the value of the crusher gage deformation resulting from first displacement of the membrane under the action of the stimulating force.

The crusher gages of annealed copper with a diameter of 15 mm and a height of 50 mm were installed between the lower face end of the waveguide and the fixed platform, and they were calibrated by single pulses. The mode of energy evolution in the discharge channel and η value were modified varying the interelectrode space length l_{sp} (Fig. 3a) at constant parameters of the electric circuit and two values of the stored energy in a pulse (W_{01} = 1.25 kJ and W_{02} = 2.5 kJ). Oscillograms of the discharge current $I(t)$ and the voltage $U(t)$ were recorded in the experiment; after their treatment the value of the criterion η was determined by the relation

$$\eta = \frac{\int_0^\tau I(t)U(t)dt}{W_0}, \quad (5)$$

where τ is the duration of the first half-wave of the discharge current.

The curves shown in Fig. 3b make it possible to observe the action of the discharge mode on the value of plastic deformation of the crusher gage, which

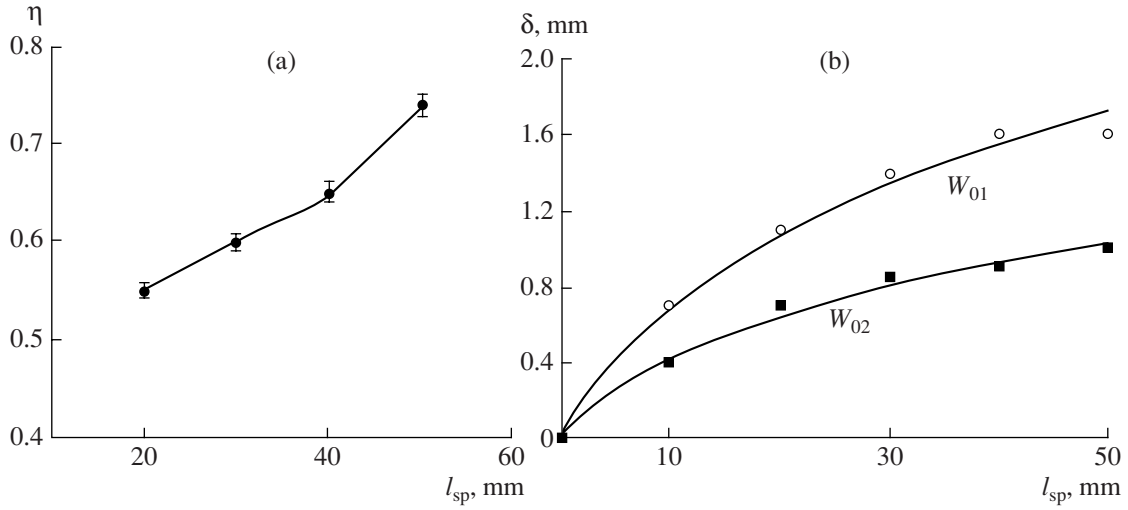

Fig. 3. Experimental dependences: (a) the part of the energy evolved in the first half-period of the discharge current; (b) the absolute deformation of the crusher gage.

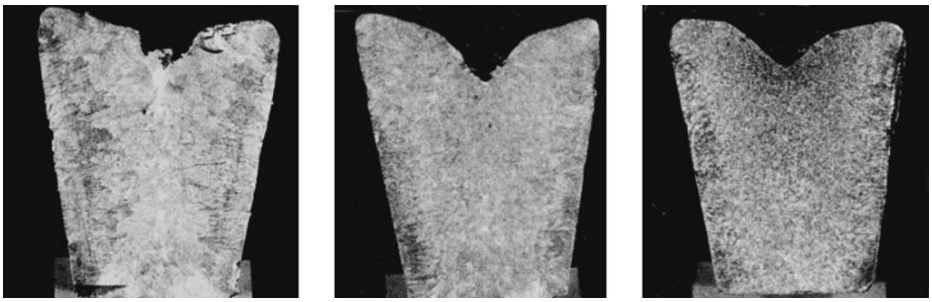

Without EHPT | With EHPT; η = 0.75 | With EHPT; η = 0.55

Fig. 4. Macrostructure of the AL7 alloy.

increases with increasing W_0 and, as expected, decreases as the discharge mode approaches the oscillation mode. For real treatment processes, this means a decrease in the intensity of mechanical melt stirring at the postdischarge stage.

Thus, the simplest estimations made at the division of a single pulse into two stages show that, to date, naturally there are no well-defined recommendations on optimal modes of electric discharge in EHPT devices, since one and the same discharge mode exerts a mutually antithetic influence on the processes proceeding in the melt at the first and second treatment stages. Hard metal quality as an integral property is determined by these processes in total; therefore, for selection of the electric discharge mode, it is necessary to specify which quality indices are of priority in each separate case.

STRUCTURE AND PROPERTIES OF METAL

Influence of the electric discharge mode on the structure and properties of hard metal was studied in the treatment of the two-component aluminum alloy AL7. Remelting of a specified charge was carried out in a muffle furnace at $T = 800°C$. After the remelting and a short-term holding, the metal was taken out of the furnace and poured into three ladles; one of them, the check one, was settled and the melt in the other two was subjected to EHPT in different discharge modes. The treatment was realized in the course of 40 s at a discharge repetition frequency of $f = 1.5$ Hz with a stored energy of $W_0 = 1.25$ kJ. The mode of energy evolution in the discharge channel was modified by variation of the interelectrode space from 20 mm (the oscillation mode, $\eta = 0.55$) to 50 mm (nearly matched mode, $\eta = 0.75$). Then all three of the ladles were simultaneously sent for casting of samples for metal analysis.

Figure 4 shows casting cuts of the "glass" type, and the table gives data that permit the estimation of the influence of EHPT on the structure and properties of the studied metal. Check castings are characterized by a rough coarse-grain macrostructure and the presence of axial porosity and dispersed pores, while the metal preliminarily treated in the liquid state has a close fine-grain macrostructure, a narrow band of columnar crystals, and a well-defined shrinkage hole. The action of

Characteristics of the AL7 alloy

Alloy characteristic	Without EHPT	$\eta = 0.75$	$\eta = 0.55$
Average diameter of equiaxial macrograin, mm	4.1	1.8	1.4
Width of band of columnar crystals, mm	12	6.8	5.2
Volume of shrinkage hole, cm^3	5.0	8.2	6.4
Micrograin dimension, μm	47	37	27
Length of $CuAl_2$ particles, mm	103	72	64
Density, g/cm^3	2.783	2.818	2.875
Hardness HB:			
cast state	34	45	61
hardening + ageing	55	56	103
Microhardness Hμ of solid solution, kg/mm^2:			
cast state	59	62	72
hardening + ageing	215	243	522

the matched discharge mode has a positive impact on structure and properties of castings; however, according to the visual inspection of the cuts and the structure data analysis, the most advantageous structure is that of the metal treated with application of the shortest interelectrode space, i.e., the oscillation discharge mode.

The microstructure of the alloy is represented by dendrites of the initial aluminum solution, Al + $CuAl_2$ + Si eutectics located at the grain boundaries, and an insignificant quantity of ferriferous phases. The check samples are characterized by coarse micrograin and inclusions of $CuAl_2$. After the EHPT in the check samples dimensions of the micrograin and $CuAl_2$ inclusions appreciably decrease, especially in the metal treated at the oscillation discharge mode. After the treatment an improvement of some properties of the alloy in both cast and thermally treated states is observed. For the alloy treated at $\eta = 0.75$ the hardness increase is several HB units, while after the EHPT at $\eta = 0.55$ the metal hardness increases practically by a factor of 2; this testifies to advantages of the oscillation discharge mode.

Thus, the mode of energy evolution in the discharge channel exerts a mutually antithetic influence on the characteristics of the discharge pressure pulse and on the dynamics of the afterdischarge vapor-gas cavity. Change of the discharge mode results in variation of the balance of perturbing forces taking place at the first and second stages of EHPT. The experimental results show that during transition from the matched discharge mode to the oscillation mode, the macro- and microstructure of the aluminum alloy, as well as a number of its properties, improve. This shows that cavitation processes and the discharge stage play a principal role in the formation of the quality of a hard metal and that application of the oscillation discharge mode in devices for melt EHPT is promising. As concerns the solution of technical problems connected with application of this mode, it is necessary to improve the construction decision of the electrodes and washing of the discharge chamber for renewal the life of the electrode system.

REFERENCES

1. Grabovyi, V.M., Ul'yanov, VA., Fomenko, K.P., et al., Efficiency of Treatment of Liquid and Crystallizing Metal in a Ladle and a Mold by Elastic Oscillations, *Protsessy razlivki stali i kachestva slitka* (Processes of Steel Casting and Ingot Qualities), Kiev: Naukova Dumka, 1989, pp. 35–38.
2. Volkov, G.V., Grabovyi, V.M., and Sinchuk, A.V., Treatment of Cast Iron by Concentrated Energy Flows, *Liteinoe Proizvodstvo*, 1998, no. 1, pp. 12–14.
3. Fedchenko, N.A., Influence of EHPT on Structure and Properties of Secondary Silumin, *Protsessy Lit'ya*, 2003, no. 2, pp. 59–64.
4. Bazin, Yu.A., Butakov, B.I., Tishkin, A.P., et al., Influence of Electrohydropulse Treatment on Structure of Short–Range Order of the Melt of Multicomponent Alloy Based on Aluminum, *Rasplavy,* 1992, no. 3, pp. 89–91.
5. Tsurkin, V.N. and Sinchuk, A.V., Thermodynamic Analysis of External Electrohydropulse Influence on the Melt State before Casting and on Metal Crystallization, *Protsessy Lit'ya*, 2004, no. 1, pp. 6–9.
6. Krivitskii, E.V. and Shamko, V.V., *Perekhodnye protsessy pri vysokovol'tnom razryade v vode* (Transition Processes at High–Voltage Discharge in Water), Kiev: Naukova Dumka, 1979.
7. Tsurkin, V.N., Sinchuk, A.V., and Ivanov, A.V., Calculation Technique for Determination of Discharge Parameter Influence on Acoustic Field Characteristics in the Melt at Electrohydropulse Treatment, *Elektron. Obrab. Mater.*, 2004, no. 1, pp. 82–87.
8. Abramov, O.V., Dobatkin, V.I., Kazantsev, V.F., et al., *Vozdeistvie moshchnogo ul'trazvuka na mezhfaznuyu poverkhnost' metallov* (Influence of High–Power Ultrasound on Interphase Metal Surface), Moscow: Nauka, 1986.
9. Petrichenko, V.V., Grabovyi, V.M., and Sholom, V.R., Kinetics of Membrane Interaction with Vapor–Gas Cavity at High–Voltage Discharge in Liquid, *Fizicheskie osnovy elektrovzryva: Sb. nauch. tr.* (Physical Bases of Electric Explosion: Coll. Sci. Papers), Kiev: Naukova Dumka, 1983, pp. 121–124.

ISSN 1068-3755, Surface Engineering and Applied Electrochemistry, 2007, Vol. 43, No. 5, pp. 359–364. © Allerton Press, Inc., 2007.
Original Russian Text © F.V. Bortsoi, 2007, published in Elektronnaya Obrabotka Materialov, 2007, No. 5, pp. 67–74.

ELECTRICAL PROCESSES IN ENGINEERING AND CHEMISTRY

Options for Development of Statistical Methods for Estimation of Distributed Parameters of Electrochemical Deposits at Macro Level

F. V. Bortsoi

Institute of Applied Physics, Academy of Sciences of Republic of Moldova, ul. Akademiei 5, Chisinau, MD 2028, Republic of Moldova

Received May 4, 2007

Abstract—In the work, the methods-analogues A'_B, B'_B, C'_B, and D'_B for research of the process of formation of the electrochemical composition, based on principles, are used for estimation of relation between the distributed parameters. It is noted that such a direction of the research of the electrochemical composition has an essential theoretical and practical value, and its principles can be applied to the development of some parameters of the properties of electrochemical objects, for example, σ_B is the parameter of dynamics of a factor of an output on a current. In addition, these methods have a high level of generality with similar methods in other fields of knowledge and allow one to improve and expand essentially the quality of the research of electrochemical compositions and to predict and improve the ways of their formation.

DOI: 10.3103/S1068375507050092

The study of technological characteristics of the process of electrochemical composition formation and enhancement of their reliability in regards to the indicators of electrolysis modes and deposit are of high theoretical and practical importance. However, the complexity and diversity of factors affecting the process of electrochemical composition formation dictate the necessity of practical research on the relationship between the parameters of electrochemical system and the deposit. The problem of electrochemical composition research is also complicated by the fact that the values of the majority of electrochemical system parameters at the electrodes are distributed. Let us note that the distributed parameters (DPs) include indicators with derivatives by at least one of the coordinates and, possibly, by all three coordinates.

One of the directions for studying the diverse regularities of the process of electrochemical composition formation is based on the estimation of relationship between DPs at various levels (macro, micro etc.) [1–3]. The particular features of this direction [1–3] can include the practicability of its methods, good prospects for its development, similarity to the methods of similar directions in the other areas of knowledge, and the possibility of development of other indicators for the estimation of the properties of electrochemical objects.

The methods of studying this direction at the macro level are based on the principle of comparing the values of relative deviations t_i and δ_j for a given DP with corresponding values of other DPs or on the determination of percentages of geometric parameters of electrode parts with the given ratios of relative deviations [1].

Relative deviation t_i corresponds to the difference between statistical unit x_i and mean value $\bar{x}$ expressed in the form of the mean square-root deviation $s_x = \sqrt{\frac{\sum_{i=1}^{n}[x_i - \bar{x}]^2}{n-1}}$ of a DP statistical ensemble X consisting of n units, or,

$$t_i(X) = \frac{x_i - \bar{x}}{s_x}. \quad (1)$$

Relative deviation δ_j is the difference between the deviations of statistical unit x_i from the neighboring $x_{i+1}(h_j = x_i - x_{i+1})$ and the mean value for such deviations $\bar{h} = \sum_{j=1}^{m}[x_i - x_{i+1}]/\mathrm{m} = \sum_{j=1}^{m} h_j/m$ in statistical ensemble X as compared to the root-mean-square values of the neighboring values $\varepsilon_x = \sqrt{\sum_{j=1}^{m}[x_i - x_{i+1}]^2/m}$ in the DP ensemble X consisting of $m = n - 1$ neighboring deviations, or,

$$\delta_j = \frac{(h_j - \bar{h})}{\varepsilon_x}. \quad (2)$$

When studying the process of the formation of electrochemical composition materials (ECM), relative deviations t_i and δ_j allow for the comparison of DP values with various measurement units according to the following principles:

(1) relative deviation values;

(2) coincidence of relative deviation signs;

(3) estimates of the fractions of the electrode geometrical parameter characterized by certain relationships between relative DP deviations.

Prerequisites for development of methods of studying DPs at macro level. Originally, it is expedient to perform a theoretical analysis of the earlier developed methods of studying the ECM formation process on the basis of estimation of relationships between DPs.

For the case of certain studied factors affecting the process of ECM formation, methods are developed based on relationship indicators A_B, B_B, C_B, and D_B (see paper [1]). Each of the above methods has its own specific features for the description of the process of the electrochemical composition formation. For example, indicator A_B assumes its values in the range of ±1 and allows for the comparison of the absolute values of univalent relative deviations t of a single parameter with the corresponding values of the other parameters. Its numeric value and sign point to the superiority of relative deviations t of a single parameter (X_1) over the corresponding values and similar sign of the other DPs ($X_{2\ldots k}$). The negative values of indicator A_B point to the numerical superiority of relative deviations t of other DPs ($X_{2\ldots k}$) with both similar and different signs over the corresponding values of the first parameter (X_1).

The value of indicator A_B can be considerably affected by the percentage of ratios between the relative deviations with opposite signs [$t_i(X_1)/t_i(X_{2\ldots k})$] that can result in the implicit description of some of the dependences between the factors under certain conditions of the theoretical analysis of the process in question.

The method of studying electrochemical compositions based on determining the fraction of geometrical electrode size with absolute values of relative deviations t_i for a single DP (X_1) higher than the relevant values of other DP ($X_{2\ldots k}$) is represented by indicator B_B that assumes the values in the range of 0–1 (0–100%). Its values point to the degree of relationship between DPs based on the ratio of absolute values of relative deviations t_i at the electrode.

The method of studying electrochemical compositions represented by indicator C_B is based on the comparison of relative deviations δ_j between the DPs of the electrolysis process. Indicator C_B assumes values in the range of ±1 and its positive sign points to the numeric superiority of deviation δ_j of the first parameter (X_1) over the corresponding values of similar signs for other DPs ($X_{2\ldots k}$). Negative values of indicator C_B point to the numeric superiority of relative deviations δ of other DPs ($X_{2\ldots k}$) of similar sign and deviations δ_j, with the opposite sign over the relevant values of the first parameter (X_1).

As in the case of indicator C_B, the value of indicator A_B can be considerably affected by the percentage of ratios of relative deviations $\delta_i(X_1)/t_i(X_{2\ldots k})$ with opposite signs, which can lead to the implicit description of certain dependences between the factors in the case of certain conditions of the theoretical analysis of the process in question.

The method of studying electrochemical compositions based on the determination of electrode parts with absolute values of relative deviations δ_j of a single DP (X_1) that are higher than the corresponding values of other DPs (X_2, X_3, X_k) is represented by indicator D_B. The latter assumes its values in the range of 0–1 (0–100%). Thus, despite the advantages of the above methods A_B, B_B, C_B, and D_B, they cannot describe the whole variety of relationships between the factors of the electrochemical composition formation process. In this connection, a necessity appears for the extension of options for studying the relationships of DPs of electrochemical processes at the macro level.

Various methods for studying DPs at the macro level. The method of studying electrochemical compositions A'_B based on the comparison of relative deviations t of DP values, which is analogous to method A_B, is described by the following expression:

$$A'_B[X_1(X_2\ldots X_k)] = \frac{\sum_{i=1}^{n}\left[\left(\left|\frac{t_i(X_1)}{t_i(X_2)}\right|-1\right)-\left(\left|\frac{t_i(X_1)}{t_i(X_3)}\right|-1\right)+\ldots+\left(\left|\frac{t_i(X_1)}{t_i(X_k)}\right|-1\right)\right]}{\sum_{i=1}^{n}\left[\left|\left|\frac{t_i(X_1)}{t_i(X_2)}\right|-1\right|-\left|\left|\frac{t_i(X_1)}{t_i(X_3)}\right|-1\right|+\ldots+\left|\left|\frac{t_i(X_1)}{t_i(X_k)}\right|-1\right|\right]}, \quad (3)$$

where k is the number of parameters in statistical complex A'_B and $t_i(X_{1,2\ldots k})$ are the relative deviations in DP statistical ensembles $X_{1,2\ldots k}$.

Analysis of expression (3) shows that the estimation of the relationship between DPs of the process of electrochemical composition formation is performed by comparing the absolute values of their relative deviations t.

Indicator A'_B assumes values in the range of ±1 and its positive sign points to the numeric superiority of absolute values of the relative deviations t of the first parameter (X_1) in question over the corresponding val-

Table 1. Values of relative deviations t_i and δ_j for parameters distributed across the cathode for electrolysis of 0.5 N lead nitrate

Electrolysis parameters	Indices	Values of relative deviations of statistical units				
Statistical units	n	1	2	3	4	5
Density of primary cathodic current distribution, $D_k(1)$	t_i	1.743	0.288	–0.192	–0.662	–1.185
	δ_j	–	0.857	–0.300	–0.310	–0.248
Voltage drop at resistances (corresponding to current density secondary distribution) $D_k(2)$	t_i	1.601	0.093	–0.027	–0.696	–0.970
	δ_j		1.032	–0.623	0.031	–0.439
Distribution of metal amount, $M(3)$ at the cathode	t_i	1.550	0.243	–0.358	–0.716	–0.942
	δ_j	–	0.929	–0.026	–0.355	–0.532

Table 2. Values of relationship indicators A_B and A'_B for parameters distributed across the cathode for electrolysis of 0.5 N lead nitrate

Indicators	$D_k(1)/D_k(2)$	$D_k(2)/D_k(1)$	$D_k(1)/M(3)$	$M(3)/D_k(1)$	$D_k(2)/M(3)$	$M(3)/D_k(2)$	$D_k(1)/[D_k(2), M(3)]$	$D_k(2)/[D_k(1), M(3)]$
A_B	0.989	–0.944	0.026	0.334	–0.923	0.991	0.972	–0.986
A'_B	0.989	–0.944	0.026	0.334	–0.923	0.991	0.878	–0.986

ues of the other parameters ($X_{2,\ldots k}$). The negative values of indicator A'_B point to the numeric superiority of relative deviation t of other DPs ($X_{2,\ldots k}$) over the corresponding values of the first parameter (X_1).

Let us compare the properties of indicators A_B and A'_B on the basis of statistical complexes composed of DPs of the electrolysis mode with directional distribution of values at the cathode. Let us note that the directional distributions of DP values include the increasing or decreasing values. The initial data presented in Table 1 for relative deviations of DPs with directional distributions are obtained experimentally for a corner Hull cell for estimating the electrolyte dissipating ability in the process of 0.5 N lead nitrate electrolysis [1]. As a result, the values of relative deviations t for DPs of the electrolysis mode feature a directional distribution at the cathode; however, relative deviations δ feature directedness of distribution only for DPs of the metal amount.

The values of indicators A_B and A'_B were calculated for the following statistical complexes:

(i) current density primary distribution, i.e., the secondary distribution for direct $D_k(1)/D_k(2)$ and inverse $D_k(2)/D_k(1)$ relationships;

(ii) current density primary distribution, i.e., the distribution of the metal amount for direct $D_k(1)/M(3)$ and inverse $M(3)/D_k(1)$ relationships;

(iii) current density secondary distribution, i.e., the distribution of the metal amount for direct $D_k(2)/M(3)$ and inverse $M(3)/D_k(2)$ relationships;

(iv) current density primary distribution, i.e., the current secondary distribution and metal amount $D_k(1)/[D_k(2), M(3)]$;

(v) current density secondary distribution, i.e., the current primary distribution and metal amount $D_k(2)/[D_k(1), M(3)]$;

The results of calculations of indicators A_B and A'_B presented in Table 2 show that in the majority of cases, these values coincide due to the directedness of the distribution of relative deviations t of the electrolysis process DPs. However, in the case of certain direct and inverse relationships between parameters A_B and A'_B of the electrolysis mode differ (underlined in Table 2). This is due to the fact that the values of indicators A_B and A'_B are affected by the values of relative deviations t and percentage of ratios $t_i(X_1)/t_i(X_{2,\ldots k})$ with opposite signs. In this connection, one can conclude that in the case of directional distributions of relative deviations t of DPs, the values of indicators A_B and A'_B are similar and the difference between the direct and inverse ratios of parameters reflects the effect of their numeric values.

It is also expedient to perform an analysis of indicators A_B and A'_B for relative deviations t with parameters of their isotropic distribution, e.g., for estimating the relationship between DPs of formulation of the electrochemical composition deposit based on iron, according to the data of paper [1], Table 3.

Analysis was performed for the following statistical complexes (Table 4):

Table 3. Relative deviations t and δ for volumes of composition deposit V_k, metal V_m, DPh V_p distributed across the cathode and DPh concentration p_V

Statistical units	Relative deviations t				Relative deviations δ			
	$t(V_k)$	$t(V_m)$	$t(V_p)$	$t(p_V)$	$\delta(V_k)$	$\delta(V_m)$	$\delta(V_p)$	$\delta(p_V)$
1	1.00	1.00	1.00	1.00	–	–	–	–
2	1.66	1.60	2.40	2.27	–0.41	–0.34	–0.65	–0.42
3	1.35	1.16	3.67	4.19	0.06	0.12	–0.60	–0.58
4	0.53	0.17	5.05	7.12	0.30	0.36	–0.64	–0.83
5	1.42	1.69	–1.98	–3.13	–0.52	–0.75	2.45	2.46
6	0.35	0.51	–1.71	–2.37	0.42	0.44	–0.23	–0.29
7	–4.39	–4.48	–3.21	–2.50	2.16	2.12	0.42	–0.07
8	–1.39	–1.23	–3.36	–4.39	–1.52	–1.51	–0.08	0.37
9	–0.53	–0.42	–1.87	–2.19	–0.50	–0.43	–0.68	–0.65

Table 4. Values of relationship indicators A_B and A'_B for DPs at the cathode composed of ECM deposit: volumes of composition deposit V_k, metal V_m, dispersed phase V_p and dispersed phase concentration p_V

Indicators	$V_k : V_m$	$V_m : V_k$	$V_k : V_p$	$V_p : V_k$	$V_k : P_V$	$P_V : V_k$	$V_m : P_V$	$P_V : V_m$
A_B	0.692	–0.277	–0.886	0.263	–0.773	0.278	–0.776	0.700
A'_B	0.692	–0.277	–0.840	0.972	–0.723	0.969	–0.715	0.984

(i) composition deposit, i.e., metal for direct $V_k : V_m$ and inverse $V_m : V_k$ relationships;

(ii) composition deposit, i.e., dispersed phase (DPh) for direct $V_k : V_p$ and inverse $V_p : V_k$ relationships;

(iii) composition formulation, i.e., DPh concentration for direct $V_k : P_V$ and inverse $P_V : V_k$ relationships;

(iv) metal, i.e., DPh concentration for direct $V_m : P_V$ and inverse $P_V : V_m$ relationships.

Judging by the values of indicators A_B and A'_B, there is a more considerable difference between the direct and inverse DP ratios (underlined in Table 4) as compared to DP with directional values of relative deviations t (see Table 2). These parameters allow the conclusion to be reached that in the case of nondirectional values of deviations t, the values of indicators A_B are much more strongly affected by the percentage of the ratios of deviations $t_i(X_1)/t_i(X_{2\ldots k})$ with opposite signs, while the effect on the value of indicator A'_B is negligible.

Thus, the A'_B method allows the quantitative study of yet another characteristics of the ECM formation process by estimating its DPs at the macro level.

Method B'_B of studying electrochemical compositions based on estimating the electrode part with the given relationships between relative deviations t of the DP values and analogous to method B_B is represented by the following expression:

$$B'_B[X_1(X_2\ldots X_k)] = \frac{\sum_{i=1}^{p} l^{\pm}_{|t_1|>|t_2\ldots t_k|}}{L} \times 100\%, \qquad (4)$$

where $l^{\pm}_{|t_1|>|t_2\ldots t_k|}$ is the size of the electrode part i with the absolute values and similar sign of relative deviations t of parameter X_i higher than the corresponding values of parameters $X_2,.X_3..X_k$; p is the number of electrode parts with the absolute values and similar sign of relative deviations t of parameter X_1, higher than the corresponding values of parameters $X_2,.X_3..X_k$; and L is the overall geometric size of the electrode.

Analysis of expression (4) shows that parameter B'_B assumes values in the range of 0–1 (0–100%) and points to the percentage of the electrode geometric size with absolute values and similar sign of relative deviations t_i of DPs (X_1) that are higher than the corresponding values of other DPs ($X_{2\ldots k}$).

The method of studying electrochemical compositions C'_B based on comparing relative deviations δ of the DP values and analogous to method C_B is described by the following expression:

$$C'_B[X_1(X_2..X_k)] = \frac{\sum_{i=1}^{m}\left[\left(\left|\frac{\delta_j(X_1)}{\delta_j(X_2)}\right| - 1\right) - \left(\left|\frac{\delta_j(X_1)}{\delta_j(X_3)}\right| - 1\right) + \ldots + \left(\left|\frac{\delta_j(X_1)}{\delta_j(X_k)}\right| - 1\right)\right]}{\sum_{i=1}^{m}\left[\left|\left|\frac{\delta_j(X_1)}{\delta_j(X_2)}\right| - 1\right| + \left|\left|\frac{\delta_j(X_1)}{\delta_j(X_3)}\right| - 1\right| + \ldots + \left|\left|\frac{\delta_j(X_1)}{\delta_j(X_k)}\right| - 1\right|\right]}, \quad (5)$$

where $\delta_j(X_{1,2\ldots k})$ is the relative deviation δ_j between statistical units i and x_{i+1} in the parameter ensembles $X_{1,2\ldots k}$ and $m = n - 1$ is the number of relative deviations δ_j in statistical ensembles of parameters $X_{1,2\ldots k}$.

An analysis of expression (5) shows that the estimation of the relationship between DPs of the process of the electrochemical composition formation is based on the comparison of absolute values of their relative deviations δ_j.

Indicator C'_B assumes its values in the range of ±1 and its positive sign points to the numeric superiority of absolute values of the relative deviations δ_j of the first parameter (X_1) in question over the corresponding values of the other parameters ($X_{2\ldots k}$). The negative values of indicator C'_B point to the numerical superiority of relative deviations δ_j of other DPs ($X_{2\ldots k}$) over the relevant values of the first parameter (X_1).

In this connection, it is expedient to compare the properties of parameters C_B and C'_B for the earlier established statistical complexes of DPs of the electrolysis mode (Table 1).

The calculation results presented in Table 5 show that in certain cases the C_B and C'_B values are significantly different (underlined) probably due to the absence of directedness in the distribution of some relative deviations δ_j.

The values for their direct and inverse complexes are also nonequivalent; i.e., there are essential differences between them. The values of indicators C_B and C'_B are also obviously affected by numeric values of relative deviations δ_j and percentage of ratios $\delta_j(X_1)/\delta_j(X_{2\ldots k})$ with opposite signs.

The method of studying electrochemical compositions D'_B based on the estimation of the electrode part with the given ratios between relative deviations δ_j of the DP values and analogous to the D_B method is represented by the following expression:

$$D'_B[X_1(X_2\ldots X_k)] = \frac{\sum_{i=1}^{q} l^{\pm}_{|\delta_1|>|\delta_2\ldots\delta_k|}}{L} \times 100\%, \quad (6)$$

where $l^{\pm}_{|\delta_1|>|\delta_2..\delta_k|}$ is the size of the electrode part i with the absolute values and similar sign of relative deviations δ_j of parameter X_1 higher than the corresponding values of parameters $X_2,.X_3..X_k$ and q is the number of electrode parts with the absolute values and similar sign of relative deviations δ_j of parameter X_1 higher than the corresponding values of parameters $X_2,.X_3..X_k$.

Analysis of expression (6) shows that parameter D'_B is analogous to parameter D_B and assumes values in the range of 0–1 (0–100%). Thus, the employment of relative deviations t_i and δ_j in the methods of studying DPs allows for the regularities of the formation of galvanic compositions, their functional properties, and the impact of various factors on the process to be established with greater reliability.

Development of certain indicators for estimation of properties of electrochemical objects. The principles of studying DPs at the macro level can also be used for the development of certain indicators for estimating the properties of electrochemical objects, e.g., for developing an indicator of current efficiency coefficient dynamics.

It is known that the current efficiency coefficient B_{Ti}, used mainly for practical purposes, is the *current fraction* and amount of electricity consumed in the given electric reaction i is as follows [4]:

$$B_{Ti} = m_{i.\Pi}/m_{i.T} \quad \text{or} \quad B_{Ti} = Q_{i.T}/Q_{i.\Pi}, \quad (7)$$

where $m_{i.\Pi}$ is the mass of substance i, which practically undergoes transformations as a result of consumption of a given amount of electricity; $m_{i.T}$ is the theoretical mass of substance i, which must undergo transformations at the consumption of the same amount of electricity; $Q_{i.T}$ is the amount of electricity that is required in theory (according to Faraday's law) for the transfor-

Table 5. Values of relationship indicators C_B and C'_B for parameters distributed across the cathode for electrolysis of 0.5 N lead nitrate

Indicators	$D_k(1)/D_k(2)$	$D_k(2)/D_k(1)$	$D_k(1)/M(3)$	$M(3)/D_k(1)$	$D_k(2)/M(3)$	$M(3)/D_k(2)$	$D_k(1)/[D_k(2), M(3)]$	$D_k(2)/[D_k(1), M(3)]$
C_B	–1.000	0.302	0.869	0.202	0.896	–0.969	–0.104	0.839
C'_B	0.778	0.390	0.869	0.202	0.910	0.819	0.879	0.865

mation of a unit amount of substance i (for which the current yield is calculated); $Q_{i.\Pi}$ is the amount of electricity that is required in practice for transformation of the same unit amount of substance i.

In the case of the occurrence of a single process at the cathode, the relative deviations of distributed values of electricity amount and deposited metal must be similar. However, if the relative deviations in the electricity and metal amounts are not similar, then the degree of their discrepancy most likely characterizes the degree of current yield variation. Relative deviations t_i can serve as relative statistical unit deviations.

Let us consider the approach for the construction of the indicator of the current yield dynamics on the basis of the initial data regarding the technical example of the estimation of the electrolyte dissipating ability (see Table 1). According to the data presented in [5], the electrolyte dissipating ability by current is $DA_c = 44\%$, while its dissipating ability by metal $DA_m = 63\%$. Let us note that in the case of the lead plating process, a current yield of $B_{T\bar{i}} = 100\%$ is achieved at the current density of 1 A/dm^2 [6].

In the case of the given example, the relative differences between the normalized deviations of metal amount $t_{i.m}$ and current density $t_{i.k}$ as compared to normalized deviations of metal amounts are calculated according to the following expression:

$$\sigma_B = (t_{i.m} - t_{i.k})/t_{i.m} = 1 - t_{i.k}/t_{i.m} \quad (8)$$

and are equal to

	1	2	3	4	5
σ_B	–0.033	0.617	0.925	0.028	–0.030

As can be seen, the relative difference between the relative deviations of current densities (voltage drop) and metal amount features a maximum, while the negative values at border points σ_B can probably be related to the measurement errors.

Thus, σ_B can serve as a basis for estimating the current yield variation. However, the value of indicator σ_B only in a narrow range of electrolysis modes reflects the regularities of current yield variation. In this connection, a necessity appears for the estimation of σ_B variation regularities using a single value in the whole range of studied ranges of electrolysis modes.

Let us assume that the following average power values are applicable for the above purposes:

$$M = \sqrt[k]{\frac{\sum x_i^k}{n}}, \quad (9)$$

where x_i is a statistical unit, n is the number of units in the statistical ensemble, k is the value allowing the determination of the type of mean values. Thus, in the case of $k = 1$, it is the arithmetic mean value, $\bar{x}$; in the case of $k = 2$, it is the root-mean-square value, $\bar{x}_q$; in the case of $k = 3$, it is the root-mean-cube value, $\bar{x}_Q$; in the case of $k = 4$, it is the fourth degree mean value, $\bar{x}_K$; and in the case of $k = -1$, it is the harmonic mean value, $\bar{x}_h$, etc.

Then, in the case of the data of the above example, the certain calculated mean values σ_B for the used range of electrolysis mode are

$$\bar{x}_K = 0.831; \quad \bar{x}_Q = 0.590; \quad \bar{x}_q = 0.498; \quad \bar{x} = 0.301; \quad \bar{x}_h = -5.107. \quad (10)$$

As can be seen from (10), σ_B values and characteristics of its variation for the first half of the statistical ensemble are better characterized by the mean arithmetic value $\bar{x}$ (0.301), while in the case of the second statistical ensemble, half of the best parameter is the fourth degree mean value, $\bar{x}_K$ (0.831).

The range of electrolysis modes in the case under consideration is probably the best characteristics of statistical ensemble σ_B, its root-mean-square value $\bar{x}_q$ (0.498). It reflects the variation of σ_B values in a greater or lesser degree in the whole range of the studied DP ranges of the given electrolysis mode.

CONCLUSIONS

The complexity and variety of factors affecting the process of electrochemical composition formation determine the necessity of their practical studies.

The methods of one of the directions for studying the given process are based on the principles of estimation of relationship between DP at various levels (macro, micro etc.). Such an approach to studies is of great theoretical and practical importance. For example, this approach is characterized by the high practicability of its methods and development prospects (e.g., at macro levels, such as A'_B, B'_B, C'_B, D'_B) and the possibility of applying their principles for the development of certain indicators of properties of electrochemical objects (e.g., σ_B is the indicator of the dynamics of the current yield coefficient).

Moreover, the methods of this direction allow for the considerable enhancement and extension of the quality of electrochemical composition studies, their prediction, and improvement of methods of their formation.

REFERENCES

1. Bortsoi, T.V., *Elektron. Obrab. Mater.*, 2006, no. 4, p. 24–36.
2. Bortsoi, T.V., *Elektron. Obrab. Mater.*, 2005, no. 5, p. 20–23.
3. Bortsoi, T.V., *Elektron. Obrab. Mater.*, 2006, no. 6, p. 10–14.
4. Rotinyan, A.L., Tikhonov, K.I., and Shoshina, N.A., *Teoreticheskaya elektrokhimiya* (Theoretical Electrochemistry), Rotinyan, A.L., Ed., Leningrad: Khimiya, 1981.
5. Tsupak, T.E., Novikov, V.T., Nachinov, G.N., and Vagramyan, T.A., *Laboratornyi praktikum po tekhnologii elektrokhimicheskikh pokrytii* (Laboratory Course in Technology of Electrochemical Coatings), Moscow: Khimiya, 1980, pp. 16-19.
6. *Spravochnik po elektrokhimii* (Guide in Electrochemistry), Sukhotin, A.M., Ed., Leningrad: Khimiya, 1981.

ISSN 1068-3755, Surface Engineering and Applied Electrochemistry, 2007, Vol. 43, No. 5, pp. 365–368. © Allerton Press, Inc., 2007.
Original Russian Text © I.N. Brovikova, 2007, published in Elektronnaya Obrabotka Materialov, 2007, No. 5, pp. 75–78.

ELECTRICAL PROCESSES IN ENGINEERING AND CHEMISTRY

Influence of the Temperature of Reactor Wall on the Kinetics of Heterogeneous Processes in H_2 + Ar Plasma

I. N. Brovikova

GOUVPO Ivanovo State Chemical and Technological University, pr. F. Engel'sa 7, Ivanovo, 153000 Russia

Received March 1, 2007

Abstract—The results of experimental study of the recombination of hydrogen atoms in a positive glow gap and flowing afterglow of direct current discharge in H_2 + Ar(0–95%) mixture are presented. On the basis of ESR measurements, the recombination probabilities are obtained for surfaces of quartz and molybdenum glass at different plasma parameters (pressure of 100–400 Pa, discharge current of 5–100 mA) and reactor wall temperatures (295–615 K). The values of activation energy for the recombination process are determined and the recombination mechanism is discussed.

DOI: 10.3103/S1068375507050109

Mixtures of molecular hydrogen with other gases are widely used as plasma-forming media in plasma technologies while performing etching processes or the surface modification of various inorganic and polymer materials. It is typical in plasmochemistry to use mixtures that contain an inert gas as a component. This increases the concentration of active particles forming in the plasma. In particular, research carried out for H_2 + Ar mixtures has shown the possibility of reaching a high degree of H_2 decomposition [1–3] and allowed us to analyze the mechanism of dissociation of molecular hydrogen in a glow discharge. However, the lack of data about the probability of the loss of hydrogen atoms in a wide range of temperatures of the reactor wall and plasma parameters hampers the practical application of mixtures of molecular hydrogen with inert gases. The object of the work was to investigate the influence of the temperature of the reactor wall on the kinetics of heterogeneous processes in plasma of a DC glow discharge in H_2 + Ar mixture.

EXPERIMENTAL METHOD

Experimental measurements were performed using the setup shown in Fig. 1. The cylindrical reactor with an internal diameter of 1.5×10^{-2} m is made of C-52 electron-tube glass. The maximal anode–cathode distance was 1.5 m. The length of the DC positive glow gap (PGG) could be varied by the anode displacement along the discharge tube. H(^{2}S) atoms generated in the

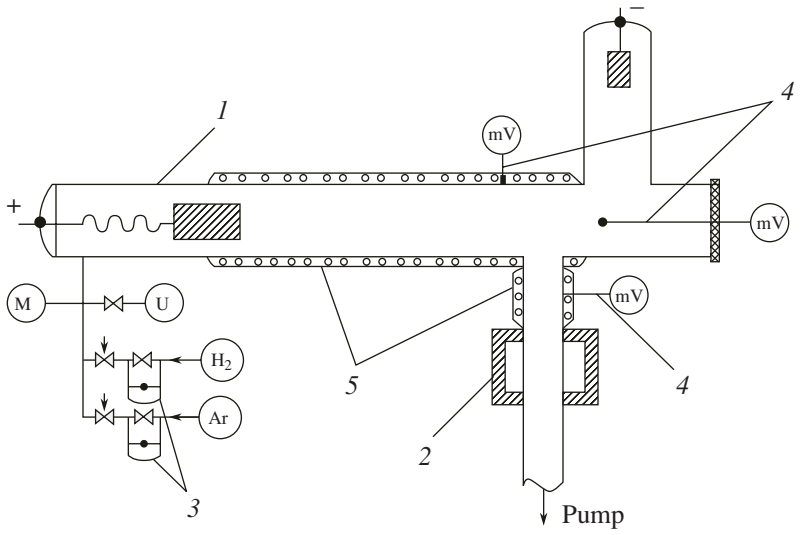

Fig.1. Schematic diagram of the experimental setup. (*1*) Reactor, (*2*) resonator of the EPR microwave spectrometer, (*3*) flowmeter, (*4*) thermocouple, (*5*) external heat exchange unit.

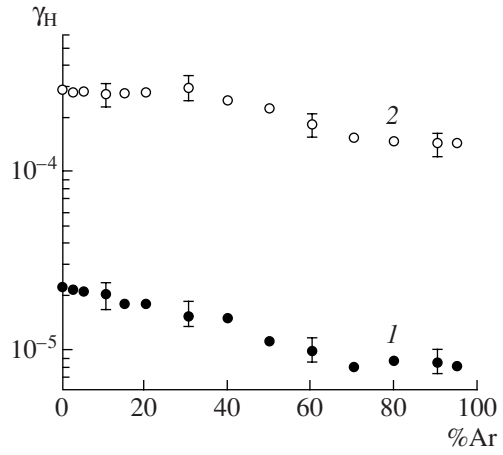

Fig. 2. Dependence of the probability of heterogeneous recombination of H(^{2}S) atoms on the argon content in a mixture (P = 200 Pa, I_p = 50 mA). (*1*) Afterglow, (*2*) plasma region.

discharge were registered with an RE 1301 EPR spectrometer. The spectrum of H(^{2}S) shows a doublet of components with equal intensities that are equidistant relative to the position of the EPR line for a free electron. The splitting amounted to 502 Oe, the H_0 value was ~3350 Oe in the registered spectrum of atomic hydrogen, and the line width was ~0.6 Oe. The distance from the plasma zone to the resonator cavity of a microwave spectrometer was 0.3 m, the pressure range of the gas mixture was of 60–400 Pa, and the discharge current was varied in the range of 5–100 mA. Hydrogen was produced in a Voden'-1 generator by the electrochemical decomposition of water. The gas was additionally purified by the flow through a liquid nitrogen trap and its purity, controlled by an IO 7304 mass spectrometer, was not worse than 0.995. The content of impurities in argon did not exceed 0.0003. The initial percentage of gases in the mixture was determined at the variation of flows of the investigated gases, which were measured by a calibrated capillary rotameter. The time of transition of atoms from the discharge zone to the place of their registration amounted ~0.1–0.03 s. The gas temperature T_0 on the PGG axis was measured by a two-thermocouple method [4]. The temperature of the reactor wall T_W exceeding those meanings, which would be settled in conditions of a natural heat exchange may be kept using an external heater.

The method of kinetic measurements based on the solution of the continuity equation for the density of fluxes of atoms, when the first order recombination reaction of atoms is assumed for the PGG and for the afterglow region, is described in detail in [5–8]. Application of this method allows one to obtain data about the concentrations of atoms and probabilities of their loss. To determine the constants (probabilities) of recombination of hydrogen atoms, we measured the H(^{2}S) concentration as a function of the PGG length for various gas flow values. The kinetic dependencies for hydrogen atoms in the afterglow region, where the surface of the tube that connects the discharge zone and the resonator of the microwave spectrometer is not subjected to the action of charged or other short-lived particles, were obtained by measurements of the time of gas contact with the surface under investigation. In this case, the measurements were reduced to determining the dependence of the concentration of atoms on the gas flow at specified plasma parameters. For the experimental calculation of the life span of hydrogen atoms in the discharge zone, which can differ from analogous values measured at afterglow, the distribution of the relative concentration of atoms over the discharge zone length at a constant velocity of the gas flow was determined.

RESULTS AND DISCUSSION

The main channels for the loss of hydrogen H(^{2}S) atoms in plasma are reactions of homogeneous recombination as follows:

$$H + H + H_2 \longrightarrow H_2 + H_2 \quad k = 2.2 \times 10^{-32}\ \text{cm}^6/\text{s}\ [8]$$

$$H + H + H \longrightarrow H_2 + H \quad k = \sim 10^{-31}\ \text{cm}^6/\text{s}\ [8]$$

and recombination of atoms on the surface of the reactor walls. According to preliminary evaluations, the input of volume reactions of the loss of hydrogen atoms for our experimental conditions (gas pressure of 60–400 Pa) does not exceed 10%; that is, the heterogeneous recombination should be considered to be the main channel of the loss of H($_2$S) atoms.

The results of measurements of the probabilities of heterogeneous recombination of hydrogen atoms in the PGG and at the afterglow of H_2 + Ar plasma for various compositions of the mixture are shown in Fig. 2. The loss of hydrogen atoms on the quartz surface (afterglow) and on the surface of the electron-tube glass (positive glow gap) occurs, as for a pure hydrogen plasma, according to the first kinetic order with respect to the concentration of atoms with a probability that does not depend on the discharge current and gas pressure. The probability of the heterogeneous loss of hydrogen atoms in the PGG of glow discharge is one order of magnitude greater than in the afterglow. The role of glow discharge consists of a continuous cleaning of adsorption centers at the bombardment of the surface of the reactor walls by active particles that leads to greater γ_H values at the boundary surfaces of the plasma zone. The obtained results show that the probability of the heterogeneous loss of hydrogen atoms decreases with the increase of the Ar content in the mixture, which is one of the reasons for the greater yield of H(^{2}S) atoms in H_2 + Ar mixture in comparison with a pure hydrogen plasma. As was shown in [9, 10], a heterogeneous recombination of atoms can occur due to the realization of two different mechanisms, i.e., (1) the

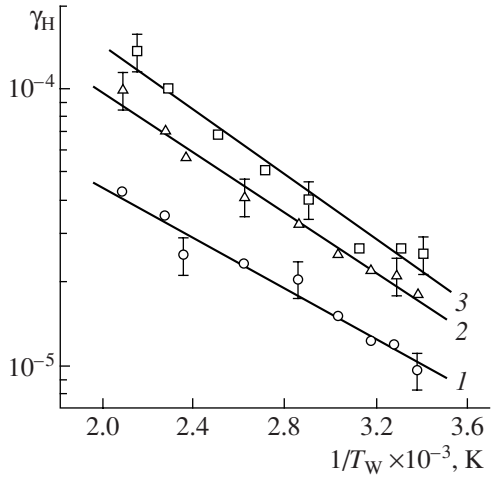

Fig. 3. Temperature dependence of the probability of recombination of $H(^2S)$ atoms on a quartz surface (afterglow). (*1*) H_2 + Ar(80%) mixture; (*2*) H_2 + Ar(20%) mixture; (*3*) H_2.

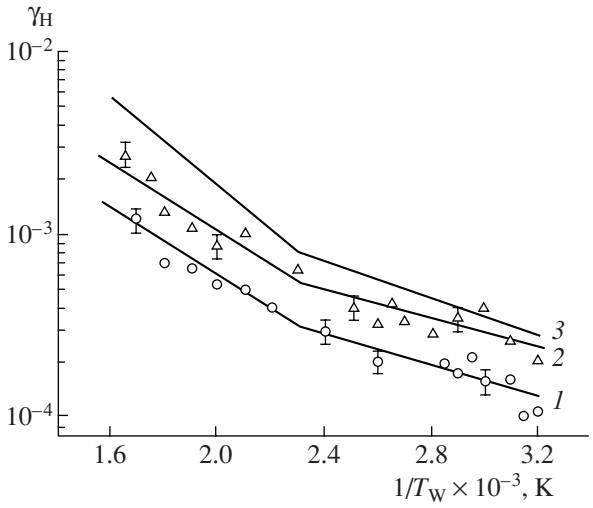

Fig. 4. Temperature dependence of the probability of heterogeneous loss of hydrogen atoms on a molybdenum glass surface in the PGG of glow discharge. (*1*) H_2 + Ar(80%) mixture; (*2*) H_2 + Ar(20%) mixture; (*3*) H_2 [5].

interaction of chemisorbed hydrogen atoms with gas phase atoms (Eley–Rideal mechanism)

$$H + S_v \longrightarrow H_s; \quad H + H_s \longrightarrow H_2 + S_v;$$

(2) the recombination of chemisorbed hydrogen atoms with physically adsorbed atoms (Langmuir–Hinshelwood mechanism)

$$H + F_v \longrightarrow H_f; \quad H_f + H_s \longrightarrow H_2 + F_v + S_v,$$

which leads to the formation of molecules in the gas phase (S_v, F_v are the vacant centers of chemical and physical adsorption). The values of probabilities of heterogeneous recombination on the quartz glass surface in the afterglow region (Fig. 3) form a unified temperature dependence; the effective activation energy of the process amounts to 10.3 ± 0.8 KJ/mol and virtually does not depend on the argon content in the mixture. The activation energy in the positive glow gap of glow discharge within the experimental error, under conditions of natural heat exchange, at a temperature of the reactor wall of 295–450 K, corresponds to the value obtained for the afterglow region and amounts to (8.2 ± 1.9) KJ/mol (Fig. 4). The unified temperature dependence of the probability of the heterogeneous loss of hydrogen atoms in the afterglow region and in the PGG of glow discharge in the H_2 + Ar mixture can suggest a unified recombination mechanism of $H(^2S)$ on the surface of quartz (afterglow) and of molybdenum electron-tube glass (PGG) for the surface temperature up to 450 K. Namely, it can suggest the Eley–Rideal mechanism, as its limiting step is determined (as is that for a pure hydrogen plasma) by the reaction of the gas phase atoms with those adsorbed on the surface at the constant density of surface active centers. At a temperature of the reactor wall of 450–615 K (forced heating), the activation energy of the recombination process in the PGG of glow discharge in H_2 + Ar mixture increases by a factor of two and amounts to (16.8 ± 2.0) KJ/mol, irrespective of the argon percentage in the mixture (Fig. 4). This may be linked with the change of the mechanism of the heterogeneous recombination of hydrogen $H(^2S)$ atoms, as well as with intensive desorption of chemisorbed water at high wall temperatures and the reduction of siloxane groups, which possess a higher adsorptive activity on the glass surface. Variation of the activation energy value was also observed in [11] in the transition to greater temperatures (exceeding 430 K) while investigating the recombination of nitrogen atoms on the surface of various sorts of quartz glass.

CONCLUSIONS

The probabilities of the heterogeneous recombination of hydrogen atoms in the DC glow discharge plasma in H_2 + Ar mixture on the surface of quartz (afterglow) and of electron-tube molybdenum glass (PGG) were measured for the temperatures of the reactor wall of 295–615 K.

The effective values of the activation energy of the process of heterogeneous recombination of $H(^2S)$ were determined. It was shown that in the positive glow gap of glow discharge, at the reactor wall temperature greater than 450 K, the activation energy of the process increases due to the dehydration of the glass surface.

REFERENCES

1. Ivanov, Yu.A., Rytova, N.M., Soldatova, I.V., et al., Mechanism of Decomposition of H_2 in a Glow Discharge in Ar + H_2, *Khimiya Vysokikh Energii*, 1988, vol. 22, no. 2, pp. 152–157.

2. Ivanov, Yu.A., Rytova, N.M., Soldatova, I.V., et al., Glow Discharge in Ar + H_2. Experiment and Mathematical Modeling, *Khimiya Vysokikh Energii*, 1988, vol. 22, no. 4, pp. 363–367.
3. Brovikova, I.N., Galiaskarov, E.G., et al., Kinetic Characteristics of the Formation and Loss of Hydrogen Atoms in the Positive Glow Gap of Glow Discharge in Ar + H_2 Mixture, *Teplofizika Vysokikh Temperatur*, 1999, vol. 37, no. 4, pp. 533–539.
4. Maksimov, A.I., Sergienko, A.F., Slovetskii, D.I., Measurement of Gas Temperature in a Glow Discharge by a Thermocouple Method, *Fizika Plazmy*, 1978, vol. 4, no. 2, pp. 347–351.
5. Brovikova, I.N., Galiaskarov, E.G., Rybkin, V.V., et al., Kinetic Characteristics of Formation and Loss of Hydrogen Atoms in the Positive Glow Gap of Glow Discharge in H_2, *Teplofizika Vysokikh Temperatur*, 1998, vol. 36, no. 5, pp. 706–711.
6. Brovikova, I.N., Kinetics of Formation and Loss of Oxigen Atoms O(^{3}P) in an Air Plasma, *Teplofizika Vysokikh Temperatur*, 2004, vol. 42, no. 6, pp. 869–872.
7. Brovikova, I.N., Galiaskarov, E.G., Kinetic Characteristics of Formation and Loss of Nitrogen Atoms in N_2 Plasma, *Teplofizika Vysokikh Temperatur*, 2001, vol. 39, no. 6, pp. 873–878.
8. Brovikova, I.N., Dissociation of Inorganic Molecules and Recombination of Atoms in a Nonequilibrium Gas-Discharge Plasma, *Cand. Sci. (Chem.) Dissertation*, Ivanovo, IKhTI, 1980.
9. Slovetskii, D.I., *Mekhanizmy khimicheskikh reaktsii v neravnovesnoi plazme* (Mechanisms of Chemical Reactions in Nonequilibrium Plasma), Moscow: Nauka, 1980.
10. Gordiets, B., Ferreira, C., Nahorny, J., Surface Kinetics of N and O Atoms in N_2–O_2 Discharges, *J. Phys. D.: Appl. Phys.*, 1996, vol. 29, pp. 1021–1031.
11. Vorob'ev, V.P., Kovtun, V.V., Kudryavtsev, N.N., Investigation of Probability of Heterogeneous Recombination of Nitrogen Atoms on the Surface of Solid Bodies Using a Coaxial Flow Reactor, *Kinetika i Kataliz*, 1989, vol. 30, no. 6, pp. 1326–1333.

ISSN 1068-3755, Surface Engineering and Applied Electrochemistry, 2007, Vol. 43, No. 5, pp. 369–378. © Allerton Press, Inc., 2007.

ELECTRICAL PROCESSES IN ENGINEERING AND CHEMISTRY

Effect of Exchangeable Cations on the Physicochemical Properties of Smectite[1]

F. Ayari[a, b], E. Srasra[b], and M. Trabelsi-Ayadi[a]

[a] *Laboratoire des Applications de la Chimie aux Ressources et Substances Naturelles et à l'Environnement (LACReSNE), Faculté des Sciences de Bizerte, Zarzouna, Bizerte, Tunisia*

[b] *Unité Matériaux du Centre de Recherche et de Technologie de l'Énergie Technopole Borj-Cedria, B.P. 95-2050 Hammam-Lif, Tunisia*

Received June 29, 2007

Abstract—The effect of exchange cations (M^{n+}: Li^+, Na^+, K^+, NH_4^+, Ca^{2+}, Mg^{2+}, Fe^{3+}, and Al^{3+}) and thermal treatment on the physicochemical properties of smectite was investigated. Before thermal treatment, unheated (25°C) M^{n+}-smectite showed increased d_{001} spacing upon glycol solvation; after heating at 300°C or above (400°C), d_{001} spacing upon glycol solvation of Al-, Fe-, Mg-, Li-smectite decreased and reached 10 Å. However, an increase in d_{001} of Ca^{2+}-, Na^+- and NH_4^+ -smectite upon glycol solvation indicated that d_{001} varied with the nature of exchangeable cation and the temperature of heating. The results generally suggested the following: d_{001} of homoionic smectite before and after heating at various temperatures depended upon the nature of exchangeable cation. The cation exchangeable capacities (CECs) and the BET surface areas (S_{BETs}) were functions of the type of exchangeable cations, since S_{BETs} drop off in the following order: Na^+-smect > Ca^{2+}-smect > Mg^{2+}-smect > NH_4^+ -smect > Li^+-smect > K^+-smect > Fe^{3+}-smect > Al^{3+}-smect. Finally, we have noted good progress in the exchangeable properties of synthesized clay in comparison with the Na homoionic smectite form, except for K homoionic clay, which have the lowest CECs, S_{BETs}, and consequently, the lowest exchangeable properties.

DOI: 10.3103/S1068375507050110

1. INTRODUCTION

The absorption and adsorption properties of clay are functions of exchangeable cations and layer silicate structure. These processes are governed by the balance between attractive and repulsive forces arising from intermolecular and electrostatic interactions between the solution and solid phases in a suspension.

Many workers have studied the relationship between the physicochemical properties of clay and the effect of the nature of exchangeable cations. The total layer charge has been found to play a major role in the expansion properties of layer silicates [1, 2]. Net particle charge is the most important factor controlling clay dispersion for the range of pH and ionic strength values [3]. Interlayer cations, net layer charge, and charge location (octahedral or tetrahedral) affect the expansion properties of smectites [4–6]. The general conclusion has been that the basal spacings of tetrahedrally charged smectites were smaller then those of octahedrally charged smectites under the same conditions of hydration and solution.

The thermal treatment of smectites saturated with Li has been shown to reduce their layer charge as well as cause a decrease in exchangeable Li [7–8]. A similar reduction in charge was also found when Mg^{2+} or Al^{3+} saturated clays were heated to 300°C [4, 9]. The mechanism of charge reduction was argued to be the migration of these cations of small radius into vacant octahedral sites to reduce the octahedral charge. Other new studies [10], concerning interaction of water with exchangeable cations of smectite clay (Li-, Na-, Ca-, Mg-, Al-smectite), show that dehydration involves desorption of the water molecules from its original adsorption site (the oxygen surface of the clay or exchangeable cation) and diffusion of the desorbed molecule to the gas phase. All data point to a strong cation dependence of the smectite–water interaction in parallel to what is observed or computed for water–cation interactions in the vapor or liquid phase [11]. It has been reported that the weight loss of molecular water depends on the nature of the counterion: the first water loss observed with all the samples (Li-, Na-, Ca-, Mg-, Al-smectite) took place at a temperature between 332 and 345 K; the second water loss was observed for smect-Li^+, smect-Ca^{2+}, smect-Ba^{2+}, smect-Mg^{2+} and smect-La^{3+} in the 377–419 K temperature range, when smect-Mg^{2+} exhibited a third peak of water loss at 508 ± 5 K. This implies that the cation type is determinative for the total water content retained in smectite since the physical state of a clay is charged with increasing water content; from solid to semirigid plastic, then to gel, and finally to suspension.

In the present study, we investigate the effect of counterions on the physicochemical properties of a

[1] The text was submitted by the authors in English.

Table 1. Most important different properties of the sample used

S_{BET} (m^2/g)	S_s (m^2/g)	CEC méq/100 g	V_{tot} (cm^3/g)
72.2	504	89	0.00581

structural formula:
$Ca_{0.043}Na_{0.404}K_{0.16}(Si_{7.56}Al_{0.44})(Al_{2.933}Fe_{0.678}Mg_{0.476})O_{22}$

Table 2. Cation exchange capacity of homoionic smectite

M^{n+}-smect	CEC (méq/100 g of calcined clay)	Ignition loss	CEC (méq/100 g of calcined clay)
Na^+-smect	72	19	89
K^+-smect	32	7	34
NH_4^+-smect	77	9	85.55
Li^+-smect	63	10	69.23
Ca^{2+}-smect	60	11	70.58
Mg^{2+}-smect	69	15	77.52
Fe^{3+}-smect	72	8.52	78.7
Al^{3+}-smect	64	12	73

smectite clay collected from Zaghouan (northeast Tunisia), then we report on the effect of heating at different temperatures (25–200–300–400°C) on the adsorption–absorption properties of smectite saturated with monovalent, divalent, and trivalent cations.

2. MATERIALS AND METHODS

2.1. Clay

Bentonite was used as the clay in this study, obtained from Zaghouan (northeast Tunisia), prepared as described elsewhere [12, 13]. The sample was characterized by X-ray diffraction, thermogravimetric, and FT-IR spectroscopic analyses. The chemical compositions of the clay were found to be as follows: 58.8% SiO_2, 3.95% MgO, 17.4% Al_2O_3, 0.84% K_2O, 0.28% CaO, 1.39% Na_2O. The cation-exchange capacity (CEC), determined according to the ammonium acetate saturation method [14]; the BET specific surface area (S_{BET}); and the total specific surface area (Ss) were also estimated. The most important properties of the sample used are illustrated in Table 1.

2.2. Preparation of Homoionic Clays

The homoionic Li^+-, NH_4^+-, K^+, Ca^{2+}-, Mg^{2+}-, Fe^{3+}-, and A^{3+}-forms were obtained by ion-exchange of the purified Na^+-form with the corresponding chlorides or nitrates (analytical grade) by repeated (seven times) exchange in 1% clay suspensions in 1 N salt solutions at their natural pH, followed by many washing cycles (centrifugation and, when necessary, dialysis) until they were chloride-free. Later, the salt-free clay samples were dried at 60°C, powdered in a mortar and pestle, and passed through a 60-mesh sieve to obtain finer grains before experiments.

Homoionic smectite was heated at different temperatures, and analysis was carried out at a constant heating rate of 100°C/h, from room temperature to 400°C, i.e., in a temperature domain where no dehydroxylation of the crystal structure takes place [15].

Characterization of synthesized clays was studies, including mineralogical analysis, measurement of CEC, pore volume, and S_{BET}. The chemical analyses were obtained by using X-ray diffraction studies (a Phillips PW1730/10 goniometer using the Kα radiation of copper). The CECs were determined by the Kjeldhal method [14] and S_{BETs} were measured by the (N_2, BET) method. We also report the results according to the ATD–ATG and AFM methods.

Consequently, we give the most important properties of synthesized clays.

3. RESULTS AND DISCUSSION

3.1. Chemical Properties of Synthesized Clays (Homoionic Smectites)

The cation exchange capacity of synthesized clays has been determined according to the ammonium acetate saturation method (Table 2); the results show that CEC was a function of the type of exchangeable cations, and it increases in the following order: Na^+-smect > NH_4^+-smect > Fe^{3+}smect > Mg^{2+}-smect > Al^{3+}-smect > Ca^{2+}-smect > Li^+-smect > K^+-smect.

The S_{BETs} and total pore volumes have been determined using the BET method [16]. The Halsey *t*-method [17] was used for the determination of the micropore volume in the presence of mesopores. This technique involves the measurement of nitrogen adsorbed by the sample at various low pressure values.

Representative nitrogen sorption isotherms are shown in Fig. 1; they are of type II with H_2 hysteresis loops, as is typical for smectite clays that contain microporous networks of broad structure [18, 19]. The surface area due to micropores, S_{mp}, was obtained from the difference (S_{BET}–S_{ex}). Reliable interpretation of these isotherms is limited to quantitative measurement of specific surfaces areas and total pore volumes; these data are provided in Table 3 and Fig. 2.

3.2. Differential Thermal Analysis and Thermogravimetric Analysis (DTA–TGA)

DTA and TGA were merely used as complementary methods with respect to the other techniques. The interpretation [20] of the DTA–TGA curves of synthesized clay samples (homoionic smectite)—for example, the

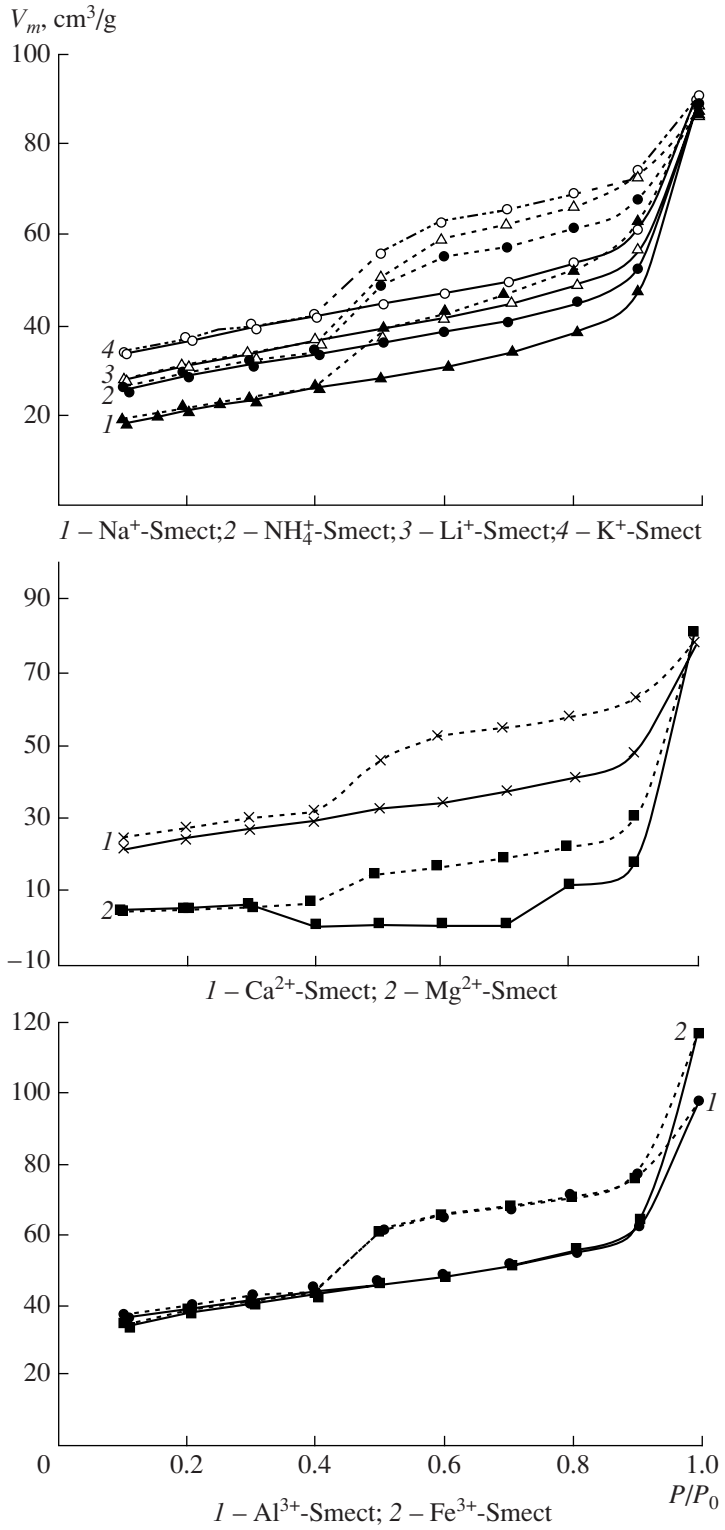

Fig. 1. Nitrogen adsorption and desorption isotherms of synthesized clays. —— Adsorption, ... desorption.

DTA–TGA curve of Na homoionic smectite—leads to the following results (Fig. 3):

—A significant endothermic peak between 130 and 180°C. These transformations are due to the removal of adsorbed and interlayer water from the clay mineral. The high intensity of the first peak confirms the presence of a swelling phase (smectite) interlayer stratified with nonswelling clay (illite) [21].

Table 3. Physical data for synthesized samples

Sample	S_{BET} (m^2/g)	$S_{ext(t\text{-}plot)}$ (m^2/g)	S_{mp} (m^2/g)	V_{tot} (cm^3/g)
Na^+-Smect	72.2	61.5	10.7	0.00581
NH_4^+-Smect	93.8	65.92	27.88	0.0551
K^+-Smect	117	69.65	47.35	0.0264
Li^+-Smect	101	72.3	28.7	0.0158
Mg^{2+}-Smect	92	65.62	26.38	0.0112
Ca^{2+}-Smect	82	65.38	16.62	0.00921
Fe^{3+}-Smect	120	74	46	0.026
Al^{3+}-Smect	122	64.8	57.2	0.019

Table 4. % loss of water

Sample: M^{n+}-smect	(%) waters hydratation loss	(%) water constitution loss	(%) Total loss of water
Na^+-Smect	13.5	4	17.5
Li^+-Smect	6.83	4.2	12.61
NH_4^+-Smect	9.58	5.5	15.1
K^+-Smect	11.4	4	15.5
Mg^{2+}-Smect	12.35	3.43	16.2
Ca^{2+}-Smect	12.17	3.32	15.5
Al^{3+}-Smect	15.13	4.5	19.6
Fe^{3+}-Smect	13.6	4.6	18.2

—A small endothermic peak between 500 and 540°C, which corresponds to the loss of hydroxyl groups from the clay mineral structure (clay dehydroxylation).

—An endothermic peak between 930 and 997°C shows the formation of a phase at high temperature [22, 23] characteristic of aluminum ferifere smectite.

Curves of TGA allow us to follow the weight loss of homoionic smectite samples (Table 2). These curves show tow losses of weight of M^{n+}-smectite samples:

—The first loss of weight occurs between 30 and 130°C. These transformations are due to the removal of adsorbed and interlayer water from the clay mineral.

—The second loss of weight occurs at 526°C due to the removal of water composition from the clay mineral.

The weight loss results are given in Table 4, which shows that the creep of smectite clays is not controlled by the mobility of the individual water molecules but by the mobility of the interlayer cations surrounded by their hydratation shells. We compare our results to those obtained from a number of comparable homoionic smectites by DTA–TGA by other authors [9, 24, 25].

3.3. Atomic Force Microscopy

Microtopography of the particles was achieved using atomic force microscopy (AFM) images, and computerized image analysis permits a direct and quantitative study of the size and shape of the synthesized clay (Fig. 4).

AFM images were recorded on a nanoscope II instrument in contact mode and in a region of $5 \times 5\ \mu m^2$ with a scan rate of 1Hz at a resolution of 256×256, for sample preparation for AFM analysis. We use the method of Occelli et al. [26]. Wafers were formed by pressing powders of samples at about 15000 kPa and were glued onto steel disks with epoxy resin; when the glue dried, the tip of the atomic force microscope was carefully guided to the middle of the wafer, thus beginning the analysis.

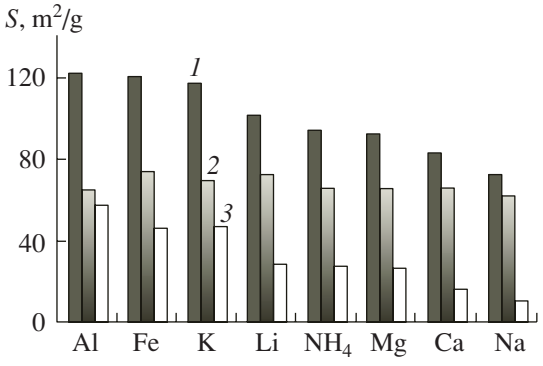

Fig. 2. Representative histograms of S_{BET}, S_{ext}, and S_{mp}.

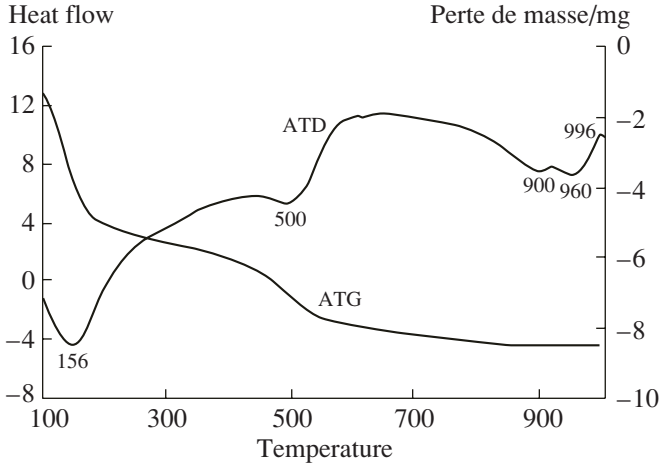

Fig. 3. DTA–TGA curves of Na homoionic smectite (Na^+-smect) sample.

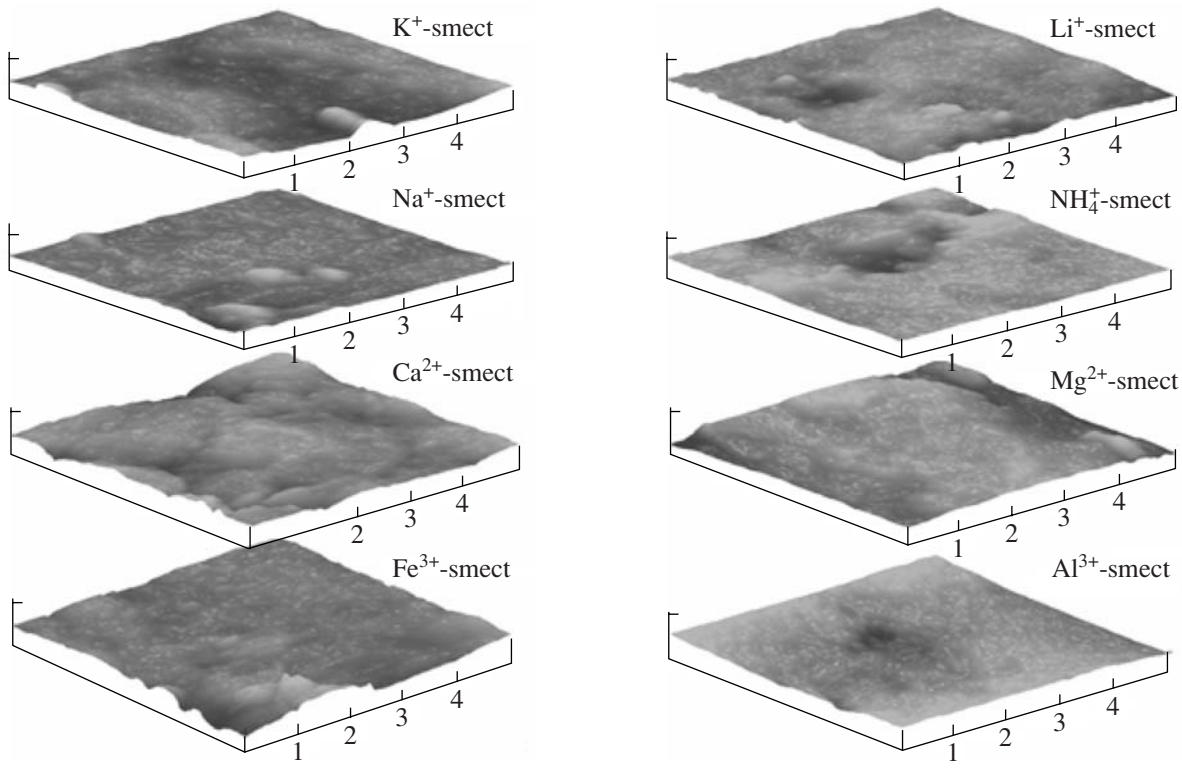

Fig. 4. AFM images of homoionic clays.

AFM reveals the network character and the development of morphology as a function of the type of exchangeable cation, which is noted by a variation in the value of the rugosity (Table 5).

3.4. Effect of Heating

Physicochemical properties of smectites depend upon their structures, their chemical compositions, and the type of exchangeable cation. The variation of XRD patterns of Li^+-, Na^+-, NH_4^+-, K^+-, Mg^{2+}-, Ca^{2+}-, Fe^{3+}- and Al^{3+}-smectite (Figs. 5 and 6) before and after heating and reexpansion after glycerol solvation was studied. Table 6 shows the swelling obtained for dry and glycerol solvated samples. The d_{001} spacing of Li^+-, K^+-, NH_4^+-, and Na^+-smectite prior to heating correspond to a hydrated structure where the cations are located in the interlayer space and solvated by water molecules adsorbed from the atmosphere.

Lithium saturation and heating caused the bentonite (smectite) to develop a hydrophobic character. Li-clay collapsed and remained unexpandable after being heated at 200–400°C (Table 4). The XRD patterns of Li-clay after heating at 200–400°C exhibit a d_{001} reflection corresponding to 10 Å, even after treatment by glycerol.

The high charge reduction guessed from the reduction of the amount of exchangeable cation (CEC) of Li-clay (with decrease from 69.3 to 7 mq/100g), after heat treatment is in good agreement with previous work. Calvet and Prost [27] showed that the clay did not swell with water when the amount of exchangeable cation was lower than 50% of the original exchange capacity.

No differences were detected between XRD patterns of Na-clay heating at 200°C–400°C and 25°C (unheated). Even after thermal treatment (up to 400°C), the hydrated sodium ions remained in the interlayer as re-hydrated sodium ions remained in the interlayer as reflected by d_{001} spacings (Fig. 6, Table 6). As a result of glycerol solvation, d_{001} spacing of treated clays increased to 17.6 Å, indicating swelling even after heating to 400°C. This behavior, as for the charge characteristics, is opposite to that of Li-clay.

Table 5. Evolution of the rugosity

M^{n+}-smect	Al^{3+}-smect	Fe^{3+}-smect	Mg^{2+}-smect	Ca^{2+}-smect	Na^+-smect	Li^+-smect	NH_4^+-smect	K^+-smect
Rq	70.7	97.2	84.3	109	107	61.2	74.7	119

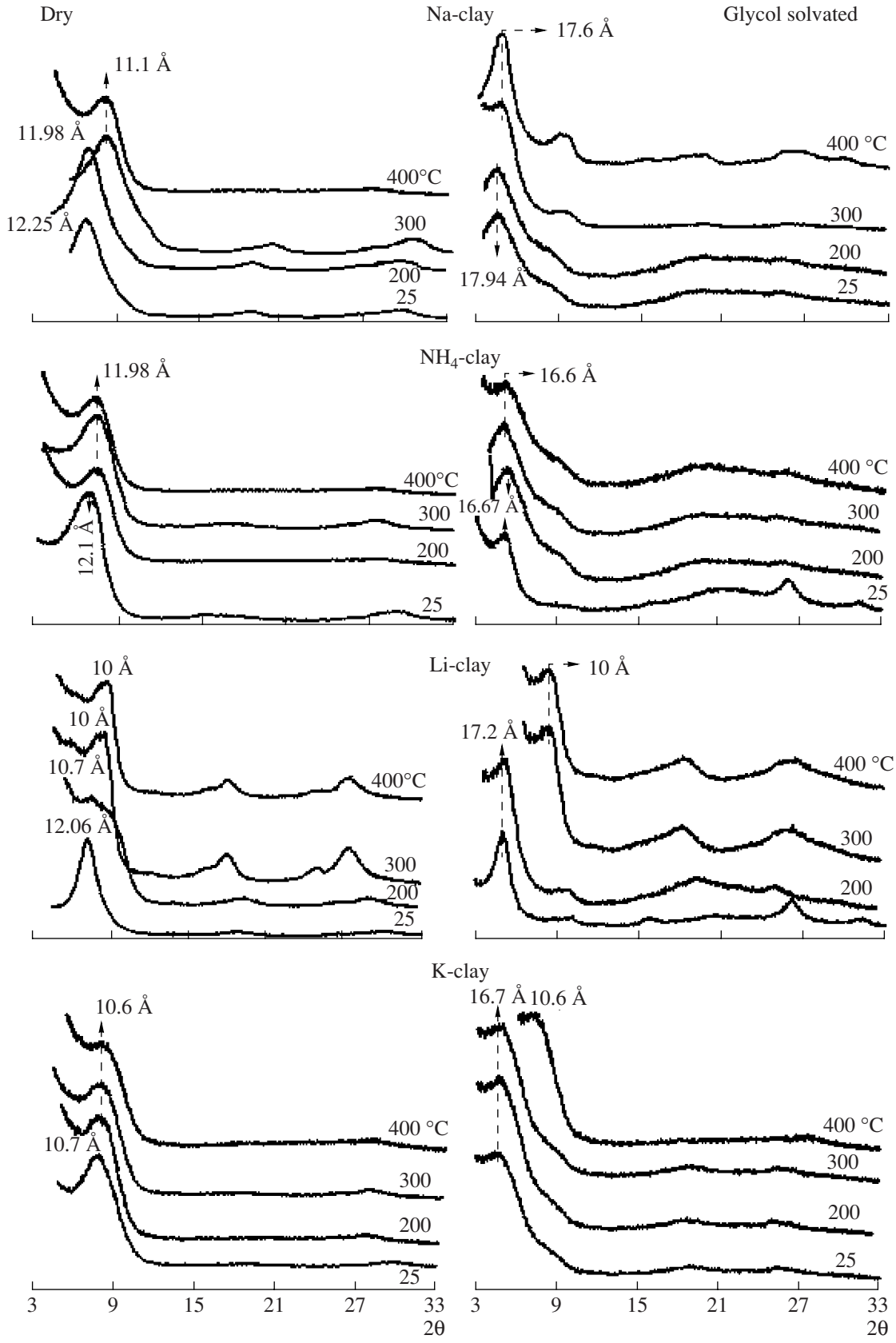

Fig. 5. X-ray diffraction patterns of smectite saturated with Li, K, NH_4 and Na at different temperatures. The dry samples (left) and those solvated by glycol (right).

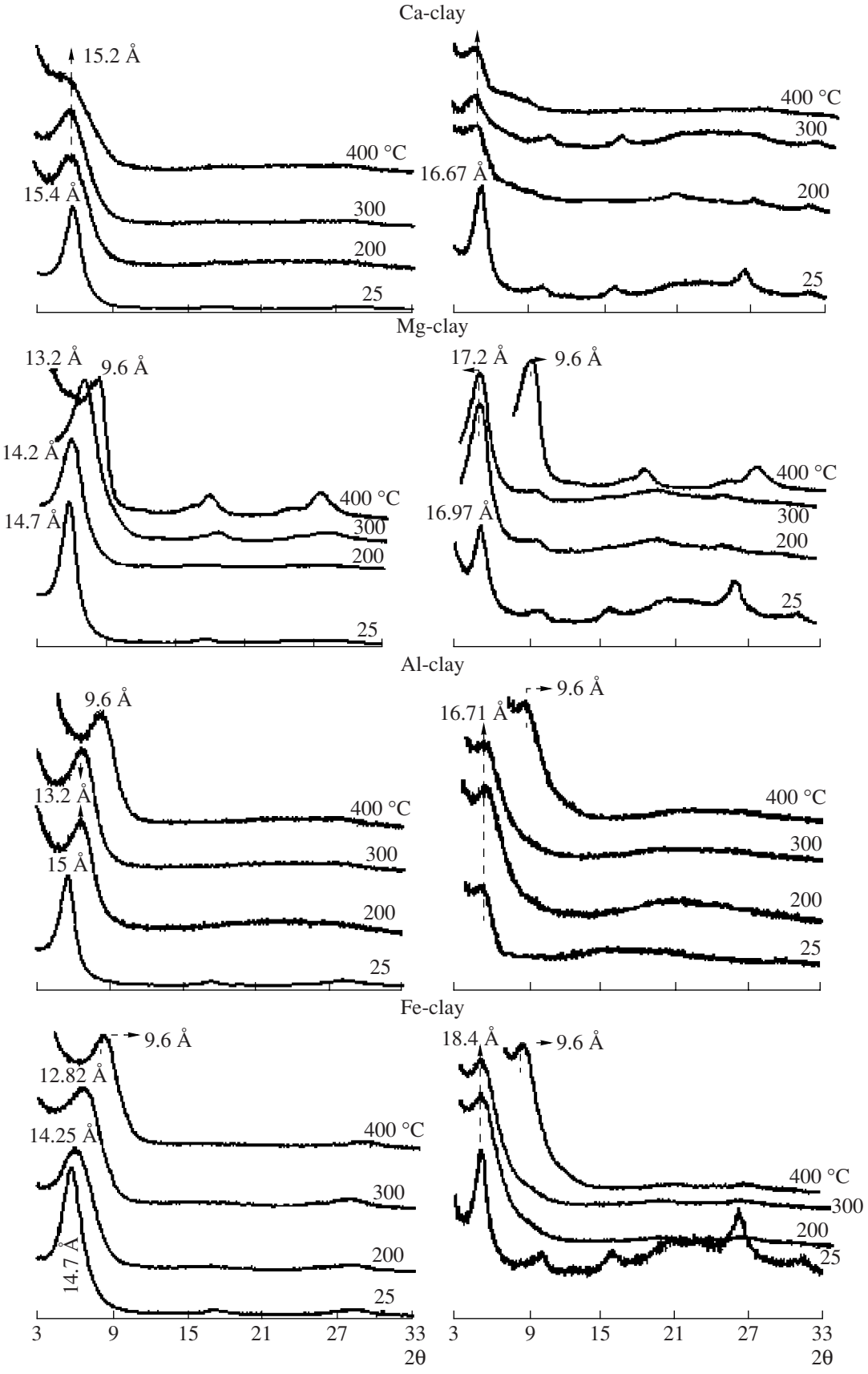

Fig. 6. X-ray diffraction patterns of smectite saturated with Ca, Mg, Fe and Al at different temperatures. The dry samples (left) and the glycol solvated (right).

Table 6. Effect of thermal treatment on pH, CEC, and d_{001} spacing of synthesized clays (M^{n+}-smectite)

Cation M-clay	Temperature of heating °C	d_{001} Dry glycol		pH	CEC (méq/100 g of calcined clay)
Na	25	12.25	17.94	6.17	*89*
	200	11.98	17.94	6.25	84
	300	11.1	17.6	6.43	80
	400	11.1	17.6	6.49	76
Li	25	12.06	17.2	6.05	*69.23*
	200	10.7	17.2	6.5	38
	300	10	10	6.63	16
	400	10	10	7	7
NH_4	25	12.1	16.67	6.2	*85.55*
	200	11.98	16.67	6.32	80
	300	11.98	16.6	6.35	76
	400	11.98	16.6	6.45	70
K	25	10.78	16.7	5.39	*34*
	200	10.6	16.7	5.42	28
	300	10.6	16.7	5.55	25
	400	10.6	10.6	5.76	12
Mg	25	14.7	16.97	5.85	*77.52*
	200	14.2	17.2	6.5	66
	300	13.2	17.2	6.64	43
	400	9.6	9.6	6.7	18
Ca	25	15.4	16.67	6.34	*70.58*
	200	15.2	17.67	6.48	60
	300	15.2	17.67	6.65	50
	400	15.2	17.67	6.83	45
Fe	25	14.7	18.4	4.98	*78.7*
	200	14.25	18.4	5.09	68
	300	12.82	18.4	5.11	53
	400	9.6	9.6	5.18	22
Al	25	15	16.7	4.89	*73*
	200	13.2	16.7	4.91	65
	300	13.2	16.7	4.97	58
	400	9.6	9.6	5.12	18

The d_{001} spacings of K-clays heated to 300°C and after glycerol solvation were similar to those of Na-clays. Expansion in the d_{001} spacing of K-clays after glycerol solvation is observed even after heating at 200 or 300°C (Table 6). Thus, it appears that K^+ does not migrate into the lattice sites, the interlamellar K^+ remaining exchangeable. Heat treatment only reduces the amount of exchangeable K^+. Apparently, K^+ in the interlayer space is progressively fixed or strongly bonded to the surface –O or –OH groups with increasing temperature.

Among the divalent cations, d_{001}, spacing of unheated (25°C) clays (Table 6) indicated that interlayer divalent cations were more hydrated than K^+. Spacings for Al^{3+}-clays and Fe^{3+}-clays were also consistent with substantial cation hydration. Heating to 300°C did not result in any substantial collapse of d_{001} spacing, which upon glycerol solvation expanded with d_{001} spacings ranging from 16.7 to 18.4 Å. However, on heating at 400°C, Mg^{2+}-, Fe^{3+}-, and Al^{3+}-clays collapse to a d_{001} spacing of 9.6 Å and do not expand with glycerol solvation (Fig. 2). These results are consistent with migration of Mg, Fe, and Al from the interlayer space

to the vacant octahedral sites. From the literature [3, 27], we reported that when Mg-montmorillonite and Ca-montmorillonite were heated at 400°C, Mg^{2+} ions could migrate into the structure, while Ca^{2+} ions could not. Alternatively, it can be suggested that these cations are strongly bonded to the clay surfaces while still remaining in the interlayers.

Results show that peak intensity reduced with increasing temperature (Figs. 5 and 6). The extent of peak intensity reduction was similar to the reduction in the capacity of cation exchange. For Li^+-, Mg^{2+}-, NH_4^+-, Fe^{3+}- and Al^{3+}-clays, after heating at 400°C, the reduction in the capacity of cation exchange was drastic and the intensity of d_{001} peaks was also very low.

The thermal treatment of smectite saturated with monovalent, divalent, and trivalent cations has been shown to reduce the CEC and to affect the hydrophobic character of Li^+-, K^+-, Mg^{2+}-, Fe^{3+}-, and Al^{3+}-clays, suggesting that these cations becomes nonexchangeable.

In general, results corroborate that this clay from Zaghouan demonstrated its good capacity to absorb these toxic metals [28] from waste water due to its frequent appearance in waste streams from many industries, and to maintain them even at high temperature, which ranges from 200 to 400°C in this study.

The pH of the suspension in distilled water was measured before and after heating, and the results show that pH depends on the nature of the cation. Among monovalent cationic clays, Li^+-, Na^+- and NH_4^+-clays had higher pH values than K-clays. Furthermore, divalent cationic clays had higher pH values than Fe^{3+}- and Al^{3+}-clays (Table 6). In the suspension of unheated clays (25°C), the dissociation of cations and subsequent hydrolysis reactions led to changes in H^+ concentration. For Fe^{3+} and Al^{3+}, even though the dissociated ions were very low, strong hydrolysis reactions released more H^+ ions and the pH was 4.89 and 4.98, respectively, for Fe^{3+}- and Al^{3+}-clays. Upon thermal treatment, the pH increased for all cationic clays, suggesting that the cations are more strongly bound to the clay surface [3]. This is clearly shown in the increase of the CEC with an increase in heating temperature (Table 6).

CONCLUSIONS

The effect of exchangeable cation saw good progress in the exchangeable properties of synthesized clay in comparison to the Na homoionic smectite form, which means good exchangeable properties: adsorption and absorption, except for K homoionic clay, which has the lowest CEC, S_{BET}, and consequently, the lowest exchangeable properties.

Upon thermal treatment, the bonding characteristics change according to the size of the cations. Smaller cations (ionic radius, <0.7 Å), Li, Mg, Fe, and Al, apparently migrate to the vacant octahedral sites. This results in severe reductions in cation exchange capacity, and the cation becomes nonexchangeable. This process occurred even at 200°C for Li^+-clays.

Larger cations Na, NH_4, K, and Ca apparently do not migrate to lattice sites on thermal treatment.

The thermal treatment of smectite saturated with monovalent, divalent, and trivalent cation has been shown to reduce the cation exchange capacity and to affect the hydrophobic character of Li^+-, K^+-, Mg^{2+}-, Fe^+-, and Al^{3+}-clays, suggesting that these cations become nonexchangeable.

Results corroborate that this clay collected from Zaghouan demonstrate good capacity to remove toxic metals [28] from waste water, since this problem has received considerable attention in recent years due primarily to the concern that those toxic metals in waste streams can be readily adsorbed by marine animals and directly enter the human food chain, thus representing a great health risk.

REFERENCES

1. Suquet, H., De la Calle, C., and Pezerat, H., *Clays Clay Miner.,* 1975, vol. 23, p. 1.
2. Horvath, I. and Novak, I., *Processings of the International Clay Conference: Mexico City*, Bailey, S.W., Ed., Wilmette, Illinois: Applied Publishing, 1975, p. 185.
3. Chorom, M. and Pengasamy, P., *Clay and Clay Minerals*, 1996, vol. 44, no. 6, p. 783.
4. Glaser, R. and Mering, J., *CR Acad Sci Paris*, 1968, vol. 46, p. 436.
5. Slade, P.G., Quirk, J.P., and Norrish, K., *Clays Clay Miner.*, 1991, vol. 39, p. 234.
6. Sato, T., Watanabe, T., and Otsuka, R., *Clays Clay Miner.*, 1992, vol. 40, p. 103.
7. Hoffmann, U. and Klemen, R., *Z Anorg Allg Chem.*, 1950, vol. 262, p. 95.
8. Jaynes, W.F. and Bigham, J.M., *Clays Clay Miner.*, 1982, vol. 35, p. 440.
9. Green-Kelly, R., *Mineral Mag.*, 1955, vol. 30, p. 604.
10. Zabat, M. and Van Damme, H., *Clay Minerals*, 2000, vol. 35, p. 357.
11. Güven, N., *Clay-Water Interface and Its Rheological Implications*, 1992, vol. 2.
12. Ayari, F., Srasra, E., and Trabelsi-Ayadi, M., *DEA. Faculté des Sciences de Bizerte*, 2003.
13. Ayari, F., Srasra, E., and Trabelsi-Ayadi, M., *Journal de Physique IV*, 2004, vol. 122, p. 229.
14. Kjeldhal, Page, A.L., Miller, R.H., and Keeney, D.R., *American Society of Agronomy; INC. Soil Science Society of America INC*, Wisconsin, USA: Publisher Madison, *Part 2. Chemical and Microbiological Proprieties*, 1982, 2nd edition, p. 597.
15. Mackenzie, R.C., *Academic Press*, 1981, p. 775.
16. Brunauer, S., Emmett, P., and Teller, E., *J. Amer. Chem. Soc.*, 1938, vol. 60, p. 309.
17. Halsey, G.D., *J. Chem. Phys.*, 1948, vol. 16, p. 931.

18. Sing, K.S.W., Everett, D.H., Haul, R.A.W., Masca, Li., Pieratti, R.A., Raquerol, J., and Siemieniewska, T., *Pure App. Chem.,* 1985, vol. 57, p. 603.
19. Carrado, K.A., *Layered Materials Science and Technology*, 2004, vol. 19, p. 213.
20. Brindley, G.W. and Nakahira, M., *J. Amer. Chem. Soc.,* 1959, vol. 42, p. 311.
21. Srasra, E., Thèse de 3^{éme} Cycle. Fac. SC. Tunis. Univ., Tunis II, 1987, p. 166.
22. Gaudette et al., *Clay and Clay Mineral.*, 1966, vol. 13, p. 33.
23. Grim, R.E. and Kulbicki, G., *Amer. Min.*, 1961, vol. 46, p. 1329.
24. Dzidic, J. and Kebarle, P., *J. Phys. Chem.*, 1970, vol. 71, p. 1466.
25. Poinsignon, C., Yvon, J., and Mercier, R., *Israel J. Chem.*, 1982, vol. 22, p. 253.
26. Occelli, M.L., Bertrand, J.A., Gould, S.A.C., and Dominguez, J.M., *Microporous.*
27. Cavert, R., *Prost. Clays Clay Miner.*, 1971, vol. 19, p. 179.
28. Förstner, U., *Contaminated Sediments*, Berlin: Allemagne, 1998, vol. 13, p. 157; *Mesoporous Mater.*, 2000, vol. 34, p. 195.

ISSN 1068-3755, Surface Engineering and Applied Electrochemistry, 2007, Vol. 43, No. 5, pp. 379–380. © Allerton Press, Inc., 2007.
Original Russian Text © L.M. Vasilyak, S.V. Kostyuchenko, N.N. Kudryavtsev, V.Ya. Pecherkin, 2007, published in Elektronnaya Obrabotka Materialov, 2007, No. 5, pp. 89–90.

EQUIPMENT AND INSTALLATIONS

Radiant Emittance of Oxide Trispiral Electrodes

L. M. Vasilyak[a], S. V. Kostyuchenko[a], N. N. Kudryavtsev[b], and V. Ya. Pecherkin[a]

[a]*ZAO Research and Production Association LIT, Krasnobogatyrskaya ul. 44-1, Moscow, 107076 Russia*
[b]*Moscow Institute of Physics and Technology, Institutskii per. 9, Dolgoprudnyi, Moscow oblast, 141700 Russia*

Received April 3, 2007

Abstract—The gray color coefficients of the bactericidal low-pressure lamp oxide electrodes from different producers are measured within a 1100–1400 K temperature range (Heraeus, Germany; LIT Technology, Russia; Philips, Holland).

DOI: 10.3103/S1068375507050122

Cathode spot temperature during low-pressure lamp operation is one of most important parameters characterizing oxide electrode quality. The temperature influences the evaporation or spraying rate of the oxide coating and the lamp lifespan, respectively. Usually, the temperature measurements and its distribution over the electrode winds are made with the help of an optical pyrometer with an evanescent filament. Furthermore, the instrumentation indications are recounted for the real temperature with the use of the predetermined emissivity (gray color) of the electrode. The gray color of the oxide coating depends on many factors, particularly on the composition and processing technique of the emission coating, as well as on its thickness (from 0.15 μm at 140 μm thick up to 0.45 μm at 5 μm thick [1]), etc. Therefore, the errors in the determination of the electrode's real temperature may be substantial if the spectral emittance of the oxide substance is unknown. The work objective is the determination of a spectral dependence of the gray color coefficient of oxide trispiral electrodes of low-pressure gas-discharge lamps from different producers.

Usually, the temperature of oxide electrode of low-pressure gas-discharge lamps is in the 1200–1350 K range [2]. The spectral emittance of the wolfram in the temperature range that is interesting for us is presented in [3]. Under the same temperatures, the radiation intensity of the wolfram electrode coated by an oxide layer will be less than that of the wolfram electrode of the gray color ratio $\varepsilon_W(\lambda, T)^*\Phi^0_W(\lambda, i) = \Phi_W(\lambda, i)$, where ε_W is the oxide layer gray color coefficient, and Φ is the radiation intensity. Therefore, in order to determine the oxide electrode gray color coefficient, it is necessary to ensure the equality of the electrode temperatures with oxide and without coating. Then, the radiation condition will be written in view of $\varepsilon_{W0}(\lambda, T) = \varepsilon_W(\lambda, T)^*\Phi_{W\text{oxide}}(\lambda, T)/\Phi_W(\lambda, T)$, where ε_{W0} is the gray color coefficient of wolfram. The electrode temperature T_{el} is determined in accordance with the known dependence of hot and cold cathode resistances ratio at room temperature as follows: R_{hot}/R_{cold} [3].

Electrode heating was conduted with the help of a stabilized dc power supply. Before the experiments, the electrode resistance was measured at room temperature. The spectral radiation intensity of the cathode spot was measured by MDR-23 monochromator and FEU-63 photomultiplier tube (voltage supply 1 kV). The gray color coefficient determination error does not exceed 15%. The error value is conditioned by several factors, in particular, by the measurement error during the reading of data from an AD converter; by the disposition error, due to the difference in the measured areas projected by the objective lens and quality of coating in the measured place; by the R_{hot}/R_{cold} ratio; and by the influence of neighbor parts that are tightly fitted to the measured electrode.

The figure shows the obtained dependencies of the gray color coefficient of oxide electrodes on the wave-

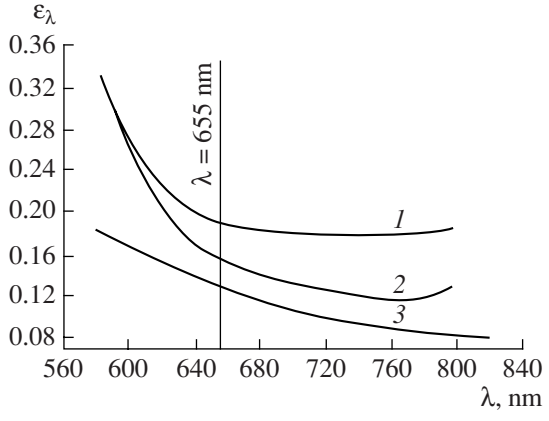

Spectral characteristics of the gray color coefficient of oxide electrodes for bactericidal lamps from different producers. (*1*) TUV–75 (Philips); (*2*) DB–250 (Research and Production Association LIT, Russia); (*3*) NNI–200 (Heraeus, Germany).

length for the bactericidal lamps on mercury vapors of low pressure from different producers. The ratio $R_{hot}/R_{cold} = 6.5$, which approximately corresponds to an electrode temperature of 1320 K. The gray color coefficient of the electrodes under study at a wavelength of 655 nm (operating wavelength of many pyrometers, including Promin'-M1 device) is equal to 0.14 for the NNI-200 lamp (Heraeus firm, Germany), 0.16 for the DB-250 lamp (Scientific-Industrial Corp. LIT, Russia, Moscow), and 0.2 for the TUV-75 lamp (Philips, the Netherlands).

The gray color coefficients obtained may be used in the measurements of oxide electrode temperatures in the 1100–1400 K range.

REFERENCES

1. Iorish, A.E., Katsman, Ya.A., Ptitsyn, S.V., and Sheingauz, A.A., *Osnovy tekhnologii proizvodstva elektrovakuumnykh priborov* (Principles of Production Engineering of the Electronic Devices), Leningrad: Energiya, 1971.
2. Okhonskaya, E.V., Reshenov, S.P., and Rokhlin, G.N., *Elektrody gazorazryadnykh istochnikov izlucheniya* (Electrodes of Gas-Discharge Radiation Sources), Saransk: Edit. of Mordvinian Univers., 1978.
3. *Fizicheskie velichiny* (Physical Magnitudes), Grigor'ev, I.S. and Meilikhov, E.Z., Eds., Moscow: Energoatomizdat, 1991.

ISSN 1068-3755, Surface Engineering and Applied Electrochemistry, 2007, Vol. 43, No. 5, pp. 381–386. © Allerton Press, Inc., 2007.
Original Russian Text © V.L. Lanin, 2007, published in Elektronnaya Obrabotka Materialov, 2007, No. 5, pp. 91–96.

EQUIPMENT AND INSTALLATIONS

Infrared Heating in the Technology of Soldering Components in Electronics

V. L. Lanin

State University of Informatics and Radioelectronics of Belarus, ul. P. Brovki 6, Minsk, 220013 Republic of Belarus

Received April 5, 2007

Abstract—Parameters of infrared heating for soldering electronic components using surface mounting are investigated and optimized. The main advantages of IR heating are as follows: high rate, low lag effect, possibility to effectively change the temperature and time profile of heating, and the relative simplicity of the equipment.

DOI: 10.3103/S1068375507050134

Infrared (IR) heating providing a high rate of the local contactless heating and effective control over the temperature profile is the most promising for group technologies of soldering. Within the entire IR spectrum with its wavelength range of 0.72–1000 μm, a small part of this range is used only for soldering, i.e., near- (0.72–1.5 μm), middle- (1.5–5.6 μm), and far- (5.6–10.0) μm IR radiation. The temperature of the body at heating depends on the radiation wavelength, its emissivity factor or reflectivity, duration of irradiation and the body's mass. Intensity of the spectral radiation of the IR source is defined as [1]

$$I_\lambda = \varepsilon_\lambda C_1 \lambda^{-5} (e^{C_2/\lambda T} - 1)^{-1}, \quad (1)$$

where ε_λ is the spectral emissivity factor of the radiator, C_1 and C_2 are the Planck constants, and T is the radiator temperature.

The shorter the radiation wavelength is, the deeper it penetrates the body; therefore, near-IR radiation possesses a deeper penetration ability than compared with middle- and far-range radiation. Various materials adsorb the IR energy in different manners. Four conditions of the transfer of IR energy to a body can be distinguished, including reflection, opacity, transparency, and translucency. The IR energy flux is partly reflected, partly absorbed, and partly passes through the body when it reaches the body surface;

$$\Phi_{inc} = \Phi_{abs} + \Phi_{ref} + \Phi_{pas}. \quad (2)$$

IR energy passes through a transparent material without heating; in a translucent material it penetrates to a definite depth and heats the body. The effective power of heating by IR radiation is as follows [2]:

$$P = k\varepsilon S\Delta T, \quad (3)$$

where k is the Stephan–Boltzmann constant, ε is the emissivity of the body, S is the body surface, and ΔT is the temperature variation.

Some problems occur due to certain peculiarities of IR radiation at its practical application for group soldering of components in electronics:

(i) nonuniform heating of various electronic components due to the diverse degree of energy absorbtion;

(ii) nonreproducibility of heating regimes because of mismatch between the radiation spectrum of the source and the absorption spectra of components and the board;

(iii) necessity to optimize the heating regimes of boards with various geometry and mass, as well as to protect of the surface of IR radiators from evaporating flux agents;

(iv) existence of shadowed board places where a direct IR radiation is absent.

The first developments in the field of application of IR heating for soldering were based on the application of IR lamps with a temperature of radiator exceeding 800–1100°C. Since the soldering temperature is usually in the range of 210–215°C, the heating regimes markedly differed from the equilibrium ones; this led to overheating in some regions on the board surface due to different emissivity factors and component mass.

IR-radiation lamps contain a tungsten helix wire placed inside a sealed quartz tube filled with an inert gas. They are most often placed inside a reflector that concentrates radiation on the object being heated. The lamps and reflectors usually produce IR radiation in a middle-IR range; near-IR radiation is weaker and far-IR radiation is minimal. This energy amounts more than 90% of the radiation used for heating the body. Because air is practically transparent for IR radiation, it is virtually not heated; thus, the convective component is minimal. The main advantages of heating with IR lamps are as follows: high rate, low lag effect, ability to effectively change the temperature and time profile of heating, and the relative simplicity of the equipment.

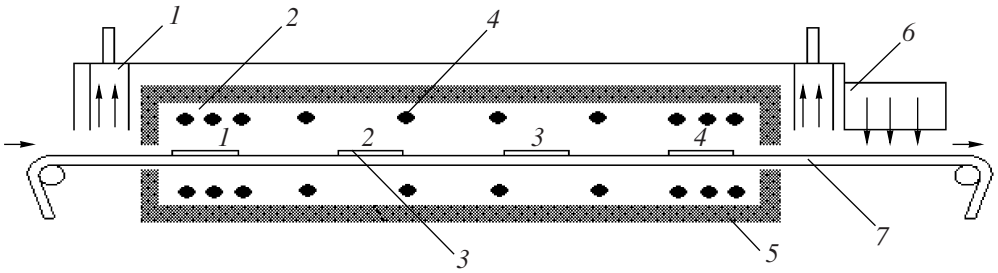

Fig. 1. Installation for IR heating with lamp radiators: (*1*) exhaust ventilation, (*2*) array of IR lamps, (*3*) board, (*4*) IR lamp, (*5*) reflector, (*6*) cooling unit, (*7*) conveyor.

The composition of the gas medium in the zone of IR soldering also influences its quality. Most often, IR installations work in the conditions of air media, but the presence of oxygen in the zone of soldering is not always desirable because the solder oxidation and destruction of organic materials occur. Therefore, in an air medium, the duration of the heating cycle is limited and should not exceed 100–150 s. The usage of an inert medium is promising (nitrogen with a small oxygen content or a hydrogen and nitrogen mixture). This improves the soldering quality because the solder oxidation is avoided, the flux activity increases, and the amount of residual ionic impurities on the boards decreases [3].

Three various configurations of installations are used in the technology of IR soldering that differ by the radiator type, including lamp, panel, and combined radiators [4]. Radiators of the first type contain several heating zones in which a set of tubular IR lamps are placed above and below the transporter where the boards to be mounted are located (Fig. 1). A great number of lamps enclosed in reflectors are located in the reflow zone, which allows for the production of a greater density of IR radiation. In the zone of preheating, the lamps are located far apart; this provides a smooth heating regime and temperature leveling of components. To eliminate the volatile compounds that are formed during soldering, a system of exhaust ventilation is used at the entrance and at the exit of the heating zone. A system for the forced cooling of boards is placed at the exit.

Installations with a panel IR heating in the form of ceramic panels of various power have the similar configuration; this allows one to form the necessary temperature and temporal profile, but with less flexibility. The configuration of a panel IR heater includes three layers. The face side is made of glass, ceramics, or metal and can function as a secondary radiator or a transparent window dependent on the used material. The second layer, or the primary heater, is made as a foil or a spiral of resistive material. The third layer, made of refractory ceramics, serves as isolation.

Panel radiators (Panel IR Systems) have become widely adopted operating in a middle and far radiation range of 3–10 μm, which represent large-sized heated ceramic panels that function at temperatures of 200–450°C [5]. These installations contain chambers with air or an inert gas; therefore, 60% of the heat energy is supplied to the heated object due to convection and 40% due to middle- or far-IR radiation. A small temperature difference between the radiator and the object allows one to perform the heating in an equilibrium regime, but advantages such as flexibility to control the regimes and low lag disappear.

In panel installations, the heating is produced due to both radiation and convection because IR radiation in the range of 5–8 μm is absorbed well by air. Installations of this type may contain several preheating zones where heaters are located at one or two sides of the transporter; this increases the transporter speed. Panel heaters produce more uniform heating of boards; moreover, radiation in the middle and far IR ranges is not sensitive to the color of the heated objects (at the temperature below 600°C). These heaters are less sensitive to the loading of the heating zone. The disadvantage of such installations is the lag effect with respect to the changes in regimes and profile of the heating zone, since each panel has a nonuniform temperature field over the surface area. In particular, panels with a metal face side have a lower temperature at the edges, while the panels with a transparent for IR radiation face surface have a greater temperature in the edge zone.

Combined systems, in which panel and lamp IR heaters form the necessary number of heating zones, enable great flexibility and possibility to use the advantages of lamp and panel heating. Preheating of the object is performed in the first and second zones using panel heaters that provide a uniform heating and specified temperature. Melting of the solder cream occurs in the third zone using quartz IR lamps, then the object is cooled in the fourth zone. The printed circuit boards are carried through the installation by a band conveyor. Installations are equipped with a built-in microprocessor system for a programmed control over the heating regimes of the boards and over all systems; the results are shown at the display.

Raduga IR installations intended for the reflow of solder creams at the assembly of boards using surface-mounted components allow one to perform soldering from both one side or from two sides of a printed circuit

board simultaneously. The installations consist of °C and a control panel. The installation design envisages a hand feed of printed boards. A temperature sensor that regulated TRM-10, along with a microprocessor control, allows for the accuracy of temperature stabilization. The temperature values on the surface of heaters are measured with a KhK thermocouple and are used by the input parameters of the control system. The temporal interval of soldering is specified by a digital MTTs 3501 timer. A temperature sensor IT 2511 controls the temperature regime of the heater in time.

A Raduga-21 conveyor installation for IR soldering consists of a five-zone heating chamber with regulated in the zones soldering temperature of IR heaters, a conveyor with a regulated speed for feeding printed boards with installed components to a heating chamber, a control panel, loading and unloading units, and electric equipment. The installation (conveyor width of 400 mm and the length of heating chamber of 1100 mm) provides a uniform heating of the board (width of 350 mm ± 2°C) in the direction perpendicular to the direction of motion for the conveyor speed for 0.015–2 m/min.

In installations for IR soldering, which contain a lower heater placed under the board intended to preheat it to a temperature of 100°C and an upper heater with a system focusing the heat radiation with the aim to heat components to be mounted to the reflow temperature of the soldering paste in the range of 220–260°C, optimization of temperature profiles is necessary (Fig. 2). Such technological parameters are also optimized as the heating rate in the working zone, dependent on the power of the heaters and their distance from the board, intensity and locality of heating. As an example of soldered articles, printed circuit boards may be named where KhK microthermocouples are fixed in metal-coated holes connected with digital temperature sensors or the boards with mounted SMD, such as chip resistors, diodes, stabilitrons, capacitors, microcircuits.

The heating rate of the upper 500-W heater with a reflector amounts to 3–5°C/s, while that of the upper and lower 500-W heater is equal to up to 10°C/s. The application of a protective mask increases the heating rate to 15°C/s due to reflection and increases the degree of the localization of heating. A further increase in the heating rate is possible due to the improvement of parabolic reflectors and the increase in their reflectivity. The rate of the temperature increase in the soldering zone decreases by a factor of 2 for the upper heater (Fig. 3) and by a factor of 3 for the lower heater (Fig. 4) when the distance from the IR heater to the board increases.

The uniformity of the zone of the thermal field during the heating of the upper and lower IR heaters was investigated. The central isothermal zone with a heating rate greater than 5°C/s has a circular shape and the consequent zones are oval in shape due to the rectangular shape of the reflector (Fig. 5a). In Fig. 5b, the zones of the thermal field of an IR heater with a rectangular 4 × 4 mm mask are shown. The isotherms have a rectangular shape with a side of 6 mm for $V > 3$°C/s, 12 mm for $V = 2.2$ and 18 mm for $V < 1$°C/s. The application of reflecting screens of various shapes increases the locality of heating. The greatest rate of heating (15°C/s) is

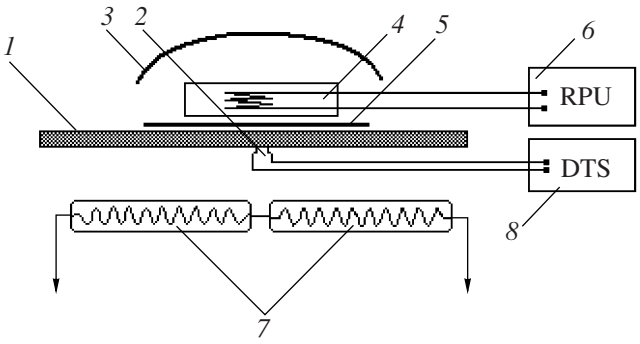

Fig. 2. Scheme for the optimization of profiles of IR heating: (*1*) board, (*2*) thermocouple, (*3*) reflector, (*4*) upper heater, (*5*) mask, (*6*) regulated power unit, (*7*) lower IR heater, (*8*) digital temperature sensor.

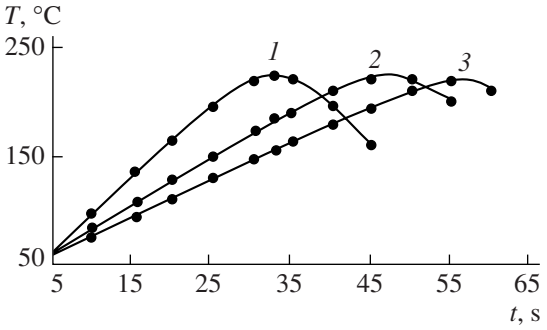

Fig. 3. Temperature dependences in the heating zone of the upper IR radiator; distance to the board, mm: (*1*) 15, (*2*) 25, (*3*) 35.

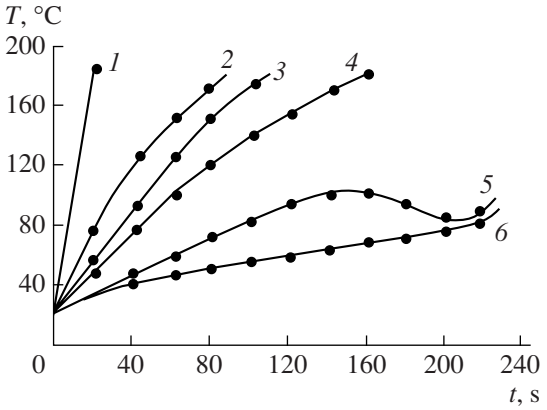

Fig. 4. Temperature dependences in the heating zone of the lower IR radiator; distance to the board, mm: (*1*) 10, (*2*) 20, (*3*) 30, (*4*) 40, (*5*) 50, (*6*) 60.

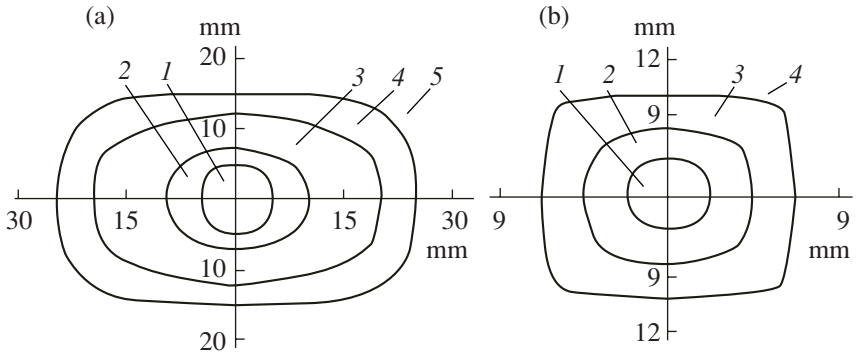

Fig. 5. Zones of the heat field V of the upper heater, °C/s. (a) (*1*) >5; (*2*) = 5; (*3*) = 3.8; (*4*) = 3.3; (*5*) <2.2; (b) (*1*) >4; (*2*) = 2.2; (*3*) = 1.1; (*4*) <0.5.

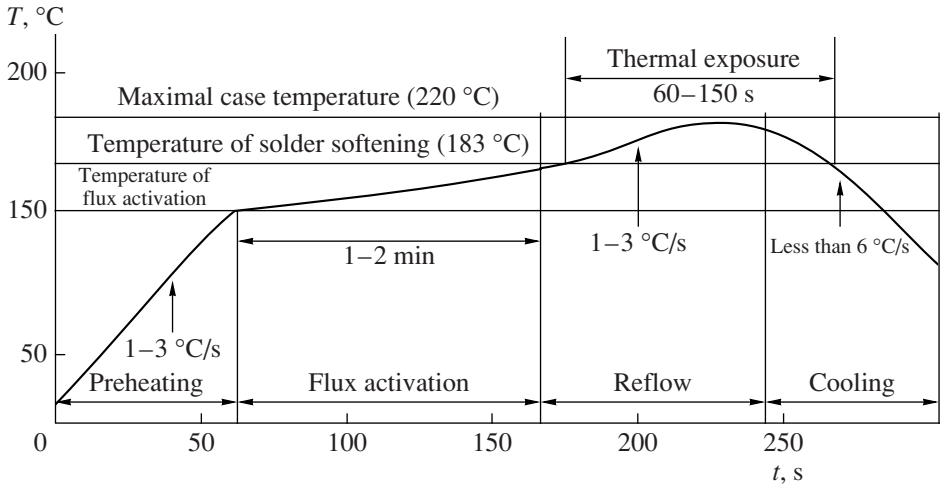

Fig. 6. Optimal temperature profile of soldering by IR heating for tin-leaded solders.

reached by decreasing the distance from the board to the upper IR heater. Application of a high-quality reflector allows for a decrease in the energy assumption by a factor of 2 and a change in the water cooling by forced air cooling at the same heating intensity.

The increase in the locality of IR heating due to a light-reflecting mask does not exert a substantial influence on the rate of temperature growth; as a whole, only the board heating decreases. The optimal regimes for IR soldering are as follows: preheating of the board by the lower heater to 90–110°C at a rate of 6–8°C/s, heating by the upper and lower heaters to the soldering temperature at a rate of 10–14°C/s. When it is necessary to localize the heating, a light-reflecting mask is used for thermosensitive components.

Regimes of soldering by reflow of solder creams are defined by the temperature profile that is optimized for IR furnaces (Fig. 6). The stage of preheating lowers the thermal shock on electronic components and printed circuit boards. At the rate of heating less than 1–3°C/s, the solvent evaporation from the solder cream occurs. A high rate of heating leads to a premature solvent evaporation and a number of defects, including damage to the components due to thermal shock, sputtering of solder drops, and the appearance of cross connections. The difference between the temperature of preheating and that of reflow should not exceed 100°C.

The stabilization stage activates the flux component and eliminates the excess of moisture from the solder cream. The temperature increase at this stage occurs at a rate of 0.6°C/s for heating of all components on the board to the same temperature. At the stage of the flux activation (60–120 s), the elimination of the oxide film from the soldered surfaces occurs. For shorter time intervals, defects of the cold-soldering type can form. At the stage of reflow the temperature increases to melting of the solder cream and a solder joint forms. To form a reliable solder joint, the maximal soldering temperature should exceed the melting temperature of the solder cream by 30–40°C. To prevent such defects as cold soldering or cross connections, the temperature of cases of electronic components should be kept greater than the solder melting temperature for 10–30 s. The rate of heating from the moment when the board

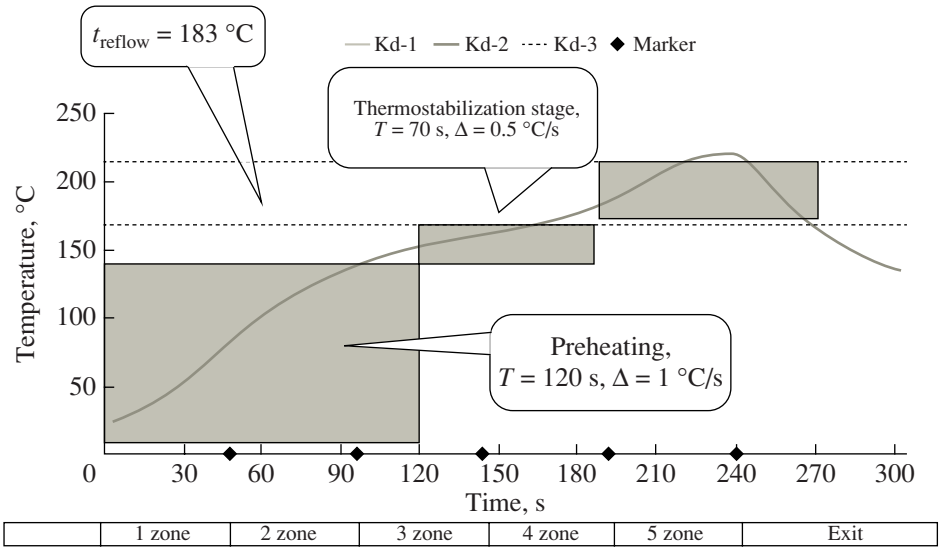

Fig. 7. Temperature profile of IR heating in the Raduga-21 installation.

reaches the solder melting point to the moment when it is maximal should not exceed 1–3°C/s.

Fast cooling decreases the formation of intermetallic compounds; however, thermal stresses appear, which leads to the damage of components at too high a rate of cooling. The cooling rate of a board should not exceed 6°C/s. The final choice of regimes is made taking into account the design of the printed circuit board, the type and dimensions of components, the number of components on the board, peculiarities of the equipment, results of test solderings, and the type of solder cream.

To measure the temperature profile of the IR installation for group soldering, a digital three-channel TERMOSKOP TA–570m thermometer was used that enables one to draw thermoplots in a real time scale on a computer display with data transfer through an RS-232C communication channel with a simultaneous indication of measured values on a built-in display. Miniature, high-precision plug-in thermoresistors, as in the DIN EN60751 standard, which, unlike thermocouples, may be connected without taking into account their polarity, were used as temperature sensors. This removes the problem of matching thermocouples of different types, and an additional cold end is not necessary. Thermocouples mounted on a flat surface have a point contact; unlike this, however, thermoresistors that have a rectangular shape provide a good heat contact over the whole surface and, therefore, more accurately represent the temperature of elements. The device has a range of temperature measurement of up to +500°C and a resolution of 1°C in the autonomous regime and 0.1°C working with computer. The basic error of measurements of the device in a temperature range to 350 ± 2°C; periodicity of measurements in the autonomous regime is 1.5 s.

Analysis of the thermoprofile of soldering has shown that the full duration of the process amounts to 240 s (Fig. 7). The stage of preheating for 120 s with the increase in the temperature gradient of 1°C/s provides for the protection of electronic components against thermal shock. The stage of thermostabilization for 70 s at the temperature gradient of 0.5°C/s provides a uniform heating of all components on the board; this prevents occurrences such as cold-soldering and tombstone defects. A board with components passes through the reflow stage for 80 s. The same values of the peak temperature equal to 225°C were reached on all soldered components. The exposure at the peak temperature for 15 s guarantees the quality of all soldered joints.

The stage of cooling has a gradient of temperature lowering of 2°C/s; this is admissible for solders on the basis of tin–lead alloys. However, for lead-free solders with tin contents of up to 96%, it is necessary to perform a forced cooling of the board with a gradient of 4°C/s so as to prevent the formation of intermetallic compounds and the growth of tin whiskers. Analysis of reasons that cause defects of the surface mounting shows that nonoptimal temperature profile of soldering is one of the causes of their formation.

Application of IR soldering is a novel, promising direction for surface mounting technology (SMT) that enables to decrease expenses for employment of equipment and simultaneously improve the quality of soldered joints. One of the advantages of IR heating is its simple equipment, which is much more efficient and expedient for the surface mounting of components.

REFERENCES

1. Zvorykin, D.B., Prokhorov, Yu.I., *Primenenie luchistogo infrakrasnogo nagreva v elektronnoi promyshlennosti*

(Application of Radiant Infrared Heating in Electronic Industry), Moscow: Energiya, 1980.

2. Henderson, I., Browne, V., IR Plus Hot Platen Heating Offers Another Option for Reflow Soldering, *EPP*, 1989, vol. 29, no. 9, pp. 78–80.
3. Wassink, K.R.J., Soldering in Electronics, *Electrochem. Publ.*, Ayr (Scotland), 1989.
4. Kundas, S.P., Dostanko, A.P., Anufriev, L.P., et al., *Tekhnologiya poverkhnostnogo montazha* (Technology of Surface Mounting), Minsk: Armita, 2000.
5. Manko, H.H., *Solders and Soldering: Materials, Design, Production and Analysis for Reliable Bonding,* N.Y., 2000.
6. Lanin, V.L., Efficiency of Heating by Means of Concentrated Flows of Energy in the Soldering Process in Electronics, *Elektron. Obrab. Mater.*, 2002, no. 2, pp. 17–20.
7. Lanin, V.L., Kapralov, V.V., Infrared Heating in the Surface Mounting Technology, *Problemy proektirovaniya i proizvodstva radioelektronnykh sredstv: Materialy III Mezhdunarodnoi nauchno-tekhnich. konf.* (Problems of Development and Production of Radioelectronic Means: Proc. III Int. Sci. and Techn. Conf.), vol. 1, Novopolotsk, 2004, pp. 81–84.
8. Lanin, V.L., Khil'kevich, A.N., Double Sided Surface Mounting of Electronic Modules, *Izvestiya Belorusskoi Inzhenernoi Akademii*, 2003, no. 1(15)/4, pp. 145–147.

ISSN 1068-3755, Surface Engineering and Applied Electrochemistry, 2007, Vol. 43, No. 5, pp. 387–390. © Allerton Press, Inc., 2007.
Original Russian Text © H.H. Gadzhieva, S.A. Faradzhev, 2007, published in Elektronnaya Obrabotka Materialov, 2007, No. 5, pp. 97–101.

OPERATING EXPERIENCE

Structural Changes in Peganum Harmala Caused by γ Radiation

H. H. Gadzhieva and S. A. Faradzhev

Institute of Radiation Problems, Azerbaijan National Academy of Sciences, ul. F. Agaeva 9, AZ 1143 Baku, Azerbaijan

Received January 19, 2007

Abstract—The structural changes of Peganum harmala connected to γ irradiation have been studied by means of radiothermoluminescence (RTL) and IR-spectroscopy methods. It is established that in small dose ($0.5 < D_\gamma \leq 25$ kGr) regions, structural changes of alkaloids do not take place; however, at doses of $25 < D_\gamma \leq 50$ kGr, there is partial decay in the region. The possibility of applying a small dose region for the radiation sterilization of Peganum harmala has been shown. The dose boundaries of radiation sterilization have been determined.

DOI: 10.3103/S1068375507050146

The herb Peganum harmala *L*, which, in addition to folk medicine, is widely used for the medical treatment of more serious diseases, including cancer [1–5]. The efficiency of harmala usage for different purposes conditions on the presence of β-carboline alkaloids-harmine, harmaline, and their derivatives [6–10] in the harmala composition. In works [4, 5, 10, 11], it was shown that β-carboline alkaloids are bioactive substances and bias cytotoxic effects to cancer cells and spasmolitic effects to the respiratory tract in bronchial asthma. The dynamics of alkaloid accumulation and the stability of their content in the Peganum harmala composition under long-term storage depend greatly on external factors, such as temperature, electromagnetic fields, radiation background, etc. [11, 12]. The low-temperature treatment (~80 K) of harmala by a microwave electromagnetic SHF field (~600–1000 MHz) permits the improvement of its gustatory quality and spasmolitic effects [12–14]. However, until now, it had not been investigated how γ radiation influences Peganum harmala composition and structure or how pharmacological properties change due to it.

Thus, in the represented work, the structural changes in Peganum harmala caused by γ radiation by means of radiothermoluminescence (RTL) and IR-spectroscopy methods have been investigated.

EXPERIMENTAL

The fine-dyspersated powder-type samples of Peganum harmala growing in Apsheron (Azerbaijan), leaves, seeds, and caulis with granule sizes of ~80 μm characterized in [1, 15] were used for the investigation. In order to obtain the radiothermoluminescence (RTL) spectra, we used the tablets made of these powders according to the procedure described in [15]. The RTL curves were recorded with thermoluminograph TLG-69M in a temperature range of 80–500 K under a sample heating rate of 0.08 K/s. For RTL analysis, the samples were irradiated at a temperature of 77 K [12].

The IR-transmission spectra of the thin films with thickness ~1 μm were recorded with Specord 71JR (Carl Zeiss) spectrophotometer in the frequencies domain of 2000–650 cm^{-1} at room temperature. The thin films were manufactured by means of monodispersed powder-type harmala mixture pressing in KBr solid mold at a ratio of 1 : 1000 and pressure of 600 kg/cm^2 with preliminary pumping under 1.33 Pa with the help of a special press mold intended for optical investigations [16].

The optical spectra of mirror reflections of Peganum harmala leaves were measured in the range of 185–900 nm with the help of a Specord UV VIS (Carl Zeiss) spectrophotometer at 300 K. For the chosen wavelengths (λ=500, 750, and 830 nm), in the visible spectrum free of harmala's self-absorption bands, the reflectance *R* (albedo) were determined. Assuming that Gur'evich–Kubelka–Munk's law [17] is true and considering surface roughness, the optical densities for λ=500, 750, and 830 nm were calculated using the formula $D = \log R/R_0$, where R_0 and R are the samples' reflectances before and after γ radiation. The values of *D* represented in the work are arithmetic mean values obtained in three parallel, independent experiments.

The samples were irradiated by γ quanta ^{60}Co with dose power dD_γ/dt = 1.03 Gr/s at temperatures of 77 and 300 K for RTL and for spectrum measurements, respectively. The absorbed dose determined with a ferrosulphate dosimeter was varied within the limits D_γ = 0.5–50 KGr.

DISCUSSION

Peganum harmala irradiation by γ quanta at a temperature of 77 K causes intensive RTL pick occurrence under 175 K and weak pick occurrence under 320 and 445 K (Fig. 1, curve *1*). Low-temperature wide pick (semi-width $T_{1/2} \approx 110$ K) at 175 K with energy of activation $E_a \approx 0.07$–0.10 eV can be connected with either the presence of alkaloids in the Peganum harmala or

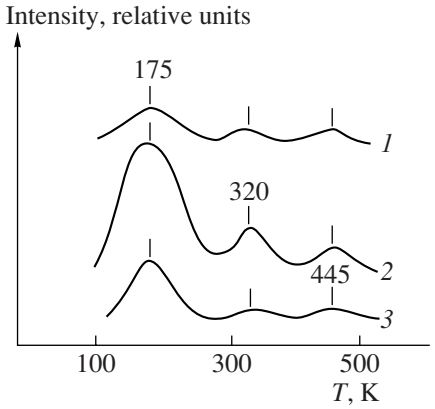

Fig. 1. Curves of the thermolightening of γ-radiated harmala at doses D_γ=1 (*1*), 10 (*2*) and 50 kGr (*3*).

with the presence of molecular water in the steric environment of alkaloids (the structures of several types of alkaloids of Peganum harmala are represented in Fig. 2). When β-carbolines extracted from Oxalis tuleroza L., the roots are radiated by ultraviolet light and the blue-purple fluorescence can be seen visually [18]. Moreover, it is shown that the main fluorescent components are harmine (7–methoxy–1–methyl–β–carboline) and harmaline (3,4 hydroharmine). The hydroxyl (OH) groups and condensed water oxygen represented in γ-irradiated biological objects also initiate the thermoluminescent phenomenon at 160–180 K [19]. The origin and nature of thermolighting picks under 320 and 445 K have not been clarified yet.

A low-temperature wide-RTL pick with a maximum at 175 K has several peculiarities, insofar as its spectrum parameters (intensity and semi-width) depend on the γ-radiation dose (Fig. 1, curves *2* and *3*). With γ-radiation-dose growth from 0.5 up to 25 kGr ($0.5 < D_\gamma \le 25$ kGr), the intensity of the thermolighting pick increases approximately in order. A further increase of the dose up to 50 kGr ($25 < D_\gamma \le 50$ kGr) is accompanied by a monotonic decrease of the given pick intensity and its narrowing by a factor of ~2 (the semi-width value drops by 60 K). Furthermore, the form of the

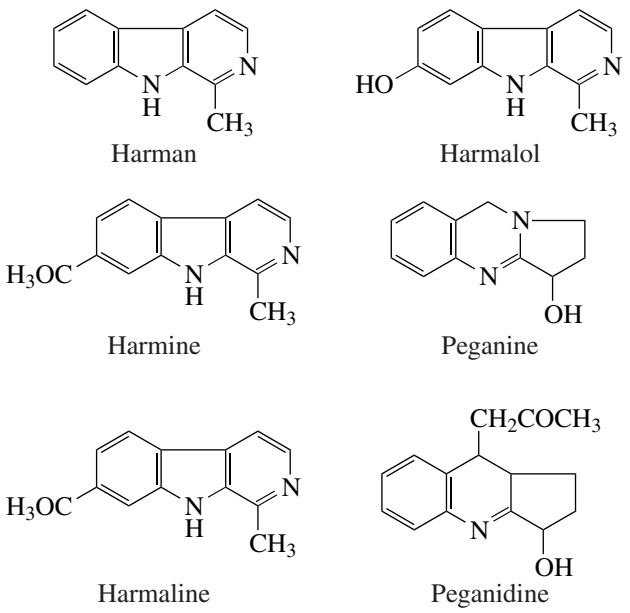

Fig. 2. The structures of several types of Peganum harmala alkaloids.

band remains stable and close to that of the Gauss. The dose dependences of the integral intensity of 1 RTL pick at 175 K and its semi-width $T_{1/2}$ in the form of the diagram are represented in Fig. 3. Using these for analysis, it is possible to say that in the frames of relatively small doses ($0.5 < D_\gamma \le 25$ kGr), weak structural changes connected mainly with the conformation transformations of alkaloids take place. For doses ($25 < D_\gamma \le 50$ kGr), strong structural changes occur until partial decay.

The structural changes in γ-irradiated Peganum harmala samples were also controlled according to their IR absorption spectra. Figure 4 depicts the IR absorption spectra of the initial (curve *1*) and the irradiated-by-γ quanta under different doses (curves *2–3*) of Perganum harmala in a frequency domain of 1800–1200 cm^{-1}. This analytical part of the spectrum is characterized by a collection of neighboring absorption bands related

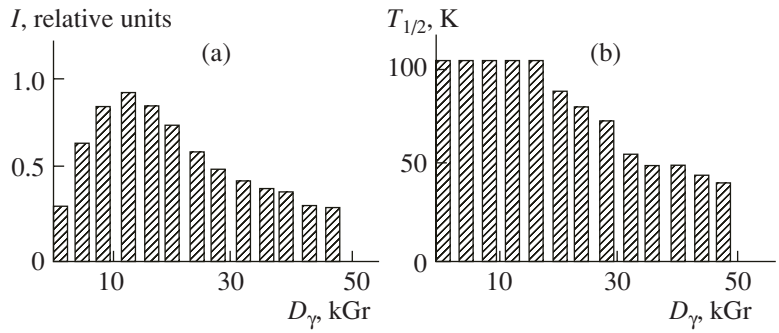

Fig. 3. The dependence of summary integral intensity *I* of RTL pick at 175 K (a) and its semi-width $T_{1/2}$ (b) via γ-radiation dose.

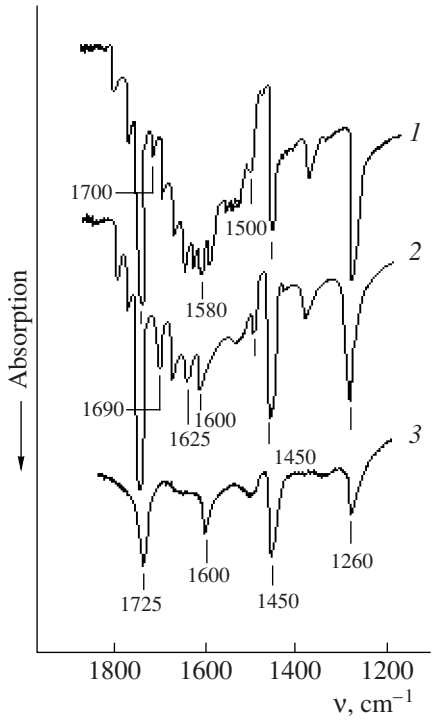

Fig. 4. IR-absorption spectra of initial (*1*) and γ-radiated harmala at D_γ (*2*) and 50 kGr (*3*).

mainly to different types of alkaloids belonging to the harmala composition. This fact is verified by the presence of carbonyl-containing groups C=O (ν ~ 1750–1700 cm^{-1}) and C=C and the presence of nitrogen-containing groups N=C (ν ~ 1690–1500 cm^{-1}) in the aromatic ring; the bands at 1600, 1580 (conjugate rings), 1500, and 1450 cm^{-1} are typical for the ring itself. Considering the complicated chemical composition and reference information about the IR spectra of individual alkaloids of harmala, the absorption bands with frequencies 1725, 1700, 1690, and 1625 cm^{-1} were referred to as harmine, peganidine, harmaline, and peranine, respectively (Fig. 4, curve *1*) [9, 20–23].

When the samples of Peganum harmala are irradiated, the IR spectra are transformed; in the area of relatively small doses ($0.5 < D_\gamma \le 25$ kGr), the intensities of the alkaloids' absorption bands are redistributed; this process is accompanied by the arising of absorption bands of harmine and harmaline (1725 and 1690 cm^{-1}) and, vice versa, by peganine and pegadine (1700 and 1625 cm^{-1}) absorption-band intensities drop (Fig. 4, curves *2–3*). Further radiation dose increasing from 25 up to 50 kGr causes intensity decreasing of all absorption bands. The observed peculiarity of harmine, harmaline, and their derivatives in the IR spectrum of γ-irradiated Peganum harmala in the analytical area of alkaloids can be explained by a structural conformational alteration causing the harmine and harmaline concentration (quantity) growth (the area of relatively

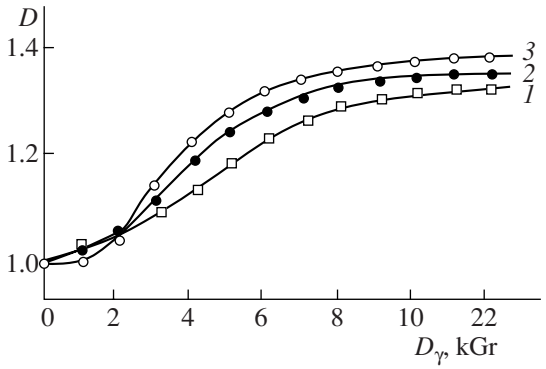

Fig. 5. Dose dependences of optical densities of wave length λ = 500(*1*), 750 (*2*), and 830 nm(*3*) on the mirror-reflectance spectra of harmala leaves.

small doses ($0.5 < D_\gamma \le 25$ kGr) and their partial decay (area $25 < D_\gamma \le 50$ kGr).

Thus, investigations of RTL and IR have revealed that no significant structural changes occur in areas of relatively small doses ($0.5 < D_\gamma \le 25$ kGr), as well as that it is possible to use them in the radiation sterilization of Peganum harmala.

If it is necessary to determine the optimal dose boundaries for radiation sterilization, the mirror-reflection spectra of initial and γ-irradiated leaves of Peganum harmala were measured in visible area (λ ~ 400–950 nm). Figure 5 depicts how optical densities of three chosen wavelengths (λ = 500, 750, and 830 nm) depend on the γ-irradiation dose. As is possible to see from the drawing, after a certain dose value, at $D_\gamma \ge 2.5$ kGr, optical densities are growing for three λ values due to the fact that the reflectance of harmala leaves increases due to surface radiation cleaning from contaminations caused by microorganisms [24]. At dose $D_\gamma \ge 7.5$ kGr, saturation has taken place. The doses corresponding to the beginning and end of the linear area, i.e., 2.5 and 7.5 kGr, are chosen as the top and bottom boundaries of radiation sterilization.

CONCLUSIONS

Using the kinetic peculiarities of RTL pick at 175 K with an energy of activation of $E_a = 0.07–0.1$ eV and IR-spectrum changes in the alkaloid analytical absorption area (ν = 2000–1000 cm^{-1}) as a dependence on the γ-radiation dose ($D_\gamma = 0.5–50$ kGr), it was clarified that for the area of relatively small doses ($0.5 < D_\gamma \le 25$ kGr), there are no sufficient structural changes in Peganum harmala and, in the area $25 < D_\gamma \le 50$ kGr, there are sufficient structural changes to the extent of the alkaloids' decay. It is shown that it is possible to use the area of relatively small doses ($0.5 < D_\gamma \le 25$ kGr) for radiation sterilization. Using a dose dependence of the mirror reflectance of Peganum harmala leaves in the visual spectrum (λ = 400–900 nm), the top and bottom boundaries were obtained.

ACKNOWLEDGMENTS

The authors would like to thank F. M. Makhmudzade for help during the experiments.

REFERENCES

1. Damirov, I.L., Primenko, L.N., Shukyurov, D.Z., and Kerimov, Yu.B., *Lekarstvennye rasteniya Azerbaidzhana* (Herbs of Azerbaijan), Baku: Maarif, 1983.
2. Preobrajenskii, V., *Vse o lekarstvennykh rasteniyakh* (All About Herbs), Donetsk: PKF "BAO", 2001.
3. McKenna, A.J. and Towers, A.J.T., *Phytochemistry*, 1981, no. 20, pp. 1001–1004.
4. Perez, J.M. Martin, Labrador, V., Fernandez Freire P. et al., *J. Appl. Toxicol.*, 2004, vol. 24(3), pp. 197–201.
5. Sobhani, A.M., Ebrahimi, S.A., and Mahmouidan, M. *J. Pharm. Sci.*, 2002, vol. 5(l), pp. 19–23.
6. Faskhutdinov, M.F., Telezhenetskaya, M.V, Levkovich, M.G., and Abdullayev, N.D., *Chem. Nat. Comp.*, 2000, vol. 36, no 6, pp. 602–605.
7. Koretskaya, N.I., *J. Org. Chem.*, 1957, vol. 27, pp. 3361–3364.
8. Harsh Pat Bais, Sang–Wuok Park, Frank R. Stermits, et al., *Phytochemistry*, 2002, vol. 61, pp. 539–543.
9. Yunusov S.Yu., *Alkaloidy. Spravochnik* (Alkaloids, Handbook), Tashkent: Fan, 1974.
10. Chuen-Chao Shi, Jyh-Fei Liao, Chieh-Fu Chen, Exudation of Fluorescent β-Carbolines from Oxalis Tuberose L. Roots, *Pharm. Toxic.*, 2001, vol. 89, p. 259.
11. Gadzhieva, N.N., Faradzhev, S.A., Magerramov, A.M., Gamidov, E.R., and Dzhafarov, E.S., Azerb. Patent A20040259 A61K35/78
12. Faradzhev, S.A., Magerramov, A.M., Gadzhieva, N.N., and Dzhafarov, E.S., Radiothermoluminescence of Peganum Harmala Growing at Apsheron (Azerbaijan) Irradiated by SHF *Proc. 4th Bah Conf. on Radiation Chemistry*, Moscow, 2005, p. 124.
13. Faradzhev, S.A., Magerramov, A.M., Gadzhieva, N.N., and Dzhafarov, E.S., Low-Temperature SHF Treatment of Peganum Harmala from Apsheron (Azerbaijan), *Abstracts 3rd International Conf. on Ecological Chemistry*, 2005, Chisinau, Moldova, pp. 435–436.
14. Faradzhev, S.A., Magerramov, A.M., Gadzhieva, N.N., and Dzhafarov, E.S., Ecotechnologic Method of Action of Low-Temperature SHF Treatment on Structure and Taste Quality of Apsheron Harmala Type Peganum Harmala, *Proc. 8th Baku Int. Congress Energy, Ecology, Economy*, Baku, 2005, pp. 184–187.
15. Gadzhieva, N.N., Magerramov, A.M., Faradzhev, S.A., and Eyubova, N.A., Peculiarities of Combustion of Peganum Harmala, *J. Znanie, Prosveshchenie Azerbaidzhanskogo obshchestva, ser. khim., biol., med.*, 2004, no. 6(22), pp. 48–55.
16. Gadzhieva, N.N., Samedov, E.A., Abdullaeva, Kh.I., Investigation of Adsorption and Radiolysis of Methane on the BeO Surface by IR Spectroscopy, *J. Appl. Spectrosc.*, 1995, vol. 62, no. 6, pp. 44–48.
17. Rozenberg, G.V., Sakhnovsky, M.Yu., Guminevsky, S.G., Methods of Absorption Spectroscopy of Weakly Absorbing Light-Scattering Substances, *Opt. Spectrosc.*, 1967, vol. 23, no. 5, pp. 797–806.
18. Kuleshov, V.I., Nikol'sky, V.G., *Radiotermoluminestsentsiya polimerov* (Radiothermoluminescence of Polymers), Moscow: Nauka, 1991, pp. 223.
19. Allen, I.R.F. and Holmstedt, B.R., The Simple beta-Carboline Alkaloids, *Phytochemistry*, 1980, vol. 19, pp 573–582.
20. Ghada Mandi Juma'a, Peganum Harmala Production, *Eur. J. Sci. Res.*, 2005, vol. 11, no. 1, pp. 6–12.
21. Vigar Uddin Ahmad, Application of Spectroscopic Methods in the Structure Elucidation of New Natural Products in Studies in Natural Products Chemistry, v. 5. Structure Elucidation (Part B), Atta-ur-Rakhman, Ed., Amsterdam: Elsevier Science Publisher, 1989, p. 197.
22. Alta-ur-Rahman and Vigar Uddin Ahmad, 13C-NMR of Natural Products, Plenum Publishing Corporation, USA, 1992, vol. 1, 2, p. 210.
23. Vigar Uddin Ahmad, Atta-ur-Rahman, Handbook of Natural Products Data, Amsterdam: Elsevier Science Publisher, 1994, vol. 2, p. 164.
24. Presentations "The Industrial Applications of Irradiation Technology". Supported by International Atomic Energy Agency (IAEA), 2003, Baku, Azerbaijan, pp. 23–32.

ISSN 1068-3755, Surface Engineering and Applied Electrochemistry, 2007, Vol. 43, No. 5, pp. 391–394. © Allerton Press, Inc., 2007.
Original Russian Text © M.B. Muradov, M.A. Nuriev, G.M. Eivazova, 2007, published in Elektronnaya Obrabotka Materialov, 2007, No. 5, pp. 102–105.

OPERATING EXPERIENCE

Electric Conductivity of Nanocompounds Based on Polymer and Chalcogenide Semiconductors CdS, Cu_2S

M. B. Muradov[a], M. A. Nuriev[b], and G. M. Eivazova[a]

[a] *Baku State University, ul. Z. Khalilova 23, Baku, AZ 1073 Azerbaijan*

[b] *Institute of Radiation Problems of Academy of Sciences of Azerbaijan, ul. F. Agaeva 9, Baku, AZ 1143 Azerbaijan*

Received February 12, 2007

Abstract—In this work, the temperature dependence of the specific surface resistances of composites on bases of gelatin with different contents of Cu_2S and CdS chalcogenide semiconductor nanoparticles is investigated. It is shown that nanocomposites have a posistor effect. It is found that the posistor effect is the result of the influence of intermolecular interactions at the polymer–nanoparticle phase interface and that the electrotransfer of charges in such systems is caused by tunneling through polymer layer between nanoparticles before the percolation threshold and flow theory after the percolation threshold.

DOI: 10.3103/S1068375507050158

In recent years, much attention has been given to nanoheterogenous composition materials in which metal and semiconductor nanoparticles are in a dielectric matrix. Of special interest are composites containing metal and semiconductor nanoparticles distributed in polymeric matrices [1, 2]. Nanoheterogenous film structures consisting of polymeric matrices with dispersed nanosized particles, the distance between them being the same, have unusual photo- and gas-sensitive properties that are unique to fine-dispersed structures [3, 4]. In such systems, a high response of electric conductivity as a result of the adsorption of various gases and vapors, even at room temperature, is observed.

Temperature dependencies of the surface resistivity of compounds based on food polymers, i.e., gelatins with different contents of the dispersed component and nanoparticles of chalcogenide semiconductors Cu_2S and CdS, are studied in the presented work.

EXPERIMENTAL

Water-swelling polymer (gelatin on glass substrate) was used to obtain compounds with nanoparticles Cu_2S and CdS.

Formation of compounds was performed in the following order: first the polymer film was enriched with Cu^{2+} or Cd^{2+} ions, then these films were processed in Na_2C aqueous solution and took the corresponding color, i.e., black for Cu_2S and orange for CdS. A multicycle treatment method was used to increase the content of nanoparticles [5, 6].

The medium size of the formed nanoparticles—15–20 nm for samples with 15 formation cycles and 50–70 nm with 30 formation cycles—was determined with the help of an ASM examination. Furthermore, the obtained nanocomposites were annealed at a temperature of 453 K for two hours. To measure surface resistance, two parallel conducting strips were applied to the film surface with the help of silver paste. A clamping electrode was used to gauge the bulk resistance. Measurements were carried out by a 6514-Keithley Instruments electrometric voltmeter (temperature rise with a constant rate of 2°/min).

RESULTS AND DISCUSSION

The temperature dependence of a gelatin/glass sample resistance is shown in Fig. 1. As is obvious from the figure, relationship $\rho(T)$ changes after annealing. If, in initial specimens, a growth in resistance is observed but, after annealing, the original resistance of the samples rises and the previous growth disappears. Specimen resistance decreases with an increase in temperature. The measured relationship $\rho(T)$ of the same specimens, preserved in air, after 24 hours is analogous to the starting samples. This appears to be connected with the sorption of moisture in the air.

In Fig. 2, the temperature dependence of the surface resistivity for gelatin/Cu_2S compounds is presented and, in Fig. 3, the same dependence is shown for gelatin/CdS compounds with different filler contents.

It is seen that the course of the curves for both compositions is similar. These curves have three inherent regions, including a) initial drop, b) resistance growth, and c) resistance reduction. We think that the initial decrease in resistance is connected through the desorption of moisture from the bulk and different occlusions and gases from the sample surface, causing the dimin-

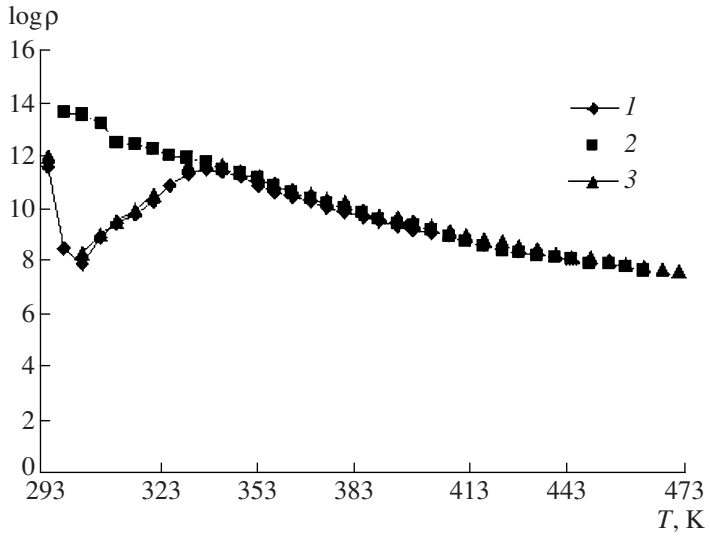

Fig. 1. Temperature dependence of specific surface resistance of the gelatin/glass system: (*1*) initial; (*2*) after thermal annealing; (*3*) the same sample measured after 24 hours.

ishing of the surface resistance. This suggestion is confirmed by the value of the temperature corresponding to the minimum value of the initial drop not changing with the increase of filler content.

A further temperature rise is followed by an increase in the nanocomposite resistance caused by gelatin purification and the desorption and widening of the volume as a result of the transition of the matrix structure from crystalline into amorphous. For these specimens, the temperature corresponding to the maximum value of resistance shifts towards high temperatures, therefore confirming the structural nature of the observed effect.

For all composites except gelatin/Cu_2S (30 cycles), the observed resistance growth with temperature increase may be considered to be the posistor effect in nanocomposites and is connected with nanoparticle dimensions. It is seen that, with an increase in the formation cycle number equivalent to the growth in the nanoparticle size, the inclination and resistance difference of this section change, thus confirming the change in the composite-resistance temperature coefficient (RTC). The largest value of this coefficient corresponds to gelatin/CdS nanocomposite with thirty cycles of formation. In our opinion, the increase in the formation

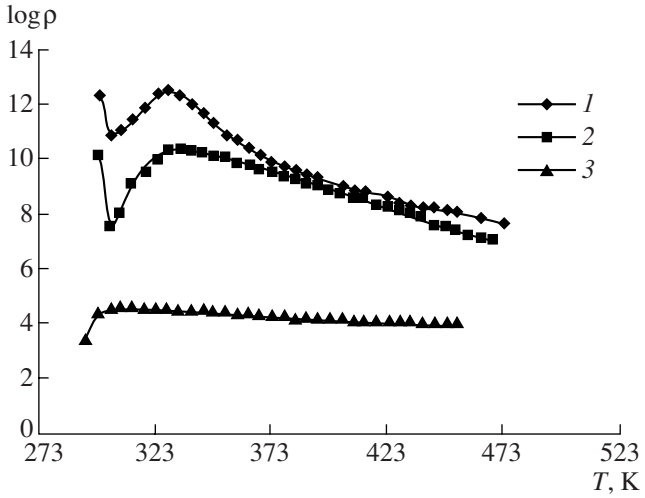

Fig. 2. Temperature dependence of the specific surface resistance of gelatin/Cu_2S nanocompositions with different cycles of formation: (*1*) 7; (*2*) 15; (*3*) 30.

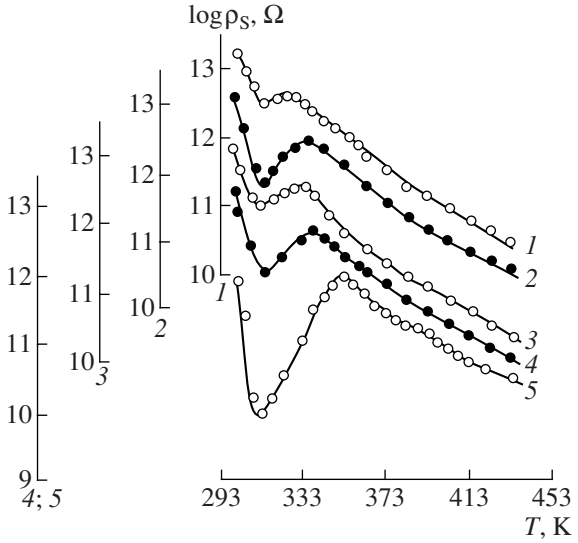

Fig. 3. Temperature dependence of the specific surface resistance of gelatin/CdS compositions with different cycles of formation: (*1*) 5; (*2*) 7; (*3*) 10; (*4*) 15; (*5*) 30.

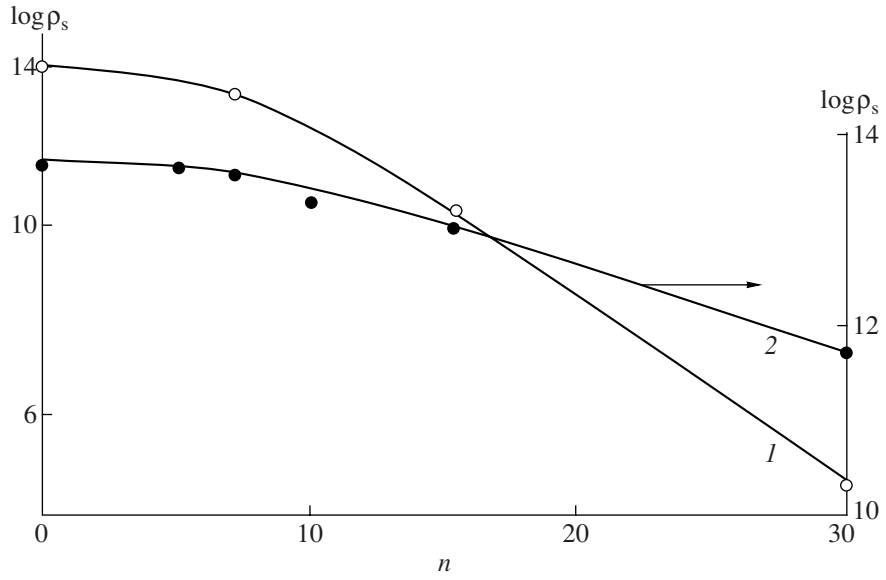

Fig. 4. Initial specific surface resistance ρ_s versus formation cycle number characteristic: (*1*) gelatin/Cu_2S; (*2*) gelatin/CdS.

cycle number results in the composite resistance growth up to the filler resistance value and, correspondingly, to the disappearance of the posistor effect, which was observed for the gelatin/Cu_2S nanocomposite (30 cycles). A further rise in temperature is followed by a regular reduction in the nanocomposite resistance.

In Fig. 4, the change in the initial surface resistivity value ρ_s is shown depending on the formation cycle number, i.e., it is shown to be circumstantially based on the content and size of nanoparticles.

It is seen that with an increase in the content or formation cycle number, the resistance of both composites reduces. This may be favored by a low concentration (0.4 M) of the Na_2S solution in which the specimen was held; the surface resistance of nanocomposites can reduce at the increase of cycle number. Tentative estimate of the depth of penetration of the layer enriched by Cu_2S particles shows that it is about 20–25% of the entire thickness [7]. Reduction of ρ_s for composites with Cu_2S nanoparticles is about 8–10 orders and for composites with CdS, it is about 1.5 orders. The lower limit of the resistance in the relationship $\rho_s = f(n)$ is defined by the value of the filler resistivity. This value for Cu_2S is several dozen kiloohms (10^3–10^4 Ohm) and, for CdS, it is several hundred megaohms (10^7–10^8 Ohm).

Comparison of these values and obtained experimental data in heterogenous systems allows for the use of the flow theory to elucidate the electric conduction mechanism. According to this theory, the current transfer process in compositional systems is connected with the generation of an infinite cluster of contacting electric conducting particles of the disperse phase. Such a conducting channel ensures the charge-carrier transfer in the bulk or on the surface of a composite.

CONCLUSIONS

In conclusion, it could be said that gelatin–chalcogenide nanocomposites of CuS and CdS semiconductors have a posistor effect. For gelatin/CuS composites, this effect is found in the temperature range of 303–333 K and for gelatin/CdS, it lies in the range of 313–353 K. The posistor effect is the result of intermolecular interactions at the polymer-nanoparticle phase interface, and electric transfer of charges in such systems is caused by tunneling through the polymer interlayer between the nanoparticles up to percolation threshold and by flow theory after the percolation threshold.

ACKNOWLEDGMENTS

This work has been carried out thanks to the financial support of UNTTs, grant No. 3486.

REFERENCES

1. Trakhtenberg, L.I., Gerasimov, G.N., Potapov, I.K., Rostovshchikova, T.N., Smirnov, V.V. and Zufman, V.Yu., Nanocompositional Metal-Polymer Films: Sensor, Catalytic, and Electrical Properties, *Vestn. Mosk. Univ., Ser. 2, Khim.*, 2001, vol. 42, no 5, pp. 325–331.
2. Volkov, A.V., Moskvina, M.A., Volkov, I.A., Volynskii, A.L. and Bakeev, N.F., Study, Structure, and Magnetic Properties of Polymer Nanocompositions Polyvinyl Alcohol—Iron Oxide, *Vysokomol. Soedin, Ser. A*, vol. 47, no 5, pp. 715–782.
3. Babkin, A.N. and Fedorov, M.I., H_2S Concentration Meter. *Sensor*, 2003, no 1, pp. 54–55.

4. Mal'tsev, E.I., Lypenko, D.A., Tolmachev, A.I., Slominskii, Yu.A., Shapiro, B.I., Brusentsova, M.A., Berendyaev, V.I., Sosnovyi, M.A., and Vannikov. A.V., Infrared Luminescence of Organic Nanocrystals in Polymer Composites, *Vysokomol. Soedin., Ser. A*, 2006, vol. 48, no 1, pp. 74–79.

5. Nicolau, V.F., Solution Deposition of Thin Solid Compound Films by Successful Ionic-Layer Adsorption and Reaction Process, *Appl. Surf. Sci.* 22/23, 1985, p. 1061.

6. Muradov, M.B., Nuriev, M.A., and Eivazova, G.M., Electric Conduction of Composites Based on Polymer Matrix and Copper Sulphide Nanoparticles, *Izv. Nats. Akad. Nauk Azerb., Ser. Fiz.-Mat. Tekhn., Fiz. Astron.*, XXV, 2007.

7. Volkov A.V., Moskvina, M.A., Karachentsev, I.V., Lebedeva, O.V., Volynskii, A.L., and Bakeev, N.F., Structure and Electric Conduction of Highly-Dispersed Compositions Polymer–CuS Obtained *in situ*, *Vysokomol. Soedin., Ser. A*, 1998, vol. 48, no 6, pp. 970–976.

ISSN 1068-3755, Surface Engineering and Applied Electrochemistry, 2007, Vol. 43, No. 5, pp. 395–397. © Allerton Press, Inc., 2007.
Original Russian Text © M.K. Bakhadyrkhanov, U. Sodikov, N.F. Zikrillaev, N. Norkulov, 2007, published in Elektronnaya Obrabotka Materialov, 2007, No. 5, pp. 106–108.

OPERATING EXPERIENCE

Elaboration of Physical Fundamentals of Nanosized Structures on the Basis of $S^{++}Mn^{--}$ and $Se^{++}Mn^{--}$ Molecule Formation in Silicon Lattice

M. K. Bakhadyrkhanov, U. Sodikov, N. F. Zikrillaev, and N. Norkulov

Tashkent State Technical University, ul. Universitetskaya 2, Tashkent, 70095 Republic of Uzbekistan

Received March 6, 2007

Abstract—One possible way to create nanosized structures on the basis of the formation of molecules ($S^{++}Mn^{--}$) and ($Se^{++}Mn^{--}$) among impurity atoms S, Se, Mn in the silicon lattice is described in the work. Relationships between the concentration of molecules ($S^{++}Mn^{--}$) and ($Se^{++}Mn^{--}$) and the concentration of impurity atoms are established.

DOI: 10.3103/S106837550705016X

At present, the technology permitting one to control the concentration, structure, and composition of nanosized structures on the basis of molecules is being worked out. The problem of the preparation of controlled nanosized structures in the body of semiconductive materials is of great scientific and practical interest in view of the purposeful control of fundamental parameters of materials and creation of new electron devices on their basis.

The formation of impurity atom molecules is the evolutionary beginning of nanosized crystals and clusters of impurity atoms in the lattice [1]. If the optimum thermodynamical conditions of the molecule formation of impurity atoms are established, it will be possible to control their distribution, concentration, and, lastly, nanosized objects in a crystal with different structures and dimensions in the lattice.

To study the impurity atom molecule formation in silicon, we have chosen manganese, selenium, and sulfur. Such impurities were selected because, in silicon, they act separately as donors and each of them generates several donor levels [2, 3]. As a consequence, donor–acceptor interactions between these impurity atoms are absent. Furthermore, the doping procedure of silicon by these impurity atoms is elaborated rather well and, finally, silicon doped by these impurities possesses unique properties [4, 6].

Doping of silicon by the impurity atoms Mn, S, and Se, as well as Mn–Se and Mn–S was carried out simultaneously from the gaseous phase, partial pressure of these impurities being equal, in the temperature range T = 1050–1250°C for 10–25 hours.

The worked out multistage diffusion procedure allows not only for the silicon surface of erosion to be relieved, which always occurs during the diffusion of these impurities, but also for the uniform doping of specimens with rather large dimensions ($3 \times 1 \times 0.5$ cm^3).

Conditions in separate ampoules being absolutely identical, the diffusion of sulfur, manganese, and selenium, as well as combinations of manganese and sulfur and manganese and selenium, was carried out. Mechanical and chemical treatment after homogenizing and preparation of ohmic contact, as well as the determination of physical parameters were carried out in all specimens under completely equal conditions. To assure the reliability of the results, five specimens were utilized for every temperature of diffusion. The findings of an investigation into the electric parameters of silicon specimens doped by sulfur and manganese, as well as by the combination of manganese with sulfur, are presented in the table.

It is ascertained that in silicon doped singly by manganese or sulfur, these impurities act as donors. The ionization energy of these impurity atom levels is determined from the photoconductivity and the Hall effect and is in good agreement with the literature data. However, as is obvious from the table, in the specimens doped jointly by sulfur and manganese Si⟨B, Mn, S⟩, at all investigated diffusion temperatures, the concentration of electroactive atoms of both sulfur and manganese became substantially lower than in specimens Si⟨B,Mn⟩ and Si⟨B,S⟩.

An interesting effect is observed in the specimens that were doped at T = 1100°C and were independent throughout the duration of diffusion; the specimens of Si⟨B,Mn,S⟩ acquire parameters close to the initial values (table); i.e., it is as though impurities of sulfur and manganese are absent. Because of this, the content of sulfur and manganese in specimens Si⟨B,Mn⟩, Si⟨B,S⟩, and Si⟨B,S,Mn⟩ doped by these impurities at T = 1100°C was examined with the help of the method of activation analysis. As the results show, the concentration of manganese and sulfur in specimens Si⟨B,S,Mn⟩ is 1.5–2 times greater than manganese in Si⟨B,Mn⟩ and

Outcome of investigation of electrical parameters of samples

Sample parameters by diffusion		Diffusion temperature	Sample parameters after diffusion			Electroactive atom concentration, cm^{-3}	
Resistivity, Ohm cm	Conductivity type	*T*, °C	Samples	Resistivity, Ohm cm	Conductivity type	Sulfur	Manganese
10	P	1250	Si⟨B, S⟩	0.4–0.5	n	2.4×10^{16}	
10	P	1250	Si⟨B, Mn⟩	$(3–4) \times 10^3$	n		2.1×10^{15}
10	P	1250	Si⟨B, S, Mn⟩	18–20	n	2.2×10^{15}	
10	P	1200	Si⟨B, S⟩	1.5–1.7	n	6×10^{15}	
10	P	1200	Si⟨B, Mn⟩	$(1–2) \times 10^3$	n		2.1×10^{15}
10	P	1200	Si⟨B, Mn, S⟩	25–30	n	2×10^{15}	
10	P	1150	Si⟨B, S⟩	6.5–7	n	3.1×10^{15}	
10	P	1150	Si⟨B, Mn⟩	$(3–4) \times 10^2$	n		2×10^{15}
10	P	1150	Si⟨B, Mn, S⟩	$(4–5) \times 10^4$	p	1.7×10^{15}	
10	P	1100	Si⟨B, S⟩	$(5–5.5) \times 10^2$	n	2.03×10^{15}	
10	P	1100	Si⟨B, Mn⟩	$(7–8) \times 10^3$	n		2×10^{15}
10	P	1100	Si⟨B, Mn, S⟩	10–11	p	$<10^{13}$	$<10^{13}$
10	P	1050	Si⟨B, S⟩	$(6–7) \times 10^3$	p	1.97×10^{15}	
10	P	1050	Si⟨B, Mn⟩	10^5	i		2×10^{15}
10	P	1050	Si⟨B, Mn, S⟩	85–90	p	1.8×10^{15}	

sulfur in Si⟨B,S⟩. This difference grows with the increase of the diffusion duration and diffusant vapor pressure.

The findings of the investigation of the spectral dependence of optical absorption photoconductivity in Si⟨B,S,Mn⟩ indicated the absence of any energy level of sulfur and manganese in the forbidden band of silicon; that is, all atoms of sulfur and manganese in these materials are electrically neutral. Such a behavior of sulfur and manganese atoms can be explained by the formation of electroneutral molecules ($S^{++}Mn^{--}$), $[S(s^2p^4) - 2e = S^{++}(s^2p^2)$ and $Mn(d^5s^2) + 2e = Mn^{--}(s^2p^2)$ among these impurity atoms.

Such molecules substitute two neighboring nodes in a silicon lattice, the covalent-tetrahedral bond in the lattice being not disturbed; therefore, atoms of sulfur and manganese cannot generate any energy levels in the forbidden band of silicon. As a result of such molecule formation, a new elementary cell of the ($Si_2S^{++}Mn^{--}$) type appears in the silicon lattice. It is noteworthy that the electroactive atom concentration of sulfur in Si⟨B,S⟩ and of manganese in Si⟨B,Mn⟩, doped at $T = 1250$°C, is $N_s = 2.4 \times 10^{16}$ cm^{-3} and $N_{Mn} = 2.1 \times 10^{15}$ cm^{-3}, correspondingly. These values are determined on the basis of experimental data (table) with consideration for the degree of ionization of the energy levels of these impurities in silicon. Thus, it is believed that the concentration of molecules ($S^{++}Mn^{--}$) is defined by the concentration of electroactive atoms of manganese in silicon at a given temperature, approximating about 10% of the electroactive atoms of sulfur in silicon. Furthermore, it is easy to verify that in specimens Si⟨B,S,Mn⟩, a concentration of sulfur electroactive atoms should remain that does not participate in the generation of molecules and is equal to no less than $N_s = 2 \times 10^{16}$ cm^{-3}; however, as is seen from the table, it is one order of magnitude less and comprises only $N \sim 2.2 \times 10^{15}$ cm^{-3}, that is, $N_c = 2 \times 10^{16}$ cm^{-3} sulfur atoms (this is just the concentration of molecules) take part in the generation of molecules. Naturally, this brings up the following question: What concentration of manganese should there be? It may be suggested that, on one hand, not only electroactive atoms of manganese, but also the electroneutral atoms participate in molecule generation. On the other hand, molecule formation stimulates the growth of manganese solubility; the more sulfur atoms there are, the more manganese atoms. The above-presented findings of the investigation into the activation analysis can serve as a corroboration of this suggestion. The concentration of molecules, depending on the concentration of sulfur in silicon, is calculated on the basis of the data presented in the table. From these data it is inferred that by controlling the concentration of sulfur in silicon, it is possible to control the concentration of molecules within a wide range, as well as the concentration and distribution of nanostructures on their base. Under common doping conditions, the control of the concentration of such molecules is limited due to the small solubility of these impurities in silicon. Because of this, the generation of nanosized structures on the basis of the given molecules and their influence on the silicon fundamental parameters is inessential. The elaborated multistage procedure of doping of silicon by impurity

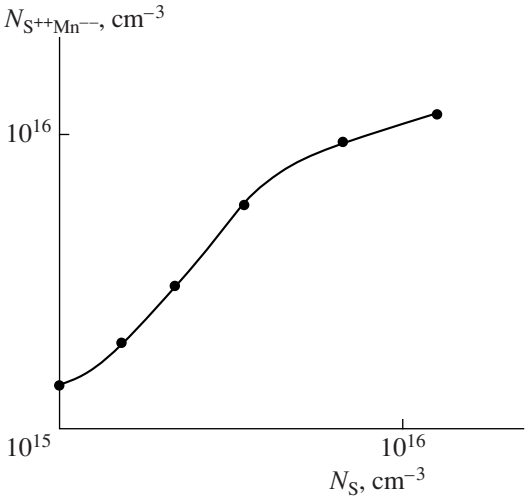

Molecule ($S^{++}Mn^{--}$) concentration versus sulfur concentration characteristic.

atoms permits a substantial increase in the concentration of the introduced impurity atoms and, respectively, the concentration of molecules and nanosized structures. The preliminary outcome of the investigation shows that, in specimens Si⟨B,S,Mn⟩ enriched with molecules ($S^{++}Mn^{--}$), an abnormally large photosensitivity in the region of $h\nu$ = 0.45–07 eV is observed, as well as an essential displacement of the fundamental absorption margin towards larger wavelengths.

Study of molecule generation among impurity atoms selenium and manganese in silicon has shown that, in this case, intensive formation of molecules $S^{++}Mn^{--}$ actually takes place. Effective thermodynamic conditions of molecule formation among atoms of selenium and manganese in Si are determined, as well as the dependence of the molecule concentration on the doping temperature.

At present, the technology permitting the control of the concentration, structure, and composition of nanosized structures on the basis of molecules ($S^{++}Mn^{--}$), ($Se^{++}Mn^{--}$) is being elaborated. The study of their effects on silicon fundamental parameters, as well as on the electric and photoelectric properties of such materials, is being conducted in order to unveil the functional capabilities of silicon with nanosized structures on the basis of molecules of impurity atoms.

REFERENCES

1. Mol'vidskii, M.G and Chadyshev, V.V., *FTP,* 1998, vol. 32, no. 5, pp. 513–552.
2. Bakhardykhanov, M.K., Askarov, Sh.I., and Norkulov N., *Phys. Stat. Sol.,* 1994, vol. 142, p. 339.
3. Taskin, A.A. and Tishkovskii, E.G., *FTP,* 2002, vol. 36, no. 6, p. 641.
4. Omel'yanovskii, M. and Fistul', V.I., *Impurities of Transient Metals in Semiconductors*, Moscow: Metallurgiya, 1983.
5. Bakhadyrkhanov, M.K., Zikrillaev, N.F., and Ayupov, K.S., *JTF,* 2006, vol. 76, no. 9, pp. 128–129.
6. Bakhadyrkhanov, M.K., Ayupov, K.S., and Sattarov, A., *FTP,* 2005, vol. 39, no. 7, pp. 823–825.

ISSN 1068-3755, Surface Engineering and Applied Electrochemistry, 2007, Vol. 43, No. 5, pp. 398–402. © Allerton Press, Inc., 2007.
Original Russian Text © M.A. Gasanov, 2007, published in Elektronnaya Obrabotka Materialov, 2007, No. 5, pp. 109–113.

OPERATING EXPERIENCE

Electric Discharge Treatment of Zeolites for Purifying the Waste Water of Polymer-Manufacturing Plants

M. A. Gasanov

Institute of Physics, Academy of Sciences of Azerbaijan, pr. Dzhavida 33, Baku, Azerbaijan

Received March 19, 2007

Abstract—We present the results of electric discharge treatment of zeolites for purifying the waste water from the manufacture of polymers. By application of the thermostimulated relaxation method, it has been revealed that in the zeolites, superficial and volumetric charges accumulate. It is shown that the electric discharge effects considerably enhance the efficiency of the adsorptive purification of waste water.

DOI: 10.3103/S1068375507050171

INTRODUCTION

At the present time, in many regions of Azerbaijan, water pollution has constituted a threat to human health and to pure water basins. Polluted waste water containing bacteria and heavy metals enter directly into water basins and the Caspian Sea, or it leaks into ground water, which is dangerous to people's health. Therefore, solving these problems and providing people and production facilities with pure water is a task of increasing urgency.

Several of these problems may be solved through electric treatment of liquids. The most important of these problems is the removal of highly dispersed inclusions. Such liquids are frequently waste waters from industrial polymer-manufacturing plants.

The waste water is formed in the course of the suspension polymerization and copolymerization of styrene during the utilization of suspension stabilizers—polyvinyl alcohols (PVAs); it essentially represents sedimentation and aggregative stable colloidal systems. In accordance with water-purification technology, it is necessary to preliminarily separate the disperse phase particles from styrene. [1].

The foaming polystyrene of PSB and PSVs grades is one of the most extensively used polystyrene plastics prepared by suspension polarization with the use of PVA as a stabilizer agent. The chief characteristics of the waste waters from the production of the indicated polystyrene, representing a mixture of mother solutions and flush waters, are presented in Table 1.

From the listed data, it becomes obvious that the waste waters are considerably polluted by organic substances—PVA monomers—as well as by the polymer, which is in a highly dispersed colloidal state. The waste waters are also polluted by mineral substances, but insignificantly, which is proven by the low values of calcined residues.

It is known that the solutions of high-molecular compounds and colloids, which are stabilized by protective compounds, are not very sensitive to addition of electrolytes. That is why heterocoagulation should be considered as the most acceptable method for the purification of waste water.

The performed experiments on the coagulation of a colloidal solution (waste water from the production of PSVs grade polystyrene) with the use of electrolytes (acids and salts), by heating, freezing out, action of ultrasonic oscillations, and destructive oxidation by hydrogen peroxide and lime chlorate did not yield positive results.

The purification of waste water by coagulation with aluminium sulfate proved to be an in efficient and very expensive method. When it is purified by coagulation with magnesium chloride, the flowrate of coagulant

Table 1

CCO (Chemical Consumption of Oxygen), mg O_2/l		– 14000
Optical density		– 100
pH		– 5
Residue, mg/l:		
	– dense	– 4600
calcined		– 60
Content, mg/l:		
	– PVA (polyvinyl alcohol)	– 500
	– styrene	– 20
color		– milk-white

increases up to 1.2–1.8 kg/m^3 water, which four to five times exceeds the consumption of magnesium chloride for the purification of diluted waste water; moreover, the purification efficiency decreases. All of the above methods require considerable flowrates of reagents to be used for purifying waste water (700 $MgCl_2$ t/year or 160–200 polycoagulants t/yr). The latter are either scarce ($MgCl_2$) or are so far not being manufactured on an industrial scale.

The purification of the waste water by the methods described above will induce an increase in the consumption of reagents. In connection with this, a reactant-free purification method has begun development, namely, an adsorptive one in an electric gas discharge.

The adsorptive processes of purification of waste water are extensively applied in the chemical industry and other branches of engineering. For the perspectives of the adsorptive method and its practical requirements, it is necessary to study the possibilities of further intensification of adsorptive processes and to develop a a means of monitoring them in the course of technological operations. One such way involves the application of electric discharges.

The effectiveness of the action of an electric discharge on the adsorptive processes is determined by its advantages, such as the possibility of direct interference in the adsorption process, power consumption, economical efficiency, and adaptability to manufacture [3–6].

In the present work, we applied the adsorptive method of simultaneous purification of waste waters from the production of polystyrene using the effects of electric discharges.

EXPERIMENTAL

Experiments were carried out with the use of clinoptilolite (zeolite—natural molecular sieves), large reserves of which can be found in the territory of the Republic of Azerbaijan (the Aidag deposit in the Tauz region).

The most recent investigations substantially expanded the range of application of natural zeolite: new technical possibilities of this mineral have been disclosed. The adsorption, ion-exchange properties of natural zeolite, and the ability to absorb electrically charged particles determine the large scale of its employment for scientific, technical, and technological purposes [2].

It has been established that the electric discharge activation of natural zeolites contributes to the more effective absorption of impurities from water; zeolites manifest a barrier role in relation to a series of substances obtainable from petroleum and oil products, benzene, phenol, etc.

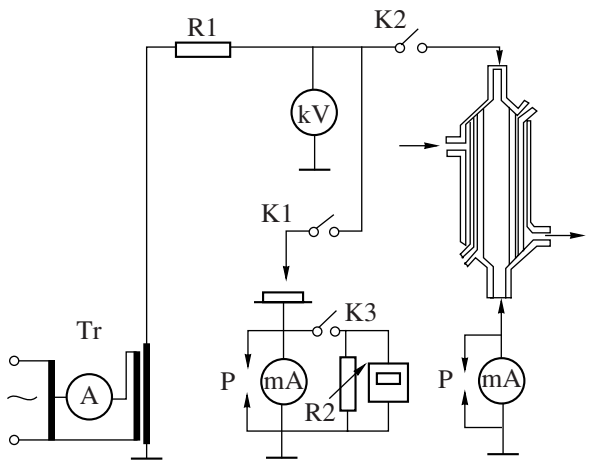

Fig. 1. The schematic electric diagram.

The indicated properties of zeolites activated by electric discharges make it possible to use them for purifying the waste water of industrial enterprises.

The experiments were carried out with the use of the influence of ozone on waste water, both separately and in combination with the adsorptive methods, as described in [7]. In all the experiments, other physical and technological parameters characterizing the purification processes remained strictly identical; therefore, it seems possible to compare the results obtained by various methods for purifying waste water.

For synthesizing ozone, we applied an ozonizing facility composed of an ozonizer proper, an AF-2 ozonometer, and a compressor providing oxygen.

The adsorbent was preliminarily subjected to heat treatment with evacuation at $T = 400$°C over 5 h.

A schematic electric diagram of treating adsorbents by electric discharges of barrier type is presented in Fig. 1.

The effect of electric discharge was tested in a special glass reactor with a built-in electrode system forming, in the interelectrode space, the configuration of a weakly nonuniform electric field with dielectric barriers. The effect of the barrier discharge was tested under an alternating voltage of 15 kV in a discharge current of 80 μA, with a treatment time of about 60 min. The technological schematic of the installation is shown in Fig. 2.

Natural zeolite, pretreated by a barrier electric discharge, was charged into a reactor. In the experiments, electrically treated and untreated samples of natural zeolite were utilized. The waste water from the production of polystyrene was passed at a certain constant flowrate through an ozonizer and a zeolite filter connected in series. After purification, each water sample, as well as that of the initial (unpurified water) sample, were subjected to chemical analysis for their contents of various impurities.

The results are presented in Table 2.

From the table, it is evident that the quantity of harmful impurities in the purified water has substan-

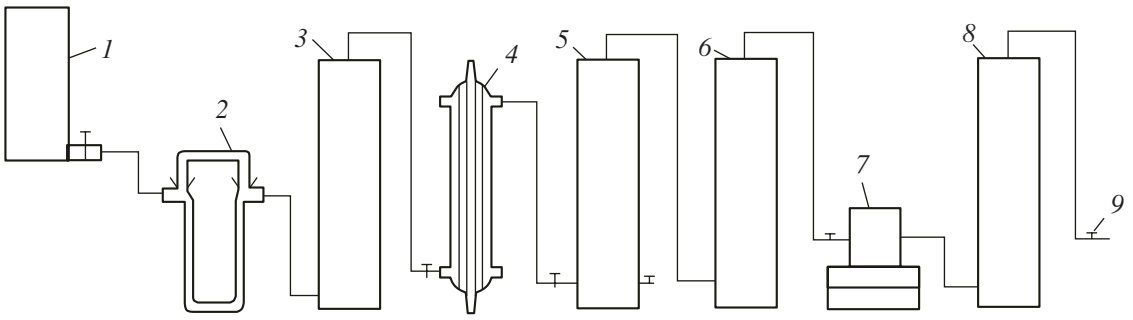

Fig. 2. Technological installation for the purification of waste water in polymeric industry. (*1*) Water reservoir; (*2*) rheometer; (*3*) settling tank; (*4*) ozonator; (*5*) reactor; (*6*) reactor; (*7*) pump; (*8*) settling tank; (*9*) valves.

tially decreased as compared to the initial one. The purified water may be utilized for production and technical purposes in a closed water-supply cycle.

Moreover, it is the activation of adsorbent and the ozonization of water that excludes the utilization of reagent, which renders the water purification process cheaper.

RESULTS AND DISCUSSION

Resolving the problem of intensifying the sorption processes with the help of electric fields and discharges requires studying the mechanism of changes in natural adsorbents subjected to electric effects. We have put forward a supposition that the adsorbability of natural, porous adsorbents under the effect of an electric field is due to the formation of the charged state, either on their surfaces or in bulk.

To reveal the charged state in the natural adsorbents of clinoptilolite, we used the thermostimulated relaxation (TSR) method, which is extensively applied to investigate the relaxation of electric charge in polymeric films and other dielectric materials [8].

The TSR method consists in the fact that the sample being tested is charged in an electric field (through polarization, corona discharge, electron bombardment, etc.); it is then discharged by short-circuiting on a current-detection device with simultaneous heating at a constant rate. The state of the sample material is judged from the obtained discharge current curve as a function of time or temperature.

The sample to be experimentally tested was natural porous clinoptilolite of $(Na_2K_2)OAl_2O_3 \cdot 10SiO_2 \cdot 8H_2O$ grade in the form of a finely fragmented glassy mass, into which the relict (clastogen) minerals are immersed. The basic mass was a fine-grained, glassy mineral represented by regular and crescent forms.

The clinoptilolite is preliminarily ground to powder, dried, and utilized in the form of tablets, cylinders or spheres. For producing granules in the form of pellets, cylinders as binders, clay, and chiefly amorphous coalite are added to the moistened zeolite powder. In some cases, metal powders are also employed as binders. It has been established that under the effect of high temperatures and pressures, the powder of natural clinoptilolite may be compressed into pellets that after

Table 2. Results of analysis of the samples of initial water and that purified by different methods

Characteristics	WATER		Treated by ozone	Preliminary treatment O_3 + clinoptilolite
	Initial	Untreated		
pH	5.1	4.5	4	3.5
CBR (chlorobutyl resin), mg O_2/l	14000	10700	9000	300
Optical density, rel. unit	100	80	60	0.25
Residue, mg/l:				
– dense	4600	3000	3000	338
– calcined	60	66	60	129
Content, mg/l:				
– of weighed substances	800	650	600	traces
– polyvinyl alcohol	500	300	200	70

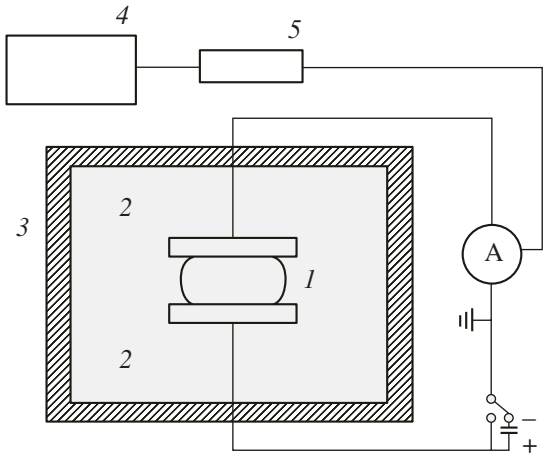

Fig. 3. Setup for electrifying the sample. (*1*) Sample; (*2*) electrodes; (*3*) thermostat; (*4*) temperature regulator; (*5*) two-coordinate self-recorder.

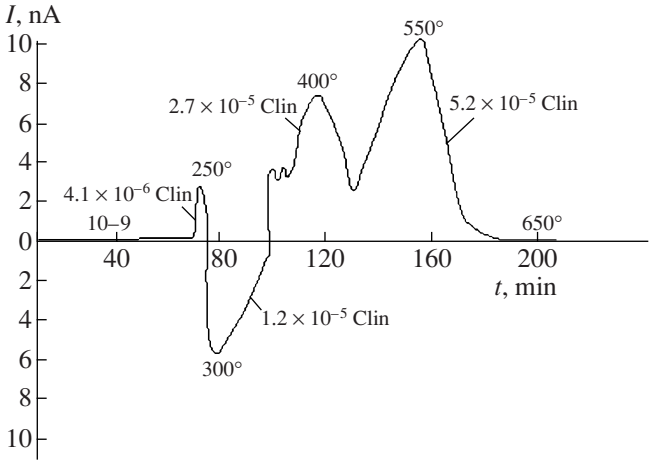

Fig. 4. Thermostimulated relaxation current of clinoptilolite as a function duration of the process.

calcination possess fairly high mechanical strength and activity.

Prior to utilization, clinoptilolite was subjected to heat treatment at $T = 350$°C with simultaneous evacuation over 5 h, and the samples were then treated by an electric discharge of corona or barrier type. Furthermore, aluminum electrodes 3 mm in diameter were applied from two opposite sides by the vacuum, thermal, spray-coating method with a thickness of the sprayed layer of $\Delta = 4$–5 μm. A sample was mounted in a special heating device between elastic, current pick-off elements made of stainless steel.

The TSR experiment was conducted by preheating a sample from room temperature to 600°C at a constant rate of 2°/min with simultaneous recording of the relaxation current curve as a function of temperature (and time) on a two-coordinate self-recorder complete with an amplifier. The linear character of heating was ensured by a special electronic device.

Figure 3 represents an installation for the electrification of samples.

Before each experiment, the sample was short-circuited for a time of 5–10 s, after which the measuring facility was switched-on, and the TSR current curve had been plotted.

The scheme in Fig. 4 represents a typical curve of a TSR current as a function of time for the clinoptilolite samples treated by a corona discharge at an alternating voltage. The presence of peaks on the TSR current curve proves the high temperature (about 250, 300, 400, 500°C) relaxations of an electric charge in the sample. The area just under the TSR current curve corresponds as a function of time to the total charge, which is relaxed in the sample.

Thus, all the factors enumerated above contribute to the enhancement of the adsorbability of clinoptilolite.

CONCLUSIONS

Hence, by application of the thermostimulation relaxation method, it has been demonstrated that the effects of electric fields and discharges on a natural, porous adsorbent—clinoptilolite of the $(Na_2K_2)OAl_2O_3 \cdot 10SiO_2 \cdot 8H_2O$) type—are conducive to the appearance of a charged state in it. It is the electric treatment of the adsorbents that expands the range of application of clinoptilolite in various technological processes.

The physical mechanisms of improvement in the adsorbability of clinoptilolite have been revealed.

REFERENCES

1. Nikitin, N.S. and Ivanov, V.I., Purification of Waste Water and Exhaust Gas in Chemical Industry, *Okhrana Truda Tekhnika Bezopasnosti*, no. 5, Moscow, 1968.
2. Tarasevich, Yu.I. and Ovcharenko, F.D., *Primenenie prirodnykh sorbentov dlya ochistki nefteproduktov i vody. Adsorbenty, ikh poluchenie, svoistva i primenenie* (The Application of Nature Sorbents for the Purification of Petroleum Products and Water. Adsorbents, Their Preparation, Properties and Application), M.M. Dubinin, Ed., 1976.
3. Gashimov, M.A., Kurbanov, K.B., Gasanov, M.A., and Zakieva, I.G., *Primenenie novykh elektrofizicheskikh metodov v protsessakh ochistki stochnykh vod* (The Application of Novel Electrophysical Methods in Processes of Purification of Industrial Waste Waters), *Izv. Azerb. Nats. Akad. Nauk, Ser. Fiz.-Mat. Tekh., Fiz. Astronom.*, 2004, no. 3, pp. 81–83.

4. Khalilov, E.N. and Bagirov, R.A., *Prirodnye tseolity, ikh svoistva, proizvodstvo i primenenie* (Natural Zeolites, their Properties, Production and Application), Baku–Berlin: 2002, p. 347.

5. Gasanov, M.A., *Tretichnaya ochistka stochnykh vod pri vozdeistvii elektricheskim razryadom. Problemy energetiki* (The Third Purification of Waste Waters under the Effect of Electric Charge. Problems of Power Engineering), Baku: Elm, 2004, no. 3, pp. 58–61.

6. Gashimov, A.M., Aliev, V.A., Kurbanov, K.B., and Gasanov, M.A., The Electric Discharge Treatment of Zeolites for Purifying the Waste Waters, Fiz. Khim. Obrab. Mater., Moscow: 2005, no. 2, pp. 86–87.

7. Gashimov, M.A., Gurbanov, K.B., Mekhtizade, R.N., and Gasanov, M.A., Physicochemical Method for Purifying the Waste Waters of Leather Production with the Use of Electric Effects, *Elektron. Obrab. Mater.*, 2004, no. 5, pp. 84–87.

8. *Elektrety* (Electrets), Sesler, M., Ed., 1983, pp. 106–148.

ISSN 1068-3755, Surface Engineering and Applied Electrochemistry, 2007, Vol. 43, No. 5, pp. 403–407. © Allerton Press, Inc., 2007.
Original Russian Text © A.P. Rizun, Yu.V. Golen', V.A. Pozdeev, T.D. Denisyuk, 2007, published in Elektronnaya Obrabotka Materialov, 2007, No. 5, pp. 114–119.

OPERATING EXPERIENCE

Development of the Engineering Process for the Destruction of Strong Grounds by Electric Discharge Initiated by Exothermal Compositions

A. P. Rizun, Yu. V. Golen', V. A. Pozdeev, and T. D. Denisyuk

Institute of Impulse Processes and Technologies, Ukrainian National Academy of Sciences, Oktyabr'skii pr., 43a, Nikolaev, 54018 Ukraine

Received March 21, 2007

Abstract—The specific features of the development of the engineering process for the destruction of strong grounds by electric discharge initiated by exothermal compositions are considered. The energetic regimes of initiated electric discharge that ensure effective destruction of strong bottom grounds have been investigated. It has been shown that the electric discharge destruction process meets all of the requirements on safe engineering and norms of efficiency in the reconstruction of working seaports and river ports and other objects.

DOI: 10.3103/S1068375507050183

The development of new, effective, and environmentally suitable and safe destruction methods of strong grounds on the territory of operating plants where the use of explosive materials (EMs) is inadmissible and the mechanical methods are inexpedient, is an extremely urgent problem, especially in advancing market relations, where reconstruction of outdated objects is required to increase competitiveness.

The objective of this study is to establish the energetic regimes of an initiated electric discharge that facilitates effective destruction of strong grounds.

The results of earlier investigations [1–3] have confirmed the reality of achieving the stated objective, through which the possibility has been established of using electric charge for the destruction bottom of grounds and surface oversize.

The essence of the electric discharge destruction method lies in the use of shock waves and hydraulic pressures generated by high-voltage electric discharge. By analogy with the use of EMs [4], shot holes are made in the object being destroyed, which are then filled with water, and an electrode system is set up instead of EMs. As high voltage is applied on the electrode system, a discharge takes place within the discharge gap. The process is accompanied by widening of the discharge channel, growth in pressure (which may reach 10^9 Pa), and by the formation of a shock wave. As a result, cracks and destruction will develop within the shot hole.

The electric discharge method has a series of advantages as compared to EMs, namely:

—The possibility of regulating the energy in the ground destruction process.

—Absence of a shattering effect, so that fragment recession is absent.

—No harmful substances are exuded in the destruction process.

—Providing of prescribed, directed scabbing.

The results of the investigation have confirmed that electric discharge destruction method is an effective and indispensable for method destruction of strong grounds. It meets all safety requirements and allows under stored energy up to 100 kJ on the depth of occurrence 20 m also to destroy and to loose the rocks by strength up to 30 MPa with productivity up to 3 m^3/hour at small energy consumption. Underwater surveys have verified the environmental safety as for the flora and fauna preservation.

The destruction productivity attainment of more strong grounds up to 5–8 m^3/hour is possible, if to enlarge the stored electric discharge energy more than three times. Besides, it takes the effective force loading schemes design, lowering the ground integral strength to the showings, acceptable for subsequent mechanical working.

It has been stated [3], that one can enlarge in a few times the energy in the discharge channel and reduce the mass–dimensions showings of the electric technical systems at the expense of the discharge initiation by exothermal compositions (EC) without the safe technique upset. The exothermal compositions are water solutions of ammonium nitrate, as oxidizer, and aluminum powder as the fuel.

High–voltage electric discharge blast–hole destruction, high–voltage electric discharge initiated detonation, and blast–hole detonation of the EM make up the ground deformation zones in view of concentric spheres, dimensions of which depend on many factors, basically on the ground's physical–mechanical properties and on the explosive dynamic load power. When

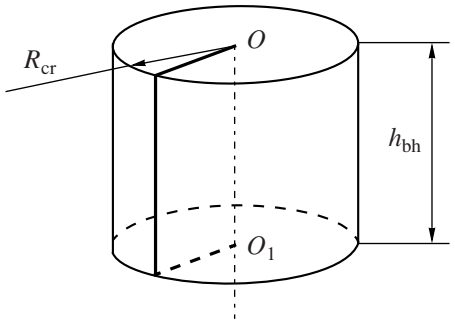

Fig. 1. The block destruction scheme in view of a radial crack.

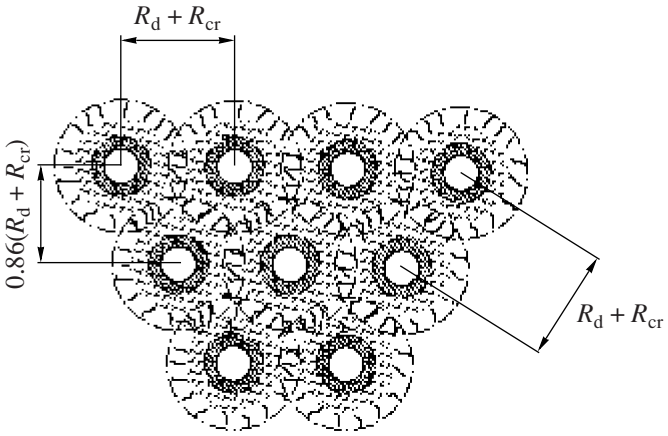

Fig. 2. The blast–holes arrangement scheme for loosing process. R_d—destruction radius; R_{cr}—cracking radius.

the electric discharge occurs on the ground–blast–hole interface, the shock wave squeezes the ground, at that the compression excesses ground's strength substantially, so that the ground is squeezed, forming a camouflet cavity, radius of which is far above than one of the blast–hole. The fracturing zone is arisen behind the camouflet one.

Different models are used for description of the ground deflected mode in the dependence on the power and duration of discharges. In the case of power electric discharge (electric explosion) a model of shock wave propagation is used. Under smaller discharges the model of cylindrical elastic wave in the infinity space may be considered. Approximated estimation of relation of fracturing (cracking) zone and discharge energy may be obtained by the method of the energetic analysis. Let a radial crack is formed in a cylinder as an action result of internal explosive circular efforts (Fig. 1). The cracks area is determined as

$$S_{cr} = R_{cr}h_{bh}, \quad (1)$$

where S_{cr}—cracks area, m^2; R_{cr}—radius of the cracks spreading zone, m; h_{bh}—blast–hole depth (loose depth), m.

Let estimate the necessary energy for such crack. Maximal circular effort is determined in Hooke's law agree:

$$F_p = E_g\frac{\delta}{l_{cr}}S_{cr}, \quad (2)$$

where F_p—maximal peripheral effort, kg/m^2; E_g—ground's coefficient of elasticity, kg/m^3; δ—cylinder's radial deformation, m; S_{cr}—cracks area, m^2; l_{cr}—cracks length ($l_{cr} = R_{cr}$), m.

One follows from (1) and (2)

$$F_p = E_g\delta h_{bh}. \quad (3)$$

Determine the middle effort as $F_p/2$. Then the work on the cracks forming (the ground strain) will be

$$A_p = \frac{1}{2}F_p\delta, \quad (4)$$

where A_p—the work on the cracks forming, J.

The deformation δ is determined from (3):

$$\delta = \frac{F_p}{E_g h_{bh}}. \quad (5)$$

Then the work on the cracks forming will be determined as

$$A_p = \frac{F_p^2}{2E_g h_{bh}}. \quad (6)$$

In turn, the efforts F_p value is in proportion to the tension stress σ_p and to the crack's area S_{cr}, i. e.

$$F_p = \sigma_p S_{cr}, \quad (7)$$

or

$$F_p = \sigma_p R_{cr} h_{bh}. \quad (8)$$

Then, the expression for the work subject to (8) takes the form

$$A_p = \frac{1}{2}\left(\frac{\sigma_p}{E_g}\right)\sigma_p h_{bh}R_{cr}^2. \quad (9)$$

As it has been shown in [5], for bottom grounds $\sigma_p \sim$ (10–20) MPa, E_g = (500–1000) MPa. Therefore, $\frac{\sigma_p}{E_g} \sim \frac{1}{500}$, and (9) takes the form:

$$A_p = \sigma_p h_{bh}R_{cr}^2 \times 10^{-3}. \quad (10)$$

On the other hand, the fracture energy in view of the cracks forming and the electric explosive energy (W_{ex}) are related in the following way:

$$A_p = \eta W_{ex}, \quad (11)$$

Table 1. Calculated meanings of the destruction zones volumes

10 g of EC PEM-40				20 g of EC PEM-40				30 g of EC PEM-40			
W, kJ	*V*, m^3/hour			*W*, kJ	*V*, m^3/hour			*W*, kJ	*V*, m^3/hour		
	30 MPa	40 MPa	60 MPa		30 MPa	40 MPa	60 MPa		30 MPa	40 MPa	60 MPa
82.50	0.84	0.64	0.44	152.5	1.56	1.2	0.8	222.5	2.28	1.72	1.16
95.00	0.96	0.72	0.48	165.0	1.68	1.28	0.84	235.0	2.44	1.8	1.2
107.50	1.12	0.84	0.56	177.5	1.84	1.4	0.92	247.5	2.6	1.96	1.38
120.00	1.28	0.96	0.64	190.0	1.96	1.52	1.0	260.0	2.72	2.0	1.32
132.50	1.38	1.04	0.68	202.5	2.12	1.56	1.04	272.5	2.88	2.12	1.44
145.00	1.52	1.16	0.76	215.0	2.28	1.68	1.12	285.0	3.0	2.2	1.48
157.50	1.64	1.2	0.8	227.5	2.32	1.76	1.2	297.5	3.08	2.36	1.52
170.00	1.76	1.32	0.92	240.0	2.48	1.88	1.28	310.0	3.28	2.44	1.6

Table 2. Distances between the blast–holes under the grounds loosing

Energy, kJ	Ground's compression strength									
	σ = 20 MPa		σ = 30 MPa		σ = 40 MPa		σ = 60 MPa		σ = 80 MPa	
	L_{st}	L_{int}	L_{st}	L_{int}	L_{st}	L_{int}	L_{st}	L_{int}	L_{st}	L_{int}
82	1.43	1.23	1.21	1.04	0.99	0.85	0.83	0.71	0.72	0.61
120	1.76	1.51	1.43	1.23	1.21	1.04	0.99	0.85	0.87	0.75
170	2.07	1.78	1.68	1.45	1.46	1.26	1.24	1.07	1.03	0.89
200	2.2	1.89	1.87	1.61	1.54	1.32	1.32	1.14	1.1	0.95
250	2.53	2.18	2.09	1.8	1.76	1.51	1.43	1.23	1.21	1.04
300	2.65	2.27	2.2	1.89	1.87	1.61	1.54	1.32	1.32	1.14
350	2.97	2.55	2.42	2.08	2.09	1.8	1.76	1.51	1.43	1.23
400	3.19	2.74	2.64	2.27	2.2	1.89	1.87	1.61	1.54	1.32
450	3.52	2.74	2.86	2.46	2.53	2.18	2.09	1.8	1.76	1.51

where η—the relative value of the explosive energy useful use; W_{ex}—electric explosive energy, kJ. In conformity with [3] η = 0.5.

Equating the right–hand parts of expressions (10) and (11) we obtain the relation

$$W_{ex} = \frac{\sigma_p h_{bh} R_{cr}^2}{\eta} \times 10^{-3}. \quad (12)$$

If *k* cracks are arisen after explosion, then

$$W_{ex} = \frac{k}{\eta} \times 10^{-3} \sigma_p h_{bh} R_{cr}^2. \quad (13)$$

Find from (13) the loose zone radius subject to cracks forming radius:

$$R_{cr} = \sqrt{\left(\frac{10^3 \eta}{k}\right) \frac{W_{ex}}{\sigma_p h_{bh}}}. \quad (14)$$

Usually the cracks number overlapping the cracking zone for strong rocks amounts $k = 20$ [5]. Then expression (14) will take the form

$$R_{cr} = \sqrt{B_E \frac{W_{ex}}{\sigma_p h_{bh}}}, \quad (15)$$

where B_E is the electric explosion energy counting factor, to be equal to

$$B_E = \frac{10^3 \eta}{k}. \quad (16)$$

B_E factor will be taken as 25. The η value under the electric explosion allows the heat leakage to the electrode system heating and the substance within the discharge channel itself.

The dependence (15) determines the cracking radii values of bottom rock, i. e., its weakening degree for subsequent mechanical working.

To estimate the destruction zones of bottom rock the rock's ultimate strength on pressing is taken into con-

Table 3. The diagrammatic work of the technological complex

The ground's strength, MPa	Working operations	Working operation time, min											Cycles number per 1 hour
		2	4	6	8	10	12	14	16	18	20	22	
20	Boring, perforator lifting												10
	Lattice girder turn												
	The electrode arrangement and the discharge												
40	Boring, perforator lifting												4.5
	Lattice girder turn												
	The electrode arrangement and the discharge												
60	Boring, perforator lifting												4
	Lattice girder turn												
	The electrode arrangement and the discharge												
80	Boring, perforator lifting												3
	Lattice girder turn												
	The electrode arrangement and the discharge												
100	Boring, perforator lifting												2.5
	Lattice girder turn												
	The electrode arrangement and the discharge												

Table 4. The productivity of electric discharge loosing vs. the ground's strength and the energy

Energy W, kJ	20 MPa		30 MPa		40 MPa		60 MPa		80 MPa		100 MPa	
	R, m	V, m^3/hour	R, m	V, m^3/hour	R, m	V, m^3/hour	R, m	V, m^3/hour	R, m	V, m^3/hour	R, m	V, m^3/hour
82.5	0.65	0.8	0.55	0.56	0.45	0.4	0.37	0.24	0.33	0.20	0.3	0.16
120.0	0.8	1.2	0.65	0.8	0.55	0.56	0.45	0.4	0.38	0.28	0.35	0.24
170.0	0.94	1.68	0.77	1.12	0.65	0.8	0.504	0.48	0.47	0.4	0.42	0.32
200.0	1.0	1.88	0.85	1.36	0.7	0.92	0.6	0.68	0.5	0.48	0.45	0.4
250.0	1.15	2.48	0.95	1.72	0.8	1.2	0.65	0.8	0.55	0.56	0.5	0.48
300.0	1.2	2.72	1.0	1.88	0.85	1.36	0.7	0.92	0.6	0.68	0.55	0.56
350.0	1.35	3.44	1.1	2.16	0.95	1.72	0.8	1.2	0.65	0.8	0.6	0.68
400.0	1.45	3.96	1.2	2.72	1.0	1.88	0.85	1.44	0.72	0.96	1.15	0.82
500.0	1.6	4.84	1.3	3.2	1.15	2.48	0.95	1.72	0.8	1.2	0.7	0.92

sideration, and, analogously with (15) the destruction zones radius may be determined from the relation

$$R_{\text{p}} = \sqrt{B_{\text{E}} \frac{W_{\text{ex}}}{\sigma_{\text{pr}} h_{\text{bh}}}}, \qquad (17)$$

where R_{d}—the destruction zone radius, m; σ_{pr}—the rock's ultimate strength on pressing, MPa.

Since the electric explosion is characterized by lowered ejection, i. e., the ratio of destruction zone radius is lesser than the blast–hole depth (cracking depth), the volume of destruction zone may be estimated in an approximated form by the formula

$$V = \pi R_p^2 h_{\text{bh}}, \qquad (18)$$

where V—the volume of destruction from every charge, m^3; h_{bh}—the blast–hole depth for the electric explosion with lowered blow-up equals to 0.6 m.

Table 1 shows calculated meanings of the destruction volumes by one-electrode system vs. sum electric charge energy being changed in (12.5–100) kJ limits and EC of 10; 20; 30 g mass.

Table 5. The productivity of electric discharge loosing vs. the ground's strength and the energy for two electrode system

Energy W, kJ	Productivity, m^3/hour					
	20 MPa	30 MPa	40 MPa	60 MPa	80 MPa	100 MPa
82.5	1.9	1.3	1	0.6	0.5	0.4
120	2.9	1.9	1.3	1	0.7	0.6
170	4	2.7	1.9	1.2	1	0.8
200	4.5	3.3	2.2	1.6	1.2	1
250	5.9	4.1	2.9	1.9	1.3	1.2
300	6.5	4.5	3.3	2.2	1.6	1.3
350	8.2	5.2	4.1	2.9	2	1.6
400	9.5	6.5	4.5	3.5	2.3	2
500	11.6	7.7	6	4.1	2.9	2.2

Using the calculated formulae (15) and (17), one can state the destruction and cracking zones. For massive loosing of bottom with subsequent mechanical working the blast–holes are arranged at distances $L_I = 0.86(R_d + R_{cr})$ with step $L_s = R_d + R_{cr}$. The blast–holes arrangement scheme is based on overlapping of the cracking zones from one charge to another in order to the critical completion of cracks having been formed in the ground. Table 2 shows the calculated step and interval values, and Fig. 2 illustrates scheme of power loading of the electric explosion at the bottom grounds under the electric charge loosing.

In order to determine the total necessary time for the loosing process, it should take into consideration the whole of preliminary work cycle, i. e., the time of blast–holes boring and also the working operations of the electrode laying and taking down.

The blast–holes boring time depends on the bottom ground strength, the blast–holes diameter, and on the perforator's type and power. Table 3 shows the diagrammatic work of the technological complex for the grounds of different strength.

Table 4 presents the calculation results of one–electrode system productivity for the grounds of different strength and the destruction energy in the dependence of cycle time. One has been stated in the bottom grounds destruction process, that the loosing volume from two electrodes working together is 1.2 times higher as compared with the case, when the electrodes work by turns. Therefore, Table 5 shows calculated dependencies of two–electrode system productivity for the grounds of different strength upon the energy liberation in the blast–hole under simultaneous operation of two electrodes.

Thus, the electric discharge in the complex with the exothermal compositions provides the required productivity of strong grounds destruction—from 5 to 8 m^3/hour, what allows to it to enter into competition with explosive materials use.

REFERENCES

1. Rizun A.R., Golen' Yu.V., and Yatsyuk S.A., Electric Discharge Destruction of Bottom Grounds, *Elektron. Obrab. Mater.*, 2006, no. 1, pp. 70–72.
2. Rizun A.R., Golen' Yu.V., and Mushtatnyii G.P., Experimental Investigations of the Electric Discharge Destruction of High-Strength Bottom Grounds, *Elektron. Obrab. Mater.*, 2006, no. 2, pp. 20–22.
3. Vovchenko A.I. and Posokhov A.A., *Upravlyaemye elektrovzryvnye protsessy preobrazovaniya energii v kondensirovannykh sredakh* (Controlled Electric Explosive Processes of the Energy Transform in the Condensed Media), Kiev: Naukova Dumka, 1992.
4. Vovk A.A., Chernyii G.I., and Kravets V.G., *Deiistvie vzryva v gruntakh* (The Explosion Action in the Grounds), Kiev: Naukova Dumka, 1974.
5. Kushnarev D.M. and Belikov M.P., *Vzryvnye raboty v gidromeliorativnom i sel'skom stroitel'stve* (Explosive Operations in the Irrigation and Drainage Construction and Farm Building), Moscow: Izd. Liter. po Stroit., 1972.